



Triple photons through third-order nonlinear optics

Adrien Borne

► To cite this version:

Adrien Borne. Triple photons through third-order nonlinear optics. Optics [physics.optics]. Université de Grenoble, 2014. English. NNT : . tel-01206943v1

HAL Id: tel-01206943

<https://theses.hal.science/tel-01206943v1>

Submitted on 30 Sep 2015 (v1), last revised 2 Dec 2016 (v2)

HAL is a multi-disciplinary open access archive for the deposit and dissemination of scientific research documents, whether they are published or not. The documents may come from teaching and research institutions in France or abroad, or from public or private research centers.

L'archive ouverte pluridisciplinaire **HAL**, est destinée au dépôt et à la diffusion de documents scientifiques de niveau recherche, publiés ou non, émanant des établissements d'enseignement et de recherche français ou étrangers, des laboratoires publics ou privés.

THÈSE

Pour obtenir le grade de

DOCTEUR DE L'UNIVERSITÉ DE GRENOBLE

Spécialité : **Physique de la matière condensée et du rayonnement**

Arrêté ministériel : 7 août 2006

Présentée par

Adrien BORNE

Thèse dirigée par **Benoît BOULANGER**

et codirigée par **Kamel BENCHEIKH**

préparée au sein de l' **Institut Néel**

et de l'**Ecole Doctorale de Physique de Grenoble**

Triple photons through third-order nonlinear optics

Thèse soutenue publiquement le **22 septembre 2014**,
devant le jury composé de :

M. Eric LACOT

Professeur à l'Université Joseph Fourier - Grenoble 1, Président

Mme Sara DUCCI

Professeur à l'Université Denis Diderot - Paris VII, Rapporteur

M. John DUDLEY

Professeur à l'Université de Franche-Comté, Rapporteur

M. Pierre BOURDON

Ingénieur de recherche senior à l'ONERA, Examineur

M. Sébastien TANZILLI

Chargé de recherche au LPMC, CNRS / Université Sophia Antipolis, Examineur

M. Benoît BOULANGER

Professeur à l'Université Joseph Fourier - Grenoble 1, Directeur de thèse

M. Kamel BENCHEIKH

Chargé de recherche au LPN, CNRS, Co-Directeur de thèse



"L'auteur étudie le lancement de la tomate qui provoquait la *réaction yellante* chez la cantatrice et démontre que plusieurs aires de la cervelle étaient impliquées dans la réponse, en particulier le trajet légumier, les nuclei thalamiques et le figure musicien de l'hémisphère nord."

– Georges Perec, *Mise en évidence expérimentale d'une organisation tomatotopique chez la soprano (Cantatrix sopranica L.)*

Remerciements

"Lorsqu'on quitte un lieu de bivouac, prendre soin de laisser deux choses.
Premièrement: rien. Deuxièmement: ses remerciements."

– Sylvain Tesson, *Dans les forêts de Sibérie*

Les trois protagonistes de l'affaire qui suit ont rythmé mes trois dernières années en m'emmenant avec eux pour une folle randonnée au long cours. Chemins mal balisés aux passages exposés, bruit lancinant de la source à 10 Hz, noir éclatant des galeries sans ouverture, questionnements obsédants, `crtl+↑+R` compulsifs. Il serait donc indélicat, sinon de remercier, au moins de mentionner ces étonnants amis imaginaires, les triplets de photon. Tantôt Riri, Fifi, Loulou, tantôt Alexeï, Ivan et Dimitri Karamazov. Terriblement attachants, les zèbres.

Toutes les boussoles, frontales et bonnes rigolades acheminées en nombre par mes collègues, mes amis et ma famille nécessitent la rédaction de ces quelques pages.

Je souhaite tout d'abord remercier mille fois Benoît, le "vieux renard rusé", pour la grande confiance qu'il m'a accordé, pour son implication de mes tout premiers pas de thésard à la sentence finale, pour son calme olympien si chaleureux et réconfortant. Egalement pour la rapidité avec laquelle il a assimilé mon prénom de six lettres seulement, et pour ses expressions saisissantes. Faute de grives, on mange des merles, en effet. Un grand merci à Kamel pour ses conseils quantiques et son encadrement malgré la distance.

Je tiens à remercier vivement tous les membres du jury, Pierre Bourdon, Sara Ducci, John Dudley, Eric Lacot et Sébastien Tanzilli d'avoir accepté d'évaluer mon travail et pour l'intérêt qu'ils y ont porté. Merci pour les questions, les suggestions, les commentaires. Mention spéciale à Pierre pour m'avoir accueilli à l'ONERA pour les calculs sur les matériaux chalcogénures.

Merci à tout le groupe de Grenoble pour la bonne humeur quotidienne : à.... Audrey de m'avoir initié aux triplets lorsque je n'étais que jeune stagiaire, puis d'avoir veillé avec attention à mes questionnements existentiels qui suivirent. Benjamin, Tomotaka, et Pierre, *mes* magnifiques "stagiaires/visiteurs" successifs pour l'aide précieuse à la traque des loups, chants russes et autres *Dies Irae*. Patricia pour l'enthousiasme et l'énergie débordants, les petits trucs magiques de manips et toutes les folles histoires qui vaudraient la peine d'être publiée sous le titre de *Jambe de bois et autres contes*. Corinne pour son aide quotidienne et ses conseils précieux dans la salle toute noire avec les sources capricieuses et les expériences désespérantes. David également pour son aide dans cette même salle toute noire : face à l'adversité, nous ne sommes jamais trop

nombreux. Jérôme pour les tailles et les polissages des terribles cristaux de dioxyde de titane. Vincent, Ichiro, puis Elodie et Pathy pour la compagnie rassurante “de l’autre côté du rideau” et les innombrables blagues. Sandra pour le sourire sans égal, qui devrait me remercier de lui avoir appris le français ! Véronique, arrivée *in extremis* avant la fin de ma thèse, pour les discussions et les conseils de l’avant-soutenance. Bonne chance pour les manip à venir.

Merci également à l’équipe Nano-Optique et Forces de l’Institut de m’avoir permis d’effectuer mes clivages de fibres sur leur diamant tranchant, au pôle Instrumentation pour le prêt de la caméra, à Johan et aux pôles Cryogénie, Electronique et Optique pour le travail sur le détecteur bientôt dans les bacs, et aux collègues de la fac pour mes débuts devant le tableau.

Pour tous les bons moments au labo, merci également aux *autres*¹. Et en particulier à toute la joyeuse bande de thésards et assimilés : Anne-Miranda, Mehdi-Ben, Joséphine, Manue, Marta, Vinicius, Lei, Sonia, Sophie, Denis, Pauline, Khalil, Justin, et puis les zozos d’optique que je ne vais quand même pas nommer deux fois. En souvenir des *bremzels* suisses et glaces à l’italienne 10 boules (plus peut-être ?), des moments en canoë et bataille de boules de neiges, des interminables bols de carottes rapées, de la Bobine et autres bars écossais dans les églises, et tant d’autres. Je n’oublie pas Manu, le voisin d’en face, l’homme chat.

"Ils étaient toute une bande, une fine équipe. Ils se connaissaient bien ; ils avaient, déteignant les uns sur les autres, des habitudes communes, des goûts, des souvenirs communs. Ils avaient leur vocabulaire, leurs signes, leurs dadas. Trop évolués pour se ressembler parfaitement, mais, sans doute, pas encore assez pour ne pas s’imiter plus ou moins consciemment, ils passaient une grande partie de leur vie en échanges. Ils s’en irritaient souvent ; ils s’en amusaient plus souvent encore."

– Georges Perec (encore !), *Les choses*

Les triplets de photons, c’est bien beau, mais c’est pas le tout ! Merci aussi aux formidables copains d’ici et de plus loin, champenois, bourguignons, canadiens, rhônalpins. Ceux qui donnent mal à la tête à faire le tour du monde trois fois par an (oui ça c’est toi Amou !). Aux musiciens de tous ces groupes évidemment, j’en ai passé du temps avec vous ; aux montagnards ; aux théâtres ; à mes joyeux colocs... Vous êtes nombreux à avoir fait, de près ou de loin, mes trois dernières années. Une liste de noms, c’est plutôt ennuyeux (et je risquerais de faire des oublis). Mettez donc votre nom ici, de votre écriture élégante et de votre encre fraîche, ce sera nettement plus beau : merci ! Vous êtes loin d’être oubliés, sachez-le.

A mes auteurs et musiciens préférés, votre soutien et votre inspiration sont sans faille. Aux noix de coco et à la dame de FIP qui liront ces pages sans aucun doute.

Mes derniers mots – un immense merci – vont à ma famille qui a toujours été là pour moi. Pauline, Benjamin, papa, maman, pépère, mémère. Dans la langue d’ici : merci infiniment / indéfiniment, les deux mots vont bien, peu importe, et puis on a toujours un peu mélangé les mots de ce côté du pays. Je vous embrasse tous bien fort. Je pense à Julia et Henri.

Merci.

Vienne, novembre 2014

¹*autres* : nom masc. plur. nullement péjoratif pour désigner les sympathiques collègues qui ne font pas d’optique. Par choix, semble-t-il...

Contents

Table of contents	v
Introduction	1
1 Elements of theory	3
1.1 Classical parametric optics	4
1.1.1 Characteristics of electromagnetic waves in a dielectric medium	4
1.1.2 Linear optics	8
1.1.3 Nonlinear optics	11
1.2 Classical parametric crystal optics	20
1.2.1 Linear crystal optics	20
1.2.2 Nonlinear crystal optics	24
1.3 Classical parametric fiber optics	26
1.3.1 Generalities on step-index fibers	26
1.3.2 Transverse propagating modes	27
1.3.3 Nonlinear optics in a fiber geometry	32
1.4 Quantum nonlinear optics	35
1.4.1 Generators for quantum fields evolution	35
1.4.2 Propagation of the quantized electromagnetic field in a linear medium . .	35
1.4.3 Propagation of the quantized electromagnetic field in a nonlinear medium	38
1.4.4 Quantum states of light	40
1.4.5 Coherence of down-converted modes through parametric processes	41
1.5 Conclusion	44
2 State of the art and motivations	45
2.1 Motivations in the framework of nonlinear quantum optics	46
2.1.1 Twin photons	46
2.1.2 Photonic states with $N \geq 3$ particles	47
2.1.3 Motivation for triplet photon generation	48
2.2 Experiments and theory of triplet photon generation	49
2.2.1 Triplet photon generation through cubic nonlinear processes	49

2.2.1.1	Classical understanding of triple photons	49
2.2.1.2	Pioneer experiment	49
2.2.1.3	Alternative nonlinear media for the direct cubic interaction . . .	51
2.2.1.4	Quantum treatment	52
2.2.2	Alternatives to the direct generation of triplets	54
2.3	Correlation studies	58
2.3.1	Photon recombination	58
2.3.2	Theoretical quantum tomography	61
2.3.3	Coincidence measurements	62
2.4	Conclusion and experimental strategies	63
3	Third-harmonic generation and triple photon generation in bulk crystals:	
	KTP and rutile TiO₂	65
3.1	Bi-injected TPG in KTP	66
3.1.1	Description of the experiment	66
3.1.2	Spectral properties	68
3.1.2.1	Experimental data	68
3.1.2.2	Classical theory	69
3.1.3	Energetic properties, Kerr effect	70
3.1.3.1	Experimental data	70
3.1.3.2	Refinement of the model	71
3.1.4	Conclusion	75
3.2	Towards TPG in rutile TiO ₂	76
3.2.1	TiO ₂ characterization through a THG experiment in a cylindrical geometry	76
3.2.1.1	Rutile TiO ₂ in the literature	76
3.2.1.2	Theory on THG for TiO ₂	77
3.2.1.3	Description of the experiment	79
3.2.1.4	Phase-matching properties and Sellmeier equations	83
3.2.1.5	Third-order nonlinear coefficients	85
3.2.2	TPG in rutile TiO ₂	87
3.2.2.1	TPG phase-matching conditions	87
3.2.2.2	Theoretical conversion efficiency	89
3.2.2.3	Experimental attempt	91
3.2.2.4	Calculations out of phase-matching	92
3.2.3	Conclusion	93
3.3	Prospective for resonant TPG from a synchronously pumped third-order optical parametric oscillator	94
3.3.1	Synchronously pumped OPO	94
3.3.2	TPG configurations in OPO	95
3.3.2.1	DROPO	95
3.3.2.2	TROPO	102
3.3.3	Conclusion	105

4	Third-harmonic generation and triple photon generation in optical fibers	107
4.1	THG and TPG in $\text{GeO}_2 : \text{SiO}_2$ optical fibers	108
4.1.1	Fiber properties	108
4.1.2	Interaction and phase matching	110
4.1.3	Fiber characterization through a THG experiment	114
4.1.3.1	Experimental setup	114
4.1.3.2	THG involving LP_{01} and LP_{03} modes	116
4.1.3.3	THG involving other modes than LP_{01} and LP_{03}	134
4.1.3.4	Interactions other than THG	140
4.1.4	Spontaneous TPG	145
4.1.4.1	Conversion efficiencies calculation	145
4.1.4.2	Towards the experiment	148
4.1.5	Conclusion	153
4.2	Phase-matching properties of chalcogenide fibers	155
4.2.1	Chalcogenides photonic-crystal fibers	155
4.2.1.1	Properties of chalcogenides	155
4.2.1.2	Photonic-crystal fibers	155
4.2.1.3	Modelling of the photonic crystal fiber	158
4.2.2	Phase-matching condition and fiber design	161
4.2.3	Conclusion	166
	Conclusion	167
	A Notation table	173
	B TPG phase-matching in rutile TiO_2	175
	C Threshold intensities of the OPO configuration	179
C.1	Doubly resonant OPO	179
C.2	Triply resonant OPO	181
	D Form of the nonlinear component of the effective phase mismatch	183
D.1	Triplet photon generation	184
D.2	Third-harmonic generation	185
	E Résumé en français	187
	F Scientific production related to this PhD work	199
F.1	Publications	199
F.2	Oral communications	199
F.2.1	International invited conferences	199
F.2.2	Oral communications in international conferences	200
F.2.3	Posters in international conferences	200
F.2.4	Oral communications in national conferences	200

Bibliography	201
--------------	-----

Introduction

“L’immense majorité des gens ne sont pas obligés de regarder leur dîner droit dans les yeux avant de l’attaquer.”

– Tristan Egolf, *Le seigneur des porcheries*

This thesis focuses on the generation of triple photons by a third-order optical nonlinear parametric interaction in solid-state matter.

A triple photon, also called photon triplet, triplet as a shortcut or even triphoton, is a photonic three-particle highly correlated state. The most direct way of generating such a state comes from third-order nonlinear optics, *i.e.* the coupling between four electromagnetic waves. The corpuscular vision of light gives a fairly simple picture of it: a photon splits into three photons of lower energy, namely the triplet, during its interaction with a nonlinear medium. The energy conservation is then fulfilled. The coupling between light and matter occurs thanks to the third-order electric susceptibility of this medium. This medium is traditionally a crystal, as it allows the fulfillment of the momentum conservation, also called the phase-matching condition in the ondulatory point of view. The strong coherence of this generated state comes from the fact that the three photons arise from the same origin.

This phenomenon is then very similar to the one producing twin photons by a second-order nonlinear interaction. The apparition of twin photons in the 1970s has been at the heart of many developments in the fields of quantum optics, as in the demonstration of the violation of Bell inequalities [1]. Today they are fundamental elementary blocks of quantum information. Triplet photons might potentially also be involved in this story. They could for instance be used in an heralded pair protocol [2]: one of the three photons could herald the two others, forming a pair. But the motivations for generating such states with the peculiar property of entanglement are above all fundamental: their non-classicality is different from that of twins and their generation is an experimental challenge [3–14].

The first experimental demonstration of triplet photon generation (TPG) was performed in our group in Grenoble in 2004, in a configuration slightly different from the above description [13]. Two other beams were indeed stimulating the process, and therefore increasing the probability of generating triplets. The direct spontaneous generation, *i.e.* without any seeding which is called the third-order parametric fluorescence, has not been demonstrated so far. It is imputed to the extreme weakness of the conversion efficiency in bulk crystals because the waves

are not tightly confined, albeit the very large incoming intensities, of the order of 100 GWcm^{-2} [15]. Nonetheless, it has been shown that the important amount of stimulated photons hides the triplet correlations [16].

It is thus important to find a configuration that would enable the generation of triple photons with less seeding photons, or even none, in order to keep the coherence. The goal of this work is precisely to investigate two strategies so as to meet this need, from both experimental and theoretical points of view. The first strategy deals with TPG in bulk crystals, with the aim to place these crystals into a cavity in order to artificially increase the interaction length. The second one focuses on TPG in optical fibers, so that the interaction length can also be very long, and in addition the electromagnetic field can be much more confined, therefore involving larger intensities. A last advantage of isotropic fibers is that any second-order process that would pollute the TPG process is forbidden.

Chapter 1 gives the theory toolbox useful for the understanding of this work. The subject is approached with some general classical parametric optics, using polychromatic electromagnetic fields. These general considerations are then adapted to the specific cases of crystal optics on the one hand, and of fiber optics on the other hand. Finally, as the states we are studying cannot be fully understood through classical physics, basic quantum optics on nonlinear interactions are given.

Chapter 2 develops the motivations for studying triphoton states. It also gives a state of the art on the generation and the correlations studies of triple photons, before reminding our strategies.

Chapter 3 is devoted to the study of two oxide bulk crystals: KTP and rutile TiO_2 . An experimental energetic and spectral study of bi-stimulated TPG in KTP is performed. Then, linear and nonlinear properties of titanium dioxide are investigated experimentally through third-harmonic generation (THG), which is the exact reverse process of frequency degenerated TPG: three photons merge into one photon of higher energy. However, TPG in rutile TiO_2 is not possible to achieve due to a likely lack of phase matching. Finally, the potential of employing these crystals in an synchronously pumped optical parametric oscillator (OPO) is studied theoretically.

Chapter 4 deals with TPG in optical fibers. Because THG has a higher conversion efficiency than TPG, and these two processes fulfill the same phase-matching condition, THG is at first considered for designing at best TPG. A full experimental characterization is performed in germanium-doped silica fibers by studying their spectral, energetic, modal and polarization properties. A preparation of the TPG experiment in the same fibers is also done through a modal preparation of the beams and the investigation of the filtering stage. However, quantum calculations show that the generation rate is still too low for the present configuration. To overcome these difficulties, orientations are given on the basis of quantum calculations.

Lastly, the phase-matching properties for TPG in chalcogenide photonic-crystal fibers (PCF) are studied. These materials have giant nonlinearities, three order of magnitudes higher than oxides, which imply therefore higher conversion efficiencies.

Chapter

1

Elements of theory

"Il faut bien que je supporte deux ou trois chenilles si je veux connaître les papillons."

– Antoine de Saint-Exupéry, *Le petit prince*

Contents

1.1	Classical parametric optics	4
1.1.1	Characteristics of electromagnetic waves in a dielectric medium	4
1.1.2	Linear optics	8
1.1.3	Nonlinear optics	11
1.2	Classical parametric crystal optics	20
1.2.1	Linear crystal optics	20
1.2.2	Nonlinear crystal optics	24
1.3	Classical parametric fiber optics	26
1.3.1	Generalities on step-index fibers	26
1.3.2	Transverse propagating modes	27
1.3.3	Nonlinear optics in a fiber geometry	32
1.4	Quantum nonlinear optics	35
1.4.1	Generators for quantum fields evolution	35
1.4.2	Propagation of the quantized electromagnetic field in a linear medium	35
1.4.3	Propagation of the quantized electromagnetic field in a nonlinear medium	38
1.4.4	Quantum states of light	40
1.4.5	Coherence of down-converted modes through parametric processes	41
1.5	Conclusion	44

In this first chapter, we introduce some theory elements helpful for the understanding of this work. We first give some generalities on propagation of electromagnetic waves in a dielectric medium by reminding both linear and nonlinear properties of interactions between light and

matter. We then adapt them to our two experimental cases of crystal and fiber optics. We finally introduce some useful quantum optics, as the states generated through those interactions cannot be fully understood classically.

1.1 Classical parametric optics

1.1.1 Characteristics of electromagnetic waves in a dielectric medium

The triplet state of light that will be studied is generated from a nonlinear interaction between a laser light and a transparent solid-state medium. This light is considered as an electromagnetic wave propagating without loss in a homogeneous, dielectric and not magnetic medium. It is described in the laboratory cartesian frame with unit vectors $(\vec{u}_X, \vec{u}_Y, \vec{u}_Z)$ through its electric \vec{E} and magnetic \vec{H} fields. The light is taken to be progressive with a velocity c in the vacuum, unidirectional along \vec{u}_Z , linearly polarized along \vec{e} , and polychromatic with a peak centered at the circular frequency $\omega_0 = \frac{2\pi c}{\lambda_0}$ in the visible or near infrared range. It can be regarded at first as a plane wave, although this point is discussed in the next subsection 1.1.2. We adopt a classical description in this section.

Electric field As the temporal periodicity T of this field is much larger than the period $2\pi/\omega_0$ in the slowly varying envelope approximation, we decompose this plane wave in the Fourier space as follows [17]:

$$\begin{aligned}\vec{E}(\vec{r}, t) &= \int_{\mathbb{R}} \frac{d\omega}{2\pi} \vec{E}(\vec{r}, t, \omega) \\ &= \int_{\mathbb{R}} \frac{d\omega}{2\pi} \vec{E}(\vec{r}, \omega) e^{-i\omega t} \\ &= \int_{\mathbb{R}} \frac{d\omega}{2\pi} \underline{E}(\vec{r}, \omega) e^{i(k(\vec{r}, \omega)Z - \omega t)} \vec{e},\end{aligned}\tag{1.1}$$

where \vec{r} stands for (X, Y, Z) . $\underline{E} = |E| e^{i\phi}$ is the complex amplitude of the electric field, in Vm^{-1} ; $|E|$ and ϕ its real amplitude and initial phase respectively. We justify in Section 1.1.2 that the amplitude of the wave vector \vec{k} takes the form:

$$k(\vec{r}, \omega) = \frac{n(\vec{r}, \omega)\omega}{c},\tag{1.2}$$

n being the optical index of the medium that the light passes through.

The field at negative frequencies stands for its complex conjugate:

$$\underline{E}(\vec{r}, -\omega) = \underline{E}^*(\vec{r}, \omega).\tag{1.3}$$

Polarization The propagation of this oscillating electric field in a dielectric medium results in small valence electrons displacements around their equilibrium positions, these charges being strongly bounded together. As a result, electric dipole moments arise, leading to an induced macroscopic electronic polarization. Likewise, other polarization origins are possible even though

they are not occurring in the experimental situations described in this manuscript. First, displacements of atoms or ions lead to an atomic or ionic polarization. Second, in the case of polar molecules, the reorientation of the dipole moments under the action of the electric field brings an orientation polarization [18].

Optical nonlinearity In the limit where the amplitude of the exciting optical field at a given frequency ω remains small enough compared to the interatomic field, typically 10^{10} Vm^{-1} or equivalently 100 kWcm^{-2} in power density [19], the electrons motion remains confined in the bottom of the potential well, so that the resulting polarization evolves linearly with the field amplitude and thus oscillates at the same frequency ω : this is the linear polarization. However, this is not true anymore with intense electric fields, typically produced by lasers. In such a nonlinear regime, the induced dipole moments radiate not only at ω but also at other frequencies arising from a nonlinear polarization. As different spectral components are involved in the process, it is referred to as parametric optics.

Such effects have been first observed in 1961 by Franken *et al.* [20], very shortly after the laser invention, and theorized a year later by Armstrong *et al.* [21], opening the field of nonlinear optics.

For input power intensities below 100 GWcm^{-2} , the induced nonlinear polarization stays small and may be considered as a perturbation of the linear polarization. It is therefore modeled by expanding it in a Taylor series of the applied electric field \vec{E} . Then in the Fourier frequential domain, the total electronic polarization can be written [22]:

$$\begin{aligned} \vec{P}(\vec{r}, \omega) &= \sum_{n=0}^{+\infty} \vec{P}^{(n)}(\vec{r}, \omega) = \vec{P}^{(0)}(\vec{r}) + \varepsilon_0 \sum_{n=1}^{+\infty} \left[\bar{\chi}^{(n)}(\omega) : \left(\bigotimes_n \vec{E}(\vec{r}, \omega) \right) \right] \\ &= \vec{P}^{(0)}(\vec{r}) + \varepsilon_0 \left[\bar{\chi}^{(1)}(\omega) \cdot \vec{E}(\vec{r}, \omega) + \bar{\chi}^{(2)}(\omega = \omega_1 + \omega_2) : \left(\vec{E}(\vec{r}, \omega_1) \otimes \vec{E}(\vec{r}, \omega_2) \right) \right. \\ &\quad \left. + \bar{\chi}^{(3)}(\omega = \omega_1 + \omega_2 + \omega_3) : \left(\vec{E}(\vec{r}, \omega_1) \otimes \vec{E}(\vec{r}, \omega_2) \otimes \vec{E}(\vec{r}, \omega_3) \right) + \dots \right], \end{aligned} \quad (1.4)$$

where ε_0 is the vacuum permittivity, \bigotimes the tensorial product, and $:$ and \cdot are the contracted products. The expansion coefficient $\bar{\chi}^{(n)}$ is called the n^{th} order electric susceptibility tensor that is a rank $n + 1$ tensor, which amplitude decreases with n . Typically, non-zero elements of $\bar{\chi}^{(2)}$ tensors equal 10^{-12} mV^{-1} , while non-zero elements of $\bar{\chi}^{(3)}$ tensors reach $10^{-21} \text{ m}^2 \text{ V}^{-2}$. The tensor elements take real values in the case of a lossless medium, which corresponds to the present study where the propagation occurs in the transparency range of the materials we considered. The linear polarization is written $\vec{P}^{(1)}$, while the nonlinearities of order n are indicated as $\vec{P}^{(n)}$. $\vec{P}^{(0)}$ is the static polarization. It is important to notice that the induced polarization at a given frequency radiates an electric field at the same frequency. Therefore, incident and induced fields have to be considered together, as the different contributions cannot be separated.

It is also possible to give the temporal development of the polarization [19]:

$$\begin{aligned}
 \vec{P}(\vec{r}, t) &= \vec{P}^{(0)}(\vec{r}) + \varepsilon_0 \sum_{n=1}^{+\infty} \left[\int \cdots \int_{-\infty}^{+\infty} d\tau_1 \dots d\tau_n \bar{\bar{R}}^{(n)}(\vec{r}, t - \tau_1, \dots, t - \tau_n) : \left(\bigotimes_{i=1}^n \vec{E}(\vec{r}, \tau_i) \right) \right] \\
 &= \vec{P}^{(0)}(\vec{r}) + \varepsilon_0 \left[\int_{-\infty}^{+\infty} d\tau \bar{\bar{R}}^{(1)}(\vec{r}, t - \tau) \cdot \vec{E}(\vec{r}, \tau) \right. \\
 &\quad + \iint_{-\infty}^{+\infty} d\tau_1 d\tau_2 \bar{\bar{R}}^{(2)}(\vec{r}, t - \tau_1, t - \tau_2) : \left(\vec{E}(\vec{r}, \tau_1) \otimes \vec{E}(\vec{r}, \tau_2) \right) \\
 &\quad \left. + \iiint_{-\infty}^{+\infty} d\tau_1 d\tau_2 d\tau_3 \bar{\bar{R}}^{(3)}(\vec{r}, t - \tau_1, t - \tau_2, t - \tau_3) : \left(\vec{E}(\vec{r}, \tau_1) \otimes \vec{E}(\vec{r}, \tau_2) \otimes \vec{E}(\vec{r}, \tau_3) \right) + \dots \right],
 \end{aligned} \tag{1.5}$$

where $\bar{\bar{R}}^{(n)}$ are the temporal Fourier transforms of the susceptibility $\bar{\bar{\chi}}^{(n)}$. From now on, we will work under the assumption that there is no static polarization, in conformity with the materials we will consider.

Constitutive equations It is suitable to describe the propagation of light in terms of the displacement vector \vec{D} (Cm^{-2}), conveying both the incident electric field and the induced polarization [23]:

$$\vec{D}(\vec{r}, t) = \varepsilon_0 \vec{E}(\vec{r}, t) + \vec{P}(\vec{r}, t). \tag{1.6}$$

As light propagates in non-magnetic media, there is no induced magnetization \vec{M} . The magnetic field \vec{H} (Am^{-1}) is then directly proportional to the magnetic induction vector \vec{B} (T), the magnetic equivalent of \vec{D} [23]:

$$\vec{B}(\vec{r}, t) = \mu_0 \vec{H}(\vec{r}, t), \tag{1.7}$$

μ_0 being the vacuum permeability.

Maxwell equations Then, the evolution of light in a dielectric (*i.e.* electrical insulator) and non-magnetic medium is described through the following Maxwell equations [23]:

$$\vec{\nabla} \cdot \vec{D}(\vec{r}, t) = 0, \tag{1.8}$$

$$\vec{\nabla} \cdot \vec{B}(\vec{r}, t) = 0, \tag{1.9}$$

$$\vec{\nabla} \times \vec{E}(\vec{r}, t) = -\frac{\partial \vec{B}(\vec{r}, t)}{\partial t}, \tag{1.10}$$

$$\vec{\nabla} \times \vec{B}(\vec{r}, t) = \mu_0 \frac{\partial \vec{D}(\vec{r}, t)}{\partial t}. \tag{1.11}$$

For the considered plane wave propagating along Z , Equations (1.1) and (1.10) allow us to write the magnetic induction as a function of the Fourier components of the electric field:

$$\begin{aligned}
 \vec{B}(\vec{r}, t) &= \int_{\mathbb{R}} \frac{d\omega}{2\pi} \vec{B}(\vec{r}, t, \omega) \\
 &= \int_{\mathbb{R}} \frac{d\omega}{2\pi} \frac{n(\vec{r}, \omega)}{c} \vec{u}_z \times \vec{E}(\vec{r}, \omega) e^{-i\omega t} \\
 &= \int_{\mathbb{R}} \frac{d\omega}{2\pi} \frac{n(\vec{r}, \omega)}{c} \underline{E}(\vec{r}, \omega) e^{i(k(\omega)Z - \omega t)} \vec{u}_Z \times \vec{e}.
 \end{aligned} \tag{1.12}$$

Propagation equation Combining the constitutive and Maxwell equations (1.6), (1.10), and (1.11) together leads to the spatial and temporal evolution equation for the electromagnetic wave, namely the propagation equation:

$$\vec{\nabla} \times (\vec{\nabla} \times \vec{E}(\vec{r}, t)) + \frac{1}{c^2} \frac{\partial^2 \vec{E}(\vec{r}, t)}{\partial t^2} = -\mu_0 \frac{\partial^2 \vec{P}(\vec{r}, t)}{\partial t^2}. \tag{1.13}$$

The wave propagating along the Z -axis, one can rewrite (1.13) in the Fourier domain for each frequency ω :

$$\frac{\partial^2 \vec{E}(\vec{r}, \omega)}{\partial Z^2} + \left(\frac{\omega}{c}\right)^2 \vec{E}(\vec{r}, \omega) = -\mu_0 \omega^2 \vec{P}(\vec{r}, \omega). \tag{1.14}$$

The right-hand side of Equations (1.13) and (1.14) is called the source term, composed of a linear and a nonlinear contributions.

While Section 1.1.2 focuses on the linear component of the polarization, Section 1.1.3 gives details on the nonlinear polarization.

Energetic considerations, conservation law Before going further into the resolution of Equation (1.14), it is important to have a look at the energetic properties of light, so as to define quantities that are actually directly usable for practical situations. These properties can be described by the Poynting vector $\vec{\pi}$ (Wm^{-2}) [17]:

$$\vec{\pi}(\vec{r}, t) = \frac{1}{\mu_0} [\vec{E}(\vec{r}, t) \times \vec{B}(\vec{r}, t)]. \tag{1.15}$$

It is also relevant to consider the electromagnetic energy density:

$$w(\vec{r}, t) = \frac{1}{2} \vec{E}(\vec{r}, t) \cdot \vec{D}(\vec{r}, t) + \frac{1}{2} \vec{H}(\vec{r}, t) \cdot \vec{B}(\vec{r}, t). \tag{1.16}$$

$\vec{\pi}$ and w are linked by the following energy conservation law [24]:

$$\frac{dw(\vec{r}, t)}{dt} + \vec{\nabla} \cdot \vec{\pi}(\vec{r}, t) = 0. \tag{1.17}$$

From an experimental point of view, we then define three measurable quantities: the power density, the power and the energy.

- The mean value over the temporal period T of the Poynting vector defines the power density I (Wm^{-2}), usually called intensity by misnomer. This is the radiated power per unit area [17]:

$$I(\vec{r}) = \langle \|\vec{\pi}(\vec{r}, t)\| \rangle_T = \frac{1}{T} \int_T \vec{\pi}(\vec{r}, t) \cdot \vec{u}_Z dt = \frac{1}{2\mu_0} \left\langle \text{Re} \left\| \vec{E}(\vec{r}, t) \times \vec{B}^*(\vec{r}, t) \right\| \right\rangle_T. \quad (1.18)$$

In the limit where $T \gg \frac{2\pi}{\omega_0}$ and for polychromatic planes waves, the power density takes the form:

$$I(\vec{r}) = \frac{\varepsilon_0 c}{2T} \int_{\mathbb{R}} \frac{d\omega}{2\pi} n(\vec{r}, \omega) |\underline{E}(\vec{r}, \omega)|^2. \quad (1.19)$$

- Taking the flux of the Poynting vector by integrating over the transverse space defines the electromagnetic power \mathcal{P} (W) going through a surface S :

$$\mathcal{P}(Z, t) = \iint_S dSI(\vec{r}, t). \quad (1.20)$$

- Lastly, one can define the energy \mathcal{E} (J) by integrating the instantaneous power over time:

$$\mathcal{E}(Z) = \int_{\mathbb{R}} dt \mathcal{P}(Z, t). \quad (1.21)$$

1.1.2 Linear optics

We now come back to the propagation equation by considering at first the polarization through its linear component only. This polarization $\vec{P}^{(1)}(\vec{r}, t)$, or $\vec{P}^{(1)}(\vec{r}, \omega)$ in the Fourier space, can be written [17]:

$$\begin{aligned} \vec{P}^{(1)}(\vec{r}, t) &= \int_{\mathbb{R}} \frac{d\omega}{2\pi} \vec{P}^{(1)}(\vec{r}, \omega) e^{-i\omega t} \\ &= \varepsilon_0 \int_{\mathbb{R}} \frac{d\omega}{2\pi} \bar{\bar{\chi}}^{(1)}(\omega) \cdot \vec{E}(\vec{r}, \omega) e^{-i\omega t}. \end{aligned} \quad (1.22)$$

Linear susceptibility From Equations (1.6) and (1.22) up to the first order, we come up with:

$$\vec{D}(\vec{r}, t) = \varepsilon_0 \int_{\mathbb{R}} \frac{d\omega}{2\pi} \left[1 + \bar{\bar{\chi}}^{(1)}(\omega) \right] \cdot \vec{E}(\vec{r}, \omega) e^{-i\omega t}, \quad (1.23)$$

where $\bar{\bar{\chi}}^{(1)}$ is the linear electric susceptibility, a rank 2 tensor (3×3 matrix), whose elements are dimensionless.

Eigenvalues in the dielectric frame: principal indices As real (transparent medium) and symmetric (non-magnetic medium), the $\bar{\bar{\chi}}^{(1)}$ tensor is diagonalizable in a so-called optical or dielectric frame [23], denoted (O, x, y, z) . This can be shown using the conservation equation (1.17) along with definitions (1.15) and (1.16), and Maxwell equations (1.10) and (1.11). Therefore:

$$\overline{\overline{\chi}}^{(1)}(\omega) = \begin{pmatrix} \chi_{xx}^{(1)}(\omega) & 0 & 0 \\ 0 & \chi_{yy}^{(1)}(\omega) & 0 \\ 0 & 0 & \chi_{zz}^{(1)}(\omega) \end{pmatrix}. \quad (1.24)$$

Such a frame makes calculation easier, and will be used mostly next. The x , y and z -axes are called the principal axes of the dielectric frame. The linear susceptibility $\overline{\overline{\chi}}^{(1)}$ is related to the relative permittivity $\overline{\overline{\epsilon}}_r$ through the relationship:

$$\overline{\overline{\epsilon}}_r(\omega) = 1 + \overline{\overline{\chi}}^{(1)}(\omega). \quad (1.25)$$

Propagation equation Equation (1.14) then becomes:

$$\frac{\partial^2 \vec{E}(\vec{r}, \omega)}{\partial Z^2} + \left(\frac{\omega}{c}\right)^2 \left(1 + \overline{\overline{\chi}}^{(1)}(\omega)\right) \cdot \vec{E}(\vec{r}, \omega) = 0. \quad (1.26)$$

The first order susceptibility is linked to the refractive index n introduced in Equation (1.2) by the equation:

$$\left[1 + \overline{\overline{\chi}}^{(1)}(\omega)\right] \cdot \vec{E}(\vec{r}, \omega) = n(\vec{r}, \omega) \left[\vec{E}(\vec{r}, \omega) - \left(\vec{e} \cdot \vec{E}(\vec{r}, \omega)\right) \vec{e}\right]. \quad (1.27)$$

n is a scalar quantity. In the general case, it varies as a function of the direction of propagation \vec{r} . We will see later on that it is expressed as a function of the principal refractive indices n_x , n_y and n_z that are defined as:

$$n_i(\omega) = \sqrt{1 + \chi_{ii}^{(1)}(\omega)}, \quad i \in \{x, y, z\}. \quad (1.28)$$

Equations (1.23) and (1.24) show that \vec{E} and \vec{D} vectors are not collinear in the general case: they make an angle ρ called the double refraction angle. It will also be discussed in Section 1.2.1.

This dielectric frame differs from the orthogonal laboratory frame (O, X, Y, Z) already mentioned. In the case of a propagation in a crystal, it also differs from the crystallographic frame (O, a, b, c) related to the primitive cell [25]. It can be noted that the latter frame is not necessarily orthogonal.

The wave propagation direction, along the wave vector \vec{k} , is located using the spherical angles (θ, φ) as depicted in figure 1.1.

Linear solutions

- **Plane wave solution** A first solution of the linear equation (1.26) is the progressive plane wave, which justifies the assumption already made. In the temporal domain, and for a given frequency (see Equation (1.1)):

$$\vec{E}(\vec{r}, t, \omega) = \underline{E}(\vec{r}, \omega) e^{i(k(\vec{r}, \omega)Z - \omega t + \phi)} \vec{e}. \quad (1.29)$$

- **Gaussian solution** The Gaussian form in space and time for the electric field is also a solution of this linear equation. It is moreover a better description as far as laser

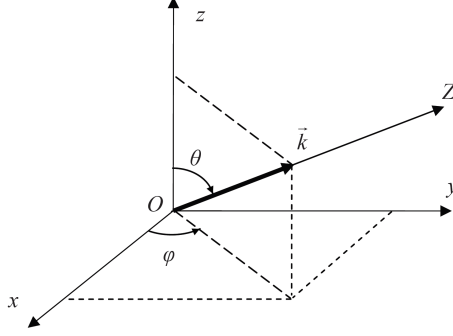


Figure 1.1 – Wave vector \vec{k} in the dielectric frame (O, x, y, z) .

experiments are concerned. Here, for a temporal pulsed beam, and at a given frequency, the modulus and phase of the electric field are:

$$|\vec{E}(\vec{r}, t, \omega)| = E_0 \frac{W_0}{W(Z)} e^{-\left(\frac{x^2+y^2}{W^2(Z)}\right)} e^{-\left(\frac{t}{\tau/2}\right)^2}, \quad (1.30)$$

$$\arg(\vec{E}(\vec{r}, t, \omega)) = k(\vec{r}, \omega) \left(Z + \frac{X^2 + Y^2}{2R(Z)} \right) - \Phi(Z) - \omega t + \phi, \quad (1.31)$$

where W_0 is the minimum value of the beam transverse extension, called the beam waist radius; τ the pulse duration; W the radius of the beam, taken at $1/e^2$ of its maximum; R the radius of curvature; and Φ the Gouy phase. These three last quantities are expressed as a function of the Rayleigh parameter Z_R as [26]:

$$W(Z) = W_0 \sqrt{1 + \left(\frac{Z}{Z_R}\right)^2}, \quad (1.32)$$

$$R(Z) = Z \left(1 + \left(\frac{Z_R}{Z}\right)^2 \right), \quad (1.33)$$

$$\Phi(Z) = \arctan\left(\frac{Z}{Z_R}\right), \quad (1.34)$$

and

$$Z_R(\vec{r}, \omega) = \frac{\pi n(\vec{r}, \omega) W_0^2}{M^2 \lambda}. \quad (1.35)$$

M^2 is the quality factor [27]. $M^2 = 1$ for an ideal gaussian beam, and $M^2 > 1$ in most actual situations. The beam position is defined here at the waist, *i.e.* $Z = 0$. Z_R defines the longitudinal length where the beam can actually be considered as a plane wave, as shown in Figure 1.2.

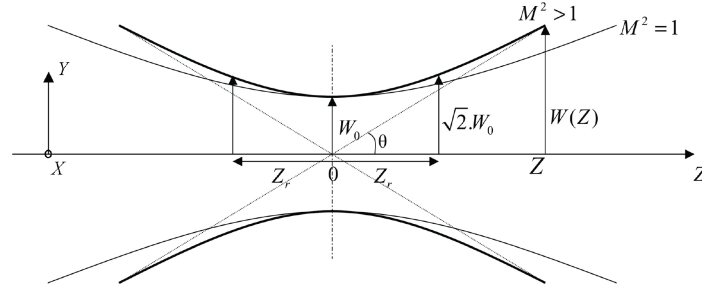


Figure 1.2 – Spatial evolution of a gaussian beam.

Dispersion of the refractive index, Sellmeier equation The principal refractive indices are frequency dependent: this phenomenon is called dispersion. Indeed, atoms in the matter can be interpreted as harmonic oscillators in a potential well perturbed by an electromagnetic field. The polarization induced by the oscillators depends on the exciting wavelength. This Lorentz theory for oscillators leads to the so-called Sellmeier equation [28]:

$$n_i(\lambda) = \sqrt{C_{i,1} + \sum_{k=2}^m \frac{C_{i,k}}{1 - P_{i,k} \lambda^{-q_{i,k}}}}, \quad i \in \{x, y, z\}. \quad (1.36)$$

The P coefficients are the poles and define the resonance wavelengths of the absorbers. The C coefficients define the poles strengths. The powers q are usually taken to 2. $(m - 1)$ corresponds to the number of oscillators. All those coefficients are empirical and depend on the medium. In most cases, between two absorbers (*i.e.* in the transparency range considered), the dispersion law is monotonically increasing and said to be “normal”, as opposed to “anormal” in the other case.

Propagation losses We work in non-absorptive spectral ranges as much as possible, *i.e.* far from resonant transitions. Nevertheless, absorption will be significant in some cases and the intensity will follow a Beer-Lambert law:

$$I(Z, \omega) = I(0, \omega) e^{-\alpha(\omega)Z}, \quad (1.37)$$

with α the attenuation constant, linked to the imaginary part of the first-order susceptibility. In the case of propagation in optical fibers developed in Section 1.3, several other effects are also responsible for losses: Rayleigh scattering at lower wavelengths ($\alpha(\lambda) \propto \lambda^{-4}$) because of inhomogeneities arising during the fabrication process [29], scattering at the core-cladding interface, fiber macroscopic and microscopic bends, and absorption by impurities such as OH^- ions introduced during the manufacture [30].

1.1.3 Nonlinear optics

There is no threshold for nonlinear terms to appear: they are always present, but only detectable for high enough excitation intensities, typically larger than 1 MW/cm^2 . Still, some frequency, momentum and symmetry compatibilities are required, and are the purpose of this section.

Among all the nonlinear contributions, the third-order nonlinear term is the one that is going to interest us. It is obvious that second-order nonlinear effects are more efficient than third-order ones, as part of the Taylor expansion (1.4), and also have to catch our attention.

Propagation equation with a nonlinear polarization We now develop the polarization up to the third order in Equation (1.14):

$$\frac{\partial^2 \vec{E}(\vec{r}, \omega)}{\partial Z^2} + \left(\frac{n(\vec{r}, \omega) \omega}{c} \right)^2 \vec{E}(\vec{r}, \omega) = -\mu_0 \omega^2 \left[\vec{P}^{(2)}(\vec{r}, \omega) + \vec{P}^{(3)}(\vec{r}, \omega) \right]. \quad (1.38)$$

$\vec{P}^{(2)}(\vec{r}, \omega)$ and $\vec{P}^{(3)}(\vec{r}, \omega)$, given in Equations (1.39) and (1.40), are the spectral second- and third-order nonlinear polarizations respectively, Fourier transforms of the temporal polarizations $\vec{P}^{(2)}(\vec{r}, t)$ and $\vec{P}^{(3)}(\vec{r}, t)$:

$$\begin{aligned} \vec{P}^{(2)}(\vec{r}, t) &= \int_{\mathbb{R}} \frac{d\omega_0}{2\pi} \vec{P}^{(2)}(\vec{r}, \omega_0) e^{-i\omega_0 t} \\ &= \varepsilon_0 \iint_{\mathbb{R}^2} \frac{d\omega_0}{2\pi} \frac{d\omega_1}{2\pi} \bar{\chi}^{(2)}(\omega_0 = \omega_1 + \omega_2) : \left[\vec{E}(\vec{r}, \omega_1) \otimes \vec{E}(\vec{r}, \omega_0 - \omega_1 = \omega_2) \right] e^{-i\omega_0 t}, \end{aligned} \quad (1.39)$$

$$\begin{aligned} \vec{P}^{(3)}(\vec{r}, t) &= \int_{\mathbb{R}} \frac{d\omega_0}{2\pi} \vec{P}^{(3)}(\vec{r}, \omega_0) e^{-i\omega_0 t} \\ &= \varepsilon_0 \iiint_{\mathbb{R}^3} \frac{d\omega_0}{2\pi} \frac{d\omega_1}{2\pi} \frac{d\omega_2}{2\pi} \bar{\chi}^{(3)}(\omega_0 = \omega_1 + \omega_2 + \omega_3) \\ &\quad : \left[\vec{E}(\vec{r}, \omega_1) \otimes \vec{E}(\vec{r}, \omega_2) \otimes \vec{E}(\vec{r}, \omega_0 - \omega_1 - \omega_2 = \omega_3) \right] e^{-i\omega_0 t}, \end{aligned} \quad (1.40)$$

where ω_0 , ω_1 , ω_2 and ω_3 are the frequencies of the interacting waves.

The $\vec{P}^{(2)}$ and $\vec{P}^{(3)}$ polarizations involve the second- and third-order nonlinear susceptibilities $\bar{\chi}^{(2)}$ and $\bar{\chi}^{(3)}$ respectively. In the most general case, the $\bar{\chi}^{(2)}$ tensor is composed of 27 independent elements: $\chi_{ijk}^{(2)}$, with $\{i, j, k\} \in \{x, y, z\}^3$; the $\bar{\chi}^{(3)}$ tensor of 81 independent elements: $\chi_{ijkl}^{(3)}$, with $\{i, j, k, l\} \in \{x, y, z\}^4$. Some symmetry considerations and approximations allow to reduce the number of independent elements. First, the orientation symmetry of the material can be considered in the light of the Neumann principle [25]. Note in particular that any centrosymmetric medium cannot allow three waves coupling to occur, since the tensor $\bar{\chi}^{(2)}$ is zero. In addition, under the assumption of propagation without absorption, the Kleinman principle [31] states that the $\bar{\chi}$ tensors are symmetric through permutation of the cartesian indices. Finally, under the same assumption, causality and time invariance, the ABDP symmetry [21] links the $\bar{\chi}$ elements at different frequencies through permutation of pulsations and cartesian indices.

Three-wave coupling, energy conservation The $\vec{P}^{(2)}(\vec{r}, \omega_0)$ component of Equation (1.39) is induced from the coupling of the electric field at the two frequencies ω_1 and ω_2 . It itself radiates a field at the frequency $\omega_0 = \omega_1 \pm \omega_2$. Therefore, such a process couples three wave components. It is referred to as a quadratic interaction, since it is quadratic in incident electric field.

From the previous comment, we will from now on speak about three different fields \vec{E}_0 , \vec{E}_1

and \vec{E}_2 , respectively centered at frequencies ω_0^c , ω_1^c and ω_2^c . Those fields coupled through a quadratic interaction obey the energy conservation law:

$$\hbar\omega_0 = \hbar\omega_1 + \hbar\omega_2, \quad (1.41)$$

where $(\omega_1, \omega_2) < \omega_0$, and \hbar is the Planck constant. Thus, let us shift a little from the classical frame as a corpuscular vision is here obvious [32] and allows us to draw up a list of the possible quadratic processes.

- The **parametric fluorescence, or spontaneous parametric down-conversion** (SPDC), is equivalent to a spontaneous scission of a photon of higher energy into two photons of lower energies: $\hbar\omega_0 \rightarrow \hbar\omega_1 + \hbar\omega_2$.
- The **sum-frequency generation** (SFG) is the reverse process: two photons merge into a photon of higher energy: $\hbar\omega_1 + \hbar\omega_2 \rightarrow \hbar\omega_0$. The degenerate case of the SFG interaction is called second-harmonic generation (SHG): $\frac{\hbar\omega_0}{2} + \frac{\hbar\omega_0}{2} \rightarrow \hbar\omega_0$. When a static field is involved in the process, an electro-optic interaction called Pockels effect can occur: $\hbar\omega + 0 \rightarrow \hbar\omega$.
- The **difference-frequency generation** (DFG) is a stimulated scission: $\hbar\omega_0 - \hbar\omega_1 \rightarrow \hbar\omega_2$. The optical rectification is its degenerate case, leading to the creation of a static field: $\hbar\omega - \hbar\omega \rightarrow 0$.

These three parametric interactions are depicted in Figure 1.3. In the energy diagrams, the dotted lines are virtual energy levels that do not correspond to existing energy levels in matter, excited out of resonance. The solid lines are ground states.

Four-wave coupling, energy conservation In the same fashion as previously, the $\vec{P}^{(3)}(\vec{r}, \omega_0)$ component of Equation (1.40) is induced from the coupling of the three electric field frequencies ω_1, ω_2 and ω_3 , so that it is called the cubic nonlinear polarization. It radiates at a new frequency $\omega_0 = \omega_1 \pm \omega_2 \pm \omega_3$. This process couples four wave components.

We will also refer to these wave packets as four different fields $\vec{E}_0, \vec{E}_1, \vec{E}_2$, and \vec{E}_3 , respectively centered at frequencies $\omega_0^c, \omega_1^c, \omega_2^c$ and ω_3^c . Their energies can be linked through two different energy conservation relationships [33]:

$$(A) \quad \hbar\omega_0 = \hbar\omega_1 + \hbar\omega_2 + \hbar\omega_3, \quad (1.42)$$

$$(B) \quad \hbar\omega_0 + \hbar\omega_1 = \hbar\omega_2 + \hbar\omega_3. \quad (1.43)$$

The nonlinear cubic processes of type A are listed below.

- The **parametric fluorescence, or spontaneous parametric down-conversion** (SPDC), is the spontaneous scission of a photon of higher energy into three photons of lower energies: $\hbar\omega_0 \rightarrow \hbar\omega_1 + \hbar\omega_2 + \hbar\omega_3$.
- The **sum-frequency generation** (SFG) is the fusion reverse process: three photons merge into a photon of higher energy, $\hbar\omega_1 + \hbar\omega_2 + \hbar\omega_3 \rightarrow \hbar\omega_0$. Its degenerate case is the

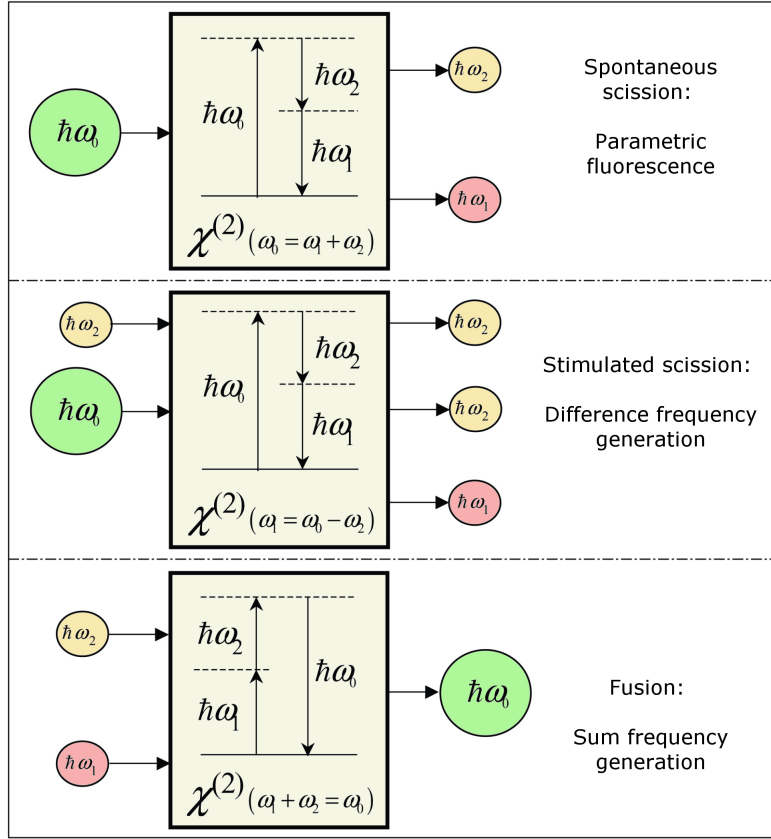


Figure 1.3 – Energy diagrams for the second-order parametric interactions.

third-harmonic generation (THG): $\frac{\hbar\omega_0}{3} + \frac{\hbar\omega_0}{3} + \frac{\hbar\omega_0}{3} \rightarrow \hbar\omega_0$. Alike in quadratic interactions, when static fields are involved, electro-optic effects can occur: for instance $\hbar\omega + 0 + 0 \rightarrow \hbar\omega$.

- The **difference-frequency generation** (DFG) is a stimulated scission. It can be monostimulated: $\hbar\omega_0 - \hbar\omega_1 \rightarrow \hbar\omega_2 + \hbar\omega_3$, or bistimulated: $\hbar\omega_0 - \hbar\omega_1 - \hbar\omega_2 \rightarrow \hbar\omega_3$.

The nonlinear cubic processes of type B are given below.

- The **four wave-mixing**¹ (FWM) corresponds to the merging of two photons that splits into two photons of different energies: $\hbar\omega_0 + \hbar\omega_1 \rightarrow \hbar\omega_2 + \hbar\omega_3$. Its totally degenerate case is called the Kerr effect, or self-phase modulation (SPM): $\hbar\omega + \hbar\omega \rightarrow \hbar\omega + \hbar\omega$. The cross-phase modulation (XPM) is the partially degenerated process: $\hbar\omega_0 + \hbar\omega_1 \rightarrow \hbar\omega_0 + \hbar\omega_1$. When working outside the transparency range, two photons at the same frequency can be absorbed resonantly ($\text{Im}(\bar{\chi}^{(3)}) \neq 0$): this is the two-photon absorption.
- The **Raman and Brillouin effects** follow the same photonic schemes, but include a phononic transition between to real energy levels in matter. It will be discussed further in Section 4.1.3.4.

The different cubic interactions are schemed in Figure 1.4. We can already note that type A

¹Note that this term can be misleading since all those processes are about mixing four waves.

cubic interactions are of particular interest for us as they will be involved in the production of photon triplets.

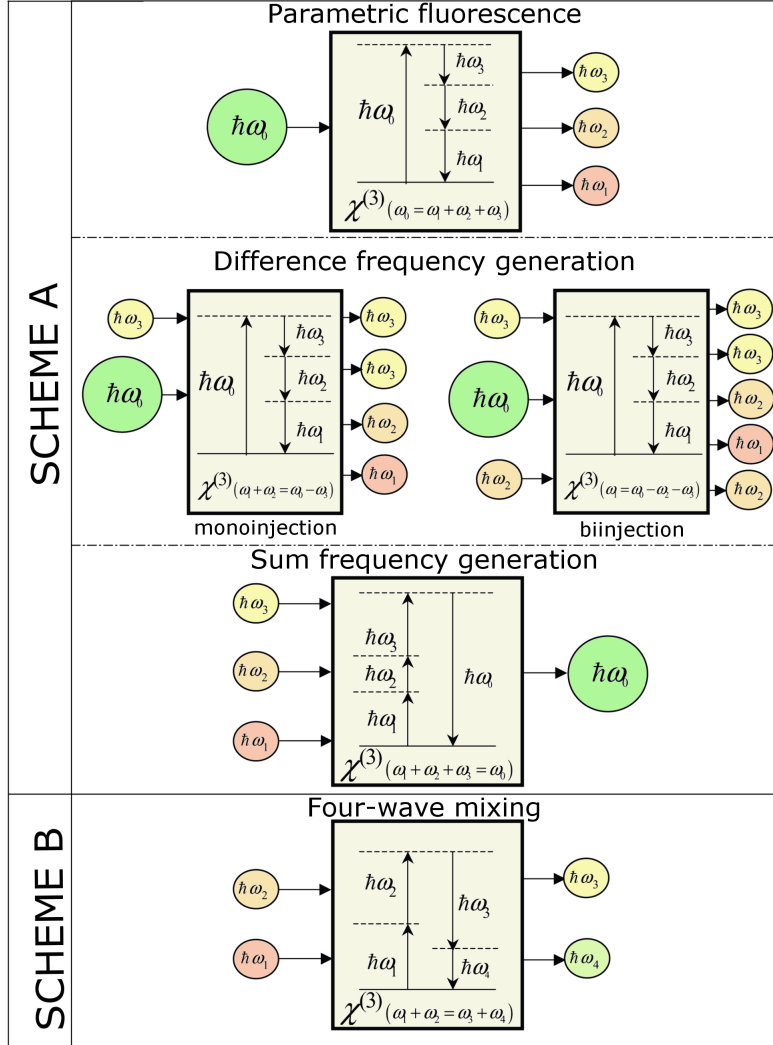


Figure 1.4 – Energy diagrams for the third-order parametric interactions.

Coupled amplitude equations We remind that the plane wave described in Equation (1.1) evolves spatially as:

$$E(\vec{r}, \omega) = \underline{E}(\vec{r}, \omega) e^{ik(\vec{r}, \omega)Z}, \quad (1.44)$$

and that \vec{r} stands for (X, Y, Z) .

We make the assumption that this spatial evolution is small compared to the wavelength: this slowly varying envelope hypothesis can be written for the first derivative as [34]:

$$\left| \frac{\partial^2 E(\vec{r}, \omega)}{\partial Z^2} \right| \ll k(\vec{r}, \omega) \left| \frac{\partial E(\vec{r}, \omega)}{\partial Z} \right|. \quad (1.45)$$

Now putting the electric field (1.44) together with (1.45) in the propagation equation (1.38)

gives:

$$\frac{\partial \vec{E}(\vec{r}, \omega)}{\partial Z} = i \frac{\mu_0 \omega^2}{2k(\vec{r}, \omega)} \left[\vec{P}^{(2)}(\vec{r}, \omega) + \vec{P}^{(3)}(\vec{r}, \omega) \right] e^{-ik(\vec{r}, \omega)Z}. \quad (1.46)$$

This equation clearly shows that the source terms $\vec{P}^{(2)}(\vec{r}, \omega)$ and $\vec{P}^{(3)}(\vec{r}, \omega)$, responsible for the quadratic and cubic processes already discussed, are two competitive effects. For clarity, we are going to set them apart alternately in the previous equation. We also assume that the interacting waves are collinear, which will be the case of the experiments in the next chapters.

– **Quadratic evolution equations** With the second-order term only, and using Equation (1.39), we come up with the complex amplitude equation [22]:

$$\frac{\partial E(\vec{r}, \omega)}{\partial Z} = i\kappa(\vec{r}, \omega) \int_{\mathbb{R}} \frac{d\tilde{\omega}}{2\pi} \chi_{\text{eff}}^{(2)}(\vec{r}, \omega, \tilde{\omega}) E(\vec{r}, \tilde{\omega}) E(\vec{r}, \omega - \tilde{\omega}), \quad (1.47)$$

with

$$\kappa(\vec{r}, \omega) = \frac{\omega}{2cn(\vec{r}, \omega) \cos^2(\rho(\omega))}, \quad (1.48)$$

and $\chi_{\text{eff}}^{(2)}$ the second-order effective susceptibility coefficient defined by [19]:

$$\chi_{\text{eff}}^{(2)}(\vec{r}, \omega, \tilde{\omega}) = \vec{e}(\vec{r}, \omega) \cdot \vec{\chi}^{(2)}(\omega = \tilde{\omega} + (\omega - \tilde{\omega})) : [\vec{e}(\vec{r}, \tilde{\omega}) \otimes \vec{e}(\vec{r}, \omega - \tilde{\omega})]. \quad (1.49)$$

The \vec{e} vectors are unitary electric field vectors.

Equation (1.47) has to be fulfilled for the infinity of frequencies constituting the total electric field. Put together, they form a set of coupled equations.

At this point, it is important to make some comments:

- The field at negative frequencies can be replaced by its hermitian conjugate at opposite frequency, as stated in (1.3).

- The integral has to be restricted to the transparency range of the material.

- The k vectors in the argument of E that sum together will also reduce the spectrum to three wave packets around three different frequencies (ω_0 , ω_1 and ω_2). This is why we will equivalently rewrite the coupled equations (1.47) in a more familiar way using the three fields \underline{E}_0 , \underline{E}_1 and \underline{E}_2 complex amplitudes:

$$\begin{cases} \frac{\partial \underline{E}_0(\vec{r}, \omega_0)}{\partial Z} &= i\kappa(\vec{r}, \omega_0) \int_{\mathbb{R}} \frac{d\omega_1}{2\pi} \chi_{\text{eff}}^{(2)}(\vec{r}, \omega_0, \omega_1) \underline{E}_1(\vec{r}, \omega_1) \underline{E}_2(\vec{r}, \omega_0 - \omega_1) e^{-i\Delta k^{(2)}(\vec{r}, \omega_0, \omega_1)Z} \\ \frac{\partial \underline{E}_1(\vec{r}, \omega_1)}{\partial Z} &= i\kappa(\vec{r}, \omega_1) \int_{\mathbb{R}} \frac{d\omega_0}{2\pi} \chi_{\text{eff}}^{(2)}(\vec{r}, \omega_0, \omega_1) \underline{E}_0(\vec{r}, \omega_0) \underline{E}_2^*(\vec{r}, \omega_0 - \omega_1) e^{+i\Delta k^{(2)}(\vec{r}, \omega_0, \omega_1)Z} \\ \frac{\partial \underline{E}_2(\vec{r}, \omega_2)}{\partial Z} &= i\kappa(\vec{r}, \omega_2) \int_{\mathbb{R}} \frac{d\omega_0}{2\pi} \chi_{\text{eff}}^{(2)}(\vec{r}, \omega_0, \omega_1) \underline{E}_0(\vec{r}, \omega_0) \underline{E}_1^*(\vec{r}, \omega_0 - \omega_2) e^{+i\Delta k^{(2)}(\vec{r}, \omega_0, \omega_2)Z}, \end{cases} \quad (1.50)$$

where $\Delta k^{(2)}$ is the phase mismatch between the wave vectors of the radiated polarization and the incoming fields:

$$\Delta k^{(2)}(\vec{r}, \omega_0, \omega_1) = \Delta k^{(2)}(\vec{r}, \omega_0, \omega_1, \omega_0 - \omega_1) = k(\vec{r}, \omega_0) - k(\vec{r}, \omega_1) - k(\vec{r}, \omega_0 - \omega_1). \quad (1.51)$$

- **Cubic evolution equations** From (1.40) and (1.46) with the third-order source term only, we can also write similar equations for the cubic interactions of type A (to be adapted for type B) [33]:

$$\left\{ \begin{aligned} \frac{\partial \underline{E}_0(\vec{r}, \omega_0)}{\partial Z} &= i\kappa(\vec{r}, \omega_0) \iint_{\mathbb{R}^2} \frac{d\omega_1}{2\pi} \frac{d\omega_2}{2\pi} \chi_{\text{eff}}^{(3)}(\vec{r}, \omega_0, \omega_1, \omega_2) \underline{E}_1(\vec{r}, \omega_1) \underline{E}_2(\vec{r}, \omega_2) \\ &\quad \times \underline{E}_3(\vec{r}, \omega_0 - \omega_1 - \omega_2) e^{-i\Delta k^{(3)}(\vec{r}, \omega_0, \omega_1, \omega_2)Z} \\ \frac{\partial \underline{E}_1(\vec{r}, \omega_1)}{\partial Z} &= i\kappa(\vec{r}, \omega_1) \iint_{\mathbb{R}^2} \frac{d\omega_0}{2\pi} \frac{d\omega_2}{2\pi} \chi_{\text{eff}}^{(3)}(\vec{r}, \omega_0, \omega_1, \omega_2) \underline{E}_0(\vec{r}, \omega_0) \underline{E}_2^*(\vec{r}, \omega_2) \\ &\quad \times \underline{E}_3^*(\vec{r}, \omega_0 - \omega_1 - \omega_2) e^{+i\Delta k^{(3)}(\vec{r}, \omega_0, \omega_1, \omega_2)Z} \\ \frac{\partial \underline{E}_2(\vec{r}, \omega_2)}{\partial Z} &= i\kappa(\vec{r}, \omega_2) \iint_{\mathbb{R}^2} \frac{d\omega_0}{2\pi} \frac{d\omega_1}{2\pi} \chi_{\text{eff}}^{(3)}(\vec{r}, \omega_0, \omega_1, \omega_2) \underline{E}_0(\vec{r}, \omega_0) \underline{E}_1^*(\vec{r}, \omega_1) \\ &\quad \times \underline{E}_3^*(\vec{r}, \omega_0 - \omega_1 - \omega_2) e^{+i\Delta k^{(3)}(\vec{r}, \omega_0, \omega_1, \omega_2)Z} \\ \frac{\partial \underline{E}_3(\vec{r}, \omega_3)}{\partial Z} &= i\kappa(\vec{r}, \omega_3) \iint_{\mathbb{R}^2} \frac{d\omega_0}{2\pi} \frac{d\omega_1}{2\pi} \chi_{\text{eff}}^{(3)}(\vec{r}, \omega_0, \omega_1, \omega_2) \underline{E}_0(\vec{r}, \omega_0) \underline{E}_1^*(\vec{r}, \omega_1), \\ &\quad \times \underline{E}_2^*(\vec{r}, \omega_0 - \omega_1 - \omega_3) e^{+i\Delta k^{(3)}(\vec{r}, \omega_0, \omega_1, \omega_3)Z} \end{aligned} \right. \quad (1.52)$$

where $\chi_{\text{eff}}^{(3)}$ is the third-order effective susceptibility coefficient, defined by:

$$\begin{aligned} \chi_{\text{eff}}^{(3)}(\vec{r}, \omega_0, \omega_1, \omega_2) &= \vec{e}_0^*(\vec{r}, \omega_0) \cdot \vec{\chi}^{(3)}(\omega_0 = \omega_1 + \omega_2 + (\omega_0 - \omega_1 - \omega_2)) \\ &\quad : [\vec{e}_1^*(\vec{r}, \omega_1) \otimes \vec{e}_2^*(\vec{r}, \omega_2) \otimes \vec{e}_3^*(\vec{r}, \omega_0 - \omega_1 - \omega_2)], \end{aligned} \quad (1.53)$$

and $\Delta k^{(3)}$ the phase mismatch between the four wave vectors:

$$\begin{aligned} \Delta k^{(3)}(\vec{r}, \omega_0, \omega_1, \omega_2) &= \Delta k^{(3)}(\vec{r}, \omega_0, \omega_1, \omega_2, \omega_0 - \omega_1 - \omega_2) \\ &= k(\vec{r}, \omega_0) - k(\vec{r}, \omega_1) - k(\vec{r}, \omega_2) - k(\vec{r}, \omega_0 - \omega_1 - \omega_2). \end{aligned} \quad (1.54)$$

Manley-Rowe equations One can derive power density equations from the coupled amplitude equations defined above. They are Manley-Rowe equations [35], accounting for electromagnetic energy exchange in a non-dissipative medium, and can be gathered into:

$$\frac{\partial I_{\text{tot}}(\vec{r})}{\partial Z} = 0, \quad (1.55)$$

where I_{tot} is the sum of all field intensities. Nonlinear processes conserve the total intensity, and therefore do not conserve the total photon current $N = \int d\omega n(\omega) = \int d\omega \frac{I(\omega)}{\hbar\omega}$, which was already suggested by the corpuscular schematics in Figures 1.3 and 1.4.

Parameters of interest Δk and χ_{eff} are two parameters of interest and some comments arise. The phase mismatch only depends on the linear properties, while the effective susceptibility depends on both the linear and nonlinear properties.

- **Phase mismatch** Because the incoming waves and the resulting polarization propagate at different frequencies, their phase velocities are different, the indices dispersion being not flat. Consequently, the dephasing between these waves implies constructive and destructive

interferences in turns along the propagation [22]. The spatial periodicity of this energy transfert is called coherence length L_c and is defined as:

$$L_c(\vec{r}, \{\omega_i\}) = \frac{\pi}{\Delta k(\vec{r}, \{\omega_i\})}. \quad (1.56)$$

When the phase mismatch of a given interaction is zero, we speak of a phase-matched interaction. Only the spectral components of the polychromatic interacting waves that are very close to fulfill the phase-matching condition propagate efficiently, the nonlinear polarization at the Fourier component ω_i and the field it radiates at the same frequency constructively interfering all the way through the propagation. This phase-matching condition writes as:

$$\Delta k(\vec{r}, \{\omega_i\}) = 0. \quad (1.57)$$

We develop in Sections 1.2.2 and 1.3.3 two ways of achieving the phase-matching condition: birefringent phase matching in anisotropic crystals, and intermodal phase matching in isotropic optical fibers. Note that the phase-matching condition is equivalent to the momentum conservation relationship.

We point out that parametric fluorescence, as well as SFG or DFG involving the same photon frequencies, necessarily fulfill the same phase-matching condition.

At perfect phase matching, taking the argument of the complex amplitude $\underline{E}=|E|e^{i\phi}$ in the coupled quadratic (1.50) or cubic of type A (1.52) equations gives a relationship between the initial phases [21]:

$$\phi_0 - \left(\sum_{i=1}^N \phi_i \right) = \pm \pi/2, \quad (1.58)$$

with $+$ sign in the case of a scission of photon 0 into photons i , and $-$ sign in the opposite case. $N = 2$ or 3 for a quadratic and cubic interactions respectively.

- **Effective susceptibility** We emphasize here that it is not only important to choose a direction of propagation and polarizations that are close to conserve the momentum, but also that exhibit a high effective susceptibility coefficient.

Spatial and temporal walk-off When different input beams are involved in a nonlinear interaction, one has to care about the spatial and temporal overlaps between these beams since they can reduce the conversion efficiencies of the process. We already mentionned the double refraction angle that separates beams of different polarizations. This phenomenon is referred to as spatial walk-off.

In the case of short pulses, the group velocities at different wavelengths differ because of the chromatic dispersion: this is the temporal walk-off. For instance, it reaches 4.5 mm for 15 ps pulses around the wavelengths 1470 and 1660 nm.

Solutions of the coupled equations Giving general analytical solutions for the coupled equations (1.50) and (1.52) is not an easy task. The general solutions that are given in terms

of Jacobi elliptical functions are relevant when the initial values of the fields are not zero. Otherwise, one has to make a resolution with quantum fields (see Section 1.4). The resolution will be adapted in our experimental cases when needed later in this manuscript.

Summary In order to achieve a nonlinear interaction, the energy conservation relationship has to be fulfilled. For it to be efficient, it is important to ensure the linear momentum conservation. In addition, the effective susceptibility has to be non-zero and the highest possible. Finally, it is important to maximize the spatial and temporal overlaps of the interacting waves. In particular, the double refraction angle is preferred to be the lowest possible, zero at best.

$$\left\{ \begin{array}{ll} \Delta\mathcal{E} = 0 & \Rightarrow \sum_{i=0}^N \pm \omega_i = 0 \\ \hbar\Delta k = 0 & \Rightarrow \sum_{i=0}^N \pm n(\vec{r}, \omega_i) \cdot \omega_i = 0 \\ \overline{\chi}^{(n)} \vec{e}_0 \cdot \bigotimes_{i=1}^n \vec{e}_i \neq 0 & , \end{array} \right. \quad (1.59)$$

with + sign for ingoing waves, and − sign for outgoing waves; $N \in \{2, 3\}$.

Note lastly that in the case of a cubic interaction, any quadratic effect would be parasitic and has to be avoided.

1.2 Classical parametric crystal optics

We consider in this work optically anisotropic crystals, so that their refractive indices vary as a function of the direction of propagation. This section aims to present basics on crystal optics.

1.2.1 Linear crystal optics

Refractive index, Fresnel equation From Equation (1.27) expressed in the dielectric frame, one can get an analytic equation for the refractive index in any propagation direction [23], namely the Fresnel equation:

$$\frac{\sin^2(\theta) \cos^2(\varphi)}{n^{-2}(\omega, \theta, \varphi) - n_x^{-2}(\omega)} + \frac{\sin^2(\theta) \sin^2(\varphi)}{n^{-2}(\omega, \theta, \varphi) - n_y^{-2}(\omega)} + \frac{\cos^2(\theta)}{n^{-2}(\omega, \theta, \varphi) - n_z^{-2}(\omega)} = 0. \quad (1.60)$$

Since this equation generally leads to two different solutions, the refractive index can take two different values in any particular direction of propagation of the optical wave. Therefore, this phenomenon has taken the name of birefringence.

These solutions, denoted $n^{(+)}$ et $n^{(-)}$, map a surface in the three-dimensional space called the indices surface. Their mathematical form is the following [36]:

$$n^{(\pm)}(\omega, \theta, \varphi) = \sqrt{\frac{2}{\alpha \mp (\alpha^2 - 4\beta)^{1/2}}}, \quad (1.61)$$

with $n^{(-)} \leq n^{(+)}$, and where:

$$\begin{aligned} \alpha(\omega, \theta, \varphi) &= \sin^2(\theta) \cos^2(\varphi) (n_y^{-2}(\omega) + n_z^{-2}(\omega)) + \sin^2(\theta) \sin^2(\varphi) (n_x^{-2}(\omega) + n_z^{-2}(\omega)) \\ &\quad + \cos^2(\theta) (n_x^{-2}(\omega) + n_y^{-2}(\omega)), \end{aligned} \quad (1.62)$$

$$\begin{aligned} \beta(\omega, \theta, \varphi) &= \sin^2(\theta) \cos^2(\varphi) n_y^{-2}(\omega) n_z^{-2}(\omega) + \sin^2(\theta) \sin^2(\varphi) n_x^{-2}(\omega) n_z^{-2}(\omega) \\ &\quad + \cos^2(\theta) n_x^{-2}(\omega) n_y^{-2}(\omega). \end{aligned} \quad (1.63)$$

The quantity $\Delta n(\omega, \theta, \varphi) = n^{(+)}(\omega, \theta, \varphi) - n^{(-)}(\omega, \theta, \varphi)$ is also called birefringence.

Optical classes Depending on whether the principal indices n_x , n_y and n_z differ from each other or not, three classes of medium arise. Whether one material belongs to one class or another depends on its orientation symmetry [25].

- The **isotropic class** is defined when the three principal refractive indices are equal: $n_x = n_y = n_z$. The refractive index is therefore unique, and the indices surface is a one-layer sphere, as depicted in Figure 1.5 (a). In this work, the optical fibers can be considered isotropic at first glance, as any glass without deformation would be.
- In the case of the **uniaxial class**, two of the three eigenvalues are equal and are called the ordinary indices n_o , while the third one is the extraordinary index n_e . This class exhibits two indices surfaces: a sphere of radius n_o , and an ellipsoid of revolution with minor and major semi-axes n_o and n_e respectively. The major axis of the ellipsoid is the z axis, called

the optical axis. The optical axis of a material is by definition the direction where the optical indices are degenerated. There is only one such axis for this class of crystal, which justifies indeed the term uniaxial.

The two surfaces $n^{(+)}$ and $n^{(-)}$ are conventionally named $n^{(o)}$ and $n^{(e)}$ in this case. Equation (1.61) can then be further simplified:

$$\begin{cases} n^{(o)}(\omega, \theta, \varphi) = n^{(o)}(\omega) = n_o(\omega) \\ n^{(e)}(\omega, \theta, \varphi) = n^{(e)}(\omega, \theta) = \frac{1}{\sqrt{\left(\frac{\cos(\theta)}{n_o(\omega)}\right)^2 + \left(\frac{\sin(\theta)}{n_e(\omega)}\right)^2}} \end{cases} \quad (1.64)$$

The rutile TiO_2 crystal presented later in this work belongs to the uniaxial class, since it is of orientation symmetry $\frac{4}{m}mm$. It is said to be uniaxial positive because $n_o < n_e$, the opposite case being uniaxial negative. Figure 1.5 (b) shows the indices surfaces for an uniaxial positive crystal.

- The third category is the **biaxial class**, gathering together all crystals with three different principal indices. The indices layers are here more complicated, being tangled. They do not exhibit a revolution axis anymore, as shown in Figure 1.5 (c) in the usual convention: $n_x < n_y < n_z$. This convention is not restrictive at all as the choice for naming the axes of the dielectric frame is not unique. However, note that in the litterature, this choice is often referred to as “positive biaxial”, as opposed to “negative uniaxial” when $n_z < n_y < n_x$. In the principal planes of the dielectric frame, the prints are still circles and ellipses. Two optical axes, hence the name biaxial, characterize this class: each of them are symmetrical from the z -axis in the $(x0z)$ plane and makes an angle V from this z -axis [19]:

$$V = \text{asin} \left(\sqrt{\frac{n_y^{-2}(\omega) - n_x^{-2}(\omega)}{n_z^{-2}(\omega) - n_x^{-2}(\omega)}} \right). \quad (1.65)$$

The KTP crystal, a shortcut for KTiOPO_4 , also presented in this work is a biaxial crystal, since of orientation symmetry $mm2$.

Eigenmodes of polarization, vectorial configurations For a given propagation direction, the two optical indices $n^{(+)}$ and $n^{(-)}$ are associated to two linearly polarized electric fields $\vec{E}^{(+)}$ and $\vec{E}^{(-)}$, solutions of the propagation equation (1.26) [19]. Consequently, two sets of vectors $(\vec{E}^{(+)}, \vec{D}^{(+)}, \vec{B}^{(+)}, \vec{k}^{(+)}, \vec{\pi}^{(+)})$ and $(\vec{E}^{(-)}, \vec{D}^{(-)}, \vec{B}^{(-)}, \vec{k}^{(-)}, \vec{\pi}^{(-)})$ are related to these two optical indices.

The displacement vectors $\vec{D}^{(+)}$ and $\vec{D}^{(-)}$ are orthogonal to each other, and thus define two orthogonal polarization planes: $\Pi^{(+)}$ spanned by $(\vec{D}^{(+)}, \vec{k}^{(+)})$ and $\Pi^{(-)}$ spanned by $(\vec{D}^{(-)}, \vec{k}^{(-)})$, $\vec{k}^{(+)}$ and $\vec{k}^{(-)}$ being collinear. The electric fields $\vec{E}^{(\pm)}$ lie in the $\Pi^{(\pm)}$ planes, while being not orthogonal in the general case [37]. More generally, while all the vectors of the first set

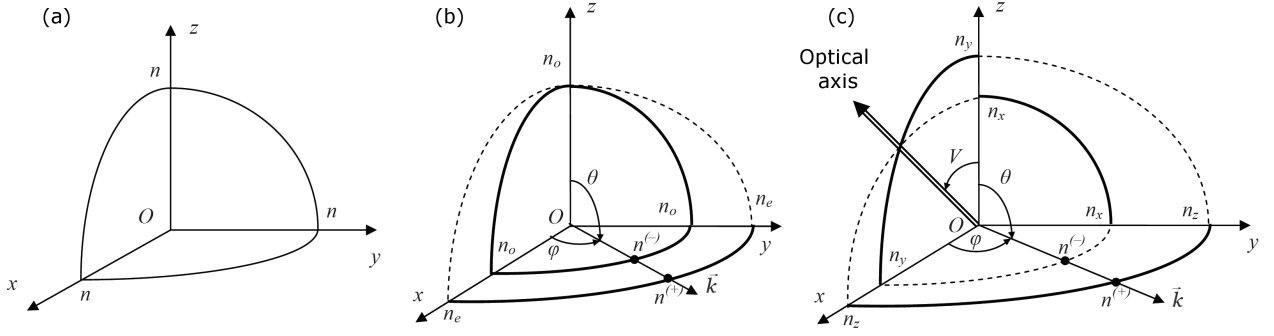


Figure 1.5 – Prints of the indices surface in the principal planes of the dielectric frame in one eighth of the three-dimensional space, for the three optical classes: (a) isotropic, (b) uniaxial (positive), (c) biaxial (positive).

$(\vec{E}^{(+)}, \vec{D}^{(+)}, \vec{B}^{(+)}, \vec{k}^{(+)}, \vec{\pi}^{(+)})$ are coplanar in $\Pi^{(+)}$, the vectors of the second set $(\vec{E}^{(-)}, \vec{D}^{(-)}, \vec{B}^{(-)}, \vec{k}^{(-)}, \vec{\pi}^{(-)})$ lie in $\Pi^{(-)}$ [17]. See Figure 1.6 for a geometrical representation.

One can note that the vectors \vec{D} and \vec{E} are not colinear in general, as well as \vec{k} and $\vec{\pi}$. They are separated by the same angle, the double refraction angle ρ already mentionned above [23]:

$$\rho^{(\pm)} = (\widehat{\vec{D}^{(\pm)}, \vec{E}^{(\pm)}}) = (\widehat{\vec{k}^{(\pm)}, \vec{\pi}^{(\pm)}}) = \arccos(\vec{D}^{(\pm)} \cdot \vec{E}^{(\pm)}). \quad (1.66)$$

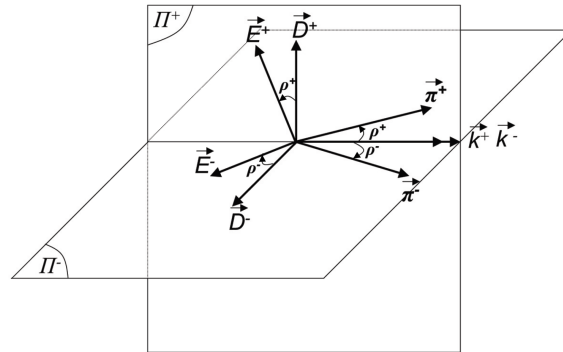


Figure 1.6 – Vectorial configuration for the two sets of vectors $(\vec{E}^{(\pm)}, \vec{D}^{(\pm)}, \vec{B}^{(\pm)}, \vec{k}^{(\pm)}, \vec{\pi}^{(\pm)})$

When the sollicitated indices sheet is a sphere, the double refraction angle is zero. In the other cases, such an angle exists, and makes the (+) and (-) waves go appart from each other through the propagation. When achieving nonlinear interactions with waves at different polarizations in the experiments further, we will favour directions that reduce as much as possible the ρ angle to maximize the spatial overlap. This overlap is schemed in shading on Figure 1.7 in the case where $\rho^{(-)}$ is zero, which will be one of our experimental case further.

Below are the expressions of the unitary electric field vectors \vec{e} in the uniaxial and biaxial crystals, for the propagation direction along $\vec{k}(\omega, \theta, \varphi)$ [19], also represented in Figure 1.8.

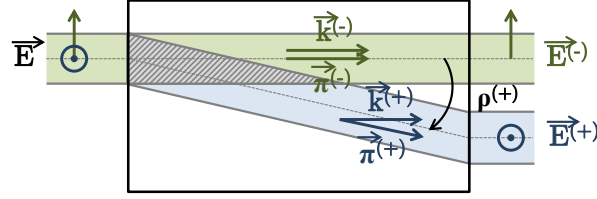


Figure 1.7 – Spatial overlap between ordinary and extraordinary waves in the case where $\rho^{(-)} = 0$.

– **Uniaxial class**

$$\begin{cases} e_x^{(o)} = -\sin(\varphi) \\ e_y^{(o)} = \cos(\varphi) \\ e_z^{(o)} = 0 \end{cases} \quad \text{and} \quad \begin{cases} e_x^{(e)} = -\cos(\theta \mp \rho^\pm(\theta, \omega)) \cos(\varphi) \\ e_y^{(e)} = -\cos(\theta \mp \rho^\pm(\theta, \omega)) \sin(\varphi) \\ e_z^{(e)} = \sin(\theta \mp \rho^\pm(\theta, \omega)) \end{cases}, \quad (1.67)$$

where

$$\rho^\pm(\theta, \omega) = \text{acos} \left(\frac{n_o^{-2}(\omega) \cos^2(\theta) + n_e^{-2}(\omega) \sin^2(\theta)}{\sqrt{n_o^{-4}(\omega) \cos^2(\theta) + n_e^{-4}(\omega) \sin^2(\theta)}} \right). \quad (1.68)$$

The + and – signs are for the negative and positive uniaxial cases respectively. The double refraction angle is only zero in the sagittal plane (xOy) and along the optical axis z .

- **Biaxial class** For the present study, it is enough to restrict the expressions of the unitary electric fields to the principal planes (xOy) and (xOz) [19].

In the (xOy) plane:

$$\begin{cases} e_x^{(-)} = -\sin(\varphi \mp \rho^\pm(\varphi, \omega)) \\ e_y^{(-)} = \cos(\varphi \mp \rho^\pm(\varphi, \omega)) \\ e_z^{(-)} = 0 \end{cases} \quad \text{and} \quad \begin{cases} e_x^{(+)} = 0 \\ e_y^{(+)} = 0 \\ e_z^{(+)} = 1 \end{cases}, \quad (1.69)$$

where

$$\rho^\pm(\varphi, \omega) = \mp \text{acos} \left(\frac{n_y^{-2}(\omega) \cos^2(\varphi) + n_x^{-2}(\omega) \sin^2(\varphi)}{\sqrt{n_y^{-4}(\omega) \cos^2(\varphi) + n_x^{-4}(\omega) \sin^2(\varphi)}} \right). \quad (1.70)$$

In the (xOz) plane, the existence of the optical axis creates a discontinuity in the two indices sheets, leading to a discontinuity of the sign of the electric field. From the x -axis to the optical axis:

$$\begin{cases} e_x^{(-)} = 0 \\ e_y^{(-)} = 1 \\ e_z^{(-)} = 0 \end{cases} \quad \text{and} \quad \begin{cases} e_x^{(+)} = -\cos(\theta \mp \rho^\pm(\theta, \omega)) \\ e_y^{(+)} = 0 \\ e_z^{(+)} = \sin(\theta \mp \rho^\pm(\theta, \omega)) \end{cases}. \quad (1.71)$$

And from the optical axis to the z -axis:

$$\begin{cases} e_x^{(-)} = 0 \\ e_y^{(-)} = -1 \\ e_z^{(-)} = 0 \end{cases} \quad \text{and} \quad \begin{cases} e_x^{(+)} = -\cos(\theta \pm \rho^\pm(\theta, \omega)) \\ e_y^{(+)} = 0 \\ e_z^{(+)} = \sin(\theta \pm \rho^\pm(\theta, \omega)) \end{cases}, \quad (1.72)$$

where

$$\rho^\pm(\theta, \omega) = \arccos \left(\frac{n_x^{-2}(\omega) \cos^2(\theta) + n_z^{-2}(\omega) \sin^2(\theta)}{\sqrt{n_x^{-4}(\omega) \cos^2(\theta) + n_z^{-4}(\omega) \sin^2(\theta)}} \right). \quad (1.73)$$

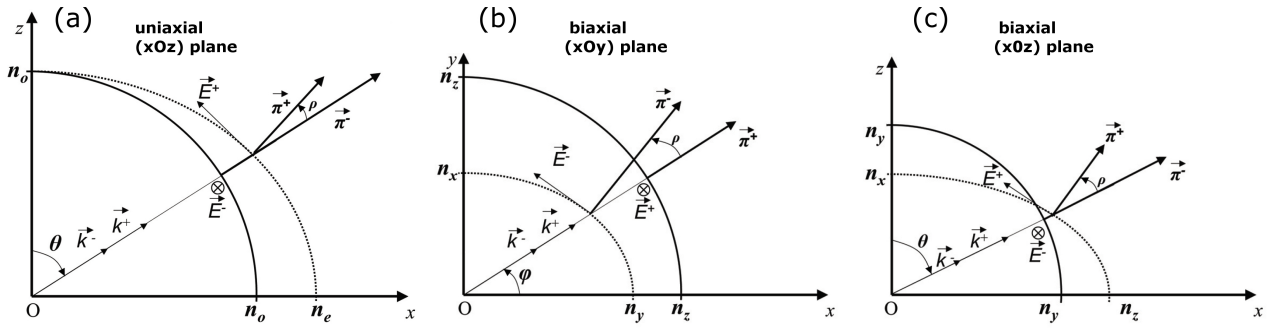


Figure 1.8 – Indices surfaces for (a) a positive uniaxial crystal in the (xOz) plane, (b) a biaxial crystal in the (xOy) plane and (c) a biaxial crystal in the (xOz) plane.

1.2.2 Nonlinear crystal optics

Phase matching by birefringence The best way to achieve phase matching in anisotropic media is to compensate the wavelength dispersion of the refractive index with the birefringence. The choice of the polarizations $e^{(-)}$ or $e^{(+)}$ of the waves make possible the solicitation of the internal $n^{(-)}$ or external $n^{(+)}$ indices sheet.

- For **quadratic processes**, there are two types of possible combinations of the optical indices that allow to energy and momentum conservation in Equations (1.59). Those two types give the three combinations [38, 39]:

$$\begin{cases} \text{I} & n^{(-)}(\omega_0, \theta, \varphi) \omega_0 - n^{(+)}(\omega_1, \theta, \varphi) \omega_1 - n^{(+)}(\omega_2, \theta, \varphi) \omega_2 = 0 \\ \text{IIa} & n^{(-)}(\omega_0, \theta, \varphi) \omega_0 - n^{(+)}(\omega_1, \theta, \varphi) \omega_1 - n^{(-)}(\omega_2, \theta, \varphi) \omega_2 = 0 \\ \text{IIb} & n^{(-)}(\omega_0, \theta, \varphi) \omega_0 - n^{(-)}(\omega_1, \theta, \varphi) \omega_1 - n^{(+)}(\omega_2, \theta, \varphi) \omega_2 = 0 \end{cases} \quad (1.74)$$

- For **cubic interactions**, three types are possible leading to seven possible combinations [40]:

$$\left\{ \begin{array}{ll} \text{I} & n^{(-)}(\omega_0, \theta, \varphi) \omega_0 - n^{(+)}(\omega_1, \theta, \varphi) \omega_1 - n^{(+)}(\omega_2, \theta, \varphi) \omega_2 - n^{(+)}(\omega_3, \theta, \varphi) \omega_3 = 0 \\ \text{IIa} & n^{(-)}(\omega_0, \theta, \varphi) \omega_0 - n^{(+)}(\omega_1, \theta, \varphi) \omega_1 - n^{(+)}(\omega_2, \theta, \varphi) \omega_2 - n^{(-)}(\omega_3, \theta, \varphi) \omega_3 = 0 \\ \text{IIb} & n^{(-)}(\omega_0, \theta, \varphi) \omega_0 - n^{(+)}(\omega_1, \theta, \varphi) \omega_1 - n^{(-)}(\omega_2, \theta, \varphi) \omega_2 - n^{(+)}(\omega_3, \theta, \varphi) \omega_3 = 0 \\ \text{IIc} & n^{(-)}(\omega_0, \theta, \varphi) \omega_0 - n^{(-)}(\omega_1, \theta, \varphi) \omega_1 - n^{(+)}(\omega_2, \theta, \varphi) \omega_2 - n^{(+)}(\omega_3, \theta, \varphi) \omega_3 = 0 \\ \text{IIIa} & n^{(-)}(\omega_0, \theta, \varphi) \omega_0 - n^{(+)}(\omega_1, \theta, \varphi) \omega_1 - n^{(-)}(\omega_2, \theta, \varphi) \omega_2 - n^{(-)}(\omega_3, \theta, \varphi) \omega_3 = 0 \\ \text{IIIb} & n^{(-)}(\omega_0, \theta, \varphi) \omega_0 - n^{(-)}(\omega_1, \theta, \varphi) \omega_1 - n^{(+)}(\omega_2, \theta, \varphi) \omega_2 - n^{(-)}(\omega_3, \theta, \varphi) \omega_3 = 0 \\ \text{IIIc} & n^{(-)}(\omega_0, \theta, \varphi) \omega_0 - n^{(-)}(\omega_1, \theta, \varphi) \omega_1 - n^{(-)}(\omega_2, \theta, \varphi) \omega_2 - n^{(+)}(\omega_3, \theta, \varphi) \omega_3 = 0 \end{array} \right. \quad (1.75)$$

The refractive indices depending on the propagation direction, the phase-matching condition is only reached in a particular direction, called the phase-matching direction.

1.3 Classical parametric fiber optics

This work also involves nonlinear interactions in optical fibers. This part is therefore dedicated to some basic knowledge about fiber optics, transverse mode, longitudinal propagation within fiber and about how to achieve a nonlinear conversion in isotropic fibers.

1.3.1 Generalities on step-index fibers

Geometry An optical fiber is a dielectric waveguide that confines the electromagnetic field in a cylindrical geometry. For the light to propagate, an optical fiber takes advantage of the physical phenomenon of total internal reflection [41]. We consider here the fibers we used experimentally, step-index fibers, made of two concentric cylinders of isotropic glasses: the inner one is the core, of radius a , and the outer one is the cladding of radius b ($b > a$). Their respective refractive indices are n_{cl} and n_{co} , $n_{cl} < n_{co}$, as shown in the sketch 1.9. The index difference is denoted as $\Delta n(\omega) = n_{co}(\omega) - n_{cl}(\omega)$.

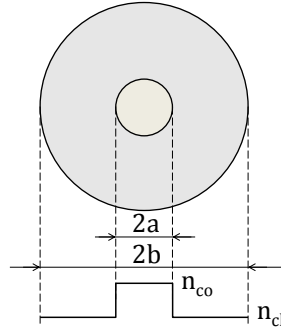


Figure 1.9 – Transverse geometry of a step-index fiber.

The application of the total internal reflection condition defines an angular cone of acceptance for an incoming beam to be guided in the fiber. This cone is identified by an angle θ_0 from the revolution axis of the fiber. It is a function of the indices n_{cl} and n_{co} , and leads to the definition of the so-called numerical aperture NA [42]:

$$\text{NA}(\omega) = \sin(\theta_0(\omega)) = \sqrt{n_{co}^2(\omega) - n_{cl}^2(\omega)}. \quad (1.76)$$

Microstructured fibers, also called photonic-crystal fibers (PCF), have also been considered in this work and will be studied in Section 4.2. An example of microstructured fiber with a hexagonal geometry is pictured Figure 1.10. For numerical calculation, we will see in Chapter 4 that such fibers can be replaced by equivalent step-index fibers [43, 44], which justify the approach we give here.

Fabrication process The fabrication process of a step-index fiber is the following. A bulk glass is synthesized and purified to obtain a so-called preform. This preform is then stretched into a thin optical fiber through an homothetic transformation.

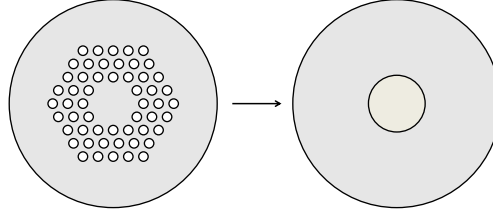


Figure 1.10 – Microstructured fiber of hexagonal geometry, approximated by a step-index fiber.

Effective index of a wave The wavenumber of a wave propagating in a fiber cannot be expressed as in Equation (1.2) where the refractive index of the material n is only a property of the material, linked to the first-order susceptibility. It also has to reflect the guiding structure [42, 44]. The combination of those two requirements together defines a so-called effective index for the wave, n_{eff} , *i.e.* the index actually experienced by the propagating wave. It takes the form of the Sellmeier equations of Section 1.1.2. In step-index fibers, n_{eff} is isotropic in the core. The wavenumber is then defined as the isotropic quantity:

$$\beta(\omega) = \frac{n_{\text{eff}}(\omega)\omega}{c}. \quad (1.77)$$

It is useful to define a normalized propagation constant [42]:

$$b(\omega) = \frac{\beta^2(\omega) - k_{\text{cl}}^2(\omega)}{k_{\text{co}}^2(\omega) - k_{\text{cl}}^2(\omega)} = \frac{n_{\text{eff}}^2(\omega) - n_{\text{cl}}^2(\omega)}{n_{\text{co}}^2(\omega) - n_{\text{cl}}^2(\omega)}, \quad (1.78)$$

with $k_{\text{cl}} = k_0 n_{\text{cl}}$, $k_{\text{co}} = k_0 n_{\text{co}}$ and $k_0 = \frac{\omega}{c}$ the vacuum propagation constant.

When $\Delta n(\omega) \simeq 0$, *i.e.* in weak guidance cases, then $b(\omega) \simeq \frac{n_{\text{eff}}(\omega) - n_{\text{cl}}(\omega)}{n_{\text{co}}(\omega) - n_{\text{cl}}(\omega)}$. Consequently, it comes:

$$\begin{aligned} n_{\text{eff}}(\omega) &= n_{\text{cl}}(\omega) + \Delta n(\omega) \cdot b(\omega) \\ &= n_M(\omega) + n_W(\omega), \end{aligned} \quad (1.79)$$

where the medium contribution n_M is distinguished from that of the guiding n_W as in [45]. At this point, the normalized propagation constant b needs to be known to infer the effective index n_{eff} from Equation (1.79). This is the aim of the next Subsection 1.3.2.

Guiding condition Total internal reflection is achieved when [46]:

$$n_{\text{cl}}(\omega) \leq n_{\text{eff}}(\omega) \leq n_{\text{co}}(\omega), \quad (1.80)$$

or equivalently $k_{\text{cl}}(\omega) \leq \beta(\omega) \leq k_{\text{co}}(\omega)$. In terms of the normalized propagation constant, the guiding condition becomes:

$$0 \leq b(\omega) \leq 1. \quad (1.81)$$

1.3.2 Transverse propagating modes

Modes The propagation equation (1.14) still applies. But the geometry of the fiber have to be taken into account: according to the boundary conditions, the electric field has to be continuous

at the core-cladding interface and has to be zero at the cladding boundary [47]. Several solutions can arise from these considerations, called transverse modes of propagation. Each mode has its own effective index, and consequently its own guiding condition.

Eigenvalue equation From evident geometrical considerations, it is convenient to use the cylindrical coordinates (r, θ, Z) . Then, the linear spectral wave equation (1.26) becomes:

$$\frac{\partial^2 \vec{E}(\vec{r}, \omega)}{\partial r^2} + \frac{1}{r} \frac{\partial \vec{E}(\vec{r}, \omega)}{\partial r} + \frac{1}{r^2} \frac{\partial^2 \vec{E}(\vec{r}, \omega)}{\partial \theta^2} + \frac{\partial^2 \vec{E}(\vec{r}, \omega)}{\partial Z^2} + k^2(\omega) \vec{E}(\vec{r}, \omega) = 0, \quad (1.82)$$

where $k(\omega) \in \{k_{\text{cl}}(\omega), k_{\text{co}}(\omega)\}$ for a step-index fiber. When $\frac{\Delta n(\omega)}{n_{\text{co}}(\omega)} \ll 1$, which is the case of the fibers we used in the present study, the propagation will mostly occur along the fiber axis. The limit angle for total internal reflexion is indeed given by $\theta_{\text{lim}}(\omega) = \text{asin}\left(\frac{n_{\text{co}}(\omega)}{n_{\text{cl}}(\omega)}\right)$. It is therefore possible to adopt a scalar approach for the resolution of (1.82): the electric field will be mainly polarized in the transverse plane, and can be taken as linearly polarized along $\vec{e} \perp \vec{u}_z$ [48].

Equation (1.82) can be solved by separating the variables of the electric field as $\underline{E}(\vec{r}, \omega) = \underline{R}(r, \omega) \underline{\Theta}(\theta, \omega) \underline{A}(Z, \omega)$. For a wave propagating along $+Z$, it comes:

$$\begin{cases} \underline{\Theta}(\theta) = \alpha_1 \cos(n\theta) + \alpha_2 \sin(n\theta) \\ \underline{A}(Z) = e^{i\beta(\omega)Z} \end{cases}, \quad (1.83)$$

where $\{\alpha_1, \alpha_2\} \in \mathbb{R}^2$ and $n \in \mathbb{N}$. And \underline{R} can be found by solving the following Bessel equation:

$$\partial_r^2 \underline{R}(r, \omega) + \frac{1}{r} \partial_r \underline{R}(r, \omega) + \left(k^2(\omega) - \beta^2(\omega) - \left(\frac{n}{r} \right)^2 \right) \underline{R}(r, \omega) = 0. \quad (1.84)$$

It is useful to define the three following parameters [49]:

$$\begin{cases} u(\omega) = a \sqrt{(k_0(\omega) n_{\text{co}}(\omega))^2 - \beta^2(\omega)} \\ v(\omega) = a k_0(\omega) \sqrt{n_{\text{co}}^2(\omega) - n_{\text{cl}}^2(\omega)} = a k_0(\omega) \text{NA}(\omega), \\ w(\omega) = a \sqrt{\beta^2(\omega) - (k_0(\omega) n_{\text{cl}}(\omega))^2} \end{cases} \quad (1.85)$$

linked by the relationship:

$$v^2 = u^2 + w^2. \quad (1.86)$$

Equation (1.84) becomes:

$$\begin{cases} \partial_r^2 \underline{R}(r, \omega) + \frac{1}{r} \partial_r \underline{R}(r, \omega) + \left(\left(\frac{u(\omega)}{a} \right)^2 - \left(\frac{n}{r} \right)^2 \right) \underline{R}(r, \omega) = 0 & \text{for } r \leq a \text{ (core)} \\ \partial_r^2 \underline{R}(r, \omega) + \frac{1}{r} \partial_r \underline{R}(r, \omega) + \left(\left(\frac{n}{r} \right)^2 - \left(\frac{w(\omega)}{a} \right)^2 \right) \underline{R}(r, \omega) = 0 & \text{for } r \geq a \text{ (cladding)}, \end{cases} \quad (1.87)$$

Eliminating diverging solutions, it is solved using Bessel functions [50, 51]:

$$\begin{cases} \underline{R}(r, \omega) = C_1 J_n \left(\frac{u(\omega) r}{a} \right) & \text{for } r \leq a \\ \underline{R}(r, \omega) = C_2 K_n \left(\frac{w(\omega) r}{a} \right) & \text{for } r \geq a, \end{cases} \quad (1.88)$$

$\{C_1, C_2\} \in \mathbb{R}^2$. J_n are Bessel functions of first kind, oscillating functions around zero whose amplitudes decrease with r . The higher u , the more \underline{R} oscillates in the core. K_n are modified Bessel functions of first kind, monotonically decreasing. The higher w , the faster \underline{R} decreases in the cladding.

Normalized frequency The v parameter is of particular importance as it controls the number of modes propagating in the fiber. It is referred to as the reduced or normalized frequency. A mode guided in the fiber necessarily fulfills the following equations equivalent to (1.80):

$$u \leq v, \quad w \leq v. \quad (1.89)$$

Continuity conditions

- **Global solution.** The radial component has to be continuous at the core-cladding interface. Therefore, the total solutions for the transverse distributions, or modes are :

$$\begin{cases} \underline{E}(\vec{r}, \omega) = C J_n \left(\frac{u(\omega) r}{a} \right) \begin{vmatrix} \cos(n\theta) \\ \sin(n\theta) \end{vmatrix} e^{i\beta(\omega)z} & \text{for } r \leq a \\ \underline{E}(\vec{r}, \omega) = C \frac{J_n(u(\omega))}{K_n(w(\omega))} K_n \left(\frac{w(\omega) r}{a} \right) \begin{vmatrix} \cos(n\theta) \\ \sin(n\theta) \end{vmatrix} e^{i\beta(\omega)z} & \text{for } r \geq a, \end{cases} \quad (1.90)$$

$C \in \mathbb{R}$.

- **Characteristic equation.** A second continuity relationship applies for the normal derivative of \underline{E} . In this scalar approach [46, 50]:

$$\begin{aligned} u(\omega) \frac{J'_n(u(\omega))}{J_n(u(\omega))} &= w(\omega) \frac{K'_n(w(\omega))}{K_n(w(\omega))} \\ \Leftrightarrow u(\omega) \frac{J_{n\pm 1}(u(\omega))}{J_n(u(\omega))} &= \pm w(\omega) \frac{K_{n\pm 1}(w(\omega))}{K_n(w(\omega))}. \end{aligned} \quad (1.91)$$

The equivalence comes from identities on Bessel functions.

Weak guiding, LP modes The relationship (1.91) links u to w , or equivalently the reduced frequency v to the normalized propagation constant b by using

$$b(\omega) = 1 - \left(\frac{u(\omega)}{v(\omega)} \right)^2 = \left(\frac{w(\omega)}{v(\omega)} \right)^2, \quad (1.92)$$

derived from Equations (1.78), (1.85) and (1.86).

For each n , there exists m solutions in $b(v)$ as shown in Figure 1.11. Therefore, the modes are defined by the two parameters n and m : n for the definition of the Bessel functions; and for each n , m for the number of possible propagating constants b . b consequently becomes b_{nm} . These modes are classified in LP_{nm} transverse distributions, LP standing for linearly polarized [42]: n is called order and is the number of nodal lignes in the transverse plane; m is called degree and is half the number of extrema in the radial directions. Some modes are shown in Figure 1.12.

Each modal distribution LP_{nm} , with $n \neq 0$, is degenerated: taking $\cos(n\theta)$ in Equation (1.90) gives even modes, while considering $\sin(n\theta)$ leads to odd modes.

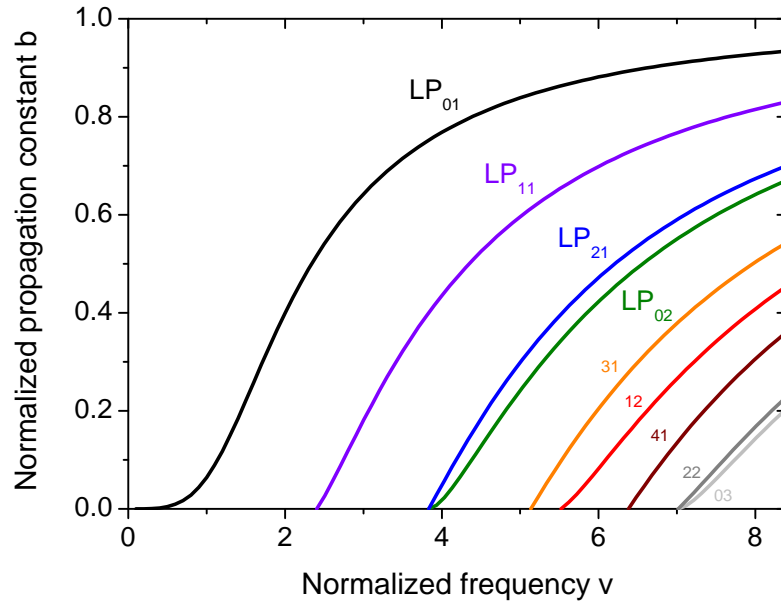


Figure 1.11 – $b(v)$ chart for the first order and degree transverse LP modes.

Notes

- When the approximation of weak guiding does not stand, exact solutions are transverse electric TE ($E_Z = 0$), transverse magnetic TM ($B_Z = 0$), and hybrid HE and EH ($E_Z \neq 0$ and $H_Z \neq 0$) modes. See for example [50, 52]. LP modes can be considered as degenerate situations of transverse and/or hybrid modes.
- For graded-index optical fibers with a parabolic index shape, the transverse modes can be written in terms of the generalized Laguerre functions $L_n^{(l)}$, and are called Laguerre-Gauss modes [53]:

$$\underline{R}(r, \omega) = \sqrt{\frac{2vn!}{(n+l)!}} (vr^2)^{l/2} e^{-(v/2)r^2} L_n^{(l)}(vr^2). \quad (1.93)$$

The mode is here more likely to be guided by a lens focusing effect than by the internal total reflexion. Note that the Bessel functions previously mentioned can be expressed in terms of the generalized Laguerre polynomials.

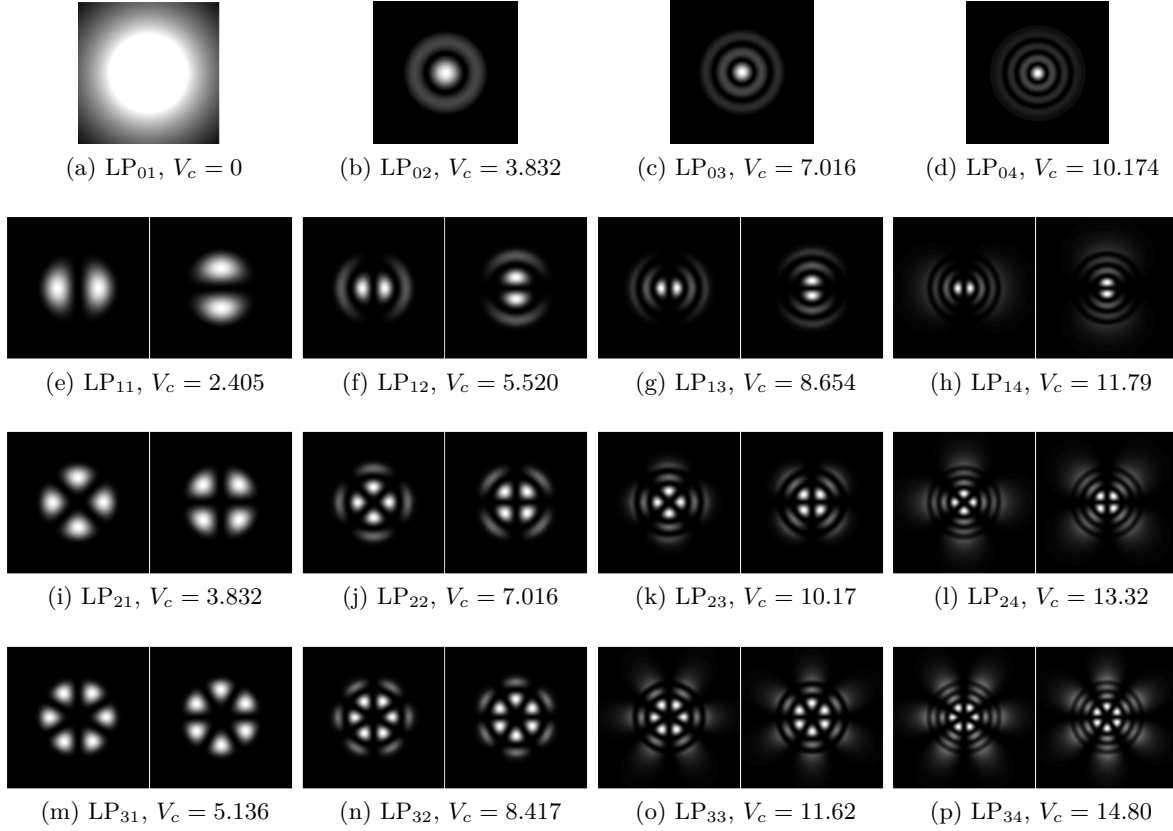


Figure 1.12 – Transverses modes of the first orders n and degrees m together with their normalized cut-off frequencies. For each modal distribution LP_{nm} , the picture on the left-hand side is for the even modes, and on the right-hand side for odd modes. There is no odd LP_{0m} modes.

Normalized cut-off frequency The condition $b_{nm}(\omega) = 0$ is fulfilled at the normalized cut-off frequency $V_{c,nm}$ [47]. It corresponds to the zeros of the Bessel function. The first zero occurs for $V_{c,nm} \simeq 2.405$: below this number, the fundamental mode is the only one that can propagate, and the fiber is said to be monomode. When not monomode, the fiber is multimode. It obviously depends on the considered wavelength. As a consequence, the cut-off wavelength is expressed through:

$$\lambda_{c,nm} = \frac{2\pi a \sqrt{n_{co}^2 - n_{cl}^2}}{V_{c,nm}}. \quad (1.94)$$

The normalized cut-off frequencies for the first orders and degrees modes are given in Figure 1.12.

Analytical expressions for $u(v)$ Differentiating the characteristics equation (1.91) with respect to v and using (1.86), one can get:

$$\frac{du}{dv} = \frac{u}{v} \left[1 - \frac{K_n^2(w)}{K_{n-1}(w) K_{n+1}(w)} \right]. \quad (1.95)$$

It can be solved analytically with some hypotheses given by Gloge [46]. Then, the fundamental LP_{01} mode can be expressed as :

$$u_{01}(v, \omega) = \frac{(1 + \sqrt{2}) v(\omega)}{1 + (4 + v^4(\omega))^{1/4}}. \quad (1.96)$$

And for any other mode, we have:

$$u_{nm}(v, \omega) = V_{c,nm} \exp \left[\frac{1}{s_{nm}} \left(\operatorname{asin} \left(\frac{s_{nm}}{V_{c,nm}} \right) - \operatorname{asin} \left(\frac{s_{nm}}{v(\omega)} \right) \right) \right], \quad (1.97)$$

with $s_{nm} = \sqrt{V_{c,nm}^2 - n^2 - 1}$.

With Equations (1.96) or (1.97) for u_{nm} and (1.92) for b , it is now possible to get an analytical expression for the effective dispersion n_{eff}^{nm} of Equation (1.79):

$$n_{\text{eff}}^{nm}(\omega) = n_{\text{cl}}(\omega) + \Delta n(\omega) \left[1 - \left(\frac{u_{nm}(v, \omega)}{v(\omega)} \right)^2 \right]. \quad (1.98)$$

Effective mode area For a given LP_{nm} mode, it is relevant to define an effective mode area, A_{eff}^{nm} , that is different from the core surface [42]:

$$A_{\text{eff}}^{nm}(\omega) = \frac{1}{f_{nm}(\omega)} = \frac{\langle |E_{nm}|^2 \rangle^2}{\langle |E_{nm}|^4 \rangle} = \frac{\left[\iint_{\mathbb{R}^2} dS |E_{nm}(\omega, r, \theta)|^2 \right]^2}{\iint_{\mathbb{R}^2} dS |E_{nm}(\omega, r, \theta)|^4}, \quad (1.99)$$

with $dS = r dr d\theta$ in polar coordinates. It therefore depends of the geometrical parameters of the fiber. $A_{\text{eff}}(\omega) = \pi W^2(\omega)$, with W the beam size radius, in the case of a Gaussian beam.

1.3.3 Nonlinear optics in a fiber geometry

The general nonlinear coupled equations (1.50) for quadratic interactions, and (1.52) for cubic interactions still apply for light propagation in a guided geometry. Still, few comments arise from the fiber situation and are developed in this section. They are related to isotropy, overlap areas and effective momenta.

Isotropy, modal phase matching Optical fibers without induced birefringence are isotropic media, and consequently no quadratic interaction can occur because of the existence of the inversion center. This is the reason why we only care about cubic interactions in this section.

In addition, as already mentionned in Subsection 1.2.2, because of the absence of birefringence, it is impossible to fulfill the phase-matching condition in fibers for all fields into the same modal transverse distribution. However, nothing forbids interactions between fields of different modal distribution as long as the modes overlap, and the phase-matching condition $\Delta k = 0$ is fulfilled. We highlight those two points below.

Overlap integral, effective interaction area When different modes are involved in a non-linear interaction, the overlap area has to be calculated and should obviously not be zero for the process to occur. Therefore, an important parameter to consider is the overlap integral. The normalized overlap integral $f_{n_i m_i}$ between the transverse modes $\text{LP}_{n_i m_i}$, $i \in \llbracket 0, 3 \rrbracket$ is written as

the inverse of the effective interaction area S_{eff} . For type A cubic interactions, it is given by [54, 55]:

$$\begin{aligned}
 f_{n_i m_i}(\omega_i) \Big|_{i \in [0,3]} &= \frac{\langle \underline{F}_{n_0 m_0} \underline{F}_{n_1 m_1}^* \underline{F}_{n_2 m_2}^* \underline{F}_{n_3 m_3}^* \rangle}{\sqrt{\langle |\underline{F}_{n_0 m_0}|^2 \rangle \langle |\underline{F}_{n_1 m_1}|^2 \rangle \langle |\underline{F}_{n_2 m_2}|^2 \rangle \langle |\underline{F}_{n_3 m_3}|^2 \rangle}} \\
 &= \frac{\iint_{\mathbb{R}^2} dS \underline{F}_{n_0 m_0}(\omega_0, r, \theta) \underline{F}_{n_1 m_1}^*(\omega_1, r, \theta) \underline{F}_{n_2 m_2}^*(\omega_2, r, \theta) \underline{F}_{n_3 m_3}^*(\omega_3, r, \theta)}{\sqrt{\iint_{\mathbb{R}^2} dS |\underline{F}_{n_0 m_0}(\omega_0, r, \theta)|^2 \cdot \iint_{\mathbb{R}^2} dS |\underline{F}_{n_1 m_1}(\omega_1, r, \theta)|^2 \cdot \iint_{\mathbb{R}^2} dS |\underline{F}_{n_2 m_2}(\omega_2, r, \theta)|^2 \cdot \iint_{\mathbb{R}^2} dS |\underline{F}_{n_3 m_3}(\omega_3, r, \theta)|^2}} \\
 &\equiv f_{0123}(\omega_{0,1,2,3}) = \frac{1}{S_{\text{eff}}(\omega_{0,1,2,3})},
 \end{aligned} \tag{1.100}$$

where F^* is F complex conjugate. Note that since signed amplitudes are involved in this equation, this overlap integral is reduced to zero if the products $\underline{F}_{n_0 m_0} \underline{F}_{n_1 m_1}^* \underline{F}_{n_2 m_2}^* \underline{F}_{n_3 m_3}^*$ compensate each other when summed over the transverse plane due to the different symmetries of the modal distributions involved.

Nonlinear effective momenta The contributions of the material and waveguide in Equation (1.79) directly affect the phase mismatch, called effective phase mismatch from now on. In addition to these “linear” contributions, it is necessary to take into account a “nonlinear” part coming from self-phase modulation (SPM, or Kerr effect) and cross-phase modulation (XPM) between the waves [45]. Those cubic effects have already been schemed previously: $\omega_i + \omega_i \rightarrow \omega_i + \omega_i$ for SPM at the spectral component ω_i ; $\omega_i + \omega_j \rightarrow \omega_i + \omega_j$ for XPM between spectral components ω_i and ω_j . The “nonlinear” part of the effective index Δk_{NL} is often taken as arising from the SPM of the pump and XPM between the pump and the down-converted fields. For a TPG interaction, we demonstrate in Appendix D that it takes the form [12]:

$$\Delta k_{NL}(\omega_0, \omega_1, \omega_2) = [\gamma_0 - 2(\gamma_{01} + \gamma_{02} + \gamma_{03})] P, \tag{1.101}$$

where P is the total incident power, and γ_0 and γ_{0j} are the SPM and XPM coefficients respectively defined as:

$$\gamma_0(\omega_0) = \frac{\omega_0 \chi_{\text{eff}}^{(3)}}{2\epsilon_0 c^2 n_{\text{eff}}^2(\omega_0) A_{\text{eff}}(\omega_0)}, \tag{1.102}$$

and

$$\gamma_{0j}(\omega_0, \omega_j) = \frac{\omega_j \chi_{\text{eff}}^{(3)}}{2\epsilon_0 c^2 n_{\text{eff}}(\omega_0) n_{\text{eff}}(\omega_j) S_{\text{eff}}^{\text{XPM}}(\omega_0, \omega_j)}. \tag{1.103}$$

A_{eff} is defined in Equation (1.99); and $S_{\text{eff}}^{\text{XPM}}$ is given by:

$$S_{\text{eff}}^{\text{XPM}}(\omega_0, \omega_j) = \frac{\langle |\underline{F}_{n_0 m_0}|^2 \rangle \langle |\underline{F}_{n_1 m_1}|^2 \rangle}{\langle |\underline{F}_{n_0 m_0}|^2 |\underline{F}_{n_1 m_1}|^2 \rangle}. \tag{1.104}$$

The effective phase mismatch now becomes:

$$\begin{aligned}
 \Delta k_{\text{eff}}^{(3)}(\omega_0, \omega_1, \omega_2) &= \Delta k_M(\omega_0, \omega_1, \omega_2) + \Delta k_W(\omega_0, \omega_1, \omega_2) + \Delta k_{NL}(\omega_0, \omega_1, \omega_2) \\
 &= \frac{1}{c} [n_{\text{co}}(\omega_0) + \Delta n(\omega_0) b_{n_0 m_0}(\omega_0)] \omega_0 \\
 &\quad - \sum_{j=1}^3 \frac{1}{c} [n_{\text{co}}(\omega_j) + \Delta n(\omega_j) b_{n_j m_j}(\omega_j)] \omega_j \\
 &\quad + \left[\gamma_0(\omega_0) - 2 \sum_{j=1}^3 \gamma_{0j}(\omega_j) \right] P.
 \end{aligned} \tag{1.105}$$

Coupled equations We still decompose the longitudinal (Z) and transverse (r, θ) variations of the electric field, *i.e.*: $\underline{E}(\vec{r}, \omega) = \underline{F}(r, \theta, \omega) \underline{A}(Z, \omega)$. From the previous considerations on the effective index n_{eff} , the effective phase-mismatch Δk_{eff} and the overlap integral f , the system of coupled equations (1.52) for the longitudinal evolution of a cubic interaction of type A integrated over the transverse plane becomes:

$$\left\{ \begin{aligned}
 \frac{\partial \underline{A}_0(Z, \omega_0)}{\partial Z} &= i\kappa_{\text{eff}}(\omega_0) \iint_{\mathbb{R}^2} \frac{d\omega_1}{2\pi} \frac{d\omega_2}{2\pi} \chi_{\text{eff}}^{(3)}(\omega_0, \omega_1, \omega_2) \underline{A}_1(Z, \omega_1) \underline{A}_2(Z, \omega_2) \underline{A}_3(Z, \omega_0 - \omega_1 - \omega_2) \\
 &\quad \times f_{0123}(\omega_0, \omega_1, \omega_2) \mathcal{F}_1(\omega_1) \mathcal{F}_2(\omega_2) \mathcal{F}_3(\omega_0 - \omega_1 - \omega_2) [\mathcal{F}_0(\omega_0)]^{-1} e^{-i\Delta k_{\text{eff}}^{(3)}(\vec{r}, \omega_0, \omega_1, \omega_2)Z} \\
 \frac{\partial \underline{A}_1(Z, \omega_1)}{\partial Z} &= i\kappa_{\text{eff}}(\omega_1) \iint_{\mathbb{R}^2} \frac{d\omega_0}{2\pi} \frac{d\omega_2}{2\pi} \chi_{\text{eff}}^{(3)}(\omega_0, \omega_1, \omega_2) \underline{A}_0(Z, \omega_0) \underline{A}_2^*(Z, \omega_2) \underline{A}_3^*(Z, \omega_0 - \omega_1 - \omega_2) \\
 &\quad \times f_{0123}(\omega_0, \omega_1, \omega_2) \mathcal{F}_0(\omega_0) \mathcal{F}_2(\omega_2) \mathcal{F}_3(\omega_0 - \omega_1 - \omega_2) [\mathcal{F}_1(\omega_1)]^{-1} e^{+i\Delta k_{\text{eff}}^{(3)}(\vec{r}, \omega_0, \omega_1, \omega_2)Z} \\
 \frac{\partial \underline{A}_2(Z, \omega_2)}{\partial Z} &= i\kappa_{\text{eff}}(\omega_2) \iint_{\mathbb{R}^2} \frac{d\omega_0}{2\pi} \frac{d\omega_1}{2\pi} \chi_{\text{eff}}^{(3)}(\omega_0, \omega_1, \omega_2) \underline{A}_0(Z, \omega_0) \underline{A}_1^*(Z, \omega_1) \underline{A}_3^*(Z, \omega_0 - \omega_1 - \omega_2) \\
 &\quad \times f_{0123}(\omega_0, \omega_1, \omega_2) \mathcal{F}_0(\omega_0) \mathcal{F}_1(\omega_1) \mathcal{F}_3(\omega_0 - \omega_1 - \omega_2) [\mathcal{F}_2(\omega_2)]^{-1} e^{+i\Delta k_{\text{eff}}^{(3)}(\vec{r}, \omega_0, \omega_1, \omega_2)Z} \\
 \frac{\partial \underline{A}_3(Z, \omega_3)}{\partial Z} &= i\kappa_{\text{eff}}(\omega_3) \iint_{\mathbb{R}^2} \frac{d\omega_0}{2\pi} \frac{d\omega_1}{2\pi} \chi_{\text{eff}}^{(3)}(\omega_0, \omega_1, \omega_3) \underline{A}_0(Z, \omega_0) \underline{A}_1^*(Z, \omega_1) \underline{A}_2^*(Z, \omega_0 - \omega_1 - \omega_3) \\
 &\quad \times f_{0123}(\omega_0, \omega_1, \omega_2) \mathcal{F}_0(\omega_0) \mathcal{F}_1(\omega_1) \mathcal{F}_2(\omega_0 - \omega_1 - \omega_3) [\mathcal{F}_3(\omega_3)]^{-1} e^{+i\Delta k_{\text{eff}}^{(3)}(\vec{r}, \omega_0, \omega_1, \omega_3)Z}.
 \end{aligned} \right. \tag{1.106}$$

\underline{A} is the longitudinal spectral electric field expressed in $\text{Vm}^{-1}\text{rad}^{-1}$; κ_{eff} is expressed as:

$$\kappa_{\text{eff}}(\omega) = \frac{\omega}{2n_{\text{eff}}(\omega)c}. \tag{1.107}$$

The effective susceptibility is often taken as $\chi_{\text{eff}}^{(3)} = \frac{3}{4}\text{Re}(\chi_{xxxx}^{(3)})$ [30]. f_{0123} is the overlap integral of Equation (1.100) between the four modal distributions $\text{LP}_{n_i m_i}$. \mathcal{F}_i comes from the normalization of the transverse component of the electric field, which magnitude is already reported in \underline{A} . It takes the form:

$$\mathcal{F}_i(\omega) = \sqrt{\langle |\underline{F}_{n_i m_i}(r, \theta, \omega)|^2 \rangle}. \tag{1.108}$$

Note that it is possible to make the \mathcal{F}_i coefficient disappear in the previous coupled equations, but \underline{A} no longer expresses as a spectral electric field². This ends the presentation of the useful basic elements on linear and nonlinear properties in optical fibers.

²In the fiber optics community, it is common practice to work with powers, or their square root [30].

1.4 Quantum nonlinear optics

The classical treatment already reported gives most of the understanding of the nonlinear optical effects that are relevant for the present study. Nonetheless, the quantization of the fields makes new features appear. In particular, the triplet photon state generated through third-order parametric fluorescence, which is a spontaneous emission, require a quantized treatment as strong correlations between down-converted photons arise. Therefore, this section aims to give some useful tools on quantum optics.

1.4.1 Generators for quantum fields evolution

Quantum operators, Heisenberg picture and evolution equation We associate quantum operators $\hat{E}, \hat{D}, \hat{B}, \hat{P}$ with each classical field $\vec{E}, \vec{D}, \vec{B}, \vec{P}$, so that as their expectation values match with their classical version.

We adopt here the Heisenberg representation, where only operators evolve through time and space. We can describe the time evolution of any physical operator \hat{O} by the energy operator $\hat{\mathcal{H}}$, or Hamiltonien, through the evolution equation [56]:

$$\frac{\partial \hat{O}(\vec{r}, t)}{\partial t} = \frac{1}{i\hbar} [\hat{O}(\vec{r}, t), \hat{\mathcal{H}}(t)]. \quad (1.109)$$

Time and energy are indeed conjuguate variables in quantum mechanics. Similarly, as space and momentum are another pair of conjuguate variables, the spatial evolution can be described with the momentum operator $\hat{\mathcal{G}}$. The evolution equation can be written [56, 57]:

$$\frac{\partial \hat{O}(\vec{r}, t)}{\partial Z} = -\frac{1}{i\hbar} [\hat{O}(\vec{r}, t), \hat{\mathcal{G}}(Z)]. \quad (1.110)$$

As in the previous section with classical equations, we still choose to describe the spatial evolution, here with its momentum operator, rather than the temporal evolution.

1.4.2 Propagation of the quantized electromagnetic field in a linear medium

Let us first have a look at the propagation in a linear dielectric medium. Constitutive and Maxwell equations (1.6) to (1.11) are linear and hermitian, and are thus still valid with quantum operators. We can therefore derive a linear quantum propagation equation for the electric field \hat{E} , in the same way as we did classically in Section 1.1.2 [58].

Electric field operator The quantized linearly polarized electric field \hat{E} can still be decomposed on a plane wave basis, as in (1.1), in terms of space-dependent operators $\hat{a}(\vec{r}, \omega)$. They are indeed more convenient than the time-dependent operators $\hat{a}(\vec{k}, t)$ that depend on the medium through the wavevector \vec{k} . This makes one additional reason why the evolution equation (1.110) will be preferred to (1.109). Therefore, time periodicity will be required, instead of the usual spatial periodicity [56]. We consider the decomposition in a continuous basis, hence with continuous variables, by taking the temporal periodicity to infinity, as it is much larger than any other relevant time. Such a continuous description seems to be more appropriate in experiments without a cavity [59]. Then, the quantized electric field operator takes the form [59, 60]:

$$\begin{aligned}
 \hat{\vec{E}}(\vec{r}, t) &= i \int_{\mathbb{R}} \frac{d\omega}{2\pi} \sqrt{\frac{\hbar\omega}{2\varepsilon_0 c S n(\vec{r}, \omega)}} \hat{a}(\vec{r}, \omega) e^{-i\omega t} \vec{e} \\
 &= i \int_{\mathbb{R}^+} \frac{d\omega}{2\pi} \sqrt{\frac{\hbar\omega}{2\varepsilon_0 c S n(\vec{r}, \omega)}} \left[\hat{a}(\vec{r}, \omega) e^{-i\omega t} + h.c. \right] \vec{e} \\
 &= \hat{\vec{E}}^{(+)}(\vec{r}, t) + \hat{\vec{E}}^{(-)}(\vec{r}, t),
 \end{aligned} \tag{1.111}$$

where $h.c.$ stands for hermitian conjugate; \hat{a} and its hermitian conjugate \hat{a}^\dagger , which are the creation and annihilation operators respectively, form a complete set of operators; note that $\hat{a}(\vec{r}, -\omega) = \hat{a}^\dagger(\vec{r}, \omega)$; S is the field transverse area. The operator $\hat{\vec{E}}$ is hermitian contrarily to its spectral components $\hat{\vec{E}}(\vec{r}, \omega) = \sqrt{\frac{\hbar\omega}{4\pi\varepsilon_0 c S n(\vec{r}, \omega)}} \hat{a}(\vec{r}, \omega)$. $\hat{\vec{E}}^{(+)}$ and $\hat{\vec{E}}^{(-)}$ are convenient to separate the contributions of the annihilation and creation operators.

Commutators, Heisenberg inequality The creation and annihilation operators follow the non-commutation relationships for bosonic continuous fields [59]:

$$\left[\hat{a}(\vec{r}_i, \omega_i), \hat{a}^\dagger(\vec{r}_j, \omega_j) \right] = \delta(\vec{r}_i - \vec{r}_j) \delta(\omega_i - \omega_j), \tag{1.112}$$

$$\left[\hat{a}(\vec{r}_i, \omega_i), \hat{a}(\vec{r}_j, \omega_j) \right] = \left[\hat{a}^\dagger(\vec{r}_i, \omega_i), \hat{a}^\dagger(\vec{r}_j, \omega_j) \right] = 0, \tag{1.113}$$

with δ the Dirac function and $[,]$ the commutator.

Such a non-commutation relation for any conjuguate variables X and Y , of standard deviations ΔX and ΔY respectively, leads to the Heisenberg inequality:

$$\Delta X \Delta Y \geq \frac{|\langle [X, Y] \rangle|}{2}. \tag{1.114}$$

In other words, it is impossible to know the accurate values of the X and Y parameters simultaneously.

$\hat{\vec{B}}$, $\hat{\vec{P}}^{(1)}$ and $\hat{\vec{D}}_L$ operators The quantum operators for the magnetic induction, linear polarization and electric displacement are given below. Their derivation follows the classical development given in Equations (1.12), (1.22) and (1.23) respectively.

$$\begin{aligned}
 \hat{\vec{B}}(\vec{r}, t) &= i \int_{\mathbb{R}} \frac{d\omega}{2\pi} \sqrt{\frac{\hbar\omega n(\vec{r}, \omega)}{2\varepsilon_0 c^3 S}} \hat{a}(\vec{r}, \omega) e^{-i\omega t} \vec{u}_Z \times \vec{e} \\
 &= \hat{\vec{B}}^{(+)}(\vec{r}, t) + \hat{\vec{B}}^{(-)}(\vec{r}, t),
 \end{aligned} \tag{1.115}$$

$$\begin{aligned}
 \hat{\vec{P}}^{(1)}(\vec{r}, t) &= i \int_{\mathbb{R}} \frac{d\omega}{2\pi} \sqrt{\frac{\hbar\omega\varepsilon_0}{2c S n(\vec{r}, \omega)}} \left(n^2(\vec{r}, \omega) - 1 \right) \hat{a}(\vec{r}, \omega) e^{-i\omega t} \vec{e} \\
 &= \hat{\vec{P}}^{(1+)}(\vec{r}, t) + \hat{\vec{P}}^{(1-)}(\vec{r}, t),
 \end{aligned} \tag{1.116}$$

$$\begin{aligned}
 \hat{\vec{D}}_L(\vec{r}, t) &= \varepsilon_0 \hat{\vec{E}}(\vec{r}, t) + \hat{\vec{P}}^{(1)}(\vec{r}, t) \\
 &= i \int_{\mathbb{R}} \frac{d\omega}{2\pi} \sqrt{\frac{\hbar \omega \varepsilon_0 n^3(\vec{r}, \omega)}{2cS}} \hat{a}(\vec{r}, \omega) e^{-i\omega t} \vec{e} \\
 &= \hat{\vec{D}}_L^{(+)}(\vec{r}, t) + \hat{\vec{D}}_L^{(-)}(\vec{r}, t).
 \end{aligned} \tag{1.117}$$

$\hat{\vec{E}}$, $\hat{\vec{B}}$, $\hat{\vec{P}}^{(1)}$ and $\hat{\vec{D}}_L$ are hermitian operators.

Hamiltonian The Hamiltonian is defined in terms of the power density $\hat{\pi}$, or Poynting vector operator. It does not depend on the medium, unlike the energy density as shown by the Equations (1.15) and (1.16) [56].

$$\begin{aligned}
 \hat{\pi}(\vec{r}, t) &= \frac{1}{\mu_0} \left[\hat{\vec{E}}^{(-)}(\vec{r}, t) \times \hat{\vec{B}}^{(+)}(\vec{r}, t) + \hat{\vec{B}}^{(-)}(\vec{r}, t) \times \hat{\vec{E}}^{(+)}(\vec{r}, t) \right] \cdot \vec{u}_Z \\
 &= \iint_{\mathbb{R}^{2+}} \frac{d\omega d\omega'}{2\pi 2\pi} \frac{\hbar}{2S} \sqrt{\frac{\omega \omega' n(\vec{r}, \omega')}{n(\vec{r}, \omega)}} \left[\hat{a}^\dagger(\vec{r}, \omega) \hat{a}(\vec{r}, \omega') e^{i(\omega - \omega')t} + h.c. \right].
 \end{aligned} \tag{1.118}$$

Then for the Hamiltonian $\hat{\mathcal{H}}$ to be an energy, an integration of the flux over the temporal period $T \gg \frac{2\pi}{\omega}$ is needed:

$$\begin{aligned}
 \hat{\mathcal{H}}(\vec{r}) &= S \int_{t_0}^{t_0+T} dt \hat{\pi}(\vec{r}, t) \\
 &= \int_{\mathbb{R}^+} \frac{d\omega}{2\pi} \hbar \omega \hat{a}^\dagger(\vec{r}, \omega) \hat{a}(\vec{r}, \omega).
 \end{aligned} \tag{1.119}$$

Note that it is not necessary to take the limit $T \rightarrow +\infty$ as long as all frequencies are multiples of $\frac{2\pi}{T}$.

Linear momentum As emphasized before, we now need to define the momentum operator $\hat{\mathcal{G}}$ in order to derive fields from the spatial evolution equation (1.110). The linear momentum density is expressed by \hat{g}_L [56]:

$$\hat{g}_L(\vec{r}, t) = \left[\hat{\vec{D}}_L^{(-)}(\vec{r}, t) \times \hat{\vec{B}}^{(+)}(\vec{r}, t) + \hat{\vec{B}}^{(-)}(\vec{r}, t) \times \hat{\vec{D}}_L^{(+)}(\vec{r}, t) \right] \cdot \vec{u}_Z. \tag{1.120}$$

It can be simplified in the case of the propagation in a dielectric medium as:

$$\begin{aligned}
 \hat{g}_L(\vec{r}, t) &= \hat{\vec{D}}_L^{(-)}(\vec{r}, t) \hat{\vec{E}}^{(+)}(\vec{r}, t) + \hat{\vec{E}}^{(-)}(\vec{r}, t) \hat{\vec{D}}_L^{(+)}(\vec{r}, t) \\
 &= \iint_{\mathbb{R}^{2+}} \frac{d\omega d\omega'}{2\pi 2\pi} \frac{\hbar}{2cS} \sqrt{\frac{\omega \omega' n^3(\vec{r}, \omega')}{n(\vec{r}, \omega)}} \left[\hat{a}^\dagger(\vec{r}, \omega) \hat{a}(\vec{r}, \omega') e^{i(\omega - \omega')t} + h.c. \right].
 \end{aligned} \tag{1.121}$$

Finally, the linear momentum operator $\hat{\mathcal{G}}_L$ writes as:

$$\begin{aligned}
 \hat{\mathcal{G}}_L(\vec{r}) &= S \int_{t_0}^{t_0+T} dt \hat{g}_L(\vec{r}, t) \\
 &= \int_{\mathbb{R}^+} \frac{d\omega}{2\pi} \hbar k(\omega) \hat{a}^\dagger(\vec{r}, \omega) \hat{a}(\vec{r}, \omega).
 \end{aligned} \tag{1.122}$$

As the Hamiltonian stands for the total energy of the field, the linear momentum operator represents the total linear momentum of the field.

Linear solution for propagation This momentum operator together with the evolution equation (1.110) and the bosonic commutation relationships (1.112) and (1.113) lead to a plane wave longitudinal evolution for \hat{a} , as it was the case in the classical approach, *i.e.*:

$$\hat{a}(\vec{r}, \omega) = \hat{a}(\vec{r}_t, 0, \omega) e^{ik(\vec{r}, \omega)Z}, \tag{1.123}$$

with \vec{r}_t for the transverse coordinates (X, Y) .

1.4.3 Propagation of the quantized electromagnetic field in a nonlinear medium

Nonlinear momentum We have to introduce the nonlinear momentum operator $\hat{\mathcal{G}}_{NL}$ in order to be able to describe the spatial evolution of the fields in the nonlinear medium. The approach is the same as previously, and we begin by expressing the nonlinear polarization $\hat{\vec{P}}_{NL}$ that now takes part of the displacement vector, and the nonlinear momentum density \hat{g}_{NL} . The Hamiltonian, not affected by the nonlinearity, stays unchanged. We still work under the assumption of the slowly varying envelope, which is justified considering that our experiments are performed with nanosecond or picosecond pulse durations. In that case, the plane wave envelope is modulating as: $\hat{a}(\vec{r}, \omega) = \hat{a}(\vec{r}, \omega) e^{ik(\vec{r}, \omega)Z}$.

The nonlinear polarization operator up to the third-order is given by:

$$\begin{aligned}
 &\vec{P}_{NL}(\vec{r}, t) \\
 = &\varepsilon_0 \int_{\mathbb{R}} \frac{d\omega_0}{2\pi} \left[\int_{\mathbb{R}} \frac{d\omega_1}{2\pi} \bar{\chi}^{(2)}(\omega_0 = \omega_1 + \omega_2) : [\vec{E}(\vec{r}, \omega_1) \otimes \vec{E}(\vec{r}, \omega_0 - \omega_1)] \right. \\
 &+ \left. \iint_{\mathbb{R}^2} \frac{d\omega_1 d\omega_2}{2\pi 2\pi} \bar{\chi}^{(3)}(\omega_0 = \omega_1 + \omega_2 + \omega_3) : [\vec{E}(\vec{r}, \omega_1) \otimes \vec{E}(\vec{r}, \omega_2) \otimes \vec{E}(\vec{r}, \omega_0 - \omega_1 - \omega_2)] \right] e^{-i\omega_0 t} \\
 = &\hat{\vec{P}}_{NL}^{(+)}(\vec{r}, t) + \hat{\vec{P}}_{NL}^{(-)}(\vec{r}, t).
 \end{aligned} \tag{1.124}$$

Note that the third-order nonlinear term only takes into account the type A interactions of Section 1.1.3, TPG being part of them.

The nonlinear momentum density operator is then expressed by:

$$\begin{aligned}
 & \hat{g}_{NL}(\vec{r}, t) \\
 &= \hat{P}_{NL}^{(-)}(\vec{r}, t) \hat{E}^{(+)}(\vec{r}, t) + \hat{E}^{(-)}(\vec{r}, t) \hat{P}_{NL}^{(+)}(\vec{r}, t) \\
 &= \varepsilon_0 \left[i \left(\frac{\hbar}{2\varepsilon_0 c S} \right)^{3/2} \iiint_{\mathbb{R}^{3+}} \frac{d\omega_0}{2\pi} \frac{d\omega_1}{2\pi} \frac{d\omega'}{2\pi} \chi_{\text{eff}}^{(2)}(\vec{r}, \omega_0, \omega_1) \sqrt{\frac{\omega' \omega_1 (\omega_0 - \omega_1)}{n(\vec{r}, \omega') n(\vec{r}, \omega_1) n(\vec{r}, \omega_0 - \omega_1)}} \right. \\
 & \quad \times \hat{a}(\vec{r}, \omega_1) \hat{a}(\vec{r}, \omega_0 - \omega_1) \hat{a}^\dagger(\vec{r}, \omega') e^{i(\omega' - \omega_0)t} e^{-i\Delta k^{(2)}(\omega', \omega_1, \omega_0 - \omega_1)Z} + h.c. \\
 & \quad - \left(\frac{\hbar}{2\varepsilon_0 c S} \right)^2 \iiint_{\mathbb{R}^{4+}} \frac{d\omega_0}{2\pi} \frac{d\omega_1}{2\pi} \frac{d\omega_2}{2\pi} \frac{d\omega'}{2\pi} \chi_{\text{eff}}^{(3)}(\vec{r}, \omega_0, \omega_1, \omega_2) \sqrt{\frac{\omega' \omega_1 \omega_2 (\omega_0 - \omega_1 - \omega_2)}{n(\vec{r}, \omega') n(\vec{r}, \omega_1) n(\vec{r}, \omega_2) n(\vec{r}, \omega_0 - \omega_1 - \omega_2)}} \\
 & \quad \times \hat{a}(\vec{r}, \omega_1) \hat{a}(\vec{r}, \omega_2) \hat{a}(\vec{r}, \omega_0 - \omega_1 - \omega_2) \hat{a}^\dagger(\vec{r}, \omega') e^{i(\omega' - \omega_0)t} e^{-i\Delta k^{(3)}(\omega', \omega_1, \omega_2, \omega_0 - \omega_1 - \omega_2)Z} + h.c. \left. \right],
 \end{aligned} \tag{1.125}$$

with $\Delta k^{(2)}$ and $\Delta k^{(3)}$ already given in Equations (1.51) and (1.54), and $\chi_{\text{eff}}^{(2)}$ and $\chi_{\text{eff}}^{(3)}$ from (1.49) and (1.53).

The temporal integration gives the nonlinear momentum operator:

$$\begin{aligned}
 & \hat{\mathcal{G}}_{NL}(\vec{r}) \\
 &= S \int_{t_0}^{t_0+T} dt \hat{g}_{NL}(\vec{r}, t) \\
 &= \left[i \iint_{\mathbb{R}^{2+}} \frac{d\omega_0}{2\pi} \frac{d\omega_1}{2\pi} \hbar \beta(\vec{r}, \omega_0, \omega_1) \hat{a}(\vec{r}, \omega_1) \hat{a}(\vec{r}, \omega_0 - \omega_1) \hat{a}^\dagger(\vec{r}, \omega_0) e^{-i\Delta k^{(2)}(\omega_0, \omega_1, \omega_0 - \omega_1)Z} + h.c. \right. \\
 & \quad - \iiint_{\mathbb{R}^{3+}} \frac{d\omega_0}{2\pi} \frac{d\omega_1}{2\pi} \frac{d\omega_2}{2\pi} \hbar \Gamma(\vec{r}, \omega_0, \omega_1, \omega_2) \\
 & \quad \times \hat{a}(\vec{r}, \omega_1) \hat{a}(\vec{r}, \omega_2) \hat{a}(\vec{r}, \omega_0 - \omega_1 - \omega_2) \hat{a}^\dagger(\vec{r}, \omega_0) e^{-i\Delta k^{(3)}(\omega_0, \omega_1, \omega_2, \omega_0 - \omega_1 - \omega_2)Z} + h.c. \left. \right],
 \end{aligned} \tag{1.126}$$

with

$$\beta(\vec{r}, \omega_0, \omega_1) = \sqrt{\frac{\hbar}{8\varepsilon_0 c^3 S}} \sqrt{\frac{\omega_0 \omega_1 (\omega_0 - \omega_1)}{n(\vec{r}, \omega_0) n(\vec{r}, \omega_1) n(\vec{r}, \omega_0 - \omega_1)}} \chi_{\text{eff}}^{(2)}(\vec{r}, \omega_0, \omega_1), \tag{1.127}$$

and

$$\Gamma(\vec{r}, \omega_0, \omega_1, \omega_2) = \frac{\hbar}{4\varepsilon_0 c^2 S} \sqrt{\frac{\omega_0 \omega_1 \omega_2 (\omega_0 - \omega_1 - \omega_2)}{n(\vec{r}, \omega_0) n(\vec{r}, \omega_1) n(\vec{r}, \omega_2) n(\vec{r}, \omega_0 - \omega_1 - \omega_2)}} \chi_{\text{eff}}^{(3)}(\vec{r}, \omega_0, \omega_1, \omega_2). \tag{1.128}$$

Nonlinear solution for propagation The evolution equation with the total momentum operator defined previously is:

$$\frac{\partial \hat{a}(\vec{r}, t)}{\partial Z} = -\frac{1}{i\hbar} \left[\hat{a}(\vec{r}, t), \hat{\mathcal{G}}_L(\vec{r}) + \hat{\mathcal{G}}_{NL}(\vec{r}) \right]. \tag{1.129}$$

It becomes:

$$\frac{\partial \hat{a}(\vec{r}, \omega)}{\partial Z} = -\frac{1}{i\hbar} \left[\hat{a}(\vec{r}, \omega), \hat{\mathcal{G}}_{NL}(\vec{r}) \right]. \tag{1.130}$$

We can consider the strong pump as a classical field, labeled 0, so that we have: $\hat{a}_0(\vec{r}, \omega) = \underline{a}_0(\vec{r}, \omega)$.

In the case of a quadratic parametric fluorescence, we can deduce the evolution equation of down-converted indistinguishable photons (field s) with the use of the commutation equalities (1.112) and (1.113):

$$\frac{\partial \hat{a}_s(\vec{r}, \omega)}{\partial Z} = \int_{\mathbb{R}^+} \frac{d\tilde{\omega}}{2\pi} \beta(\vec{r}, \omega, \tilde{\omega}) \underline{a}_0(\vec{r}, \omega + \tilde{\omega}) \hat{a}_s^\dagger(\vec{r}, \tilde{\omega}) e^{-i\Delta k^{(2)}(\omega + \tilde{\omega}, \tilde{\omega}, \omega)Z}. \quad (1.131)$$

Note that the values of $\Delta k^{(2)}$ reduces the integral interval. In the case of a monochromatic pump, only one couple of down-converted photons remains. This is easily understood as the energy and momentum equations fix the two unknown frequency quanta.

For a type A cubic parametric fluorescence, the evolution equation of the indistinguishable photons leads us to the following differential equation:

$$\frac{\partial \hat{a}_s(\vec{r}, \omega)}{\partial Z} = -i \iint_{\mathbb{R}^{2+}} \frac{d\hat{\omega} d\tilde{\omega}}{2\pi 2\pi} \Gamma(\vec{r}, \omega, \hat{\omega}, \tilde{\omega}) \underline{a}_0(\vec{r}, \hat{\omega}) \hat{a}_s^\dagger(\vec{r}, \hat{\omega} - \omega - \tilde{\omega}) \hat{a}_s^\dagger(\vec{r}, \tilde{\omega}) e^{-i\Delta k^{(3)}(\hat{\omega}, \omega, \tilde{\omega}, \hat{\omega} - \omega - \tilde{\omega})Z}. \quad (1.132)$$

The same comments as before apply for the restriction of the integral intervals. But here, the two energy and momentum equations are not sufficient to determine an unique couple of triple photons, which dilute them spectrally.

1.4.4 Quantum states of light

Spectral density We define the photon number operator as the quantum equivalent of the classical modulus squared amplitude. It is given at any frequency ω by:

$$\hat{n}(\omega) = \hat{a}^\dagger(\omega) \hat{a}(\omega). \quad (1.133)$$

Its expectation value defines the spectral photon density:

$$n(\omega) = \langle \psi | \hat{n}(\omega) | \psi \rangle, \quad (1.134)$$

where $|\psi\rangle$ is the quantum state of the system at the entrance of the propagation medium, in compliance with the Heisenberg picture where the evolution is imputed in the operators. We now need to discuss about vacuum and coherent states before giving the form for this quantum state.

Vacuum state The vacuum state $|0\rangle$ is the ground state, with the lowest energy possible. No photon fills it. Still, because of the Heisenberg inequality $\Delta \mathcal{E} \Delta t \geq \hbar$, its energy is not zero for a finite time. The variance of the transverse electric field, $\langle 0 | \hat{E}_t^2 | 0 \rangle$, is not zero either, bringing about the so-called vacuum quantum fluctuations that well explains the spontaneous emission phenomenon. At any frequency, the vacuum state fulfills the following equation:

$$\hat{a}(\omega) |0\rangle = 0. \quad (1.135)$$

Coherent state An ideal classical laser light has well-defined amplitude and phase. This cannot be the case for its quantum counterpart as the Heisenberg inequality applies. Therefore, fluctuations are associated with these amplitude and phase variables. The laser light is described by a state for which these uncertainties equal each other, and minimize the uncertainty principle $\Delta q \Delta p = \frac{\hbar}{2}$, where q is the position and p the momentum [61]. Such states are quasi-classical states since they look like classical states as much as allowed by quantum mechanics. They are called coherent state, referred to as $|\alpha\rangle$ and are eigenstates of the annihilation operator \hat{a} [62]:

$$\hat{a}(\omega) |\alpha(\omega)\rangle = \alpha(\omega) |\alpha(\omega)\rangle. \quad (1.136)$$

The operator \hat{a} being non hermitian, the eigenvalue α is complex.

The beams we consider are spectrally gaussian. Thus the spectral density can be written:

$$n(\omega) = \langle \hat{n}(\omega) \rangle = n(\omega^c) e^{-\left(\frac{\omega - \omega^c}{\Delta\omega}\right)^2}, \quad (1.137)$$

for $\omega \in \mathbb{R}^+$; ω^c the central frequency of the field. Therefore, the eigenvalue α takes the form:

$$\alpha(\omega) = \sqrt{n(\omega^c)} e^{-\frac{1}{2}\left(\frac{\omega - \omega^c}{\Delta\omega}\right)^2 + i\varphi}, \quad (1.138)$$

where φ is a phase term. The photon number and phase fluctuations can be written as:

$$\Delta N^2 = \Delta\varphi^{-2} = |\alpha|^2.$$

Quantum state of the system The quantum state $|\psi\rangle$ of the system is described by the tensorial product of the different fields at the entrance of the system, except for the pump field described classically. For cubic interactions of type A, three modes remain, denoted with subscripts 1, 2 and 3:

$$|\psi\rangle = |\psi\rangle_1 \otimes |\psi\rangle_2 \otimes |\psi\rangle_3 \equiv |\psi_1, \psi_2, \psi_3\rangle. \quad (1.139)$$

When vacuum quantum fluctuations are involved, *i.e.* for spontaneous parametric generation, the state is written with vacuum states:

$$|\psi\rangle = |0_1, 0_2, 0_3\rangle. \quad (1.140)$$

If the generation is stimulated, the stimulation field is taken to be a coherent state, written as follows in the case of a stimulation by field 3 for example:

$$|\psi\rangle = |0_1, 0_2, \alpha_3\rangle. \quad (1.141)$$

1.4.5 Coherence of down-converted modes through parametric processes

Correlations, entanglement From the evolution equations (1.131) and (1.132), we see that the mode operators are linearly dependent in the case of quadratic interactions, while they are not for cubic interactions. On the basis of this mere observation, we can expect that quantum properties of triplets will differ from those of twin photons. But it will be seen thereafter that it is not the only argument for this statement.

A triplet state generated from parametric fluorescence is created from the involvement of the quantum vacuum fluctuations. It indeed exhibits quantum properties: its three constituting photons have special links, correlations. Those photons are said to be entangled as the quantum state characterizing the triplet state is non-separable, in other words cannot be written as products of single particle states [63]. Those states are indeed entangled in frequency and wavenumber because of the energy and linear momentum conservation laws; and can also be in polarization depending on the interaction configuration [64].

In the case of a generation of triplets through DFG, it will be seen in Section 2.3.1 that the stimulation influences the correlation properties of the triplet state, which then depends on the number of stimulating photons.

To probe the nature of the correlations, several options are possible: direct experiments on quantum fluctuations, quantum tomography through Wigner function reconstruction, or recombination through SFG for instance, as described in the next sections.

Quantum fluctuations Direct estimation of the quantum intensity fluctuations can be made through intensity correlation measurement based on a Hanbury Brown and Twiss interferometer [65]. This experiment measures the coincidences between two intensities I_1 and I_2 , and allows us to infer the second-order normalized intensity correlation function:

$$g^{(2)}(\tau) = \frac{\overline{I_1(t) I_2(t + \tau)}}{\overline{I_1(t)} \overline{I_2(t)}}. \quad (1.142)$$

Three-photon correlations can be estimated through the third-order normalized intensity correlation function [58], function of the three intensities I_1, I_2 and I_3 , *i.e.*:

$$g^{(3)}(\tau_1, \tau_2) = \frac{\overline{I_1(t) I_2(t + \tau_1) I_3(t + \tau_2)}}{\overline{I_1(t)} \overline{I_2(t)} \overline{I_3(t)}}. \quad (1.143)$$

The corresponding block diagram of the measurement is given in Figure 1.13. To get the phase fluctuations, experiments based on homodyne detection can be used [66].

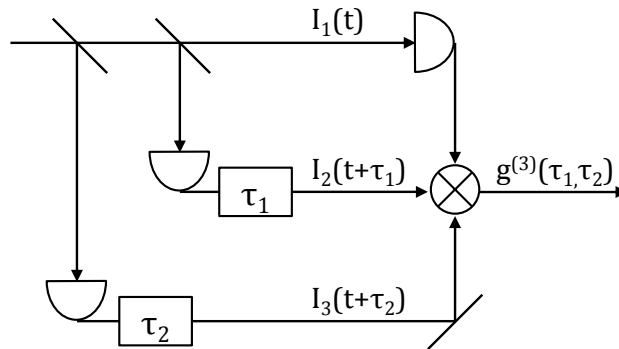


Figure 1.13 – Third-order intensity correlation measurement.

Quantum state tomography, Wigner function When working with continuous variables, it is relevant to describe the quantum state in the phase space by the Wigner function, instead

of the density matrix $\hat{\rho}$, the eigenstate basis being continuous and of infinite dimension. For a pure state with a density matrix $\hat{\rho} = |\psi\rangle\langle\psi|$, this function can be written [67]:

$$W(q, p) = \frac{1}{2\pi} \int_{\mathbb{R}} dx e^{jpx} \left\langle q - \frac{x}{2} \left| \hat{\rho} \right| q + \frac{x}{2} \right\rangle,$$

with q and p the quadratures of the electric field, that is to say quantities that represent the real and imaginary parts of the complex amplitude of the annihilation and creation operators [58]. This Wigner function extends the notion of probability distribution in the phase space $\{q, p\}$, with the probability of finding the electric field at (q, p) within $dqdp$ expressed as $d^2P = W(q, p) dqdp$ just like in statistical physics. But as the uncertainty principle can lead to negative values, it is referred to as a quasi-probability distribution [68]. Hence these negativities sign the non-classicality of a state.

The projection of the Wigner distribution along a direction θ gives a marginal probability distribution P_θ , expressed as [68]:

$$P_\theta(q) = \langle q | \hat{\rho} | q \rangle = \int_{\mathbb{R}} dp W(q \cos \theta - p \sin \theta, q \sin \theta + p \cos \theta).$$

The marginal probability distributions can be experimentally accessible through homodyne detection, and together reconstruct the Wigner function. This is quantum state tomography [69].

Recombination The best alternative for experiments involving a large number of photons is to consider a SFG experiment between triple photons, which corresponds to the photon fusion of the triple state (see Figure 1.14) [16]. It follows works performed on photon pairs generated by $\chi^{(2)}$ SPDC [60, 70]. The only difference between classical and quantum analyses of such an experiment lies in the expression of the electric field, quantum operator or classical vector, that experiences or not the non-commutation relationship (1.112). If the experimental SFG and the classical analysis give the same intensity spectrum or equivalently the same temporal autocorrelation, the three photons would be non-correlated, or incoherent for quantum mechanics, which corresponds to the classical case.

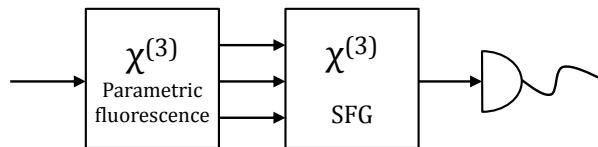


Figure 1.14 – Recombination protocol.

But if they are different, some quantum coherence is preserved. The amplitude and phase relationships link in a quantum way the correlated triple photons together. It is thus important to preserve the quantum coherence if we intend to use triplets as new tools for quantum information and its potential future protocols.

1.5 Conclusion

This first chapter has dealt with basic elements for the understanding of this work. It has been shown that a nonlinear interaction has to fulfill the phase-matching condition to be efficient, in addition to the energy conservation relationship. A careful attention has to be brought to maximizing the effective coefficient, as well as the temporal and spatial overlaps.

In anisotropic crystals and isotropic optical fibers, two different kinds of phase matching can be achieved: birefringent phase matching in the first case, and modal phase matching in the second. Next chapters will make direct use of these theoretical results: THG and TPG in anisotropic crystals in Chapter 3; THG and TPG in optical fibers in Chapter 4.

Lastly, the quantum analysis that is necessary for the calculation of spontaneous TPG and for the understanding of the non-classicality of this new state of light can follow the derivation made in the present chapter.

State of the art and motivations

“Je me félicitais que notre passé fût assez long pour nous servir d’exemples,
et pas assez lourd pour nous en écraser.”

– Marguerite Yourcenar, *Mémoires d’Hadrien*

Contents

2.1	Motivations in the framework of nonlinear quantum optics	46
2.1.1	Twin photons	46
2.1.2	Photonic states with $N \geq 3$ particles	47
2.1.3	Motivation for triplet photon generation	48
2.2	Experiments and theory of triplet photon generation	49
2.2.1	Triplet photon generation through cubic nonlinear processes	49
2.2.2	Alternatives to the direct generation of triplets	54
2.3	Correlation studies	58
2.3.1	Photon recombination	58
2.3.2	Theoretical quantum tomography	61
2.3.3	Coincidence measurements	62
2.4	Conclusion and experimental strategies	63

The most direct way to generate photon triplets is to take advantage of the third-order parametric fluorescence, depicted in Figure 1.4. In the present chapter, we first give our motivations for studying such photonic states, in the light of twin photons, the quadratic equivalent to triplets. We then give a state of the art of the generation of triple photons, whether it is direct through a cubic interaction or indirect through quadratic cascading processes. We also summarize what has been reported in the literature on the correlations among those states. Finally, we give the orientation of this thesis in this context.

2.1 Motivations in the framework of nonlinear quantum optics

2.1.1 Twin photons

Our motivations are first deeply fundamental. To apprehend this, let us go first into a quick review over some recent history of quantum physics.

Entanglement Twin photons are the quadratic equivalent of triple photons: they can for example be generated through second-order nonlinear optical interactions. They are one example of two-particle systems that are said to bear perfect correlations, or in Erwin Schrödinger’s words, to be entangled [63]. Before any measurement in any basis, the state of the two photons can be known but not the individual state of either of them: the twins share a single wave function. But when a measurement is performed so that the state of one photon is known, the outcome for the other photon is also known with certainty, no matter the distance separating them.

EPR debate Entanglement is a fascinating quantum phenomenon that went on the rise with the debate pointed out by Albert Einstein, Boris Podolsky and Nathan Rosen in their famous paper dating from 1935 [71]. With a causal point of view, they made some propositions about the completeness, reality and locality of a theory.

- Completeness: *“Every element of the physical reality must have its physical counterpart in the physical theory.”*
- Reality: *“If without in any way disturbing a system, we can predict with certainty (i.e. with a probability equal to unity) the value of a physical quantity, then there exists an element of physical reality corresponding to this physical quantity.”*
- Locality: *“Since at the time of measurement, the two systems no longer interact, no real change can take place in the second system in consequence of anything that can be done in the first system.”*

They showed that these propositions are in contradiction with the quantum description of two perfectly correlated spin-half particles. They concluded that quantum mechanics has thus to be incomplete. This constituted the EPR paradox. Therefore, no local realism can describe independently the two particles constituting the entangled state. These contradictions have been reformulated many years later by John Bell into quantitative criteria based on a theory of local hidden variables, the well-known Bell inequalities [72].

Non-locality Some of the experimental tests performed violated Bell inequalities. The first convincing demonstrations were led by Alain Aspect in the early eighties [1, 73, 74]: twin photons were emitted from a radiative cascade in calcium atoms (atomic jet), excited at resonance by a krypton laser and a tunable laser. Many other experimental demonstrations have followed, always in favour of quantum mechanics, rejecting therefore the local realism and the local hidden variable scenarii. The experiments of Aspect have been reproduced over kilometers with the

same result [75]. This opened the door to the field of quantum information, with quantum cryptography, quantum computing or quantum teleportation.

2.1.2 Photonic states with $N \geq 3$ particles

Triplet state Quantum optics has been deeply influenced by twin photons. One can think that N -particle highly correlated systems can play an important role in this story as well. Among them, a step ahead to the twins would be the three-particle systems. Regarding the generation of such states through optical techniques, we will enter into details in Section 2.2. Nevertheless, we can already note that, following the work on twin photons, the most natural way to generate three-photon states is offered by cubic nonlinear optics. This has not been the only technique investigated by the community because of the weakness of magnitude of third-order nonlinearities. All these triple states of light exhibit anyway strong correlations.

GHZ, W states It has been shown that three-particle systems can be entangled into two inequivalent ways [76, 77], Greenberger-Horne-Zeilinger (GHZ) and W states, *i.e.* that it is not possible to obtain one state from the other by means of local operations and classical communication. On one hand, GHZ states [8, 78] are three-particle maximally entangled states. They are fragile in the sense that entanglement is hold as long as none of the three particles is traced out. On the other hand, W [9, 10] states are maximally robust entangled states, as two over three particles can remain entangled under the projection of the state of one particle. For polarization entanglement, those states can for instance be written as:

$$|\text{GHZ}\rangle = \frac{1}{\sqrt{2}}(|\text{HHH}\rangle + |\text{VVV}\rangle), \quad (2.1)$$

$$|\text{W}\rangle = \frac{1}{\sqrt{3}}(|\text{HHV}\rangle + |\text{HVH}\rangle + |\text{VHH}\rangle), \quad (2.2)$$

where $|\text{H}\rangle$ and $|\text{V}\rangle$ stand for horizontal and vertical polarization respectively. As far as we are concerned, our experiments presented in the next section do not generate such polarization-entangled states but continuous-variable correlated states analogous to them [11], here with energy (or time) and momentum (or position) correlations. They are similar to the continuous-variable twin photons [79–81]. This is indeed a consequence of the energy and momentum conservations of phase-matched parametric interactions. Some references in the literature also discuss hyper-entangled states [82].

In 2009, Wen and Rubin considered three- and two-mode triphoton states entangled in time and space [83]. Specifically, three-mode states are given by:

$$|\psi\rangle = \iiint \frac{d\omega_1}{2\pi} \frac{d\omega_2}{2\pi} \frac{d\omega_3}{2\pi} \iiint d\vec{\alpha}_1 d\vec{\alpha}_2 d\vec{\alpha}_3 F\left(L, \Delta\vec{k}\{\omega\}_{1,2,3}, \{\vec{\alpha}\}_{1,2,3}\right) |1_{\vec{k}_1}, 1_{\vec{k}_2}, 1_{\vec{k}_3}\rangle, \quad (2.3)$$

where F is a function depending on several parameters: the circular frequency ω_i , the transverse wave vectors $\vec{\alpha}_i$ of photons in mode \vec{k}_i , the interaction length L , and the phase-mismatch $\Delta\vec{k}$. With the same notations and considering the appropriate function F' , two-mode states account for a degeneracy between two photons. They take the form:

$$|\psi\rangle = \iint \frac{d\omega_1}{2\pi} \frac{d\omega_2}{2\pi} \iint d\vec{\alpha}_1 d\vec{\alpha}_2 F' \left(L, \Delta\vec{k} \{\omega\}_{1,2}, \{\vec{\alpha}\}_{1,2} \right) |2_{\vec{k}_1}, 1_{\vec{k}_2}\rangle. \quad (2.4)$$

By looking at the second-order coherence function in the temporal and spatial domains (see Equation (1.142)) they showed that three-mode states are similar to W states whereas two-mode states are analogous to GHZ states concerning their robustness to one photon measurement.

2.1.3 Motivation for triplet photon generation

From the previous section, we see that investigating tri-photon states of light would enable the exploration of fundamental questions about quantum mechanics. As twin photons influenced the practical applications of quantum optics, tri-photon states may also potentially be part of the story in the future and open new routes in quantum information.

More particularly, one of the three photons of the triplet could herald the presence of the two others, forming a pair. A protocol of heralded generation in the case of entangled photon pairs can be found in [84], and experimental demonstrations in [85, 86].

Triplet states could also allow the elaboration of quantum cryptography protocols using a third part. For instance, two photons of confidence could be used instead of one when considering twin photons. A quantum key distribution scheme with entangled twins that uses Bell's inequality to establish security has been proposed by Artur Ekert in [87] and demonstrated in [88, 89]. Another scheme based on Wigner's inequality for the security test has been demonstrated the same year [90]. Entanglement-based quantum key distribution with photon pairs, has been realized over kilometric distances [91].

In addition, three-particle entanglement could be used for quantum teleportation of a state to either one of two locations [92]. Only one of these two receivers can indeed reconstruct the state, in accordance with the no-cloning theorem [93]. Three-particle entangled state is also used in the paper from Bruß *et al.* [94] in their proposal to realize the quantum cloning machine of Bužek-Hillery [95].

Lastly, the direct generation of photon triplets is also challenging in the field of nonlinear optics as the third-order susceptibilities involved in the process, therefore the conversion efficiencies, are very low. It might as well impact the development of new optical parametric sources.

2.2 Experiments and theory of triplet photon generation

A first subsection is dedicated to the direct generation of photon triplets from cubic optical nonlinear interactions, while a second one reports on more indirect proposals and experimental demonstrations.

2.2.1 Triplet photon generation through cubic nonlinear processes

2.2.1.1 Classical understanding of triple photons

Triple photon generation (TPG) takes part in the general framework of nonlinear optics given in Section 1.1.3, whose first theoretical understanding came from Armstrong and co-workers in [21]. More specifically, the direct TPG interaction belongs to the type A cubic scheme:

$$\lambda_0 \rightarrow \lambda_1 + \lambda_2 + \lambda_3. \quad (2.5)$$

Its classical theory has been led by the team in Grenoble, through derivation of solutions to the coupled equations in the form of Jacobi elliptic functions [33]. These derivations are made in the case of three or four incoming beams in free space propagation, or in an injection-seeded optical parametric oscillator (OPO). Hypotheses of a phase-matched interaction far from the medium resonances, along with monochromatic fields were made. This theory has been compared successfully to the first experiment described in the following section.

2.2.1.2 Pioneer experiment

The first generation of photon triplets was carried out in 2004 in Grenoble by Julien Douady and Benoît Boulanger, through a bistimulated DFG configuration [13, 96]. The experimental setup is depicted in Figure 2.1.

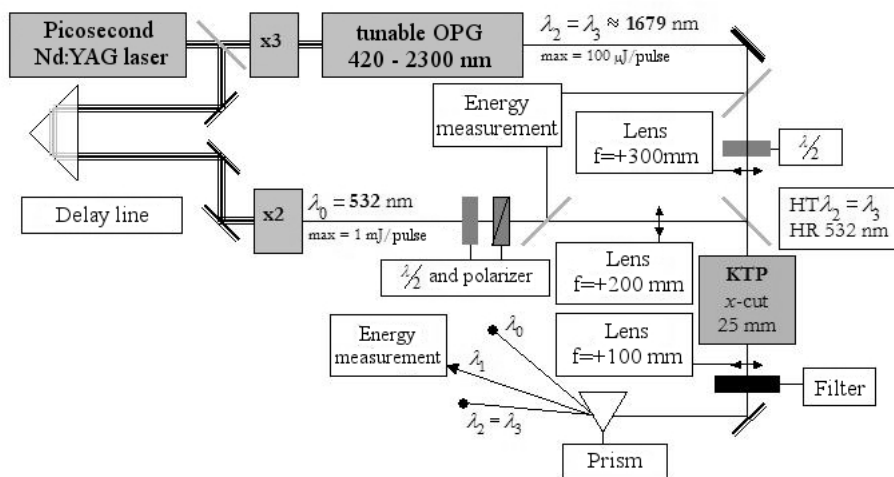


Figure 2.1 – Schematics of the 2004 experiment, adapted from [96].

As cubic nonlinearities are weak, it was necessary to work in the sub-nanosecond regime. A beam at 532nm from a Nd:YAG laser (22ps, 10Hz) frequency-doubled in a KTP crystal, together

with two beams orthogonally polarized at 1665 nm generated by a BBO optical parametric generator (OPG) gave rise to photon triplets at

$$\begin{cases} \lambda_1^c = 1474 \text{ nm} \\ \lambda_2^c = 1665 \text{ nm} \\ \lambda_3^c = 1665 \text{ nm} \end{cases}, \quad (2.6)$$

using a birefringence phase-matched cubic nonlinear interaction in a KTP crystal along the (Ox) axis of the dielectric frame. The corresponding configuration of polarization in terms of $(-)$ and $(+)$ modes was the following:

$$532^{(-)} - 1665^{(+)} - 1665^{(-)} \rightarrow 1474^{(+)}. \quad (2.7)$$

The temporal coincidence of the beams is set with the use of a delay line, composed of a prism. The generated state was obviously a mixture between down-converted triplets and stimulation beams, as shown in Figure 2.2. Still, the detection of photons at λ_1 was a clear piece of evidence of the generation of $\{\lambda_1, \lambda_2, \lambda_3\}$ triplets.

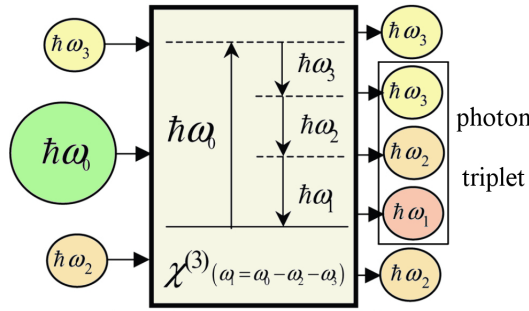


Figure 2.2 – Bi-injected generation of photon triplets.

This set of wavelengths is one of the many that would be generated if the experiment had been performed without stimulation. It is actually impossible to fix the values of three unknown quanta using the two energy and momentum conservation relationships. Fixing only one wavelength of the triplet would have been sufficient to counterbalance the spectral broadening. But a stimulation by two fields was chosen in order to overcome the extreme weakness of the cubic nonlinearity. The spectral set was chosen so that the stimulation fields were degenerated in wavelength, *i.e.* $\lambda_2 = \lambda_3$: consequently, only one stimulation beam and a half-wave plate were actually needed, instead of two physical stimulation beams. The IIa (equivalent here to IIb) phase-matching polarization configuration from Section 1.2.2 was chosen as the one minimizing the $\chi^{(2)}$ cascading schemes, with a rate of 0.5% [97]. It was also a requirement that the spectral components lied in the telecom range, and were compatible with usual detectors.

KTP, a positive biaxial crystal, was chosen for its high optical damage threshold, around 100 GWcm^{-2} [98], its wide transparency range, its well known linear and second-order nonlinear properties, and its rather high third-order electric susceptibility, although not centrosymmetric and consequently enabling quadratic interactions to occur. Along the ($0x$) propagation axis, the effective cubic susceptibility $\chi_{\text{eff}}^{(3)} = \chi_{24}^{(3)} = 1.46 \times 10^{-21} \text{ m}^2 \text{V}^{-2}$ is maximum [99], and the double

refraction angle zero, which allows the spatial overlap between incoming beams to be optimal.

Due to the typical unaccuracy of the Sellmeier equations, it was important to be able to tune the wavelength of the injection beam so that perfect phase-matching could be achieved. For comparison to the experimental wavelengths given in (2.6), the theoretical ones along (Ox) are indeed $\lambda_1^{\text{th}} = 1449.4 \text{ nm}$, $\lambda_2^{\text{th}} = \lambda_3^{\text{th}} = 1681.0 \text{ nm}$. In this experiment, the BBO OPG was tunable in the range $420 - 2300 \text{ nm}$.

From incident intensities $I(\lambda_0, Z = 0) = 350 \text{ GWcm}^{-2}$ and $I(\lambda_2, Z = 0) = I(\lambda_3, Z = 0) = 50 \text{ GWcm}^{-2}$, they were able to generate $I(\lambda_1, Z = 25\text{mm}) = 11 \text{ GWcm}^{-2}$. Afterwards, the group of Grenoble performed a systematic study that validated the theoretical classical model by examining the generated energy as a function of the pump and stimulated energies, as well as the crystal length [100, 101]. A Kerr effect was also identified during the parametric process [102].

2.2.1.3 Alternative nonlinear media for the direct cubic interaction

Other materials have been investigating for photon triplet generation. THG schemes have been considered in order to evaluate their capability regarding the realization of cubic nonlinear interactions. Compared to TPG, THG presents the advantages of bringing about higher conversion efficiencies and requiring only one incident beam, while exhibiting exactly the same phase-matching condition as frequency-degenerated TPG.

Chalcogenides The highest cubic optical nonlinear coefficients can be found in chalcogenide glasses: they are on the order of 10^{-19} to $10^{-18} \text{ m}^2\text{V}^{-2}$, three orders of magnitude higher than that of oxides [103–105]. As glasses, they are isotropic and achieving a birefringent phase-matching is therefore impossible, unless it is induced. GeSe_4 , GeAsSe_3 and AsSe_4 have been considered with applied anisotropic mechanical constraints, inducing a birefringence by elasto-optic effect [96, 97]. Unfortunately, the weak mechanical resistance did not enable to reach sufficient birefringences to perform a phase-matched experiment. The performed THG was thus non-phase-matched so that weak conversion efficiencies were reached.

Periodically poled crystals A shrewd idea to get rid of the quadratic cascades that can pollute the cubic interaction is to use a periodically poled crystal as ppKTP. The alternate orientations of regularly spaced ferroelectric domains can be used such that the second-order processes become inefficient by choosing suitable spacing period [96, 106]. Unfortunately again, the optical damage threshold of the ppKTP crystal, smaller than that of KTP due to inhomogeneities, led in the end to smaller conversion efficiencies.

Rutile TiO_2 Alternative nonlinear media are birefringent centrosymmetric crystals, as they cannot give rise to quadratic interactions due to symmetry considerations. Among them, TiO_2 in its rutile phase is a promising crystal, with a high cubic nonlinearity: $\frac{\chi_{\text{eff}}^{(3)}|_{\text{TiO}_2}}{\chi_{\text{eff}}^{(3)}|_{\text{KTP}}} \simeq 5.3$ for a type II THG at $\lambda_\omega = 613.2 \text{ nm}$ [101, 107, 108]. A part of Chapter 3 will be devoted to the continuation of this study.

Nonlinear confined media Triplets generation through third-order nonlinear conversion in thin optical fibers has also been investigated in a theoretical point of view [12, 109], but never demonstrated experimentally so far. However, as THG is governed by the same phase-matching condition as degenerate TPG, and has advantages over it as already stressed above (higher efficiency, only one physical beam needed), a first experimental step towards triplets was reported by Kamel Bencheikh *et al.* by generating THG in 2012 in [110]. It follows the first experimental observation of THG in fibers made by Gabriagues in 1983 [111], and other demonstrations that came after in strong index difference microstructured fibers [112, 113], or in monomode fibers out of phase matching for instance [114].

Optical fibers indeed present two key advantages for increasing the conversion efficiency compared to bulk crystals: the length of interaction combined with the strong confinement of the electromagnetic field. In the experimental studies mentioned above, the fiber cores are made of silica. As a consequence, although third-order nonlinearities are not so high, the transmission range of such fibers is highly compatible with telecom wavelengths and the optical damage threshold is high. Phase matching can be achieved if different transverse modes are considered for the different interacting waves so that wavelength dispersion can be compensated, exactly as birefringence acts in the case of crystals [113, 115, 116]. Note that it is quite important to use low-order transverse modes so that the overlap between them, therefore the conversion efficiency, can be high [117]. Another solution based on quasi-phase matching in fibers using refractive-index gratings has also been proposed [118].

2.2.1.4 Quantum treatment

The classical model for TPG only holds when injection beams seed the generation, *i.e.* when there are non-zero fields as initial conditions for the resolution of the system of coupled equations (1.52). If it is not the case, as for spontaneous TPG, then a quantum treatment is required. Resolutions using the Fermi golden rule and the formalism introduced in Chapter 1 are presented in this section.

Semi-classical model Before going into a fully quantum approach, an attempt of semi-classical resolution has been done for spontaneous down-conversion in the undepleted pump approximation [119]. In this calculation, each triple photon spectral density is taken to 1 photon per mode, due to vacuum fluctuations. The numerical application leads to a generation of 0.2 photons per second in a 1 m-long silica fiber of core radius $a = 1.85 \mu\text{m}$, and for 1 W of average pump power, *i.e.* a power density of about 10 MWcm^{-2} . Nevertheless, this resolution ought not to be taken too seriously as the set of coupled equations was there taken as decoupled with three invariant fields, which seems to be quite extreme.

Fermi golden rule A calculation based on the Fermi golden rule has been performed in [15] in order to determine the transition rate W from the state $|\vec{0}_1, \vec{0}_2, \vec{0}_3\rangle$ to the continuum of triplet states $|\vec{k}_1, \vec{k}_2, \vec{k}_3\rangle$. It writes as:

$$W = \frac{2\pi}{\hbar} \left| \langle \vec{k}_3, \vec{k}_2, \vec{k}_1 | \hat{\mathcal{H}} | \vec{0}_1, \vec{0}_2, \vec{0}_3 \rangle \right|^2 \rho, \quad (2.8)$$

where ρ is the density of final states, and $\hat{\mathcal{H}}$ the perturbative Hamiltonian describing the third-order nonlinear interaction.

A degenerate phase-matched configuration at $\lambda = \lambda_1 = \lambda_2 = \lambda_3 = 1665$ nm in a 25 mm-long KTP crystal ($\chi^{(3)} = 10^{-21} \text{ m}^2\text{V}^{-2}$) has been considered. A generated power $P \simeq 3 \times 10^{-17}$ W was found when using a pump intensity of 350 GWcm^{-2} at 532 nm (22 ps laser pulses at 10Hz) in a detection spectral and angular bandwidth $d\lambda = 50$ nm and $d\Omega = 10^{-5}$ str respectively: it corresponds to less than 0.01 triplets per day! For comparison, the degenerate quadratic scheme of spontaneous down-conversion at 532 nm would lead to 10^6 twins per day, *i.e.* about 100 twins per second ($\chi^{(2)} = 10^{-12} \text{ mV}^{-1}$).

Quantum resolution Following the continuous variable formalism presented in the first chapter and previously adopted in the case of twin photon generation [60], a complete quantum treatment in the approximation of a weak interaction has been performed in 2012 during the PhD thesis of Audrey Dot in the group of Benoît Boulanger in Grenoble [16, 120]. It describes not only the parametric fluorescence but also seeding schemes with one or two injection beams by resolving the coupled equations, given by (1.132) in the case of indistinguishable photons, and by considering the appropriate incoming state: $|\psi\rangle = |0_1, 0_2, 0_3\rangle, |0_1, \alpha_2, 0_3\rangle, |0_1, 0_2, \alpha_3\rangle$ or $|0_1, \alpha_2, \alpha_3\rangle$. We sum up the main results here. The spectral density n_1 of the mode 1 in the general case where two seeding beams can stimulate the process can be written as:

$$n_1(\omega_1, Z) = T_1 + T_2 + T_3 + T_4, \quad (2.9)$$

with

$$\left\{ \begin{array}{l} T_1 = \left| \int \frac{d\omega_2}{2\pi} \Phi(\omega_0^c, \omega_1, \omega_2, Z) \mathcal{A}_0(\omega_0^c, 0) \sqrt{n_2(\omega_2, 0) n_3(\omega_0^c - \omega_1 - \omega_2, 0)} \right|^2 \\ T_2 = \int \frac{d\omega_2}{2\pi} |\mathcal{A}_0(\omega_0^c, 0) \Phi(\omega_0^c, \omega_1, \omega_2, Z)|^2 n_2(\omega_2, 0) \\ T_3 = \int \frac{d\omega_2}{2\pi} |\mathcal{A}_p(\omega_0^c, 0) \Phi(\omega_0^c, \omega_1, \omega_2, Z)|^2 n_3(\omega_0^c - \omega_1 - \omega_2, 0) \\ T_4 = \int \frac{d\omega_2}{2\pi} |\mathcal{A}_p(\omega_0^c, 0) \Phi(\omega_0^c, \omega_1, \omega_2, Z)|^2 \delta(\omega_1 - \omega_1). \end{array} \right. \quad (2.10)$$

\mathcal{A}_0 is the pump field taken as monochromatic at ω_0^c and defined as $\mathcal{A}_0(\omega_0^c) = \int \frac{d\omega}{2\pi} a_0(\omega)$; n_2 and n_3 are the two spectral densities related to the stimulation modes; the parameter Φ is defined by :

$$\Phi(\omega_0^c, \omega_1, \omega_2, Z) = \Gamma(\omega_0^c, \omega_1, \omega_2, Z) Z \text{sinc}\left(\frac{\Delta k^{(3)}(\omega_0^c, \omega_1, \omega_2) Z}{2}\right) e^{-i \frac{\Delta k^{(3)}(\omega_0^c, \omega_1, \omega_2) Z}{2}}, \quad (2.11)$$

where $\Delta k^{(3)}$ and Γ are given in Equations (1.53) and (1.128) of the first chapter. Note that in the case of one or none seeding beam, this expression still holds and reduces by taking $n_2 = 0$ and/or $n_3 = 0$. We see that the term T_1 of Equation (2.10) holds in a strong bi-stimulated case, while the last term T_4 is predominant in a case where stimulations are very low, or inexistant.

The Dirac function δ is a characteristic time that does not have any spectral restrictive role here [120]. It may seem wise to take it as the characteristic time of the cavity $\tau = \frac{L}{c}$, L being the total length of the cavity. Nevertheless, it had been chosen not to take it into account by comparison of the numerical resolution to both the Fermi golden rule and a different definition of the spectral density for polychromatic fields: $n_i(\omega, Z) = \int \frac{d\bar{\omega}}{2\pi} \langle \psi | \hat{a}_i^\dagger(\omega, Z) \hat{a}_i(\bar{\omega}, Z) | \psi \rangle$ [60].

The numerical applications are performed in the case of a generation occurring in a 1 cm-long KTP crystal, allowing to compare with the experiments done at that time. The pump beam at 532 nm is composed of 4.10^{13} photons per pulse, *i.e.* an energy of 14.6 μ J, with a 15 ps pulse duration and a 10 Hz repetition rate: a number of 0.255 photons per pulse are generated in each of the down-converted fields in the parametric fluorescence regime.

We now turn to the stimulation cases, with stimulation beams centered at $\lambda_{2,3}^c = 1665$ nm and with full width at half maximum of 10 nm. In the case of a mono-stimulation by the mode 3, the terms T_1 and T_2 are zero. The terms T_3 and T_4 equal each other when $n_3(\lambda_3^c) = 1$, at the center of the injection spectrum. This corresponds to 7.3×10^{12} photons per pulse. In that case, 0.0011 photons in the mode 1 per pulse are generated through T_2 , in addition to the spontaneous emission contribution of 0.255 photons per pulse. When a stimulation by mode 2 is considered, and for $n_2(\lambda_2^c) = 1$, then 0.0453 photons per pulse are generated through amplification by the stimulation. The phase-matching conditions are responsible for the asymmetric situation between the two mono-injected results. Note that the previous numbers do not correspond to an equal number of mode 1 photons generated through parametric fluorescence or amplification, as their spectral range are very different, wider in the first case. However, they do for a seeding of 4.1×10^{13} and 1.7×10^{15} photons per pulse, for a mono-stimulation by the beams 2 and 3 respectively. These numbers can be regarded as the lower limit of an efficient mono-stimulated regime. Although they are not presented here, calculations of spectral densities had also been done for fields 2 and 3 [16, 120]. When the process is seeded with high enough intensities, the number of triple photons in each field is not the same whether the photons belong to the stimulation beam or not. This indicates that a too strong level of seeding photons may mask the correlation between triplets.

Lastly, in the bi-stimulated case, the terms T_1 and T_4 are always predominant, respectively when strong and weak seedings are considered. They equal each other at the central injection frequency, *i.e.* for $n_2(\lambda_2^c) = n_3(\lambda_3^c) = 1$, when 9.7×10^6 photons per pulse seed the process on each of the injection fields. The number of photons in field 1 generated through spontaneous down-conversion and amplification are equal for 1.3×10^8 seeding photons per pulse on each field.

The signature of the correlations between the photons of a triplet will be discussed in Section 2.3 in the light of all these numbers of generated photons.

2.2.2 Alternatives to the direct generation of triplets

The direct third-order optical nonlinear scheme is not the only way to generate triplets. In the following, we chronologically outline other approaches reported in the literature.

High energy electron-positron collisions The first proposal takes place in the framework of quantum electrodynamics. It has been reported that annihilations between electrons and positrons produce multi-photon states at very high energies. This non-optical scheme has been summarized by Suraj Gupta in [121] in 1954.

“Quantum eraser” In 1997, Anton Zeilinger and coworkers proposed a three-particle GHZ entanglement scheme based on two entangled pairs from independent emitters [122]. In this proposal, depicted in Figure 2.3a, each detection of one of the four generated photons is made so that it is not possible to know from which source this photon came from, entangling the three other photons, *i.e.* coherently superposing them. No possibility to identify the incoming twins should remain: polarization, energy and time correlations are unexploited for indistinguishable polarizations and energies, and simultaneous production and detection. Narrow bandwidth filters are used so that the coherence time of the photons is much larger than that of the pump laser. The three-particle interferometer shown in Figure 2.3b can give an estimation of the “erasure” of the source information.

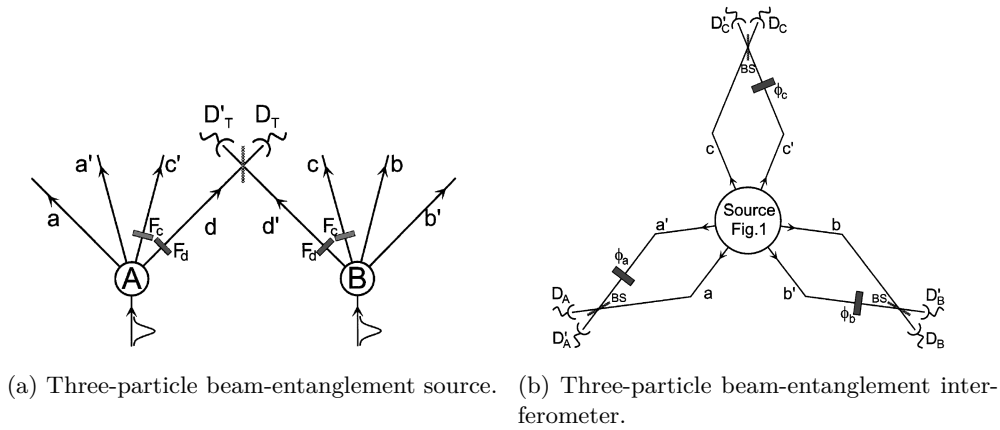


Figure 2.3 – Triplet generation based on the concept of quantum erasure. Illustrations from [122].

Finally, [122] also proposes a three-particle polarization-entanglement source reproduced in Figure 2.4. Its experimental demonstration was reported two years later in [6], and an experimental test of nonlocality can be found in [7]. Note that the major drawback of this proposal is that the creation of the GHZ three-particle entanglement rests upon a destructive measurement.

In a similar spirit, Eibl and coworkers experimentally realized a polarization three-photon W entanglement [123].

Photon pair and weak coherent state Another approach to generate photon triplets is to create an approximate product state of an entangled pair of photons and a coherent state [124]. This coherent state has to be weak enough to fulfill the approximation. In this paper, two proposals are made for polarization or momentum entanglement; and in this case too, it is a postselection protocole.

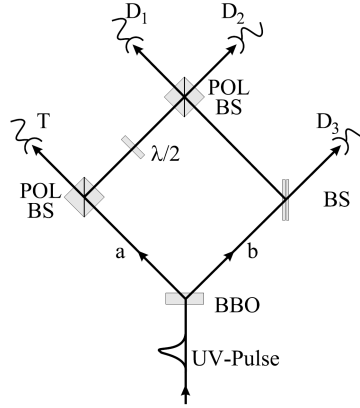


Figure 2.4 – Three-particle polarization-entanglement source, from [6].

Triexcitonic decay in quantum dots Emission of triple photons from the decay cascade of a tri-exciton through an exciton and a bi-exciton recombination in a InP quantum dot has been demonstrated in 2004 by Persson and coworkers [125]. Time-correlation measurements have been performed using a Hanbury-Brown and Twiss interferometer.

Entanglement by amplification in a cavity In 2005, Mikami *et al.* realized a three-photon polarization-entangled W state by using the process of second-order optical parametric amplification (OPA) in a BBO nonlinear crystal [126]: two degenerate beams are generated through quadratic down-conversion, the process being seeded by another beam at the same frequency. The output polarization state becomes a tripartite W state.

Combination or cascades of quadratic interactions Indirect TPG using cascaded photon pair sources has been performed in the team of Thomas Jennewein in 2010 [14]. In this experiment, a first pair is generated through second-order parametric fluorescence in a first crystal, then follows a second pair in a second crystal from the down-conversion of one of the two photons of the first pair, as depicted in Figure 2.5a. The three outgoing photons form a photon triplet state, as long as the temporal coherence is preserved. This group also demonstrated energy-time entanglement of their generated triplets [127].

Antonosyan *et al.* proposed in 2011 a cascaded configuration involving periodically poled crystals in free space as well as in an OPO cavity for the production of GHZ entangled states in polarization [129]. They also investigated the correlations properties of the down-converted states. Their work is based on previous cascaded quadratic OPO proposals [130, 131] and experimental realization [132]. Other experiments through quadratic parametric processes in cascade have also been performed in an aperiodically poled crystal [133].

In the same spirit, Keller and coworkers proposed in 1998 a theoretical proposal for triplet generation through the combination of three simultaneous quadratic interactions: two down-conversions and an up-conversion between two of the four down-generated photons [128], as represented in Figure 2.5b. On the basis of this experiment, Wen *et al.* theoretically investigated the transverse correlations of the outgoing triple photon state [134]. For other theoretical proposals of interlinked quadratic interactions, see also [135, 136].

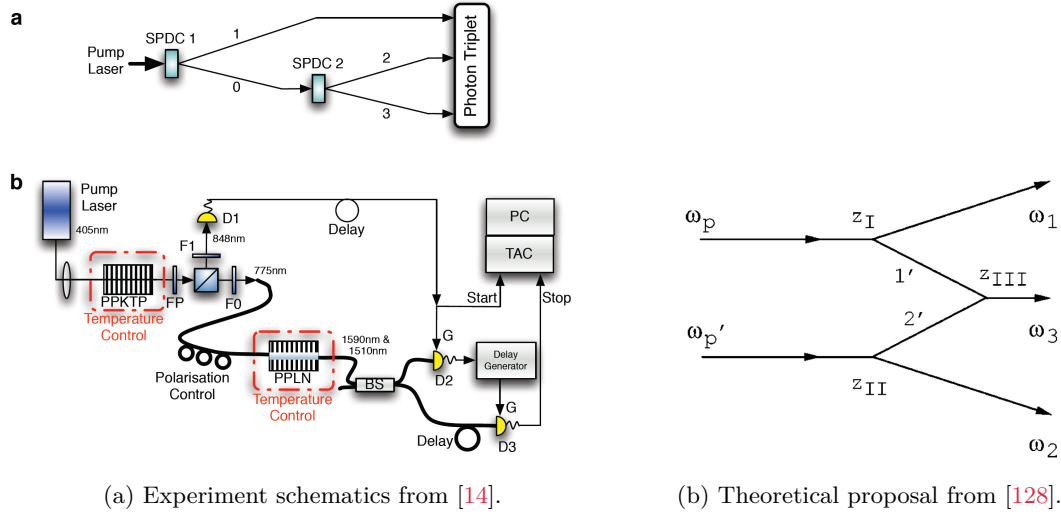


Figure 2.5 – Triplet photon generation from second-order interactions in cascade.

Triplets generation through four-wave mixing in a cold atomic medium In 2010, Wen and coworkers proposed an experiment based on two four-wave mixing processes, *i.e.* a third-order interaction of scheme B as explained in Chapter 1, in a cold atomic medium in order to generate triplet W states [137]. The experiment is depicted in Figure 2.6. Using its notations, it can be summarized with the energy relationships: $\omega_p + \omega_{c1} \rightarrow \omega_{s1} + \omega_{as1}$ and $\omega_{s1} + \omega_{c2} \rightarrow \omega_{s2} + \omega_{as2}$, the triplet state being the couple $\{\omega_{as1}, \omega_{s1}, \omega_{as2}\}$. The specificity of such a protocol is that it enables the generation of spectrally narrowband triplets since real phononic energy levels are involved in the processes.

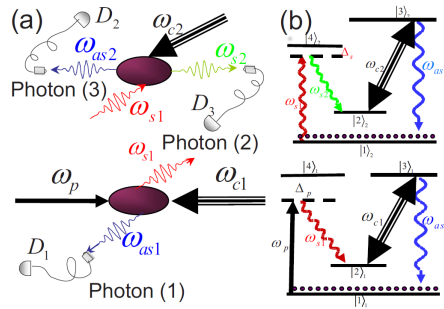


Figure 2.6 – Generation of triple photons by two four-wave mixing processes, from [137].

Atomic and photonic entanglement in cavity quantum electrodynamics We finish this section by noting a theoretical proposition dating from 1993 from Wódkiewicz and coworkers for three-particles entanglement between atomic states and photon states in a cavity [138]. Two photons are trapped into a cavity through a two-photon cascade spontaneous emission, with non-degenerate frequencies corresponding to the longitudinal modes of the cavity. By interacting with an atom in the cavity, they can induce transitions between two degenerate sublevels of the ground state of this atom. The desired GHZ state arises from the knowledge of the dynamical evolution in the cavity. For other experiments of atoms and photons entanglement in a cavity, see for example [139]. This is a mere remark here as the output state is not purely photonic as sought.

2.3 Correlation studies

As triple photons might be used in the future for quantum information, we have to care very much about quantum correlations among these states. This part concentrates on different strategies, theoretical proposals or experimental demonstrations, for this purpose.

2.3.1 Photon recombination

As already emphasized in Section 1.4.5, the quantum coherence can be measured by accessing the correlations between the quantum fluctuations of the fields associated with the photons. Such measurements are not possible with the experiments performed in our group up to now as not compatible with the sensitivity of our current detectors. The optical fluxes involved to efficiently generate detectable triplets are indeed too strong.

Therefore, inspired by the pioneering work of Izo Abram *et al.* on the analysis of the twin photons coherence through second-order sum frequency generation [70], we developed a similar study on photon triplets [16, 120]. This recombination protocol has already been discussed in Section 1.4.5 and depicted in Figure 1.14. In the twin photons case, it has been showed that a clear signature of the non-classical behaviour of the correlations arises from the spectrum of the recombination in a second crystal under phase-matching conditions. The down-converted twin photons, whose spectra are very broad when generated from parametric fluorescence, recombine together to give a summed field identical to the incoming pump beam exhibiting a narrow spectrum [140–142]. Note that the recombined spectrum through classical optics would be the convolution of the two twin photons spectra. The up-converted sum field is also characterized by a high temporal resolution as the twins recombine together within their coherence time [141, 143]. Spectral as well as temporal coherence are therefore highlighted in such an experiment. An exhaustive theoretical study of down-conversion and then up-conversion has been performed by Barak Dayan in 2007 [60].

As far as we are concerned with triple photons, two choices arise for the recombination: the three generated photons can either merge all together in a third-order sum frequency generation (TOSFG) scheme, or by combination of two in a second-order sum frequency generation (SOSFG) scheme.

TOSFG For the case of TOSFG, following the energy conservation $\omega_1 + \omega_2 + \omega_3 \rightarrow \Omega$, the calculation has been done in the general case, whether the generation is done with or without stimulation beam(s). The photon density of the recombined field is composed of many terms. Two of them remain predominant in the cases of bi-stimulation (T'_1) or parametric fluorescence (T'_2) [16]:

$$n_\Omega(\Omega, Z) \simeq T'_1 + T'_2, \quad (2.12)$$

with

$$\left\{ \begin{array}{l} T'_1 = \left| \iiint \frac{d\omega d\tilde{\omega} d\hat{\omega}}{2\pi 2\pi 2\pi} \mathcal{A}_0(\omega_0^c, 0) \Phi(\omega_0^c, \omega, \hat{\omega}, L) \Psi(\Omega, \omega, \tilde{\omega}, Z) \right. \\ \quad \times \left. \sqrt{n_2(\hat{\omega}, 0) n_3(\omega_0^c - \omega - \hat{\omega}, 0) n_2(\tilde{\omega}, 0) n_3(\omega_0^c - \omega - \tilde{\omega}, 0)} \right|^2 \\ T'_2 = \iint \frac{d\omega d\tilde{\omega}}{2\pi 2\pi} \left| \mathcal{A}_0(\omega_0^c, 0) \Phi(\omega_0^c, \omega, \tilde{\omega}, L) \Psi(\Omega, \omega, \tilde{\omega}, Z) \delta(\omega_0^c - \Omega) \right|^2. \end{array} \right. \quad (2.13)$$

Φ is given by Equation (2.11), and

$$\Psi(\Omega, \omega, \tilde{\omega}, Z) = \Phi^*(\Omega, \omega, \tilde{\omega}, Z) = \Gamma(\Omega, \omega, \tilde{\omega}, Z) Z \text{sinc} \left(\frac{\Delta k^{(3)}(\Omega, \omega, \tilde{\omega}) Z}{2} \right) e^{+i \frac{\Delta k^{(3)}(\Omega, \omega, \tilde{\omega}) Z}{2}}, \quad (2.14)$$

where $\Delta k^{(3)}$ and Γ are given by Equations (1.54) and (1.128) respectively.

From this, it was shown that the quantum coherence between three photons from a triplet always exists: when they recombine, they form the exact spectrum of the pump, *i.e.* a Dirac peak in the monochromatic case that had been considered, no matter the spectral extension of the photons generated from the TPG. This is the sense of the term T'_2 . It signs a preferential recombination of the photons arising from a same triplet together. However, the stronger the injection level, the more this quantum coherence is hidden as another term (T'_1) gets stronger. T'_1 is equivalent to its classical counterpart: a Gaussian function corresponding to the convolution of the incoming fields, that reflects random sum frequency between unrelated triplets or seeding photons and that only leaves classical coherence. Figure 2.7 shows recombination spectra for different bi-injection levels. In the experiments that had been carried out in Grenoble so far, the seeding levels did not allow to probe any quantum signature.

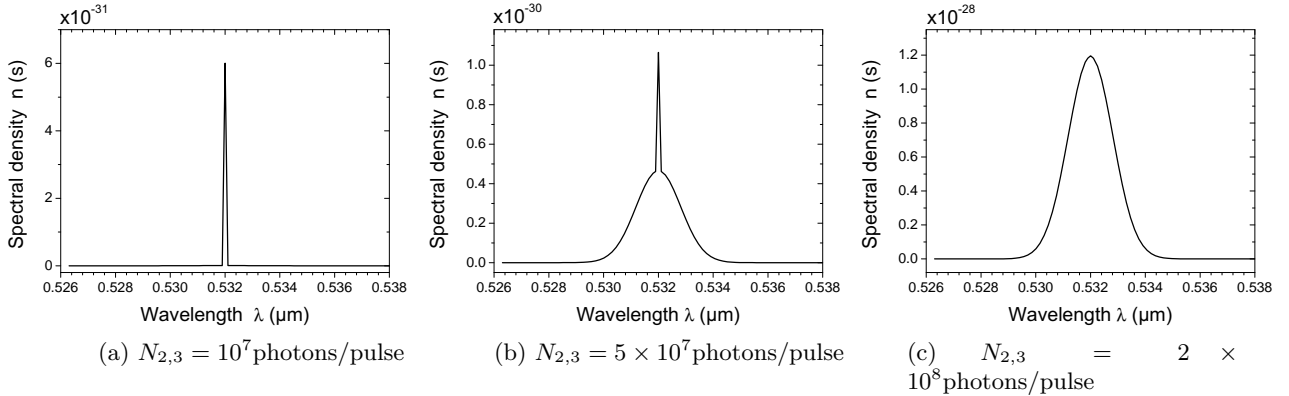


Figure 2.7 – Recombination spectra for different seeding levels, in a bi-stimulation regime for TPG. Two KTP crystals cut along the x -axis are used for generation as well as the recombination, with lengths equal to 10 and 0.1 mm respectively. The monochromatic pump power density is 25 GWcm^{-2} (4×10^{13} photon/pulse) at 532 nm. Adapted from [120].

In the case of an efficient mono-stimulation regime, *i.e.* $N_2 \geq 4.1 \times 10^{13}$ or $N_3 \geq 1.7 \times 10^{15}$ photons per pulse for $N_0 = 4 \times 10^{13}$ photon/pulse as said in Section 2.2.1.4, the peak, signature of quantum coherence, can still be visible. It disappears around $N_2 \simeq 6 \times 10^{15}$ or $N_3 \simeq 7 \times 10^{16}$ photons per pulse. Moreover, in any injection regime, the recombination spectrum and its classical counterpart have different amplitudes and extensions. For these reasons, recombination

after a mono-injected generation may be interesting to reveal non-classical correlations.

SOSFG The two-photon recombination of fields 1 and 3 in a bi-stimulation regime has also been considered. The spectral density of the summed field can be approximated as:

$$n_{\Omega}(\Omega, Z) \simeq T_1'' + T_2'', \quad (2.15)$$

with

$$\begin{cases} T_1'' &= \left| \iint d\omega d\tilde{\omega} \mathcal{A}_0(\omega_0^c, 0) \Phi(\omega_0^c, \omega, \omega_0^c - \omega - \tilde{\omega}, L) \xi(\Omega, \omega, Z) \right. \\ &\quad \left. \times \sqrt{n_3(\Omega - \tilde{\omega}, 0) n_2(\omega_0^c - \omega - \tilde{\omega}, 0) n_3(\omega, 0)} \right|^2 \\ T_2'' &= \left| \int d\omega \mathcal{A}(\omega_0^c, 0) \Phi(\omega_0^c, \omega, \Omega - \omega, L) \xi(\Omega, \omega, Z) \right|^2 \delta(\omega - \omega). \end{cases} \quad (2.16)$$

The function Φ is given by Equation (2.11) and ξ by:

$$\xi(\Omega, \omega, Z) = \beta(\Omega, \omega, Z) Z \text{sinc} \left(\frac{\Delta k^{(2)}(\Omega, \omega) Z}{2} \right) e^{+i \frac{\Delta k^{(2)}(\Omega, \omega) Z}{2}}, \quad (2.17)$$

with $\Delta k^{(2)}$ and β from Equations (1.51) and (1.127).

The same kind of comments as previously can be made here: the term T_2'' exists alone for spontaneous down-conversion and stays predominant in the low injection regime, whereas T_1'' is the strongest in the case of a strong bi-injection. The non-classical behaviour of the tri-photons is revealed as long as T_1'' dominates, since it differs from T_2'' which is actually the classical contribution. This is true for $N_2 = N_3 \leq 10^5$ photons per pulse, still for a pump power of $N_0 = 4 \times 10^{13}$ photon/pulse in a KTP crystal. This number is actually below the effective injection regime, that starts from 10^7 photons per pulse as already mentioned in Subsection 2.2.1.4.

In addition, in the case where T_1'' stays stronger, the photon-sum spectrum has the same spectral extension than the spectrum of the photons that has not been recombined. This can be easily understood when looking at the energy conservations $\omega_1 + \omega_2 + \omega_3 = \omega_p$ on one hand, and $\omega_1 + \omega_3 = \Omega$ on the other hand. Therefore in the case of a monochromatic pump, one has $\delta\omega_2 = -\delta\Omega$, in terms of the spectral distance from the central frequencies. Again, this feature highlights the preferential recombination of photons belonging to the same triplet. Figure 2.8 illustrates this property: the recombination spectrum of fields 1 and 3 is shown together with its classical counterpart, and the generated spectrum of the non-recombined field, *i.e.* field 2. The generation in the first crystal has been carried out from spontaneous down-conversion.

Everything that has been said on the recombination of the modes 1 and 3 stays true for the combinations of modes 1 and 2 (also recombination of one injected mode and one non-injected mode), as well as 2 and 3 (recombination of the two injected modes).

The same kind of conclusions arises for the SOSFG than for TOSFG, from a mono-injection scheme: although the photons do not exhibit the same kind of correlations as in the case of parametric fluorescence, the summed field is expressed differently than its classical equivalent with incoherent fields, which signs quantum coherence.

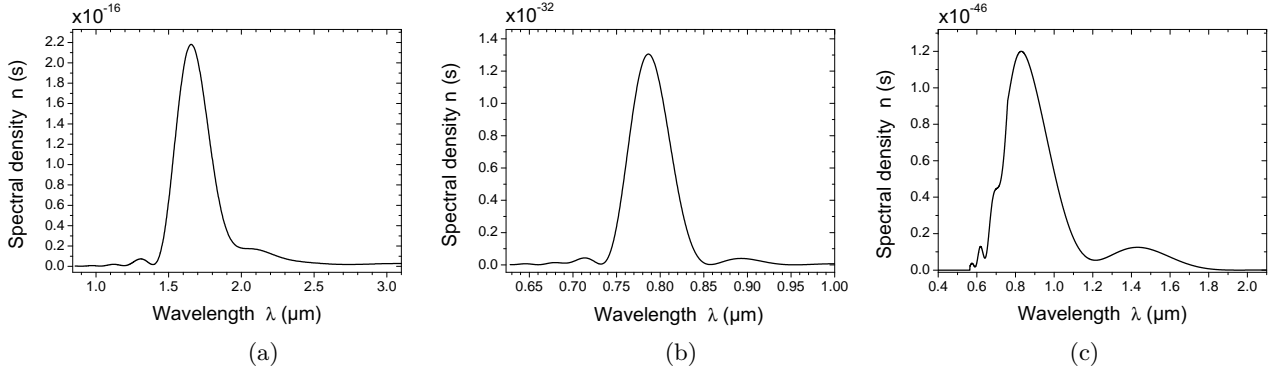


Figure 2.8 – Comparison between the spectrum of the field 2 generated from spontaneous down-conversion (a), the SOSFG recombination spectrum of fields 1 and 3 also generated from spontaneous down-conversion (b), and its classical equivalent (c). Generation and recombination crystals are 0.1 mm-long KTP crystals cut along the x -axis for the generation, and in the direction ($\theta = 34^\circ, \varphi = 30^\circ$) for the recombination. The interaction lengths have been taken very small in order to avoid any spectral limitation due to the spectral acceptance. Adapted from [120].

2.3.2 Theoretical quantum tomography

Wigner function reconstruction Quantum coherence can also be probed through quantum tomography and reconstruction of the Wigner function presented in Section 1.4.5. The Wigner function for a triplet state degenerated in pulsation and polarization has been computed and reported by Konrad Banaszek *et al.* in the case of spontaneous down-conversion [3] (see Figure 2.9), as well as by Timo Felbinger *et al.* in a doubly resonant OPO [4]. In the phase space, it has the shape of a star with three branches. It exhibits an interference pattern that takes negative values and therefore signs the non-classicality of the state, even in the case of generation in an optical cavity. This non-classicality is stronger than in the case of twins where the Wigner function, although squeezed, stays positive [144]. Wigner functions for cascading generation schemes have also been computed and give the same kind of behaviour [129, 145].

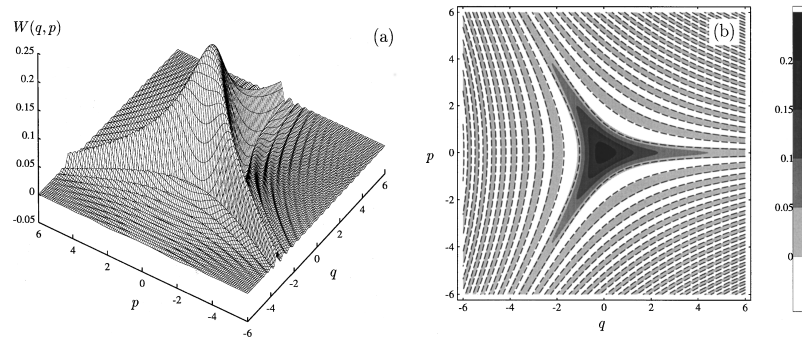


Figure 2.9 – Wigner distribution of a triplet state degenerated in frequency and polarization. (a) is a three-dimensional representation in the electric field quadratures space while (b) is a top view. From [3].

Calculations corresponding to the experiment of double stimulation presented in Section 2.2.1.2 has also been done in by Kamel Bencheikh *et al.* [15]. As triple photons are distinguishable

in wavelength and polarization (ordinary / extraordinary), the authors gave an estimation of the quantum correlations of the ordinary and extraordinary modes through joint probability distributions. Their cross-shaped behaviour shown in Figure 2.10 reveals quantum correlations between these modes, even more clearly that the conversion efficiency is high.

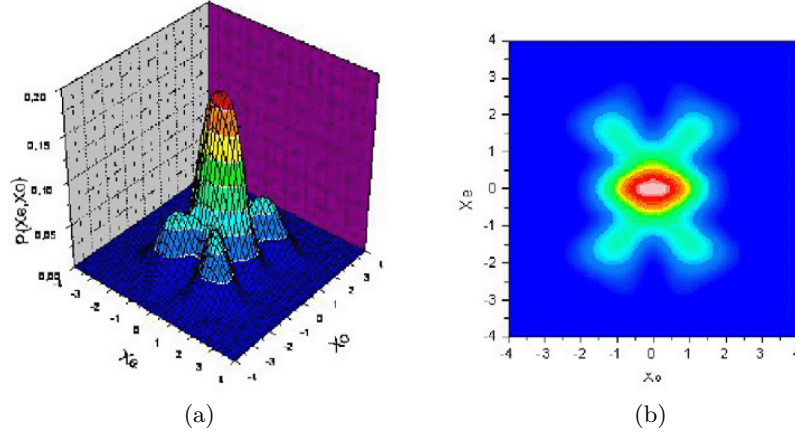


Figure 2.10 – Joint probability distributions of the ordinary and extraordinary triple photons. Three-dimensional and top views in (a) and (b) respectively. From [15].

Density matrix reconstruction Quantum state tomography has been performed in the group of Anton Zeilinger via density matrix reconstruction of the triple state generated in the framework of their experiments presented in Section 2.2.2 [5]. They showed clear polarization GHZ entanglement of their state. Density matrix reconstruction has also been used to check W entanglement in other teams [126]. Note that the density matrix or the Wigner function give the same information as they are Wigner transformed from each other.

2.3.3 Coincidence measurements

Coincidence measurements stand finally for a natural way to probe triple photon entanglement in low fluxes experiments. In the Zeilinger experiment previously discussed, GHZ entanglement in polarization was also shown with a fourfold coincidence experimental setup [6, 7]. Similar experiments measuring threefold coincidences have been carried out in the team of Harald Weinfurter with the aim to show three-photon polarization W entanglement [10, 123].

In the group of Thomas Jennewein, temporal correlations of the triplet state have been demonstrated experimentally through triple coincidence measurements with their experiment based on cascaded photon pairs exposed in Section 2.2.2 [14]. In [127], they demonstrated energy-time entanglement of their triplet state by violating uncertainty inequalities.

To finish this part on correlations of tri-photon states, note that Coelho *et al.* demonstrated in 2009 tripartite entanglement for pump, signal and idler photons at different wavelengths by performing a quadratic down-conversion in an OPO [146].

2.4 Conclusion and experimental strategies

We have seen in this chapter that the generation of triple photons is an actual challenge of nonlinear optics that is motivated by the exploration of quantum optics, and the potential new possibilities and insights for quantum information. Such a photonic state is highly correlated, and can belong to the GHZ or the W entanglement class. Its coherence properties therefore differ from those of twin photons. Its non-classicality has been investigated theoretically and/or experimentally through coincidence measurements, nonlinear photon recombination or quantum tomography. In particular, its Wigner function exhibits an interference pattern and negativities.

Different experimental demonstrations or theoretical proposals have been reported as for the generation of these triplet states. The most direct method, *i.e.* a cubic nonlinear interaction of type A, has been achieved experimentally in Grenoble with fields seeding the process so as to increase the conversion efficiency. However, this stimulation hid the correlations as their level was too high. Indirect TPGs have also been performed: cascades of quadratic nonlinear interactions in Waterloo and coherent superposition of two entangled pairs in Vienna for instance. We have also seen that various materials (oxides, chalcogenides) in a bulk or fiber geometry can be of prime interest if phase matching can be achieved.

This thesis follows the work previously done in Grenoble and therefore concentrates on the direct generation of triplet states. It is important to lower as much as possible the seeding beams as they can mask correlations. For that purpose, two experimental strategies are adopted, and described in Chapters 3 and 4.

The first one focuses on the generation in bulk crystals, more specifically KTP and rutile TiO_2 . Here, injection beams are still needed to achieve detectable triplet signals. For TiO_2 , a characterization of the phase-matching properties is done by the way of THG experiments. The study of crystals is indeed interesting for our purpose of achieving TPG with lower seeding levels because these materials can be used in a cavity (an optical parametric oscillator) so as to artificially increase the interaction length.

The second strategy concentrates on generation of triplets in $\text{GeO}_2 : \text{SiO}_2$ and chalcogenides optical fibers. Optical fibers indeed enable a strong confinement of the electromagnetic field over long interaction lengths. Moreover, because of their centrosymmetry, no quadratic process can pollute the TPG. As for bulk crystals, silica fibers are characterized through THG experiments that will enable to perform TPG through parametric fluorescence, *i.e.* without stimulation. Chalcogenide fibers are investigated from the theoretical side, by looking at the phase-matching properties. These materials are of particular interest for their giant nonlinearities.

Third-harmonic generation and triple photon generation in bulk crystals: KTP and rutile TiO₂

“Cette rampe a été supprimée depuis, pour la symétrie ; les chevaux crèvent
la soif, mais l’oeil est flatté.”

– Victor Hugo, *Les misérables*

Contents

3.1 Bi-injected TPG in KTP	66
3.1.1 Description of the experiment	66
3.1.2 Spectral properties	68
3.1.3 Energetic properties, Kerr effect	70
3.1.4 Conclusion	75
3.2 Towards TPG in rutile TiO₂	76
3.2.1 TiO ₂ characterization through a THG experiment in a cylindrical geometry	76
3.2.2 TPG in rutile TiO ₂	87
3.2.3 Conclusion	93
3.3 Prospective for resonant TPG from a synchronously pumped third- order optical parametric oscillator	94
3.3.1 Synchronously pumped OPO	94
3.3.2 TPG configurations in OPO	95
3.3.3 Conclusion	105

This chapter is devoted to TPG in bulk crystals. A first part goes into the study of bi-injected TPG in KTP. In a second part, another oxide, TiO₂ in its rutile phase, is considered as the nonlinear medium. Finally, the last section gives a theoretical investigation on TPG in a

cavity, *i.e.* a third-order optical parametric oscillator, so as to artificially increase the length of the interacting medium.

3.1 Bi-injected TPG in KTP

In this section, we show TPG in a KTP crystal in a bi-stimulated regime. The idea of the experiment follows previous works performed in the group as described in Section 2.2.1.2. We study here the spectral and energetic properties of the generated fields and model the Kerr effect that comes to attenuate the TPG efficiency.

3.1.1 Description of the experiment

A doubly stimulated TPG is performed along the x -axis of a 13 mm-long bulk KTP crystal in order to achieve type IIa = IIb phase-matching at the calculated wavelengths: $\lambda_0^{\text{th}} = 532 \text{ nm}$ for the pump, $\lambda_{2,3}^{\text{th}} = 1681.0 \text{ nm}$ with orthogonal polarizations for the stimulation fields, and $\lambda_1^{\text{th}} = \left[\frac{1}{\lambda_0^{\text{th}}} - \frac{2}{\lambda_{2,3}^{\text{th}}} \right]^{-1} = 1449.4 \text{ nm}$ for the generated field. We emphasized again that the stimulated splitting of the pump photon leads to a generated optical state that contains a mixture of triple photons and stimulation photons. Thus, each photon detected at λ_1 reveals the generation of a single triplet since it is not present at the entrance of the nonlinear crystal. As the spectral components of the beams are taken into account, these theoretical phase-matching wavelengths are the central wavelengths of polychromatic fields labeled as 0, 1, 2, 3 thereafter.

The experimental setup is depicted in Figure 3.1. The pump beam 0 is generated through second-harmonic generation in a 1.6 mm-long KTP crystal ($\chi^{(2)}$) along the direction ($\theta = 90^\circ$, $\varphi = 23^\circ$) pumped by a 10 Hz Leopard Continuum Nd:YAG laser with a full width at half maximum (FWHM) pulse duration $\tau = 15 \text{ ps}$. Its polarization is taken collinear with the y -axis of the KTP crystal ($\chi^{(3)}$). Two spherical lenses L_0 and L'_0 of focal length $f_0 = f'_0 = 150 \text{ mm}$ are put on either side of the crystal so as to optimize the SHG conversion efficiency while keeping the collimation of the beam inside the crystal.

The stimulation beam 2 = 3 is emitted by a Topas Light Conversion parametric generator that is tunable to achieve a perfect phase-matching. A half-wave plate is used for orienting the polarization of the stimulation beam at 45° of the y -axis and z -axis of the KTP crystal ($\chi^{(3)}$) according to the chosen phase-matching condition.

In order to increase the spatial overlap between the pump and stimulation beams, it was necessary to enlarged the size of the latter by a factor three with the use of a magnifying telescope made of two spherical lenses L_i and L'_i of focal lengths $f_i = 250 \text{ mm}$ and $f'_i = 75 \text{ mm}$ respectively.

The pump and stimulation beams are spatially overlapped at the recombination plate M_2 , a dichroic mirror, and temporally overlapped thanks to a delay line made of a prism P and a translation stage T on the pump beam path. This last point is indeed critical as the 15 ps pulses have to match within their 4.5 mm spatial extension for a propagation in the air. The energies of the pump and injection beams are adjusted continuously thanks to half-wave plates ($\lambda/2$) associated with Glan-Taylor prisms (GTP).

These two beams are focused in the KTP crystal with an uncoated spherical lens L_{foc} of focal length $f_{\text{foc}} = 750 \text{ mm}$. Their waist radii at $1/e^2$ have been measured with a Spiricon silicon-based camera and are equal to $W_0 = 50 \pm 6 \mu\text{m}$ and $W_{2,3} = 90 \pm 11 \mu\text{m}$ for the pump and stimulation beams respectively. In the case of infrared wavelengths, the beams are still visible using a CCD camera thanks to the phenomenon of two-photon absorption. The corresponding Rayleigh length defined in Equation (1.35) is about 27 mm from either side of the waist position inside the crystal for the two incident beams, which ensures a quasi parallel beam geometry over the full length of KTP. In order to focalize the two incident beams in the same plane even though they have different wavelengths, an adjustment has to be done on the relative position of the lenses forming the telescope placed on the path of the stimulation beam. The crystal is put on translation and rotation stages to adjust its position and orientation thanks to autocollimation.

A lens with a focal length of 100 mm is placed behind the crystal in order to collect the emergent beams. The generated beam 1 is polarized along the z -axis according to the phase-matching type. It can be separated from the other beams thanks to several proper filters (F). The powers of the different beams are measured using DET110 Si or DET 410 InGaAs Thorlabs photodiodes, calibrated with an Ophir PE10 power meter. The spectra are measured using a Chromex 250 SM monochromator.

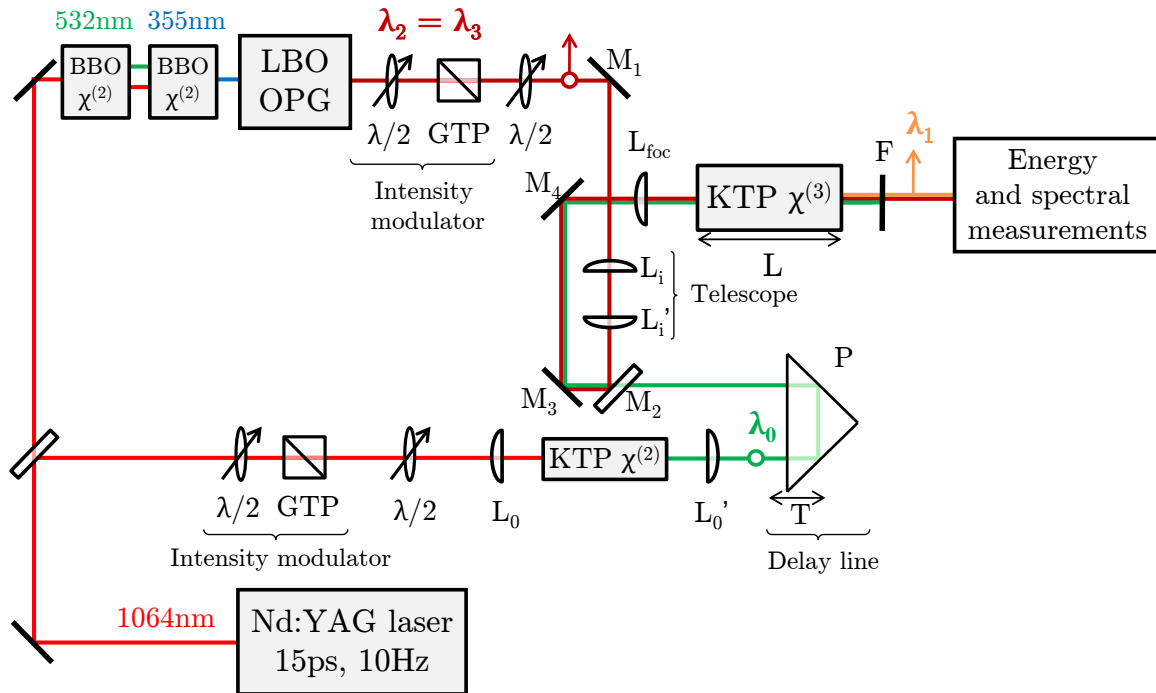


Figure 3.1 – Experimental setup of the bi-injected TPG in KTP. GTP stands for Glan-Taylor prism, $\lambda/2$ for half-wave plate. M are mirrors, L lenses, T a translation stage, P a prism and F filters.

3.1.2 Spectral properties

3.1.2.1 Experimental data

The spectra of the incident pump and stimulation beams can be considered as Gaussian with a FWHM $\Delta\lambda_0 = 0.5$ nm and $\Delta\lambda_{2,3} = 3.4$ nm respectively, as shown in Figure 3.2. The black dots are experimental data and the blue curves are the related Gaussian fits. The central wavelengths slightly differ from the calculated phase-matching wavelengths: $\lambda_0^c = 532$ nm, $\lambda_{2,3}^c = 1662$ nm and $\lambda_1^c = 1478$ nm. This stresses the fact that it is particularly important to employ a tunable source.

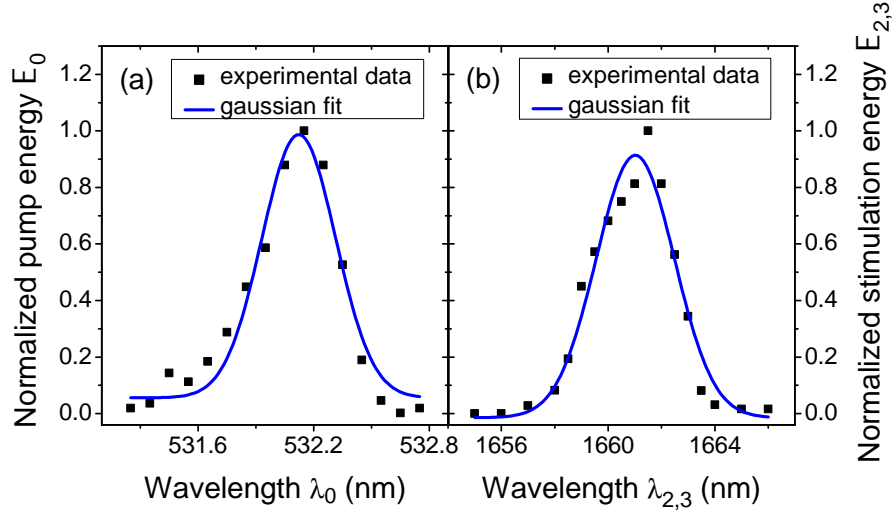


Figure 3.2 – (a) Normalized spectra of the pump beam (field 0) and (b) stimulation beams (fields 2 and 3) used for the TPG experiment.

The normalized experimental data obtained for the generated field 1 is represented by the squares in Figure 3.3. The measured spectral width is 4.7 nm at half maximum. The calculation performed using the model previously developed (*cf.* Equation 2.9) under the monochromatic pump approximation leads to a significantly smaller value of the width of 2.8 nm, as indicated by the red dashed curve.

The Sellmeier equations used for principal indices of KTP are:

$$n_i(\lambda) = \sqrt{A_i + \frac{B_i}{\lambda^2 - C_i} - D_i\lambda^2}, \quad (3.1)$$

with λ expressed in micrometers, $i \in \{x, y, z\}$ and the coefficients given in Table 3.1 [147].

i	A_i	B_i	C_i	D_i
x	3.0065	0.03901	0.04251	0.01327
y	3.0333	0.04159	0.04547	0.01408
z	3.3134	0.05694	0.05658	0.01682

Table 3.1 – Sellmeier coefficients of KTP.

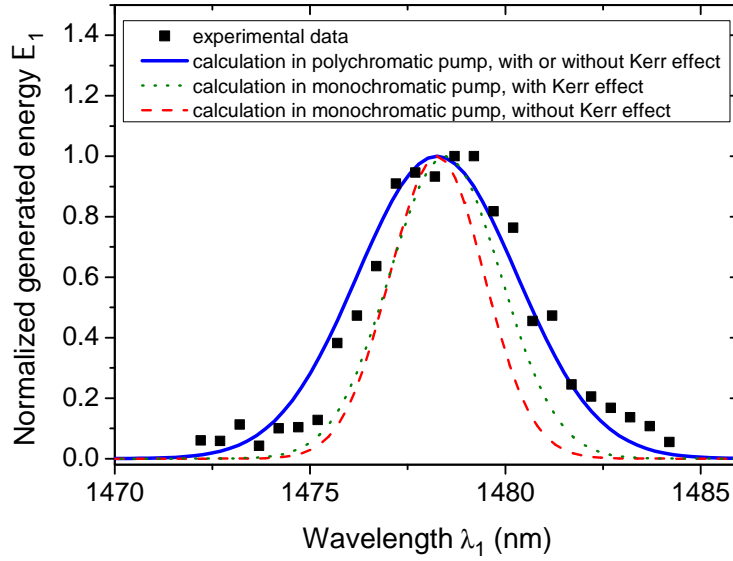


Figure 3.3 – Spectrum of the generated beam (field 1) by a bi-stimulated TPG in a KTP crystal. The incident pump energy is $\mathcal{E}_0 = 52 \mu\text{J}$ and the incident total stimulation energy is $\mathcal{E}_2 + \mathcal{E}_3 = 60 \mu\text{J}$.

3.1.2.2 Classical theory

We refined this model by taking into account the spectral linewidth of all incident beams, considered as classical. For a propagation along the x -axis, the coupled field Equations (1.132) then become:

$$\begin{cases} \frac{\partial \underline{A}_0(\omega_0, x)}{\partial x} = \frac{\partial \underline{A}_2(\omega_2, x)}{\partial x} = \frac{\partial \underline{A}_3(\omega_3, x)}{\partial x} = 0 \\ \frac{\partial \underline{A}_1(\omega_1, x)}{\partial x} = i \iint_{\mathbb{R}^{2+}} \frac{d\omega_0}{2\pi} \frac{d\omega_2}{2\pi} \Gamma(\omega_0, \omega_1, \omega_2) \\ \quad \times \underline{A}_0(\omega_0, x) \underline{A}_2^*(\omega_2, x) \underline{A}_3^*(\omega_0 - \omega_1 - \omega_2, x) e^{-i\Delta k^{(3)}(\omega_0, \omega_1, \omega_2)x}, \end{cases} \quad (3.2)$$

where Γ is defined as in (1.128). The fields are related to the spectral densities through $n_i(\omega_i, x) = |\underline{A}_i(\omega_i, x)|^2$, $i \in \llbracket 0, 3 \rrbracket$, and the spectral energies \mathcal{E}_i at the Fourier component ω_i are:

$$\mathcal{E}_i(\omega_i, x) = \hbar \omega_i n_i(\omega_i, x). \quad (3.3)$$

As the incoming beams are Gaussian, it comes:

$$\mathcal{E}_i(\omega_i, x) = \hbar \omega_i n_i(\omega_i^\circ, x) e^{-\left(\frac{\omega_i - \omega_i^\circ}{\Delta \omega_i}\right)^2}, \quad (3.4)$$

with ω_i° the central frequency and $\Delta \omega_i$ the spectral linewidth at $1/e^2$, $i \in \{0, 2, 3\}$.

The resolution of the coupled equations (3.2) gives the following expressions for the spectral energies:

$$\begin{cases} \mathcal{E}_i(\omega_i, L) = \mathcal{E}_i(\omega_i, 0), i \in \{0, 2, 3\} \\ \mathcal{E}_1(\omega_1, L) = \left| \iint \frac{d\omega_0}{2\pi} \frac{d\omega_2}{2\pi} \tilde{\Phi}(\omega_0, \omega_1, \omega_2, L) \sqrt{\frac{\mathcal{E}_0(\omega_0, 0) \mathcal{E}_2(\omega_2, 0) \mathcal{E}_3(\omega_0 - \omega_1 - \omega_2, 0)}{n_z(\omega_0) n_y(\omega_2) n_z(\omega_0 - \omega_1 - \omega_2)}} \right|^2, \end{cases} \quad (3.5)$$

with

$$\tilde{\Phi}(\omega_0, \omega_1, \omega_2, L) = \frac{\chi_{24}^{(3)}(\omega_1)}{4\varepsilon_0 c^2} \frac{\omega_1}{\sqrt{n_z(\omega_1)}} \int_0^L dx \frac{e^{i\Delta k^{(3)}(\omega_0, \omega_1, \omega_2)x}}{W^2(x)}, \quad (3.6)$$

and

$$\Delta k^{(3)}(\omega_0, \omega_1, \omega_2) = \frac{1}{c} [\omega_0 n_y(\omega_0) - \omega_1 n_z(\omega_1) - \omega_2 n_y(\omega_2) - (\omega_0 - \omega_1 - \omega_2) n_z(\omega_0 - \omega_1 - \omega_2)]. \quad (3.7)$$

L is the crystal length; n_y and n_z are the principal refractive indices involved in the process; $\chi_{24}^{(3)} = \chi_{\text{eff}}^{(3)} = 1.46 \times 10^{-21} \text{ m}^2 \text{V}^{-2}$ is the excited third-order nonlinear coefficient of KTP according to the polarization configuration and the wavelengths involved [99]. By not integrating the integral of Equation (3.6), we let us the possibility to consider a waist radius that varies in the longitudinal direction x .

The spectrum calculated using Equations (3.5) to (3.7) leads to the blue solid curve shown in Figure 3.3: it is significantly in a better agreement with the experimental data, since the consideration of spectral width of the pump leads to a FWHM of 4.9 nm. Note that here the beam radius is taken equal to that of the pump $W_0(x) = 50 \mu\text{m}$, since it is smaller than that of the injection beam, and independent on the longitudinal coordinate x , the Rayleigh length ($Z_R = 27 \text{ mm}$) being longer than the crystal length ($L = 13 \text{ mm}$) as mentioned above.

3.1.3 Energetic properties, Kerr effect

3.1.3.1 Experimental data

The total energy \mathcal{E}_1 corresponding to the full spectrum of field 1 was measured as a function of the energies of the stimulation and pump beams independently. The corresponding data are shown in Figures 3.4 and 3.5 respectively. Calculations were also performed by integrating over the previous spectra:

$$\mathcal{E}_i(L) = \int_{\mathbb{R}} d\omega_i \mathcal{E}_i(\omega_i, L), i \in \llbracket 0, 4 \rrbracket. \quad (3.8)$$

In both cases, the experimental data do not agree with these calculations shown in green dashed lines and a refinement of our model is then needed.

The maximal intensities considered in these experiments are 39 GW/cm^2 for the pump (0) and 99 GW/cm^2 for the stimulation (2 + 3) in Figure 3.4. They are 267 GW/cm^2 for the pump and 52 GW/cm^2 for the stimulation in Figure 3.5. These are the highest values ever reported in KTP without any optical damage [148].

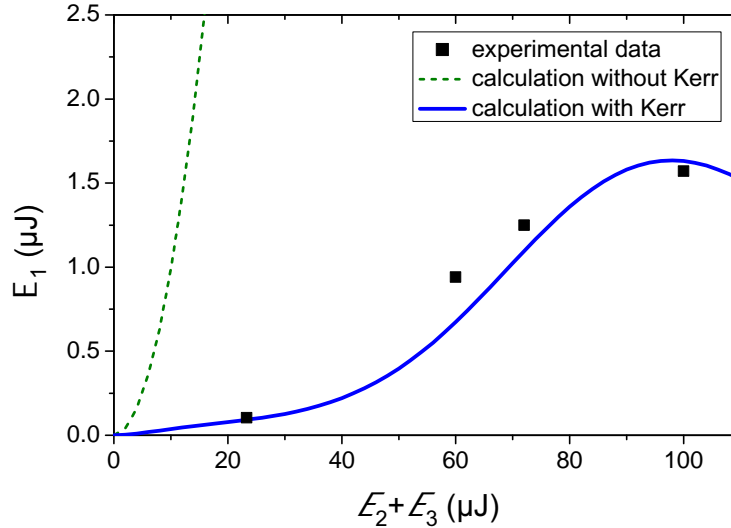


Figure 3.4 – Generated energy in the field 1 as a function of the energy of the stimulation fields 2 and 3. The incident pump energy is fixed at $\mathcal{E}_0 = 14.5 \mu\text{J}$. The fitting parameters are $v = 0.375$ and $\mu = 0.6$.

3.1.3.2 Refinement of the model

We carefully checked from energy measurements that the discrepancy between experiments and calculations was not due to the depletion of the incident beams. The occurrence of gray-tracking of KTP under the 532 nm irradiation could also be suspected [149], but we did not identify any evidence of this optical damage. Actually, another sensible reason can be found in the onset of a Kerr nonlinear response, as the incident intensities are increased.

Kerr effect The Kerr effect is the degenerate case of the third-order nonlinear four-wave mixing (see scheme B of Figure 1.4, Section 1.1.3) and fulfills the energy relationship $\omega + \omega \rightarrow \omega + \omega$. This process is always phase-matched since the frequencies of all the interacting waves are equal. It is therefore always present when light interacts with matter, but only observable when large enough intensities are reached. It comes out as a modification of the linear index n with the interacting total intensity I_{tot} [22]:

$$n_{\text{eff}}(\omega, x) = n(\omega) + n_{\text{Kerr}}(\omega) I_{\text{tot}}(x), \quad (3.9)$$

where n_{Kerr} is the nonlinear Kerr index expressed as:

$$n_{\text{Kerr}}(\omega) = \frac{\chi_{\text{eff}}^{(3)}}{\varepsilon_0 c n(\omega)^2}. \quad (3.10)$$

Two consequences arise from this index change. First, the phase-mismatch $\Delta k^{(3)}$ is progressively modified as the total intensity gradually increases, which prevents from fulfilling perfectly the phase-matching condition for each value of the incoming intensity. In the calculation, the consideration of this effect is straightforward as each refractive index in Equations (3.5) to (3.7) needs to be replaced by the corresponding effective index given by Equation (3.9). Secondly,

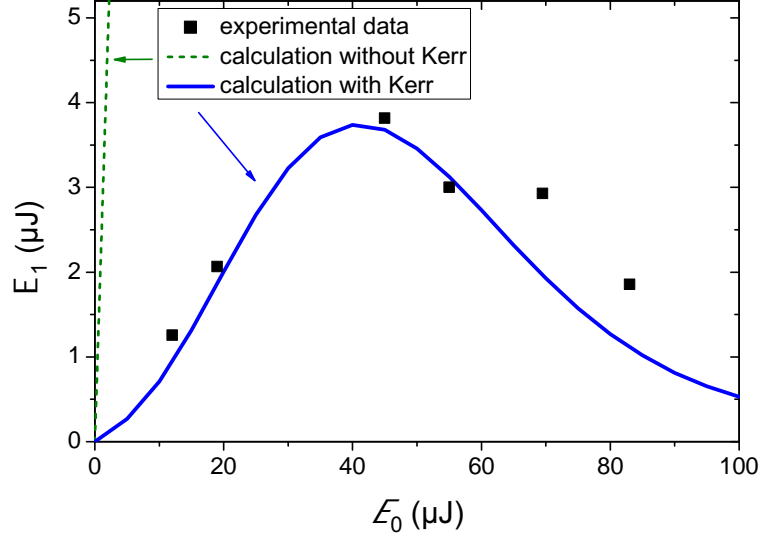


Figure 3.5 – Generated energy in the field 1 as a function of the energy of the pump field 0. The incident stimulation energy is fixed at $\mathcal{E}_2 + \mathcal{E}_3 = 63 \mu\text{J}$. The fitting parameters are $v = 0.388$ and $\mu = 0.6$.

the nonlinear medium behaves like a graded-index lens due to a transverse gradient of refractive index induced by the transverse Gaussian profile of intensity of the beams: it is maximum at the center of the beam and decreases towards the edges. The following section is devoted to the modelling of the corresponding focal length, f_{Kerr} , called the Kerr lens.

Beam size and Kerr lens A Spiricon camera placed $L' = 17 \text{ cm}$ away from the KTP exit allowed to clearly evidence the Kerr lens effect through a decrease of about 65% of the 532 nm pump beam radius when its energy varied from 20 to 160 μJ . This behaviour is shown as black squares in Figure 3.6. The two transverse Gaussian beam radii W_y and W_z are averaged, and normalized by the values corresponding to a propagation without the KTP crystal.

We can impute this beam size change to the effective focal length f_{Kerr} using a simplified model based on the ABCD ray matrix method [150]. We consider our beams as Gaussian characterized by the complex beam parameter q at any point x of the propagation, $x = 0$ being the entrance of the crystal. It is defined as:

$$\frac{1}{q(x, \lambda)} = \frac{1}{R(x)} - i \frac{\lambda}{\pi n(\lambda) W^2(x)}. \quad (3.11)$$

R is the radius of curvature of the beam and W the beam radius at $1/e^2$ of the intensity given by Equations (1.33) and (1.32) respectively. When going through different optical elements, the beam parameter q can be calculated in the ABCD formalism: each optical element is described by a 2×2 transfert matrix $\begin{pmatrix} A & B \\ C & D \end{pmatrix}$, and the incoming q_i parameter becomes q_f according to [150]:

$$q_f(x) = \frac{Aq_i(x) + B}{Cq_i(x) + D}. \quad (3.12)$$

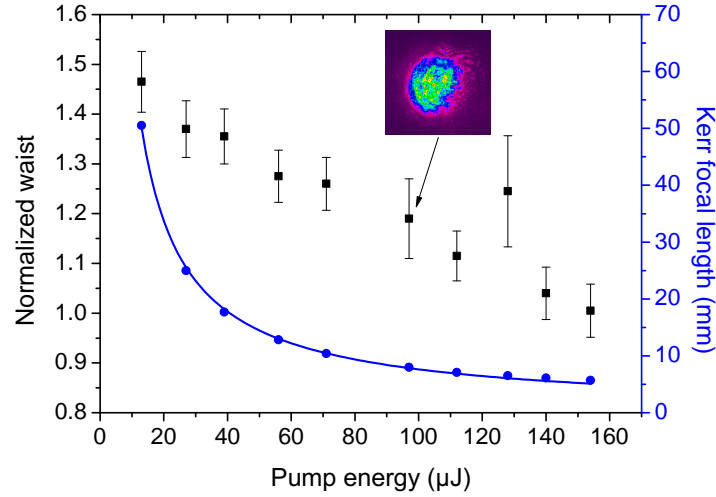


Figure 3.6 – Experimental normalized beam size at $x = L' = 17\text{cm}$ (in black squares); calculated focal length (in blue) as a function of the energy of the pump beam at 532 nm. In the inset, capture with a Spiricon camera of the pump beam with an energy of 97 μJ .

Especially, the propagation through a thin lens of focal length f is described using

$$M_{\text{lens}}(f) = \begin{pmatrix} 1 & 0 \\ -1/f & 1 \end{pmatrix}, \quad (3.13)$$

and the propagation over a distance x in a medium of optical index n by

$$M_{\text{prop}}(x, n) = \begin{pmatrix} 1 & x/n \\ 0 & 1 \end{pmatrix}. \quad (3.14)$$

In the case of the propagation in a Kerr medium with parabolic spatial variations of its refractive index, we have [151, 152]:

$$M_{\text{Kerr}}(\omega, x) = \begin{pmatrix} \cos(\gamma x) & \frac{\sin(\gamma x)}{n_{\text{eff}}\gamma} \\ -n_{\text{eff}}\gamma \sin(\gamma x) & \cos(\gamma x) \end{pmatrix}, \quad (3.15)$$

where

$$\gamma(\omega, x) = \sqrt{\frac{4n_{\text{Kerr}}(\omega) I_{\text{tot}}(x)}{n_{\text{eff}}(\omega, x)} \frac{1}{W(x)}}. \quad (3.16)$$

With a Taylor expansion of the trigonometric functions up to the second order, which stands when $\gamma x \ll 1$, Equation (3.15) can be written as:

$$\begin{aligned} M_{\text{Kerr}}(\omega, L) &\simeq \begin{pmatrix} 1 & \frac{L}{2n_{\text{eff}}} \\ 0 & 1 \end{pmatrix} \begin{pmatrix} 1 & 0 \\ -n_{\text{eff}}\gamma^2 L & 1 \end{pmatrix} \begin{pmatrix} 1 & \frac{L}{2n_{\text{eff}}} \\ 0 & 1 \end{pmatrix} + o((\gamma L)^3) \\ &= M_{\text{prop}}\left(\frac{L}{2}, n_{\text{eff}}\right) M_{\text{lens}}(f_{\text{Kerr}}) M_{\text{prop}}\left(\frac{L}{2}, n_{\text{eff}}\right) + o((\gamma L)^3). \end{aligned} \quad (3.17)$$

Through identification of the matrices (3.14), (3.13) and (3.17), this simple model shows that

the Kerr medium indeed acts like a lens of focal length f_{Kerr} put in between two plates of length $\frac{L}{2}$ and optical index n_{eff} , with the following magnitude:

$$f_{\text{Kerr}}(\omega, L) = \frac{1}{n_{\text{eff}}\gamma \sin(\gamma L)}. \quad (3.18)$$

For Gaussian beams, the beam size $W(x)$ in the longitudinal direction follows Equation (1.32) that is written again with the current notations:

$$W^2(x) = W_{\text{Kerr}}^2 \left[1 + \left(\frac{x - f_{\text{Kerr}}}{z_R} \right)^2 \right], \quad (3.19)$$

where W_{Kerr} represents the waist radius, placed at $x = f_{\text{Kerr}}$, and z_R the Rayleigh length defined in Equation (1.35).

From Equations (3.18) and (3.19), combined with the measurements of the beam radius values outside the KTP crystal ($x = L'$) presented in Figure 3.6 and at the entrance of the crystal ($x = 0$), $W_{\text{inc}} = 50 \mu\text{m}$, it is possible to infer the two quantities f_{Kerr} and W_{Kerr} , that are dependent on the total intensity I_{tot} . The Kerr focal length leads to the blue dots shown on Figure 3.6. Their extrapolation with respect to the total intensity is the blue solid line and follows: $f_{\text{Kerr}} [\text{mm}] = 536 \times (\mathcal{E}_{\text{tot}} [\mu\text{J}])^{-0.923}$. It varies between 2 to 20 mm from the entrance face, W_{Kerr} varying from 11 to 18 μm over the considered energy range.

By introducing two parameters ν and μ in Equation (3.19), the beam radius at any position x can be written as:

$$W^2(x, I_{\text{tot}}) = \left[\nu^2 (W_{\text{inc}}^2 - W_{\text{Kerr}}^2) \right] \left[\frac{x - \mu f_{\text{Kerr}}}{\mu f_{\text{Kerr}}} \right]^2 + \nu^2 W_{\text{Kerr}}^2. \quad (3.20)$$

These two fitting quantities have physical meanings. ν is introduced for taking into account the mis-overlap between the pump and stimulation beams: it is clear from Equations (3.5) and (3.6) that it therefore reduces the incident energies to the amount that actually takes part in the process. μ accounts for the deviation from our simplified Kerr effect model. We found the best convergence for $\nu = 0.375$ and $\mu = 0.6$ when the generated energy \mathcal{E}_1 is measured as a function of the stimulation energy \mathcal{E}_{2+3} , as shown in Figure 3.4; and $\nu = 0.388$ and $\mu = 0.6$ when the pump energy \mathcal{E}_0 varies as shown in Figure 3.5.

The agreement between the experimental data and our refined model is quite satisfactory, especially since the values of the fitting parameters that are found are very close to each other in the two experiments.

Note that the calculations with and without the Kerr effect match for small values of the intensity. This cannot be seen on Figures 3.4 and 3.5 as significant intensities, on the order of 10 GWcm^{-2} , are involved.

Note also that the consideration of the Kerr effect does not affect the spectrum of field 1 in the polychromatic model and barely in the case of the monochromatic approximation as shown in Figure 3.3. We indeed understand from Figure 3.5 that the incident energies involved to get the spectrum 3.3 ($\mathcal{E}_0 = 52 \mu\text{J}$, $\mathcal{E}_2 + \mathcal{E}_3 = 60 \mu\text{J}$) are hardly sufficient to highlight a Kerr effect.

3.1.4 Conclusion

In conclusion, we performed a complete experimental and theoretical study of the spectral and energy properties of triple photons generated by a third-order down-conversion parametric process in a bulk KTP crystal pumped at 532 nm and stimulated around 1662 nm in the picosecond regime. Our model takes into account the spectral linewidths of the beams and a parasitic Kerr effect modifying the phase-mismatch and the beam geometries. This Kerr effect consequently attenuates the TPG conversion efficiency for large intensities. Table 3.2 summarizes the results by giving the energy characteristics for maximum triplet generation. It corresponds to a conversion efficiency in energy, defined as $\eta_{\mathcal{E}} = \frac{\mathcal{E}_1}{\mathcal{E}_0 + \mathcal{E}_2 + \mathcal{E}_3}$, that equals 3.5%.

	pump (0)	seeding (2+3)	generation (1)
Photon number ($\times 10^{13}$ /pulse)	12	53	2.8
Energy (μJ /pulse)	45	63	3.8
Intensity (GWcm^{-2})	120	43	10

Table 3.2 – Energy characteristics of the bi-stimulated TPG in KTP.

Total intensities as high as 300 GWcm^{-2} were focused in KTP without inducing any optical damage.

3.2 Towards TPG in rutile TiO_2

TiO_2 in its rutile phase has been presented in Section 2.2.1.3 of the second chapter as a promising crystal for triple photon generation [107, 108]. This section deals with its study in detail.

3.2.1 TiO_2 characterization through a THG experiment in a cylindrical geometry

We perform at first a THG experiment that allows to determine the optical indices of rutile TiO_2 . Their precise knowledge is needed so as to infer accurate phase-matching conditions for the TPG experiment. Typically, a phase-matching direction is known with an uncertainty of 1° if the indices are precise to 10^{-4} . The THG experiment also gives access to the two susceptibility tensor elements involved in the process and their relative sign.

3.2.1.1 Rutile TiO_2 in the literature

Crystalline properties Rutile TiO_2 belongs to the tetragonal crystal class $\frac{4}{m}mm$ with lattice parameters $a = 4.5937 \text{ \AA}$ and $c = 2.9581 \text{ \AA}$ [153]. It is centrosymmetric so that no cascading quadratic process can pollute the TPG.

Linear properties Its optical class is positive uniaxial, which means that $n_o < n_e$ with n_o and n_e the ordinary and extraordinary linear indices respectively. It is transparent from 430 nm to 5800 nm, as shown in Figure 3.7 [154].

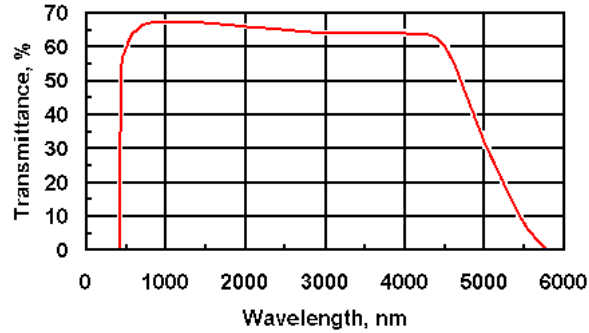


Figure 3.7 – External transmittance of a 7 mm-long rutile TiO_2 sample, from [154].

The refractive indices are greater than 2, which leads to strong Fresnel reflexion coefficients, around 20%. Furthermore, its birefringence is high, with a magnitude of about 0.25 [107, 154–157], which is not necessarily an advantage for achieving phase matching.

It is thus of particular importance to know with a good accuracy the linear optical indices in order to infer precisely the phase-matching conditions of a nonlinear interaction.

Nonlinear properties Among the 81 elements of the third-order nonlinear susceptibility tensor $\chi^{(3)}$, four are non-zero and independent elements in the $\frac{4}{m}mm$ class, under the Kleinman

symmetry approximation: χ_{11} , χ_{16} , χ_{18} and χ_{33} [19]. The contracted notations are explicated in Table 3.3.

Contracted notation χ_{ij}	Equalities between coefficients under the Kleinman assumption
χ_{11}	$\chi_{xxxx} = \chi_{yyyy}$
χ_{16}	$\chi_{xxzz} = \chi_{xzzx} = \chi_{zzxx} = \chi_{yyzz} = \chi_{yzyz} = \chi_{yzzy}$ $= \chi_{zyyz} = \chi_{zyzy} = \chi_{zzyy} = \chi_{zxzx} = \chi_{zxzx} = \chi_{zzxx}$
χ_{18}	$\chi_{xxyy} = \chi_{xyxy} = \chi_{xyyx} = \chi_{yxyx} = \chi_{yyxx} = \chi_{yyxx}$
χ_{33}	χ_{zzzz}

Table 3.3 – Non-zero $\chi^{(3)}$ coefficients under the Kleinman symmetry assumption in the $\frac{4}{m}mm$. Indices x , y and z refer to the dielectric frame.

Only two of these elements have been determined prior to the present work: $|\chi_{16}(613.2 \text{ nm})| = 5.0 \times 10^{-21} \text{ m}^2\text{V}^{-2}$ from THG [107] and $|\chi_{11}(532 \text{ nm})| = 6.15 \times 10^{-20} \text{ m}^2\text{V}^{-2}$ from coherent Raman ellipsometry [158]. Other results previously published that are based on nonlinear index n_2 measurements do not specify which coefficients were involved so that they only give estimates of the magnitude of $|\chi^{(3)}|$: $2.05 \times 10^{-21} \text{ m}^2\text{V}^{-2}$ at 1064 nm from nearly degenerate four-wave mixing experiments [159]; and $5.6 \times 10^{-20} \text{ m}^2\text{V}^{-2}$ or $3.08 \times 10^{-19} \text{ m}^2\text{V}^{-2}$ at 800 nm from non-phase-matched THG in thin films [160, 161]. Note also that calculations using the bond-orbital theory at a wavelength of 1 μm give a magnitude $|\chi^{(3)}|$ ranging between 3.4×10^{-21} and $6.8 \times 10^{-20} \text{ m}^2\text{V}^{-2}$ [162].

This part is devoted to phase-matched THG experiments. They allow determining accurate Sellmeier equations, the magnitude of χ_{18} , as well as the relative sign between χ_{16} and χ_{18} .

3.2.1.2 Theory on THG for TiO₂

Phase-matching condition There are three possible polarization schemes enabling birefringent phase-matching for THG, in accordance with (1.75). In rutile TiO₂, one of the best situation to achieve a maximal conversion efficiency is that the beams propagate in the (xOz) plane of the dielectric frame (x, y, z) with a type II configuration of polarization:

$$\omega^{(o)} + \omega^{(e)} + \omega^{(e)} \rightarrow 3\omega^{(o)}, \quad (3.21)$$

where $\omega^{(o)}$ and $\omega^{(e)}$ are the circular frequencies of the ordinary and extraordinary polarized waves respectively. The corresponding phase-matching relationship is then:

$$\Delta k^{(3)}(\theta_{\text{PM}}, \omega) = \frac{\omega}{c} [3n^{(o)}(\theta_{\text{PM}}, 3\omega) - n^{(o)}(\theta_{\text{PM}}, \omega) - 2n^{(e)}(\theta_{\text{PM}}, \omega)] = 0, \quad (3.22)$$

where $n^{(o)}$ and $n^{(e)}$ are the ordinary and extraordinary refractive indices at the considered phase-matching polarization angle θ_{PM} , which is the angle of spherical coordinates between the z -axis and the considered phase-matching direction. Equation (3.22) can be expressed in terms of the principal indices n_o et n_e with the use of (1.64). It leads to the expression of θ_{PM} :

$$\theta_{\text{PM}}(\omega) = \arccos \left[\sqrt{\frac{\left(\frac{n_o(\omega)}{n_e(3\omega)}\right)^2 \frac{4}{\left(3 - \frac{n_o(\omega)}{n_o(3\omega)}\right)^2} - \left(\frac{n_o(\omega)}{n_e(\omega)}\right)^2}{1 - \left(\frac{n_o(\omega)}{n_e(\omega)}\right)^2}} \right]. \quad (3.23)$$

Note that Equations (3.22) and (3.23) are valid at any azimuthal φ angle since TiO_2 belongs to the uniaxial optical class.

Effective coefficient The corresponding effective coefficient $\chi_{\text{eff}}^{(3)}$ is calculated from Equation (1.53) [40]:

$$\chi_{\text{eff}}^{(3)}(\theta_{\text{PM}}, \omega) = \sum_{ijkl} \chi_{ijkl}^{(3)}(3\omega = \omega + \omega + \omega) e_i^{(o)}(\theta_{\text{PM}}, 3\omega) \cdot e_j^{(e)}(\theta_{\text{PM}}, \omega) \cdot e_k^{(e)}(\theta_{\text{PM}}, \omega) \cdot e_l^{(o)}(\theta_{\text{PM}}, \omega), \quad (3.24)$$

where $\{i, j, k, l\} \in \{x, y, z\}$ and $e^{(o/e)}$ are the ordinary and extraordinary unitary electric field vectors. They can be expressed in the cartesian coordinates as in Equations (1.67). The type II effective coefficient in the $(x0z)$ plane then becomes:

$$\chi_{\text{eff}}^{(3)}(\theta_{\text{PM}}, \omega) = \sin^2(\theta_{\text{PM}} - \rho^+(\theta_{\text{PM}}, \omega)) \chi_{16}(3\omega) + \cos^2(\theta_{\text{PM}} - \rho^+(\theta_{\text{PM}}, \omega)) \chi_{18}(3\omega), \quad (3.25)$$

where ρ^+ is the double refraction angle, defined in Equation (1.68)

According to our experiments, the THG energy conversion efficiency in the considered phase-matching direction η can be calculated in the undepleted pump approximation with Gaussian beams, which gives [163]:

$$\eta = \frac{\mathcal{E}_{3\omega}(L)}{\mathcal{E}_{\omega}(L)} = \frac{128\mu_0}{3\pi\epsilon_0} \left(\frac{\chi_{\text{eff}}^{(3)}(\theta_{\text{PM}}, 3\omega) L}{\lambda_{\omega}} \right)^2 \frac{T^{(o)}(\omega) \left(T^{(e)}(\omega)\right)^2 T^{(o)}(3\omega) \tau_{3\omega} W_{3\omega}^2}{n^{(o)}(\omega) (n^{(e)}(\omega))^2 n^{(o)}(3\omega) \tau_{\omega}^3 W_{\omega}^6} G(\beta) [\mathcal{E}_{\omega}(L)]^2, \quad (3.26)$$

with

$$G(\beta) = \sqrt{\frac{6}{\pi}} \int_{\mathbb{R}} du F^2(u, \beta), \quad (3.27)$$

and

$$F(u, \beta) = \frac{e^{-u^2}}{\beta} \int_0^{\beta} d\sigma e^{-2(u+\sigma)^2}. \quad (3.28)$$

ϵ_0 and μ_0 are the vacuum permittivity and permeability, \mathcal{E}_{ω} and $\mathcal{E}_{3\omega}$ the incident fundamental and generated third-harmonic energies respectively, L the interaction length, λ_{ω} the fundamental wavelength, and $\chi_{\text{eff}}^{(3)}$ is defined by Equation (3.25). The Fresnel transmission coefficients are expressed by:

$$T^{(o,e)}(\omega) = \frac{4n^{(o,e)}(\omega)}{(1 + n^{(o,e)}(\omega))^2}. \quad (3.29)$$

For Gaussian beams, the pulse durations τ_i and beam sizes W_i , $i \in \{\omega, 3\omega\}$, fulfill:

$$\begin{cases} W_{3\omega} = \frac{1}{\sqrt{3}}W_\omega \\ \tau_{3\omega} = \frac{1}{\sqrt{3}}\tau_\omega \end{cases}. \quad (3.30)$$

Finally, $\beta = \frac{vL}{\tau_\omega}$ and $v = \left| \frac{1}{v_{g,3\omega}^{(o)}} - \frac{1}{v_{g,\omega}^{(o)}} \right|$ is the inverse group velocities.

3.2.1.3 Description of the experiment

Cylinder method The most standard method to determine the refractive indices of solid materials is the technique of minimum of deviation in a prism. But its major drawback is that many centimetric pieces of matter are needed if an accuracy $\Delta n/n$ better than 10^{-4} is targetted, which is the case for the purpose of phase matching. An alternative method that consists of measuring the phase-matching properties in a cylindrical or spherical sample with a typical precision of 0.5° has been developed in our group since 1989 [164, 165]. The relative values of the principal indices n_o/n_e can then be inferred from the evolution of the phase-matching directions with respect to the wavelength. Note that their absolute values can be obtained by choosing a principal index known at a particular wavelength. The strength of this method is that any direction perpendicular to the revolution axis of a cylinder, or any direction of a sphere, can be accessed while keeping the input laser beam at normal incidence. The refraction inside the crystal remains normal to the surface, which is indeed more suited than the slab geometry. Due to this infinite angular clearance, a large number of phase-matching conditions can then be probed in the directions where the effective coefficient is not zero, so that a huge wavelength range can be considered.

As the rutile is an uniaxial crystal, its indices surface exhibit a revolution symmetry around its (Oz) axis as stated in Section 1.2.1 and pictured in Figure 1.5 (b). Therefore, only one degree of freedom orthogonal to (Oz) is sufficient to describe the whole phase-matching properties. It has been chosen to cut a TiO₂ cylinder of revolution axis (Oy) , allowing us to describe the (xOz) plane.

The machining method of realization of oriented crystal cylinder polished on the side has been proposed and developped in the group [166]. In the case of rutile TiO₂, the cutting is made easier as it is non hygroscopic and its hardness is important, of about 6.5 in the Mohs scale. The fabrication process is pictured in Figure 3.8.

The cylinder has been cut by Jérôme Debray and Bertrand Ménaert from a slab sample of dimensions $10 \times 5 \times 10 \text{ mm}^3$ bought to the MTI Corporation company. The face orthogonal to the (Oy) revolution axis, which orientation is controled by X-rays with an accuracy of about 0.1° , is stuck on an arm connected to an oscillating axis. The slab sample, turning around its (Oy) axis, is put in contact with a turning plate receiving abrasives of various grain sizes so that

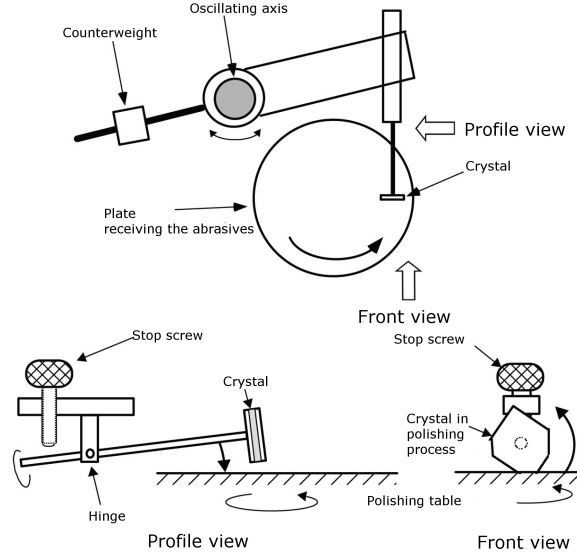


Figure 3.8 – Sketch of the processing of a cylindrical sample. Adapted from [166].

it is gradually polished until it reaches a cylindrical form. The stop screw controls the sample descent. The polishing is optimized by progressively reducing the size of the abrasives. As the first attempts led to an ellipsoid of axes $(0x)$ and $(0z)$ that may have resulted in all likelihood from the hardness anisotropy, the TiO_2 crystal has been put in between two glass plates so as to impose an isotropic wear.

The resulting TiO_2 sample is a cylinder with a radius of 4 mm, a thickness of 5 mm, a tolerance to the cylindricity less than 0.5% and a polishing of the order of $\lambda/10$. It was then stuck on a goniometric head as depicted in Figure 3.9.



Figure 3.9 – Picture of the oriented 4-mm radius TiO_2 cylinder with the y -axis as the rotation axis.

The cylinder is placed at the center of a rotation stage supplied with a vernier of angular resolution of 0.5° . Using this experimental setup and rotating the cylinder around the y -axis make possible the direct access to any direction of propagation over the whole $(x0z)$ plane of TiO_2 while keeping the perpendicular incidence [107, 167]. The phase-matching direction corresponding to a given fundamental wavelength is detected when the associated THG conversion efficiency is maximal. An angular accuracy of about $\pm 0.3^\circ$ is accessible by measuring the four symmetrical phase-matching directions in the plane of the cylinder.

Experimental setup The experimental setup is depicted schematically in Figure 3.10. The fundamental beam is generated using two tunable parametric sources. A first device emits a beam tunable from 400 nm up to 2500 nm from a Topas Light Conversion optical parametric generator (OPG) pumped by the third-harmonic of a 10 Hz Leopard Continuum Nd:YAG laser of 15 ps pulse duration (FWHM). The second source is a DFG Light Conversion generator that mixes by non-collinear difference frequency generation the idler beam of the previous OPG and the Nd:YAG beam at 1064 nm in order to generate between 2 μm and 12 μm . These parametric sources are schemed in Figure 3.11. Different half-wave plates (HWP) suitable for the considered spectral range are placed just before the rutile crystal to adjust the polarization of the incident tunable fundamental beam at 30° of the z -axis so as to achieve the type II phase-matching configuration of polarization. We used focalizing and collecting spherical lenses of 75 mm focal length (L_1 and L_2) from each sides of the crystal. The position of the focalizing lens L_1 is of particular importance and is discussed further. It has to be placed so that it focuses at the focal plane of the first half of the cylinder, allowing a parallel propagation of the fundamental beam within the crystal [168].

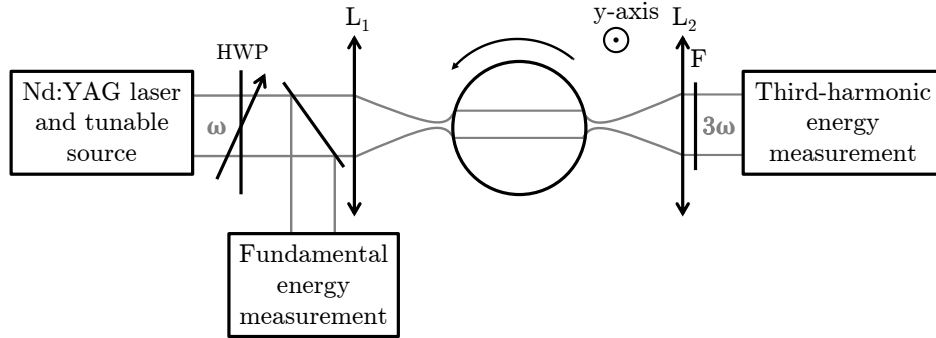


Figure 3.10 – Schematic top view of the THG experimental setup where ω and 3ω are the fundamental and third-harmonic circular frequencies. HWP stands for half-wave plate.

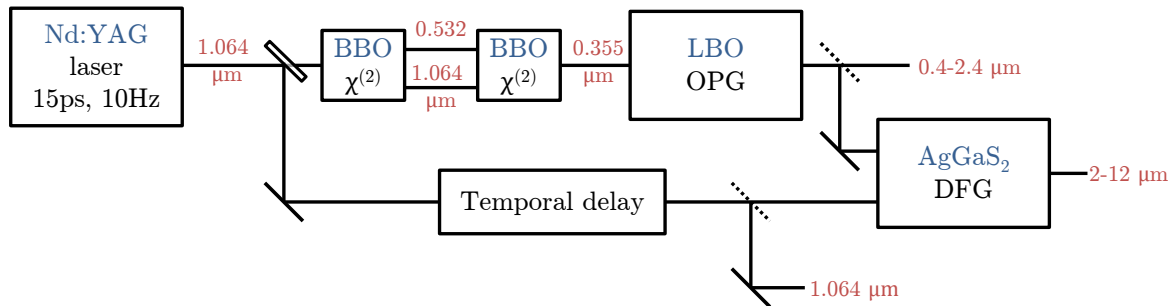


Figure 3.11 – Representation of the parametric source.

Two important requirements have to be fulfilled when working with a cylinder. The rotation axis of the goniometric head holding the cylinder has to be the revolution axis of the cylinder: adjustment can be made on this head with an HeNe laser of small diameter. In addition, to make sure the beam goes exactly through a diameter of the cylinder, the position of the latter is adjusted with a translation stage, still using an ordinary polarized HeNe laser, *i.e.* without

any spatial walk-off.

The residual fundamental beam at the exit of the crystal is removed using filters. The incoming fundamental beam power is measured using an Ophir PE10 energy-meter, while the third-harmonic is detected using a silicium Hamamatsu C2719 photodiode calibrated in energy prior to the experiments.

Orientation of the dielectric frame The (Ox) and (Oz) axes are identified easily as the directions of collinearity of the ordinary and extraordinary Poynting vectors. Then, these two axes are distinguished from each other by observing the orientation of the deviation of the extraordinary polarized wave when the sample is rotated in the (xOz) plane.

Focusing conditions A crystal cut as a cylinder behaves as a cylindrical lens of focal length f_c defined as [23]:

$$f_c(\omega) = \frac{n(\omega) R}{2(n(\omega) - 1)}, \quad (3.31)$$

with n the optical index and R the cylinder radius. For the rutile TiO_2 crystal, $n(\omega) > 2$. As a consequence, $f_c < R$ for an incident collimated propagation, and thus the focal point lies inside the cylinder. This has to be avoided for two reasons: the strong intensity due to the focusing may be prejudicial for the medium in terms of optical damage; and most importantly, the resulting divergence may distort the measurement of the phase-matching angles.

Therefore, it is necessary to properly focus the incident beam. We consider our beams as Gaussian and perform calculations using the ABCD formalism presented in Section 3.1.3.2. The matrix for the propagation in a medium is given by Equation (3.14), and the one for the refraction at a single surface of radius of curvature R between two media of indices n_1 and n_2 by [150]:

$$M_{\text{diopetre}} = \begin{pmatrix} 1 & 0 \\ \frac{n_2 - n_1}{R} & 1 \end{pmatrix}, \quad (3.32)$$

with $R > 0$ (resp. < 0) for a convexe (resp. concave) interface.

In the case of our experiment, a modelling of the propagation is performed so as to find the optimal distance between the lens L_1 and the entrance of the cylinder at any incoming wavelength to achieve a parallel propagation within the cylinder. This distance d_{foc} is shown in Figure 3.12 with respect to the wavelength. Figure 3.13 gives the calculated beam propagation in the optimal case. The optical indices for rutile are taken in [107], and for the $f = 75$ mm BK7 lenses in [169].

The fundamental beam waist radius within the TiO_2 crystal has been measured with a calibrated CCD camera equal to $W_\omega = 120 \pm 11 \mu\text{m}$, which leads to a Rayleigh length $z_R(\omega) = \frac{\pi n(\omega) W_\omega^2}{\lambda_\omega}$ equal to $30 \pm 9 \text{ mm}$ for the ordinary polarization (along the y -axis), and to $33 \pm 9 \text{ mm}$ for the extraordinary polarization. This ensures us that the beams remain parallel in the cylinder, its diameter of 8 mm being smaller than the Rayleigh length. This is a crucial point to perform accurate measurements of phase-matching angles.

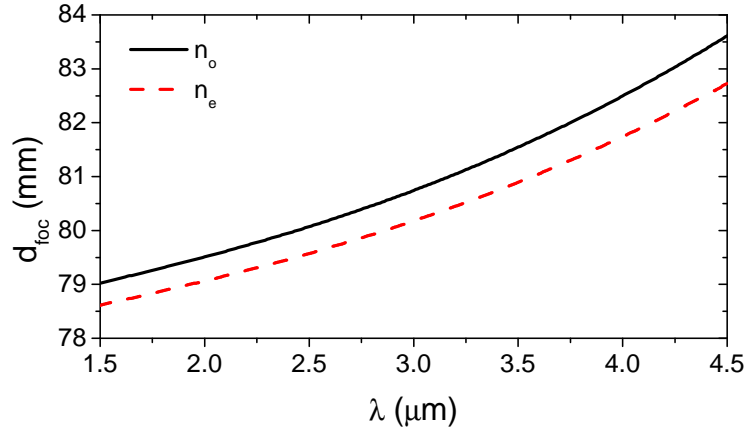


Figure 3.12 – Distance from the focalizing lens L_1 to the entrance of the crystal as a function of the wavelength for the ordinary and extraordinary waves.

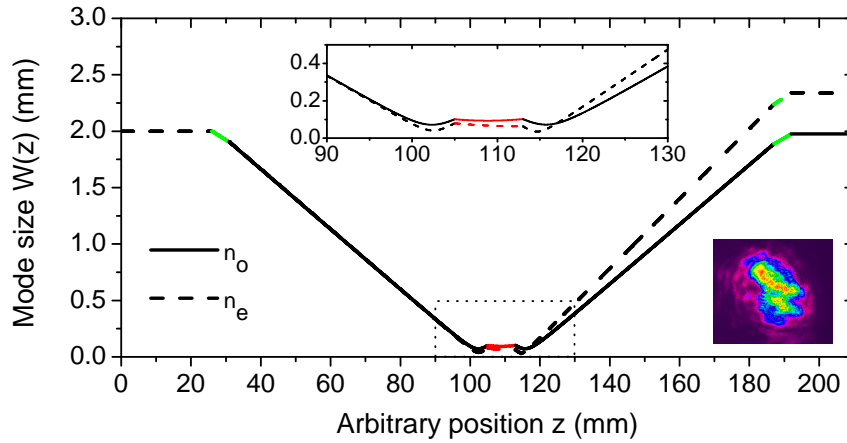


Figure 3.13 – Propagation in the plane $(x0z)$ at $\lambda = 1.8 \mu\text{m}$. In black, propagation in the air; in green, propagation in a lens; in red, propagation in the crystal. Solid and dashed lines stand for the ordinary and extraordinary waves respectively. Zoom in the crystal region in the top inset. In the bottom right-hand inset, down-converted transverse mode at 695 nm captured with the Spiricon camera 15.5 cm after the collecting lens.

3.2.1.4 Phase-matching properties and Sellmeier equations

Phase-matching measurements The protocol of THG phase-matching measurements is the following: for any angle of the cylinder, the OPG wavelength λ_ω is tuned until the signal at the third-harmonic wavelength $\lambda_{3\omega}$ reaches the peak value of the sinc^2 function. In the $(x0z)$ plane of interest, each phase-matching angle θ_{PM} has three equivalent angles: $\pi - \theta_{\text{PM}}$, $\pi + \theta_{\text{PM}}$ and $2\pi - \theta_{\text{PM}}$. We can benefit from this to increase the accuracy of our measurement. Figure 3.14 gives the phase-matching angles measured in the TiO₂ cylinder. It appears that rutile can be phase-matched for fundamental wavelengths ranging between 1836 nm and 4449 nm.

For comparison, Figure 3.14 also exhibits in dashed lines phase-matching curves calculated from the dispersion equations of the refractive indices of TiO₂ previously published [107, 154–156]. It clearly appears that the discrepancy between these calculated curves and the experi-

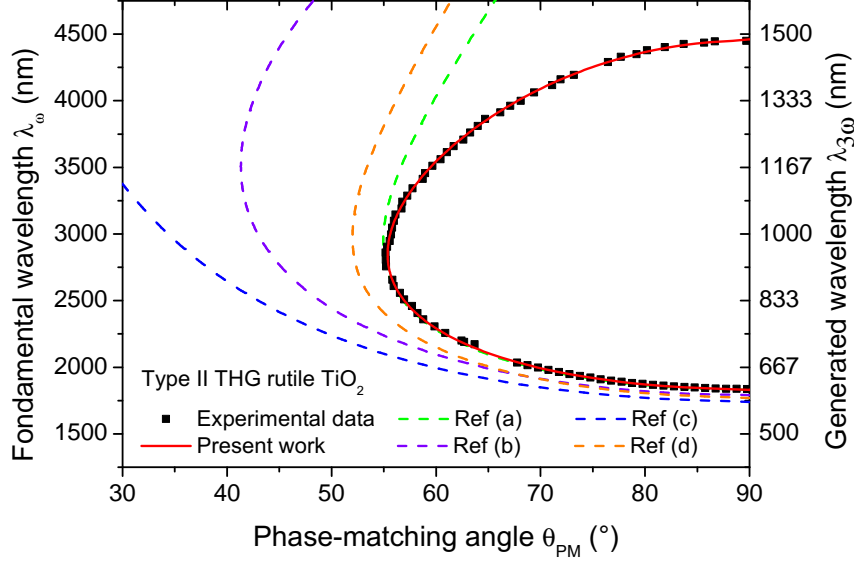


Figure 3.14 – Type II THG phase-matching curve of rutile TiO_2 . Black squares are experimental data from the cylinder experiment, and the solid red line corresponds to their numerical interpolation. Color dashed lines are phase-matching curves calculated from data of references [107] (a), [154] (b), [155] (c) and [156] (d).

mental data increases as a function of wavelength, leading to strong divergences above 2000 nm. This feature can be well understood knowing that these curves were calculated from refractive indices that had been measured only over the visible and near infrared range up to 1500 nm. It shows that it was indeed important to carry out these measurements as the chemical composition fluctuates from one sample to another in terms of stoichiometry.

Determination of Sellmeier equations At this point, it is possible to refine the TiO_2 Sellmeier equations by interpolating the phase-matching angles we obtained experimentally since they are widely distributed over the whole transparency range of the crystal. The corresponding interpolating curve is the solid red line in Figure 3.14. It is based on Equation (3.23) and a Sellmeier form [28] for the expressions of the principal refractive indices n_o and n_e expressed as following where the wavelength is expressed in nanometers:

$$n_o(\lambda) = \sqrt{3.2089 + \frac{3.4000 \times 10^{-5}}{1.2270 \times 10^{-5} - \lambda^{-2}} - 3.2545 \times 10^{-8} \lambda^2}, \quad (3.33)$$

$$n_e(\lambda) = \sqrt{2.9713 + \frac{5.1891 \times 10^{-5}}{1.2280 \times 10^{-5} - \lambda^{-2}} - 4.2950 \times 10^{-8} \lambda^2}. \quad (3.34)$$

The numerical convergence of the fit is obtained by refining the eight Sellmeier coefficients through an iterative algorithm that minimizes the sum of the l^2 norm of the distance from the experimental data to the fit. The wavelength validity domain of these equations corresponds to the experimental measurement range, *i.e.* from 612 nm to 4449 nm.

Equations (3.33) and (3.34) are plotted in Figure 3.15. They are compared with previous works that include measurements on prisms [154–157] and calculations [156]. Note that Sellmeier

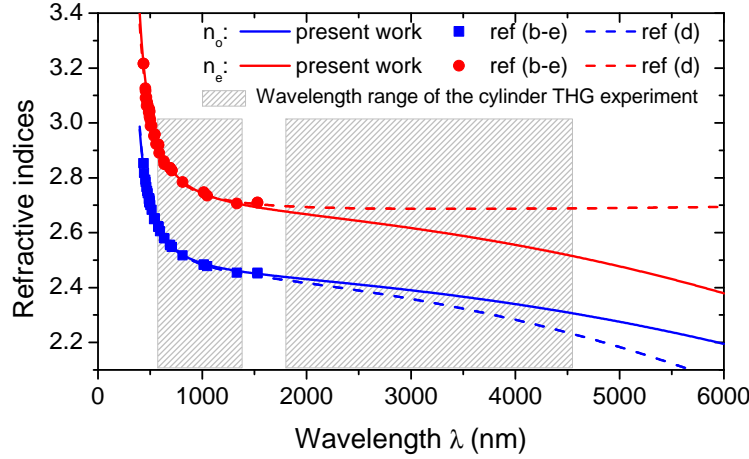


Figure 3.15 – Ordinary n_o and extraordinary n_e principal refractive indices of TiO_2 as a function of the wavelength from present work in solid lines; and from [154] (b), [155] (c), [156] (d) and [157] (e) in symbols (experiments) and dashed lines (calculations).

equations (3.33) and (3.34) are in perfect agreement with the refractive index measurements previously published, which is an additional validation of our equations. We can also see the strong discrepancy between the curves of the present work and those previously published. Figure 3.15 gives an example, from reference [156], where a splitting between the curves clearly appears above 1500 nm, this wavelength corresponding to the upper value of the range of measurement of the refractive indices in [156].

Uncertainty on the refractive indices The experimental accuracy on the angle measurement is of the order of $\pm 0.3^\circ$. This induces an uncertainty on the phase-matching wavelength for each angle of propagation, as pictured in Figure 3.16a. This uncertainty goes to zero towards the horizontal tangents of Figure 3.19 ($\theta = 90^\circ$) and increases up to about 200 nm for the fundamental wavelengths towards the vertical tangent ($\theta = 55.4^\circ$), 70 nm for the generated wavelengths. Relative uncertainties on the ordinary and extraordinary refractive indices $\Delta n_{o,e}/n_{o,e}$ are then calculated using the Sellmeier equations (3.33) and (3.34). They range between 0 and 5×10^{-3} , as pictured on Figure 3.16b.

3.2.1.5 Third-order nonlinear coefficients

The energy conversion efficiency of type II THG in the TiO_2 cylinder is measured at different phase-matching angles for two different values of the energy of the incident fundamental beam, 1.9 μJ and 16 μJ , as shown in Figure 3.17. They correspond to 7.4 MWcm^{-2} and 0.9 MWcm^{-2} respectively. The experimental setup is the same than the one used for the phase-matching measurements. The incident energy is changed by using calibrated neutral density filters. The experimental data corresponding to these two sets of measurements are consistent to each other, which attests to the good reproducibility.

The conversion efficiency can reach 1.3% which is the higher value ever reported in this crystal. From these experimental data, we were able to determine the magnitude of χ_{18} and

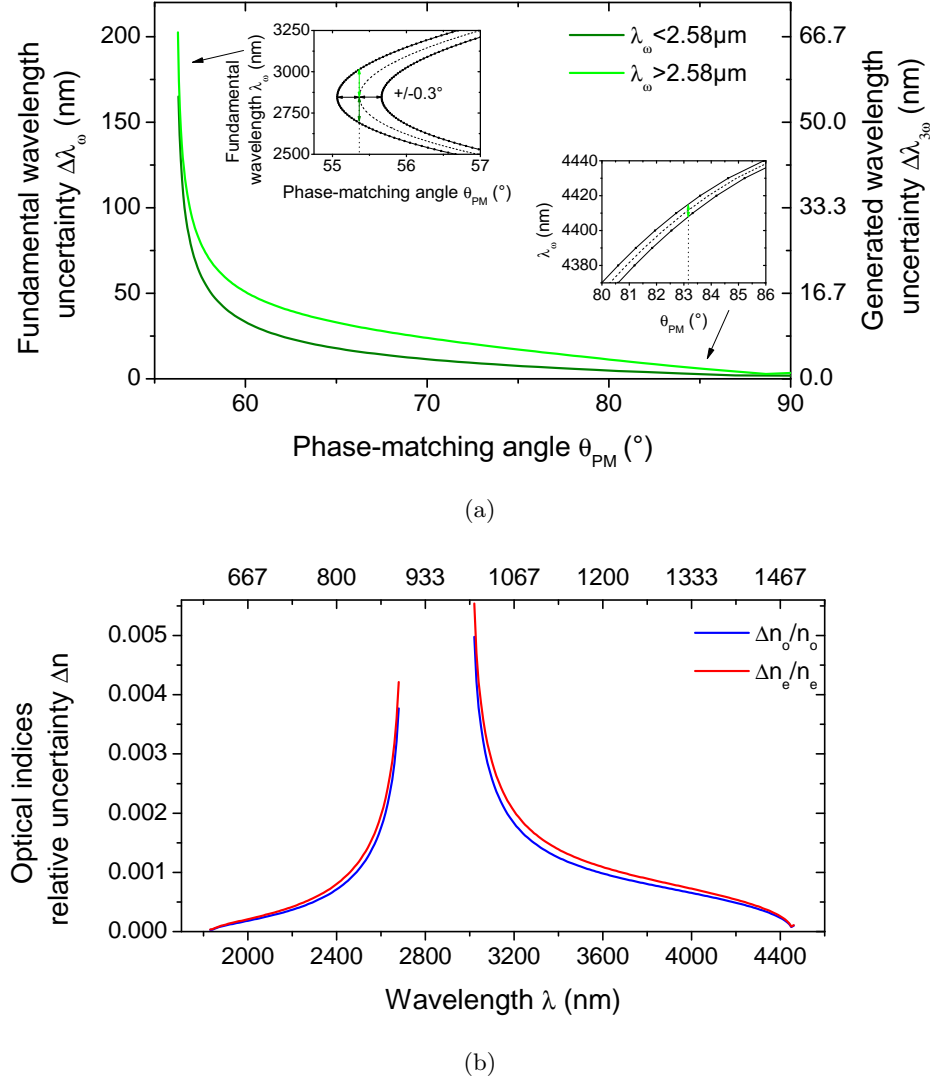


Figure 3.16 – (a) Uncertainty on the λ_ω fundamental and $\lambda_{3\omega}$ generated wavelengths as a function of the phase-matching angle θ_{PM} ; in the insets, close-ups of the phase-matching curve 3.19. (b) Uncertainty on the ordinary and extraordinary refractive indices n_o and n_e as a function of the wavelength.

its relative sign with χ_{16} since these two coefficients are involved in the effective coefficient according to Equations (3.25). We took as a reference the absolute value $|\chi_{16}(613.2\text{ nm})| = 5.0 \times 10^{-21} \text{ m}^2\text{V}^{-2}$ previously determined by type II phase-matched THG experiments in a slab sample at $\theta = 90^\circ$ where this coefficient is the only one to be involved [100, 108]. Numerical computation of the conversion efficiencies using Equations (3.25) to (3.28) and the absolute value of χ_{16} are done in the two hypotheses of identical and opposite signs for χ_{16} and χ_{18} . The two corresponding curves relative to the effective coefficient are shown in Figure 3.18 together with calculations arising from the conversion efficiency measurements in the two relative sign cases. It clearly appears that χ_{16} and χ_{18} are of opposite signs, which fixes the absolute value χ_{18} at the different wavelengths that are considered. The corresponding Miller coefficient is [170]:

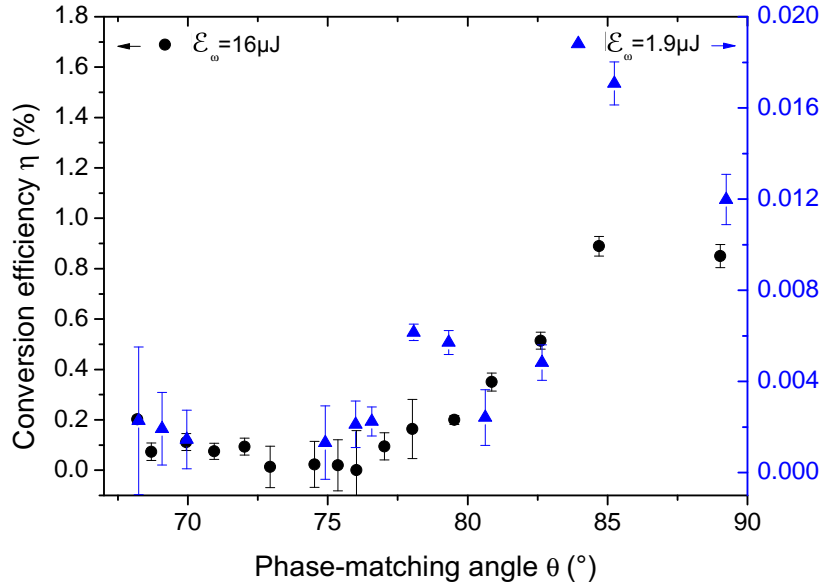


Figure 3.17 – Type II THG conversion efficiency of rutile TiO₂ as a function of the phase-matching angle for fundamental energies $\mathcal{E}_\omega = 16 \mu\text{J}$ (black dots; y-axis on the left-hand side) and $1.9 \mu\text{J}$ (blue triangles; y-axis on the right-hand side).

$$\Delta_{18} = \frac{|\chi_{18}(3\omega)|}{(n_e^2(\omega) - 1)^2 (n_o^2(\omega) - 1) (n_o^2(3\omega) - 1)} = 9.1 \times 10^{-23} \text{ m}^2 \text{V}^{-2}, \quad (3.35)$$

where n_o and n_e are the principal indices given by Equations (3.33) and (3.34) respectively.

As an example, Equation (3.35) leads to $|\chi_{18}(616.7 \text{ nm})| = 9.7 \times 10^{-20} \text{ m}^2 \text{V}^{-2}$, that is close to the absolute magnitude of χ_{11} [158], and significantly larger than χ_{16} [107].

3.2.2 TPG in rutile TiO₂

In the previous section, we performed an exhaustive study of THG phase-matching properties of rutile TiO₂. These results can be directly used for a TPG experiment, stimulated with one or two beams.

3.2.2.1 TPG phase-matching conditions

In this section are presented the TPG phase-matching conditions. We intend to use a Nd:YAG laser that can be doubled in frequency for the pump beam, *i.e.* $\lambda_0 = 1064 \text{ nm}$ or 532 nm . Because a bi-stimulated TPG provides higher conversion efficiencies, it is wiser to carry out the experiment with two stimulation beams at first in order to confirm the phase-matching wavelengths that are going to be calculated here. The same scheme with a unique stimulation beam can be considered afterwards. Consequently, frequency degeneracy on two triplet fields is required ($\lambda_2 = \lambda_3$) so as to use only one beam for the stimulation, coming from a quadratic OPG.

The phase-matching conditions are then calculated from the relationship:

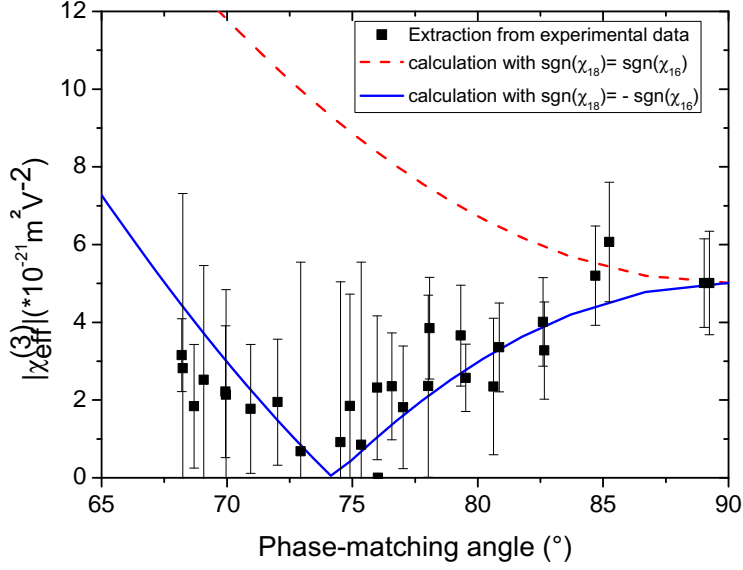


Figure 3.18 – Magnitude of the effective coefficient $\chi_{\text{eff}}^{(3)}$ as a function of the phase-matching angle. The black squares correspond to the values determined from the conversion efficiencies experimental data and Equation (3.26). The dashed red and solid blue lines are calculations considering χ_{16} and χ_{18} with same and opposite signs respectively.

$$\Delta k^{(3)}(\theta_{\text{PM}}, \omega_0, \omega_1, \omega_2) = 0 \quad (3.36)$$

$$= \frac{1}{c} \left[\omega_0 n^{(o)}(\theta_{\text{PM}}, \omega_0) - \omega_1 n^{(p_1)}(\theta_{\text{PM}}, \omega_1) - \omega_2 n^{(p_2)}(\theta_{\text{PM}}, \omega_2) - \omega_2 n^{(p_3)}(\theta_{\text{PM}}, \omega_2) \right],$$

where the refractive indices are taken from the previous THG measurements, and the polarization p of the waves 1, 2 and 3 can be o or e according to the seven polarization configurations from the system (1.75).

All these possible configurations are discussed in Appendix B. Among all them, only one remains interesting as we want to be able to detect the down-converted photons with available detectors, *i.e.* up to 5.5 μm with an InSb-based photodiode, and more particularly close to the telecom wavelengths, and to generate the stimulation photons with the available OPG. This last requirement imposes a stimulation wavelength below 2.4 μm , as shown in the schematics of the sources on Figure 3.11. In that case, the DFG stage also pictured on the same figure cannot indeed be used easily as we want to keep available the pump beamline. Therefore, we understand from the energy conservation relationship that a pump at 1064 nm would lead to down-converted tri-photons and seedings in the mid-IR, which is not possible with the present experimental setup. We will then work with a pump beam at 532 nm. The only configuration that remains when the previous requirements are considered is the type I (see the classification given in (1.75)), *i.e.*:

$$\lambda_0^{(o)} \rightarrow \lambda_1^{(e)} + \lambda_2^{(e)} + \lambda_2^{(e)}. \quad (3.37)$$

The corresponding phase-matching curves $\lambda_1(\theta_{\text{PM}})$ and $\lambda_2(\theta_{\text{PM}})$ are presented on Figures 3.19.

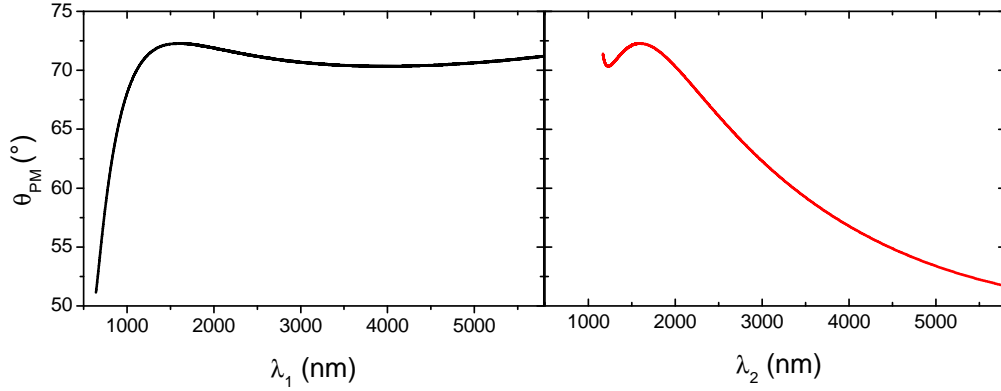


Figure 3.19 – Type I phase-matching curves with a pump at 532 nm.

A close-up around the spectral range of interest is shown in Figures 3.20a and 3.20b. The blue and green colours indicate the way to read the couples of phase-matching wavelengths λ_1 and λ_2 corresponding to each other: blue with blue, and green with green. Figure 3.20c shows the associated effective third-order nonlinear coefficient.

It has been chosen to work at $\theta = 72^\circ$, so that the wavelengths are easily generated and detected on one hand, and it is not too close from the point of vertical tangent above which no solution is left on the other hand. The two couples of solutions, identified by the blue and green dots on the previous figures, are:

$$(A) \quad \begin{cases} \lambda_1^{(e)} = 1920.7 \text{ nm} \\ \lambda_{2,3}^{(e)} = 1471.6 \text{ nm}, \end{cases} \quad (3.38)$$

and

$$(B) \quad \begin{cases} \lambda_1^{(e)} = 1379.4 \text{ nm} \\ \lambda_{2,3}^{(e)} = 1732.0 \text{ nm}. \end{cases} \quad (3.39)$$

3.2.2.2 Theoretical conversion efficiency

We compare in this section the conversion efficiencies in energy of rutile TiO₂ and KTP. For rutile, we consider here the previous scheme (B), while for KTP it is the one from Section 3.1, *i.e.* with the wavelengths in nanometers:

$$\begin{cases} \text{TiO}_2 : & \lambda_0 (532) \rightarrow \lambda_1 (1379) + \lambda_2 (1732) + \lambda_2 (1732), \text{ at } \theta = 72^\circ. \\ \text{KTP} : & \lambda'_0 (532) \rightarrow \lambda'_1 (1478) + \lambda'_2 (1662) + \lambda'_2 (1662), \text{ along } (0x). \end{cases} \quad (3.40)$$

For equivalent crystal lengths, beam transverse geometry and incoming energies, the ratio between the efficiencies η can be written as a function of quantities that only depend on the intrinsic properties of the materials, as shown in Equation (3.26): the effective susceptibilities $\chi_{\text{eff}}^{(3)}$, the refractive indices n , and the Fresnel transmission coefficients in energy T . It comes:

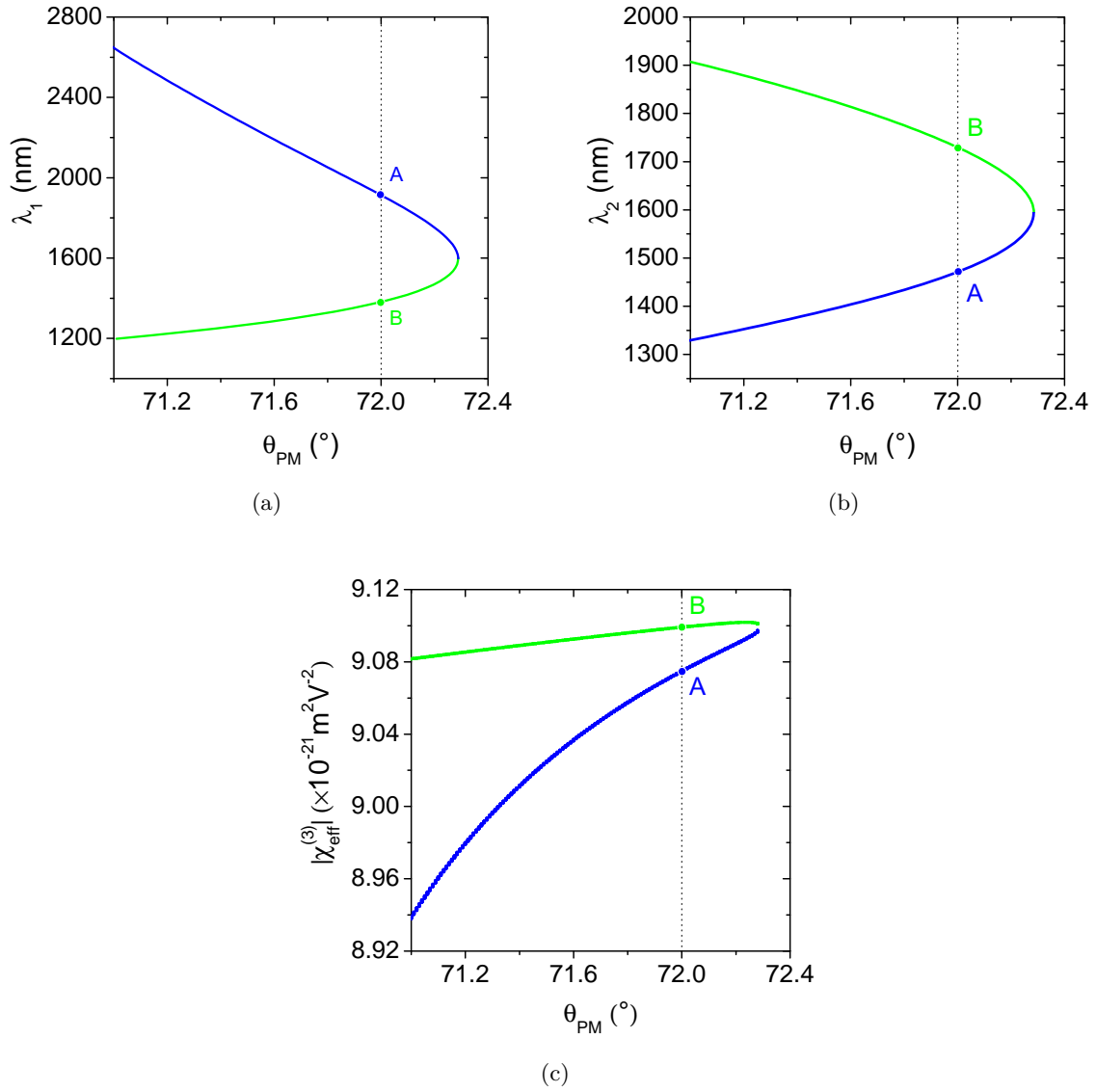


Figure 3.20 – (a) and (b) Phase-matching conditions for TPG in rutile TiO_2 : $\lambda_0^{(o)} \rightarrow \lambda_1^{(e)} + \lambda_2^{(e)} + \lambda_2^{(e)}$. (c) Corresponding absolute value of the effective cubic nonlinear coefficient.

$$\frac{\eta_{\text{TiO}_2}}{\eta_{\text{KTP}}} = \left[\frac{\chi_{\text{eff}}^{(3)}(\lambda_{0,1,2,3})|_{\text{TiO}_2}}{\chi_{\text{eff}}^{(3)}(\lambda'_{0,1,2,3})|_{\text{KTP}}} \right]^2 \frac{\prod_{i=0}^3 n_{\text{KTP}}(\lambda'_i) \prod_{i=0}^3 T_{\text{TiO}_2}(\lambda_i)}{\prod_{i=0}^3 n_{\text{TiO}_2}(\lambda_i) \prod_{i=0}^3 T_{\text{KTP}}(\lambda'_i)}, \quad (3.41)$$

with

$$\begin{cases} \prod_{i=0}^3 n_{\text{KTP}}(\lambda'_i) = n^{(-)}(\lambda'_0) n^{(+)}(\lambda'_1) n^{(-)}(\lambda'_2) n^{(+)}(\lambda'_2) \\ \prod_{i=0}^3 n_{\text{TiO}_2}(\lambda_i) = n^{(o)}(\lambda_0) n^{(e)}(\lambda_1) [n^{(e)}(\lambda_2)]^2, \end{cases} \quad (3.42)$$

and

$$\begin{cases} \prod_{i=0}^3 T_{\text{KTP}}(\lambda'_i) = T^{(-)}(\lambda'_0) T^{(+)}(\lambda'_1) T^{(-)}(\lambda'_2) T^{(+)}(\lambda'_{23}) \\ \prod_{i=0}^3 T_{\text{TiO}_2}(\lambda_i) = T^{(o)}(\lambda_0) T^{(e)}(\lambda_1) \left[T^{(e)}(\lambda_2) \right]^2. \end{cases} \quad (3.43)$$

Using the new Sellmeier equations and third-order susceptibility tensor elements for TiO₂, and the Sellmeier equations and effective susceptibility of Section 3.1 for KTP, the numerical application gives:

$$\frac{\eta_{\text{TiO}_2}}{\eta_{\text{KTP}}} = 4.36. \quad (3.44)$$

This makes rutile TiO₂ indeed an interesting generating medium, despite its high refractive indices and consequently its high Fresnel reflection coefficients. Its optical damage threshold is close to that of KTP, which justify such a direct comparison with equivalent incoming energies.

3.2.2.3 Experimental attempt

A TiO₂ sample coming from the same provider as the cylinder has been cut as a slab along $\theta = 72^\circ$ by Jérôme Debray. It is placed in the experimental setup already used for KTP and described in Section 3.1.1, with the bi-stimulation beam here at 1732 nm (resp. 1472 nm), extraordinary polarized.

No signal around 1379 nm (resp. 1921 nm) has been detected, even though the injection frequency has been widely tuned. The cylinder has been put back into the setup instead of the slab sample to have a supplementary degree of freedom. A particular care has been put on the focusing configuration so that the beams remain parallel in the sample as already explained in Section 3.2.1.3. Still, a significant difference arises here: the wavelengths of the two beams coming into the cylinder are different. Thus, these beams do not focus at the same point after the injection lens, if collimated before it. The positions of the lenses forming the telescope on the injection line are then adjusted to make the pump and injection focal points as close as possible to each other. Note that having a parallel propagation in the crystal is here less critical than during the THG measurement that led to the establishment of the refractive indices.

The angle of the cylinder have been widely tuned too without any success for finding any down-converted signal.

The only explanation we have found for this failure is that the dispersion equations of the refractive indices are not accurate enough at the working wavelengths. Actually, our THG experiments from which we determined these equations involved ordinary polarized beams at frequencies ranging between 610 nm and 1487 nm, and ordinary and extraordinary beams at frequencies ranging between 1830 nm and 4461 nm. Thus, because our TPG calculation is performed using an ordinary pump wavelength at 532 nm, we can suspect a lack of accuracy for its corresponding refractive index. Likewise for the extraordinary index at 1732 nm, the stimulating wavelength of the scheme (B). However, the extraordinary index at 1472 nm, the stimulating wavelength of the scheme (A), has been sollicitated and should then be more reliable.

An underestimation of this index $n_o(532 \text{ nm})$ of more than 10^{-3} , or an overestimation of

more than 0.16 which seems more unlikely, leads to the disappearance of any phase-matching.

To reach the refractive indices that have not been solicited during the THG experiment, a SFG (*i.e.* “non-degenerated THG”) could be considered. Such an experiment could involve as a starting point the set of wavelengths (A) from Equation (3.38). Nevertheless, this method requires the use of two tunable OPOs, which are not available at the lab.

3.2.2.4 Calculations out of phase-matching

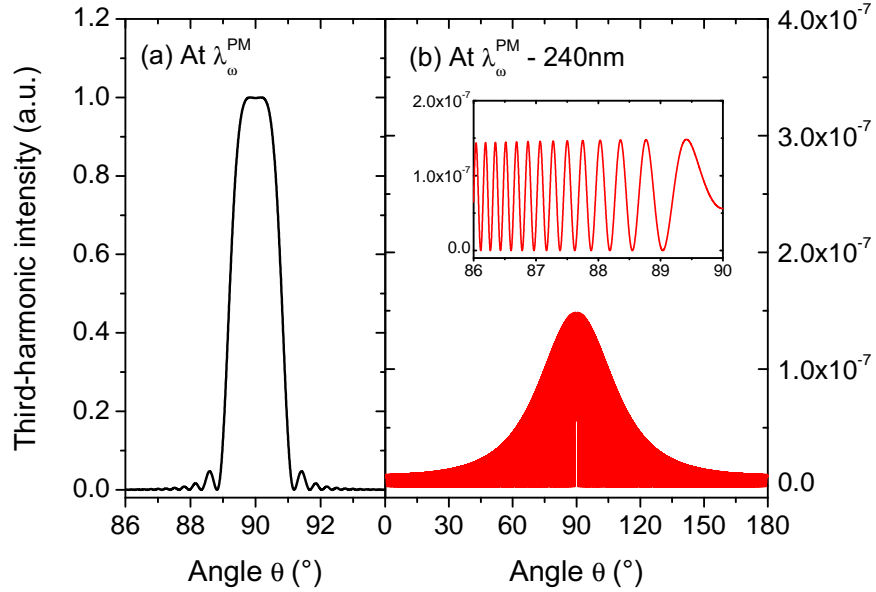


Figure 3.21 – THG angular spectrum. Calculations with monochromatic incoming fields at $\lambda_{\omega}^{\text{PM}}(\theta = 90^\circ) = 1830 \text{ nm}$ (a) and $\lambda_{\omega} = 1596 \text{ nm} = \lambda_{\omega}^{\text{PM}} - 240 \text{ nm}$ (b). The inset is a close-up view.

One idea to infer the value of $n_o(532 \text{ nm})$ is to come back to a THG experiment, but here out of matching ($\Delta k^{(3)} \neq 0$). The angular distribution obtained can be fitted by a

$\text{sinc}^2\left(\frac{\Delta k^{(3)}(\lambda_{3\omega}, \lambda_{\omega}, \lambda_{\omega})L}{2}\right)$ function, where the phase mismatch $\Delta k^{(3)}$ depends on $n_o(532 \text{ nm})$.

Figure 3.21 shows a calculation at phase-matching for a monochromatic fundamental beam at $\lambda_{\omega}^{\text{PM}} = 1830 \text{ nm}$, *i.e.* $\theta_{\text{PM}} = 90^\circ$ (a), and at $\lambda_{\omega} = 1596 \text{ nm} = \lambda_{\omega}^{\text{PM}} - 240 \text{ nm}$ (b) with a close-up view on the oscillations in the inset.

Nonetheless, it is obvious that a first limitation comes from the weakness of such a process, seven order of magnitudes below the phase-matched one as shown in Figure 3.21. We may not be able to capture it with the available detectors. A second limitation comes from the fact that the period of oscillations is of the order of 0.2° , which is below the precision of our goniometric setup. It will then be impossible to determine $n_o(532 \text{ nm})$ from a fit of Figure 3.21 (b). In addition, the beam coming from our OPG is polychromatic, with a FWHM in energy of 3.4 nm at 1662 nm as demonstrated in Figure 3.5. The linewidth at 1596 nm should not be very far from that at 1662 nm . Therefore, polychromatic calculations have been performed with that linewidth value and are shown in Figure 3.22, at $\lambda_{\omega}^{\text{PM}}(\theta = 90^\circ) = 1830 \text{ nm}$ (a), and $\lambda_{\omega} = 1596 \text{ nm}$ (b). We

see that the observation of oscillations out of phase-matching needs the use of narrow linewidth, which is not the case of our OPG source.

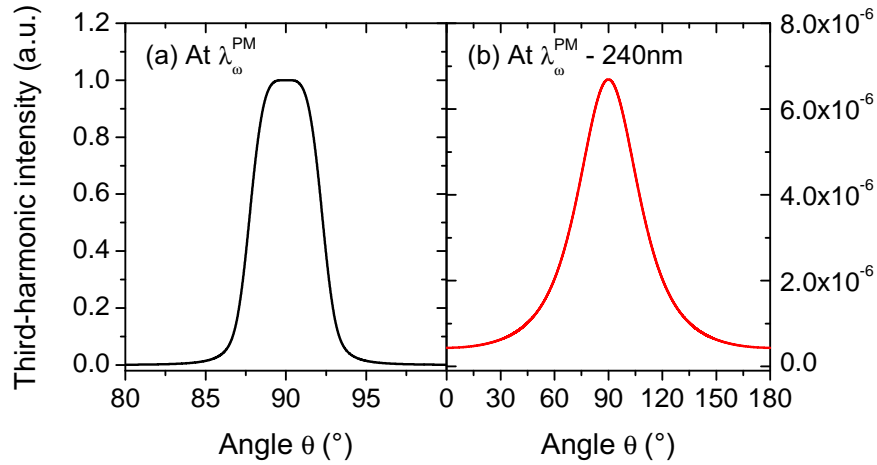


Figure 3.22 – THG angular spectrum. Calculations with polychromatic incoming fields of intensity FWHM 3.4 nm, at $\lambda_{\omega}^{\text{PM}}(\theta = 90^\circ) = 1830$ nm (a) and $\lambda = 1596$ nm = $\lambda_{\omega}^{\text{PM}} - 240$ nm (b).

3.2.3 Conclusion

We performed an exhaustive study of THG phase-matching properties of rutile titanium dioxide. We showed that this crystal enables THG phase matching for fundamental wavelengths ranging from 1836 nm to 4449 nm with an energy conversion efficiency that can reach more than 1%. The Sellmeier equations have been refined. The absolute magnitude of the χ_{18} coefficient has been determined, as well as its sign, opposite to that of χ_{16} .

Regarding the TPG, our last attempts suggest that our dispersion equations are not sufficiently accurate in the visible range close to ultraviolet, because this spectral range has not been solicited by the previous THG measurement. Figure 3.23 reminds indeed the wavelengths solicited during the TPG and THG experiments in red (below) and blue (above) respectively. For future experiments, n_o (532 nm) needs to be estimated by other means if the phase-matching conditions are intended to be calculated again. Alternatively, the experiment should be carried out with higher wavelengths, with suitable source and detection systems.

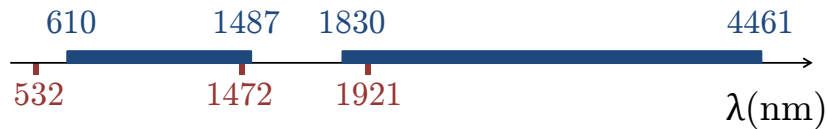


Figure 3.23 – Wavelengths solicited during the THG experiment above the arrow in blue; and during the TPG experiment (A) from Equation (3.38) below in red.

3.3 Prospective for resonant TPG from a synchronously pumped third-order optical parametric oscillator

3.3.1 Synchronously pumped OPO

A good way to increase the TPG conversion efficiency is to place the nonlinear crystal into a cavity in order to artificially increase the interaction length. Such a setup is called an optical parametric oscillator (OPO), which is widely used for the generation of pairs of photons from a second-order down-conversion process [171]. Our idea is then to use this concept for a third-order interaction. It will then be necessary to work in the picosecond regime so as to compensate the weakness of the third-order nonlinearity. But this imposes a synchronous pumping scheme of the OPO, where the pump repetition rate has to perfectly match the round-trip frequency of the OPO resonator as it is done in the case of quadratic OPOs [172] (see Figure 3.24). In this configuration, the resonating waves are amplified by the successive pump pulses. Note that the case of nanosecond OPOs is different since the amplification over the different round-trips of the resonating waves is performed by the same pump pulse.

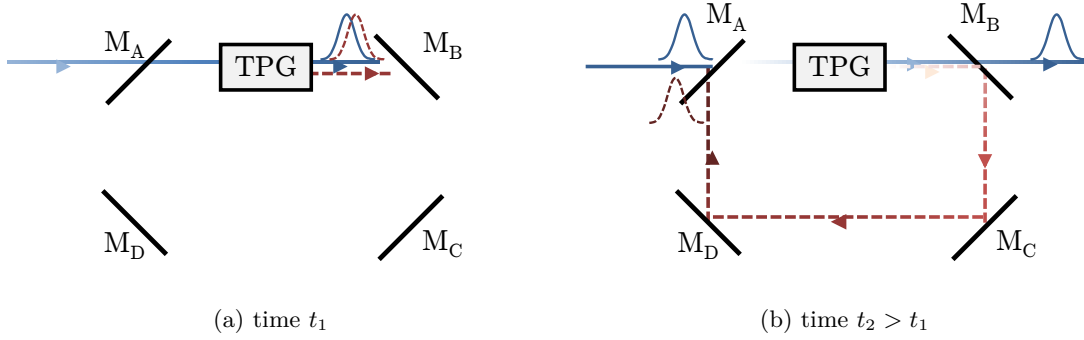


Figure 3.24 – Schematics of a synchronously pumped OPO at two different times t_1 and t_2 . The pump beam is depicted in solid line, and the down-converted beam in dashed line. $M_{A,B}$ are dichroic mirrors that have different transmissions at the pump and down-converted wavelengths; $M_{C,D}$ are standard metallic mirrors.

Temporal synchronicity The group velocity defined below is the crucial parameter for defining the matching between the cavity length and the repetition rate of the incident beams. It is given by:

$$v_g(\omega_i, \vec{r}) = \frac{c}{n(\omega_i, \vec{r}) + \omega_i \left. \frac{\partial n(\omega, \vec{r})}{\partial \omega} \right|_{\omega_i}}. \quad (3.45)$$

If $v_g(\omega_r)$ is the group velocity of the resonating wave, then the repetition rate f of the incident beam and the cavity length L_{cav} have to verify:

$$\frac{1}{f} = \frac{L}{v_g(\omega_r, \vec{r})} + \frac{(L_{\text{cav}} - L)}{c}, \quad (3.46)$$

where L is the crystal length. Due to the typical values of the group velocity, and because L_{cav} cannot reasonably exceed few meters, the value of f is typically around 100 MHz, which corresponds to several laser sources commercially available.

Note that the first path in the crystal set the phases of the down-converted waves under phase matching. And if a mode-locked pump is used, there exists a relationship between the initial phases of the different pump pulses so that the phases of the resonating signal and idler remain suited for phase matching over the different round trips.

Threshold The optical parametric oscillation can actually occur when the parametric gain compensates the losses over a round-trip in the cavity: this is a threshold process, which threshold condition will be calculated in the different experimental situations.

Coherence As for twins, the cavity losses may decorrelate the triplet beams due to partial transmission of light through the cavity mirrors. This results in a loss of coherence of the triplet state. In the literature, theoretical works reported correlations for the triple state in a dissipative cavity, strong below threshold and decreasing above threshold [129]. Felbinger *et al.* calculated the Wigner functions below and above threshold for the triplet state: the three-branches behaviour still exists, but the negativities disappear in the second case [4]. For twin photons, it has been demonstrated that tripartite entanglement (between pump, signal and idler) exists above threshold [146, 173]. Even though we will not investigate these correlation issues here, we have to stay aware about it.

The present section is a theoretical proposal of such a third-order OPO that has never been done previously. We have two targets: the mono-injected TPG, and the spontaneous TPG. In both cases, the numerical applications are done with KTP and the corresponding data from Section 3.1.

3.3.2 TPG configurations in OPO

Two different situations are considered with respect to the waves resonant in the cavity:

- 1. TPG pumped at λ_0 and injected at λ_1 , the two resonating waves being at λ_2 and λ_3 , which corresponds to a doubly resonant OPO (DROPO);
- 2. TPG pumped at λ_0 , the three generated waves at λ_1 , λ_2 and λ_3 being resonant, which corresponds to a triply resonant OPO (TROPO). We will consider two cases with respect to the injection: injection of the three modes on the one hand, and no injection, *i.e.* a spontaneous TPG, on the other hand.

3.3.2.1 DROPO

1. Partial degeneracy in wavelength and polarization The first case can be performed in a KTP crystal, along the x direction for $\lambda_0^{(-)} = 532$ nm, $\lambda_1^{(+)} = 1478$ nm and $\lambda_2^{(-)} = \lambda_3^{(+)} = 1662$ nm, as used in the travelling wave regime described in Section 3.1. Figure 3.25 is a schematic of the experimental configuration. It is a DROPO mono-injected at λ_1 , with resonant waves at

$\lambda_2 = \lambda_3$, the energy at λ_0 and λ_1 being fully extracted from the mirror M_B . With the notations of Figure 3.25, we then have $T_{A,B}(\lambda_{0,1}) = 100\%$, $R_{B,C,D}(\lambda_{2,3}) = 100\%$, and $T_A(\lambda_{2,3})$ is a finite value close to zero. Consequently, M_A and M_B are dichroic mirrors, while M_C and M_D standard metallic mirrors.

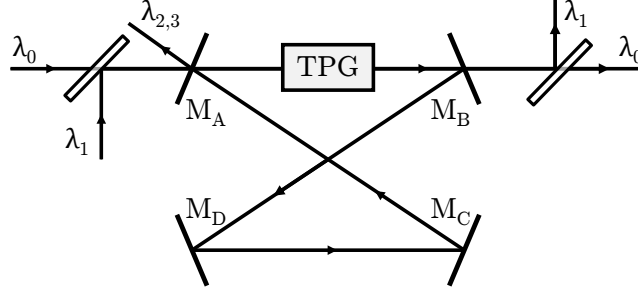


Figure 3.25 – Schematic of the partially degenerated ($\lambda_2^{(-)} = \lambda_3^{(+)} \neq \lambda_1^{(+)}$) mono-injected third-order DROPO.

Crystal length At this point, it is necessary to take care of the temporal walk-off, which corresponds to the separation of the pulses at different group velocities. We therefore define a critical length, L_c , that corresponds to the value over which the temporal pulses are distant by more than their FWHM, as shown in Figure 3.26. In the case we are interested in, the biggest temporal walk-off in KTP occurs between the two waves at $\lambda_1^{(+)}$ and $\lambda_2^{(-)}$, which leads to $L_c = 54$ mm for 15 ps pulses according to the refractive indices that are involved.

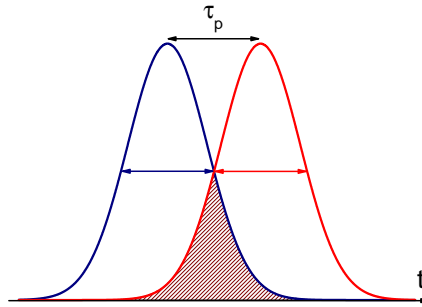


Figure 3.26 – Sketch of two temporal pulses distant from each other by their FWHM τ_p . Interaction can occur only in the shaded overlap area.

Consequently, all numerical calculations will be given for a crystal length of $L = 30\text{mm} < L_c$.

Cavity length Because of the birefringence of the KTP crystal, the group velocities $v_g(\lambda_2^{(+)})$ and $v_g(\lambda_3^{(-)})$ take two different values. The repetition rate f of the laser source being fixed, Equation (3.46) implies that the cavity length L_{cav} also has to take two different values for the two waves at $\lambda_2^{(+)}$ and $\lambda_3^{(-)}$. In particular, with a 30 mm-long KTP crystal and a $f = 80\text{MHz}$ laser source, $L_{\text{cav}}(\lambda_2^{(-)}) = 3.711\text{m}$ and $L_{\text{cav}}(\lambda_3^{(+)}) = 3.707\text{m}$. This 4mm difference for the two resonating waves needs to be compensated so that it does not increase at each cavity round-trip. For this purpose, we can think for instance of adding a delay line that would act on

the $\lambda_2^{(-)}$ wave only thanks to two Glan-Taylor prisms and a prism (see Figure 3.27); or of using another crystal such that $n(\lambda_2^{(-)}) > n(\lambda_3^{(+)})$ so as to slow down the $\lambda_2^{(-)}$ wave.

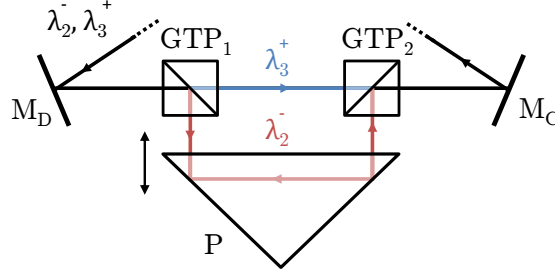


Figure 3.27 – Compensation of the group velocity difference between the resonating waves at $\lambda_2^{(-)}$ and $\lambda_3^{(+)}$ (not to scale).

Temporal field evolution The evolution of the fields in the cavity can be calculated by taking into account the nonlinear evolution given by the set of Equations (1.52) and a damping term linked to the photon lifetime in the cavity, as it is done in the case of quadratic OPOs [174, 175]. In the classical framework, at perfect phase-matching and for monochromatic fields, the temporal field evolutions write as:

$$\begin{cases} \tau_{\text{cav}} \frac{\partial \underline{E}_0(\omega_0)}{\partial t} = j\kappa(\omega_0) \chi_{\text{eff}}^{(3)}(\omega_0, \omega_1, \omega_2) L_{\text{cav}} \underline{E}_1(\omega_1) \underline{E}_2(\omega_2) \underline{E}_3(\omega_3) \\ \tau_{\text{cav}} \frac{\partial \underline{E}_1(\omega_1)}{\partial t} = j\kappa(\omega_1) \chi_{\text{eff}}^{(3)}(\omega_0, \omega_1, \omega_2) L_{\text{cav}} \underline{E}_0(\omega_0) \underline{E}_2^*(\omega_2) \underline{E}_3^*(\omega_3) \\ \tau_{\text{cav}} \frac{\partial \underline{E}_2(\omega_2)}{\partial t} = -\mathcal{T}(\omega_2) \underline{E}_2(\omega_2) + j\kappa(\omega_2) \chi_{\text{eff}}^{(3)}(\omega_0, \omega_1, \omega_2) L_{\text{cav}} \underline{E}_0(\omega_0) \underline{E}_1^*(\omega_1) \underline{E}_3^*(\omega_3) \\ \tau_{\text{cav}} \frac{\partial \underline{E}_3(\omega_3)}{\partial t} = -\mathcal{T}(\omega_3) \underline{E}_3(\omega_3) + j\kappa(\omega_3) \chi_{\text{eff}}^{(3)}(\omega_0, \omega_1, \omega_2) L_{\text{cav}} \underline{E}_0(\omega_0) \underline{E}_1^*(\omega_1) \underline{E}_2^*(\omega_2), \end{cases} \quad (3.47)$$

with κ , $\chi_{\text{eff}}^{(3)}$ and $\Delta k^{(3)}$ from Equations (1.48), (1.53) and (1.54) respectively. \mathcal{T} is the product of the transmission coefficients in amplitude of the mirror A, B, C and D; τ_{cav} the duration of a round-trip, *i.e.* the inverse of the laser repetition rate f ; and L_{cav} the length of the cavity, given by using Equation (3.46).

Threshold intensities The threshold condition is relative to the incoming intensities of the two incoming beams: $I_1^{\text{th}}(\omega_1)$ and $I_1^{\text{th}}(\omega_0)$. The detail of this calculation can be found in Appendix C. It leads to:

$$I_0^{\text{th}}(\omega_0, 0) I_1^{\text{th}}(\omega_1, 0) = \frac{\varepsilon_0^2 c^2 n(\omega_0) n(\omega_1)}{4 [\chi_{\text{eff}}^{(3)}]^2} \times \left| \frac{\tau_{\text{cav}} \ln p(\omega_{2,3}) (\kappa(\omega_2^+) + \kappa(\omega_3^-))}{2\tau_L L_{\text{cav}} \kappa(\omega_2^+) \kappa(\omega_3^-)} \right| \quad (3.48)$$

$$- \sqrt{\left(\frac{\tau_{\text{cav}} \ln p(\omega_{2,3}) (\kappa(\omega_2^+) - \kappa(\omega_3^-))}{2\tau_L L_{\text{cav}} \kappa(\omega_2^+) \kappa(\omega_3^-)} \right)^2 + \frac{1}{\kappa(\omega_2^+) \kappa(\omega_3^-)} \left(\frac{\mathcal{T}(\omega_{2,3})}{L_{\text{cav}}} \right)^2}.$$

τ_L is the travelling time in the crystal. Note that the crystal length comes into this equation through τ_L according to Equation (3.46). p stands for the losses expressed as :

$$p(\omega_i) = \sqrt{(T_F(\omega_i))^4 R_A(\omega_i) R_B(\omega_i) R_C(\omega_i) R_D(\omega_i)} = \sqrt{(T_F(\omega_i))^4 R_A(\omega_i)}, \quad i \in \{2, 3\}, \quad (3.49)$$

with T_F the Fresnel transmission coefficient in energy, given by Equation (3.29), equal to unity in the case of an anti-reflecting (AR) coated crystal; and R_i the reflection coefficients in energy of the different mirrors. As we propose to use dichroic mirrors and AR coatings, $R_A(\omega_2) = R_A(\omega_3)$ and $T_F = 1$, and then $p(\omega_2) = p(\omega_3)$, which has indeed been considered for the derivation of the expression (3.48). We note that the threshold intensities I_0^{th} and I_1^{th} are equivalently intra- or extra-cavity expressions as $T_{A,B}(\lambda_{0,1}) = 1$.

In our case, it is reasonable to assume that $\kappa_2 = \kappa_3$ because the birefringence $n^{(+)} - n^{(-)}$ at $\lambda_2 = \lambda_3$ is small. Then, Equation (3.48) reduces to:

$$\begin{aligned} I_0^{\text{th}}(\omega_0, 0) I_1^{\text{th}}(\omega_1, 0) &= \frac{\varepsilon_0^2 c^2}{4\pi^2} n(\omega_0) n(\omega_1) [n_{2,3}(\omega_{2,3}) \lambda_{2,3}]^2 \frac{1}{[\chi_{\text{eff}}^{(3)} L_{\text{cav}}]^2} \\ &\times \left| \frac{\tau_{\text{cav}} \ln p(\omega_{2,3})}{\tau_L} - \mathcal{T}(\omega_{2,3}) \right|^2. \end{aligned} \quad (3.50)$$

In the numerical calculation presented in Figure 3.28, very low transmission coefficients are considered, *i.e.* $T_A(\lambda_{2,3}) = 1\text{ or }2\%$, because of the low incoming intensities. We note that setting the damping term $[-\mathcal{T}(\omega_i) \underline{E}_i(\omega_i)]$ to zero leads to threshold intensities different from less than one order of magnitude, which is not surprising according to the values of the transmission coefficients.

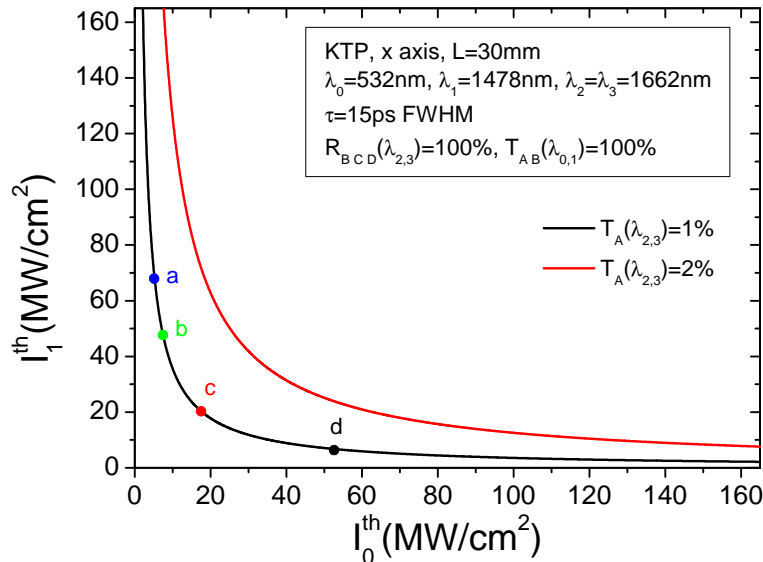


Figure 3.28 – TPG threshold intensities in the case of a DROPO monoinjected at λ_1 based on a 30 mm-long KTP crystal. Dots a, b, c and d correspond to different situations that will be considered later on in Figures 3.29 and 3.30.

OPO efficiency The calculation of the triplets number generated through this process is derived from the coupled equations (3.47). The solutions are obtained by solving an integral form that requires that more than three initial fields are non-zero to be convergent [33]. If so, the solutions are expressed in terms of Jacobi elliptical functions, but this is not the case here.

A numerical resolution becomes then obvious, iterated for each cavity round-trip. We propose to proceed in two steps. The first one is motivated by the fact that the coupled equations cannot start from zero photon fields. Only a quantum approach can describe the starting of the down-conversion as it takes into consideration the solicitation of the vacuum point energy. Therefore, Equations (2.9) derived from our quantum resolution and adapted to the case of a mono-stimulated configuration are processed numerically as long as the undepleted pump approximation still stands, as it has been the framework of our quantum derivation. In a second step, the computation of the classical equations (3.47) takes over. The field evolution in the crystal is calculated proceeding small slice by small slice, with a temporal step of 0.1 ps, so as the convergence is ensured.

The energies $\mathcal{E}_{2,3}$ corresponding to the triple photons in the modes 2 and 3 that can be generated in a 30 mm KTP crystal above threshold are calculated for different running points regarding the threshold intensities $\{I_0^{\text{th}}, I_1^{\text{th}}\}$ in the case of a transmission coefficient $T_A(\lambda_{2,3}) = 1\%$. In that case, the photon lifetime in the cavity is 125 ns, which corresponds to 100 return trips.

Due to optical damage threshold considerations, high repetition rate laser sources supply small powers, typically 40 W in average power, equivalently 500 nJ in energy for a 80 MHz repetition rate. We intend to use that kind of laser source for the TPG DROPO pump at λ_0 , and also for pumping a quadratic OPO that will be devoted to the generation at λ_1 . Due to the typical efficiency of quadratic OPOs, we can expect no more than 100 nJ for the injection beam at λ_1 .

The energetical curves are given in Figures 3.29 and 3.30 in the energy range targeted, with respect to the injection energy \mathcal{E}_1 or the pump energy \mathcal{E}_0 respectively, and for different pump (resp. injection) levels. They indicate that tens of nJ can be generated for hundreds of nJ of pump and tens of nJ of injection photons. For example, an energy of $\mathcal{E}_{2,3} = 40$ nJ per pulse and per field is generated for $\mathcal{E}_0 = 0.3$ μJ and $\mathcal{E}_1 = 30$ nJ per pulse. This is significantly greater than in the case of a mono-injected travelling wave TPG in KTP, where typically 4.1×10^{-6} triplets per pulse (equivalently 5.0×10^{-25} J) arise for the same number of incident photons, according to the quantum model.

Figure 3.29 shows that the generated energy decreases above a given injection energy. It is especially clear on the curve (d), where the maximum of generation, *i.e.* $\mathcal{E}_{2,3} = 19.7$ nJ, occurs for $\mathcal{E}_1 = 22$ nJ. Above this maximum, the pump field starts to be depleted, and consequently triplet photons are converted back into photons in the field 0. The pump depletion can indeed be clearly seen on Figure 3.31 that pictures the mode 0 energy as the function of the injection energy.

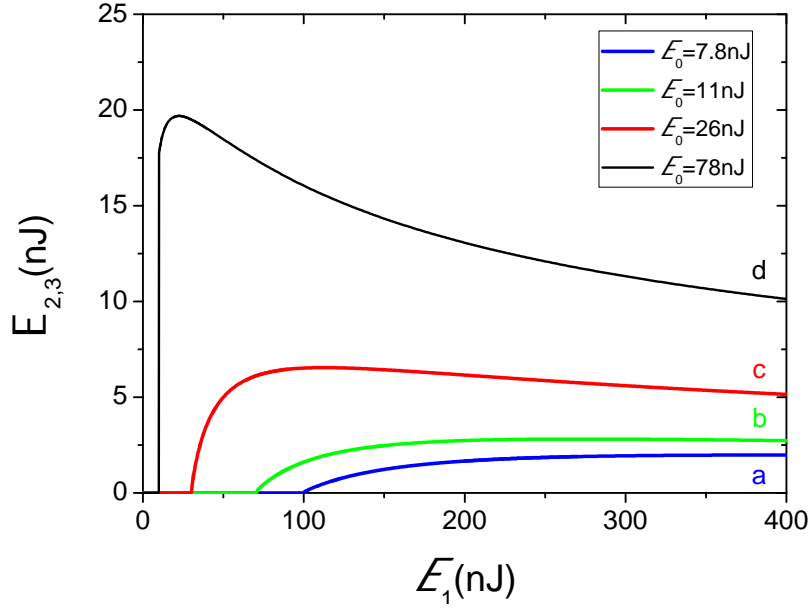


Figure 3.29 – Generated triplet energy as a function of the injection energy for a DROPO based on a 30 mm-long KTP crystal, and $T_A = 1\%$. The four curves a, b, c and d refer to four particular initial pump energies: (a) 7.8 nJ, (b) 11.1 nJ, (c) 25.8 nJ and (d) 77.6 nJ. The same letter code has been adopted for the threshold values shown in Figure 3.28.

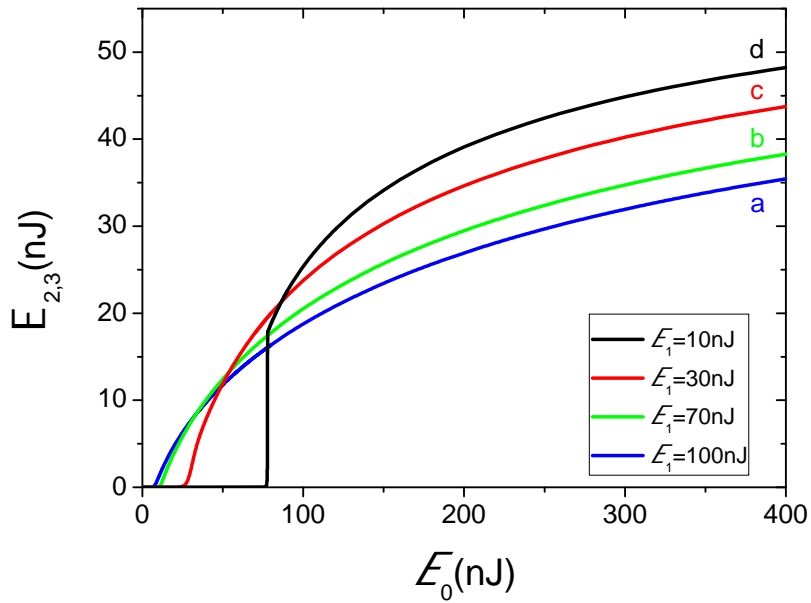


Figure 3.30 – Generated triplet energy as a function of the pump energy for a DROPO based on a 30 mm-long KTP crystal, and $T_A = 1\%$. The four curves a, b, c and d refer to four particular initial stimulation energies: (a) 100 nJ, (b) 70 nJ, (c) 30 nJ and (d) 10 nJ. The same letter code has been adopted for the threshold values shown in Figure 3.28.

The same kind of comment follows when looking at Figure 3.30.

Note that the maximum of generation does not necessarily occur for a maximum of pump and stimulation photons because it also depends on the transmission coefficient T_A . Figure 3.32 presents the generated energy $\mathcal{E}_{2,3}$ as a function of the stimulation energy \mathcal{E}_1 for different trans-

mission coefficients T_A , and for a pump energy $\mathcal{E}_0 = 26$ nJ. When working with small incident energies, one has to consider a weak transmission coefficient T_A to maximize the generation or even go beyond the threshold. If larger energies are accessible, it then becomes interesting to increase T_A .

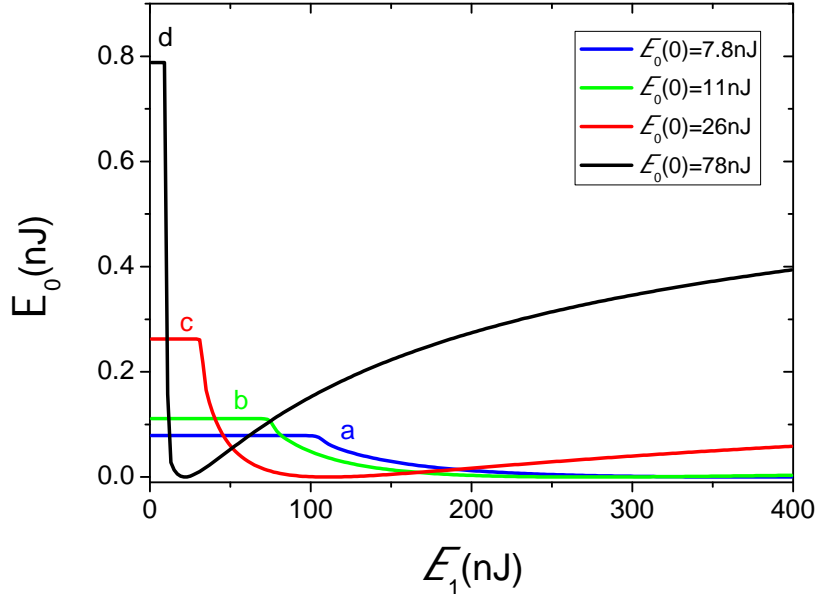


Figure 3.31 – Energy at λ_0 as a function of the injection energy for a DROPO based on a 30 mm-long KTP crystal, and $T_A = 1\%$. The four curves a, b, c and d refer to four particular initial pump energies: (a) 7.8 nJ , (b) 11.1 nJ, (c) 25.8 nJ and (d) 77.6 nJ.

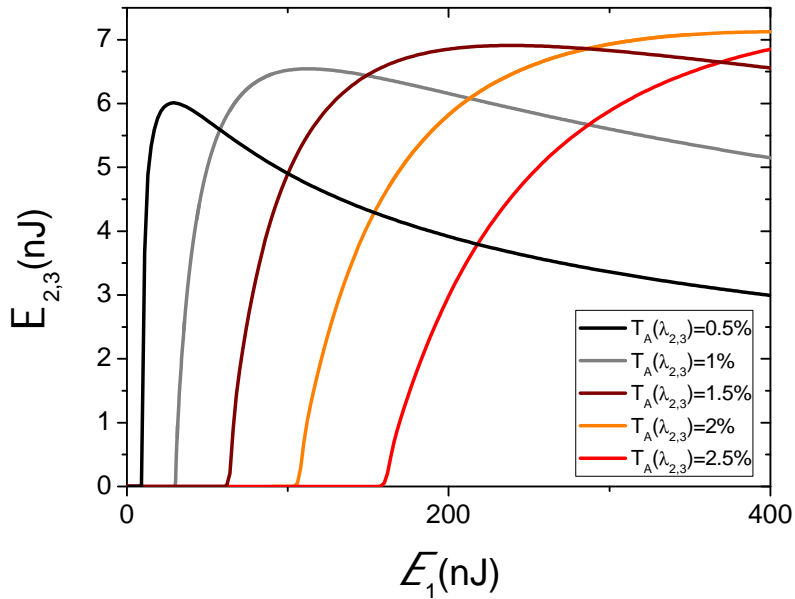


Figure 3.32 – Generated triplet energy as a function of the injection energy for a DROPO based on 30 mm-long KTP crystal, and different transmission coefficients T_A for the coupling mirror M_A . The pump energy is $\mathcal{E}_0 = 26$ nJ.

2. Total degeneracy in frequency, partial in polarization The set of wavelengths $\lambda_0^{(-)} = 532\text{nm}$, and $\lambda_{1,3}^{(+)} = \lambda_2^{(-)} = 1596\text{nm}$, phase-matched in a KTP crystal for $\theta = 90^\circ$ and $\varphi = 24.5^\circ$, can be used as well for a DROPO configuration. In that case, the cavity geometry has to be modified as sketched in Figure 3.33: mirrors M_A and M_B have to be replaced by Glan-Taylor prisms GTP_A and GTP_B , with $T_{A,B}(-) = 100\% = 1 - T_{A,B}(+)$; and the mirror M_D are partially reflecting with $T_D(\lambda_{0,2}^{(-)}) = 1$ or 2% . The OPO is still mono-injected, here at $\lambda_2^{(-)}$, and resonant at $\lambda_1^{(+)}$ and $\lambda_3^{(+)}$. Its performance and threshold intensities are very close to the ones discussed previously, the only modifications arising from the optical indices and the effective coefficient. The crystal critical length due to the group velocities dispersion is $L_c = 56\text{mm}$.

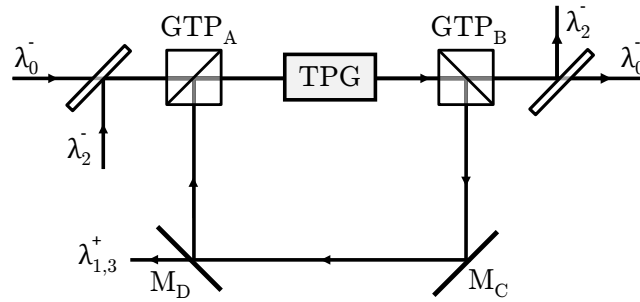


Figure 3.33 – Schematic of a frequency degenerated mono-injected third-order DROPO.

Rutile TiO_2 can also be quite interesting for that configuration. According to Section 3.2, it is for instance phase-matched at $\lambda_0^{(-)} = 612\text{nm}$ and $\lambda_{1,3}^{(+)} = \lambda_2^{(-)} = 1836\text{nm}$ along the x -axis of the crystal, *i.e.* without any spatial walk-off. In that case, the temporal walk-off leads to a critical length of $L_c = 19\text{mm}$. The nonlinear susceptibility is however bigger than that of KTP. For comparison, an energy of $\mathcal{E}_{2,3} = 43\text{ nJ}$ per pulse and per field could be generated in rutile for $L = 19\text{mm} < L_c$ and $T_A = 1\%$ when $\mathcal{E}_0 = 0.3\text{ μJ}$ and $\mathcal{E}_1 = 30\text{ nJ}$ per pulse.

3.3.2.2 TROPO

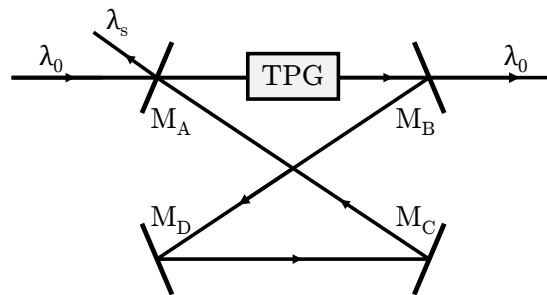


Figure 3.34 – Schematic of a fully degenerated third-order TROPO.

1. Total degeneracy in frequency and polarization The case where all the triplet photon frequencies and polarizations are identical, *i.e.* $\lambda_0^{(-)} = 532\text{nm}$, $\lambda_s^{(+)} = \lambda_{1,2,3}^{(+)} = 1596\text{nm}$ for KTP, and where there is injection at λ_s corresponds to a TPG injected on the three modes of the triplet (see Figure 3.34). We mention it here briefly because it is not particularly interesting for two

main reasons. First, the effective susceptibility is low for KTP as well as for TiO₂. In addition, the threshold intensities are quite high, as we show straight after.

The threshold condition relative to the intracavity intensities derived in Appendix C is written:

$$I_0^{\text{th}}(\omega_0, 0) I_s^{\text{th}}(\omega_s, 0) = \frac{1}{4\pi^2 \varepsilon_0^2 c^2 n(\omega_0) n^3(\omega_s)} \left(\frac{\lambda_s}{\chi_{\text{eff}}^{(3)}(\omega_0, \omega_s, \omega_s) L} \right)^2 \times \left(1 - (T_F(\omega_s))^2 \sqrt{(1 - T_A(\omega_s))(1 - T_B(\omega_s))} \right)^2, \quad (3.51)$$

with the same notations as previously. This derivation does not take into account the damping term which makes the calculation tricky in that case. But we expect its influence to be weak since the transmission coefficient T_A considered is very small. Following Equation (3.51), the extra-cavity threshold condition is:

$$\left[I_0^{\text{th}}(\omega_0, 0) I_s^{\text{th}}(\omega_s, 0) \right]_{\text{extra}} = \frac{1}{T_A(\omega_s)} \left[I_0^{\text{th}}(\omega_0, 0) I_s^{\text{th}}(\omega_s, 0) \right]_{\text{intra}}, \quad (3.52)$$

as $T_A(\omega_0) = 1$. The numerical application for these extra-cavity threshold intensities is shown in Figure 3.35 for $T_A(\omega_s) = 0.1$ and 0.5%. We note that the intra-cavity intensities are indeed smaller than in the DROPO case, whereas extra-cavity threshold intensities happen to be actually higher.

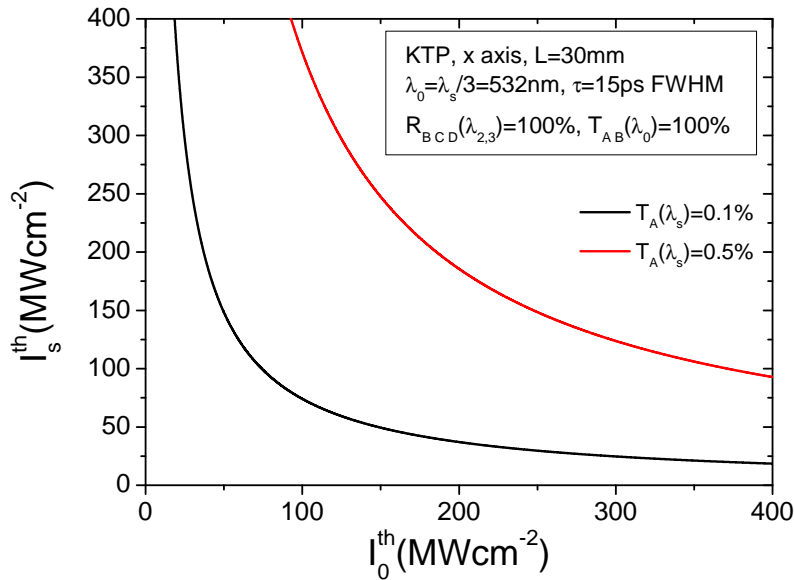


Figure 3.35 – Extra-cavity threshold intensities in the case of a frequency degenerated TROPO in a 30 mm-long KTP crystal for $T_A(\omega_s) = 0.1$ and 0.5%.

Very low transmission coefficients for the mirror A have been considered in order to obtain sensible threshold intensities that are still quite high compared to what a commercial source can provide. This configuration is then ruled out, in favour of either the previous scheme with polarization partial degeneracy and frequency total degeneracy or the next proposal.

2. Total degeneracy in frequency, partial in polarization: triggered configuration

The previous phase-matching wavelengths $\lambda_0^{(-)} = 532 \text{ nm}$, and $\lambda_s = \lambda_{1,3}^{(+)} = \lambda_2^{(-)} = 1596 \text{ nm}$ in a KTP crystal ($\theta = 90^\circ$, $\varphi = 24.5^\circ$) can again be used for another kind of TROPO configuration. It constitutes the last proposal of this section. The spirit of the present configuration is different from the previous ones, the goal being to work without any injection, *i.e.* to perform a spontaneous TPG. Due to the extreme weakness of this process in a bulk medium, as mentioned previously in Section 2.2.1.4, we propose here to take benefit of a cavity without loss for the three resonating waves at λ_s . However, the mirrors A and B are still taken as fully transparent to the pump, so that it is not recycled. Our idea is to accumulate triple photons generated at each round trip until the energy reaches an amount that is considered as sufficient for measurements. It is therefore a configuration of pulse extraction at the desired time. The extraction can for instance be triggered by an acousto-optic modulator in Bragg condition [34], as it is used in the case of mode-locked or Q-switched lasers. Briefly, an acoustic wave is created from the electric excitation of a piezoelectric oscillator stuck on one side of the modulator. Thanks to the photoelastic effect, this acoustic wave creates a periodic modulation of the refractive index that acts as a diffraction grating. The incident optical signal is then put into Bragg diffraction condition by adjusting the acoustic wavelength. At the first order of diffraction, it fulfills:

$$2\Lambda \sin \theta_B = \lambda_s, \quad (3.53)$$

where Λ is the grating period, *i.e.* the acoustic wavelength. The triplet signal is then diffracted and escapes the cavity as it is shown Figure 3.36.

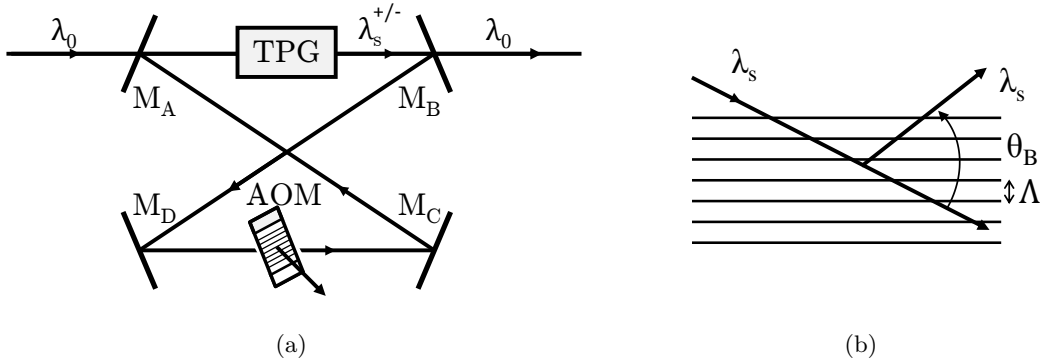


Figure 3.36 – (a) Schematic of the triggered configuration for the third-order TROPO. AOM stands for acousto-optic modulator. (b) Close-up representation of the Bragg diffraction.

There is no threshold in this configuration, since the cavity is lossless, excepted when the acousto-optic cell is activated¹. The number of photons generated over time can be calculated in the same fashion as the one described in Section 3.3.2.1: a quantum step in the undepleted pump regime for the initialization, then a classical step when the pump starts to be depleted. The result is presented in Figure 3.37. More than 10^6 round-trips are needed to build a μJ pulse using a 30 mm-long KTP crystal and a $1 \mu\text{J}$ initial pump energy. It means that 30 km of crystal

¹This is true in a first approximation only, since losses arise from absorption in the nonlinear medium (typically 1/1000 per centimeter) and AOM, from experimental reflexions on mirrors that do not strictly reach one, and from diffusion on the mirrors. These losses directly impact the coherence of the triplet fields generated.

length have been necessary! Note that here the photon lifetime is infinite before the trigger of the AOM. With a repetition rate of 80 MHz, about 13 ms are needed before the trigger of the acousto-optic modulator.

This configuration is experimentally more convenient in that it only requires a pump beam at $\lambda_0 = 532$ nm, which is available from a standard doubled Nd:YAG laser. Thereafter, it does not require the building of a quadratic OPO. This constitutes the reason why the energy of the pump considered here is slightly higher than in the previous calculations, since saved from one conversion stage.

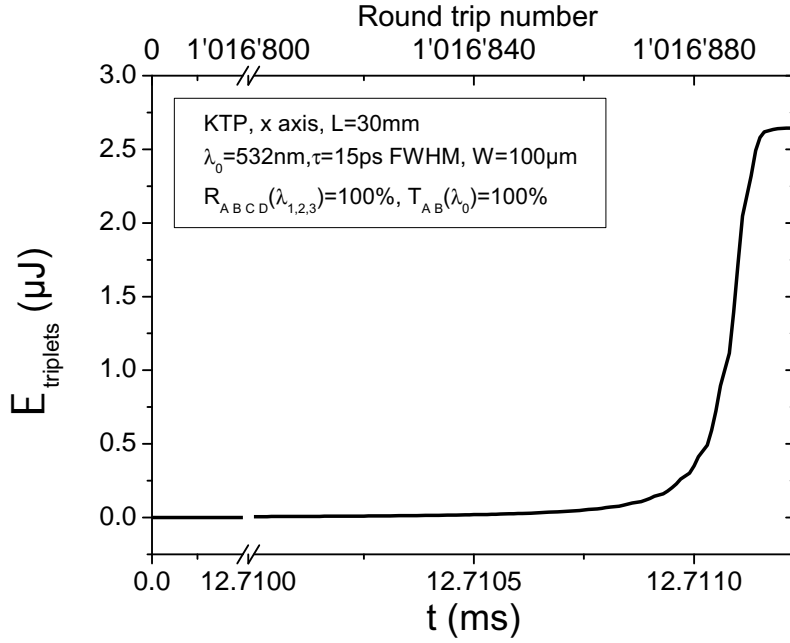


Figure 3.37 – Generated triplet energy as a function of time (or number of round-trips), for a propagation in a 30 mm-long KTP TROPO and an initial pump energy $\mathcal{E}_0 = 1$ μ J .

Note that rutile TiO_2 is again a good candidate for such a configuration, with $\lambda_0^{(-)} = 612$ nm and $\lambda_{1,3}^{(+)} = \lambda_2^{(-)} = 1836$ nm for instance.

3.3.3 Conclusion

To conclude this section, theoretical proposals of OPOs, synchronously pumped by a high repetition rate laser, have been studied with the aim of achieving direct TPG. Among them, two configurations stand out. The first one is doubly resonant and mono-injected: about $\mathcal{E}_{2,3} = 40$ nJ can be generated for $\mathcal{E}_0 = 300$ nJ of pump and $\mathcal{E}_1 = 30$ nJ of injection ($T_A = 1\%$). The second proposal is a triply resonant OPO that does not involve any injection. The cavity is truly lossless, until the pulse is extracted at the desired time by the operator: about 10^6 cavity round-trips enable to generate a μ J triplet pulse.

As for lasers and quadratic OPOs, the stability and resonance criteria are key points [27] that will have to be kept in mind for a potential future realization of an OPO considered for the experiments. This is also the case of the coherence properties of the triplet fields. These aspects have not been studied here.

Note finally that the Kerr effect has not been considered in this study of generation in a cavity either. Because of the large pump intensities involved, this effect is likely to occur and could be taken into account in the coupled equations. However, since on the one hand the pump intensity remains constant and on the other hand the increasing but weak triplet intensity do not contribute to this effect, the level of Kerr effect stays identical after each round trip in the cavity. Consequently, a shift of the pump wavelength can enable the experimentalist to compensate the deviation to the phase matching induced by this effect.

Third-harmonic generation and triple photon generation in optical fibers

“Quand les mystères sont très malins, ils se cachent dans la lumière.”

– Jean Giono, *Ennemonde et autres caractères*

Contents

4.1 THG and TPG in GeO_2 : SiO_2 optical fibers	108
4.1.1 Fiber properties	108
4.1.2 Interaction and phase matching	110
4.1.3 Fiber characterization through a THG experiment	114
4.1.4 Spontaneous TPG	145
4.1.5 Conclusion	153
4.2 Phase-matching properties of chalcogenide fibers	155
4.2.1 Chalcogenides photonic-crystal fibers	155
4.2.2 Phase-matching condition and fiber design	161
4.2.3 Conclusion	166

In this chapter, we expose third-harmonic and triple photon generations in optical fibers. In such media, one can take advantage of the interaction length as well as of a strong confinement of the electromagnetic field, without any pollution by quadratic processes since the fibers are glasses, hence centrosymmetric. The first part focuses on germanium-doped silica fibers, while the second part is dedicated to chalcogenide fibers.

4.1 THG and TPG in $\text{GeO}_2 : \text{SiO}_2$ optical fibers

We aim at realizing a TPG interaction fully degenerated in energy, *i.e.* $3\omega \rightarrow \omega + \omega + \omega$. For the experimental demonstration of such a process, we can benefit from a good understanding of what occurs in the fiber during a THG interaction, $\omega + \omega + \omega \rightarrow 3\omega$. Indeed, THG being TPG exact reverse process, the phase-matching conditions remain unchanged. But the conversion efficiency of THG is much larger than that of TPG, so that it is relevant to consider THG experiments in the first place.

4.1.1 Fiber properties

Geometry We use two multimode GeO_2 -doped SiO_2 fibers, whose core rods have been fabricated by plasma chemical vapor deposition by the Draka Comteq company. Their core radii are $a = 2.19 \mu\text{m}$ and $a = 2.30 \mu\text{m}$, their cladding radius $b = 125 \mu\text{m}$, and their maximum GeO_2 molar doping concentration $c_{\text{GeO}_2} = 37\%$ at the center of the fiber. The effective molar doping concentration in the core is $c_{\text{GeO}_2}^{\text{eff}} = 28.2\%$, inferred from averaging the parabolic index profile of the preform given in Figure 4.1 at $\lambda = 632 \text{ nm}$.

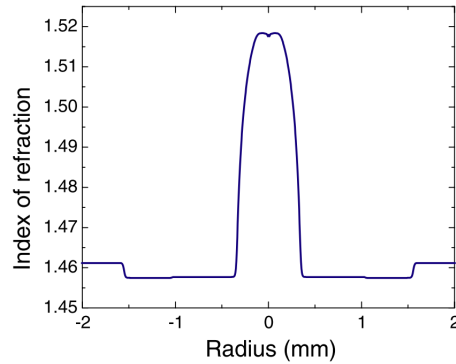


Figure 4.1 – Profile of the refractive index as a function of the radius of the preform, from [110].

Effective indices of the waves The effective Sellmeier dispersion equations have been extrapolated from effective indices measurements in two modal configurations LP_{01} around 1500 nm , and LP_{03} around 500 nm , in five specific cases where the core size equals $a = 2.20 + k \times 0.05 \mu\text{m}$, with $k \in \llbracket 0, 4 \rrbracket$. The approximation of the weakly guiding fiber is accurate, and allows us to consider the LP transverse modes developed in Chapter 1. The corresponding Sellmeier coefficients A, B, C and D are given in Table 4.1 for the following mathematical form of the effective indices n_{eff} :

$$n_{\text{eff}}^2(\lambda) = A + \frac{B}{\lambda^2 - C} + D\lambda^2, \quad (4.1)$$

where λ is expressed in micrometers.

The consideration of the LP_{01} and LP_{03} modes is justified below, in Section 4.1.2.

Cladding optical index The refractive index for the silica cladding n_{cl} follows a Sellmeier equation given by [176, 177]:

core radius	A	B	C	D
$a = 2.20 \mu\text{m}$	2.18122 2.06945	0.19313 0.0519	-1.68851 -0.08842	-0.01715 -0.10619
$a = 2.25 \mu\text{m}$	2.18551 2.09472	0.18227 0.04429	-1.64933 -0.07288	-0.01725 -0.12773
$a = 2.30 \mu\text{m}$	2.18973 1.99386	0.17126 0.09019	-1.60328 -0.16707	-0.01735 -0.0266
$a = 2.35 \mu\text{m}$	2.19359 2.12877	0.16149 0.0351	-1.56118 -0.05165	-0.01743 -0.15316
$a = 2.40 \mu\text{m}$	2.19727 2.14082	0.15213 0.03216	-1.51719 -0.04412	-0.01749 -0.16042

Table 4.1 – Sellmeier coefficients A , B , C and D from Equation (4.1) for different core sizes and the two modal distributions LP₀₁ (upper value, in black) and LP₀₃ (lower value, in blue). λ needs to be expressed in micrometers in Equation (4.1).

coefficient	value
A_1	0.6961663
l_1	0.06840430
A_2	0.4079426
l_2	0.1162414
A_3	0.8974794
l_3	9.896161

Table 4.2 – Sellmeier coefficients of silica [176, 177]. The wavelength is expressed in micrometers in Equation (4.2).

$$n_{\text{cl}}^2(\lambda) = 1 + \sum_{i=1}^3 \frac{A_i \lambda^2}{\lambda^2 - l_i^2}, \quad (4.2)$$

with A_i and l_i the coefficients given in Table 4.2, and λ expressed in micrometers.

The maximum index difference between the cladding and the core is approximately $\Delta n \simeq 0.06$ in the visible/near IR spectral range. The numerical aperture defined in Equation (1.76) therefore equals 0.32 for the fundamental wavelength, and 0.27 for the generated one, in the case of $a = 2.19 \mu\text{m}$.

Nonlinearity The effective nonlinear susceptibility is taken as $\chi_{\text{eff}}^{(3)} = 1.9 \times 10^{-22} \text{ m}^2 \text{V}^{-2}$ in the telecom bandwidth in which we aim to work, *i.e.* around 1550 nm. This approximate value originates from the phenomenological relationship given in the reference [178]: $n_2(\text{m}^2 \text{W}^{-1} \times 10^{-20}) = 0.0552 \times c_{\text{GeO}_2}^{\text{eff}} + 2.44 = 2.46$. It is consistent with n_2 values ranging between 2.20 and $2.73 \times 10^{-20} \text{ m}^2 \text{W}^{-1}$ for standard fibers around 1550 nm [30].

Losses The typical attenuation of silica fibers is around 0.2 dB/km at 1.5 μm , and increases to a few dB/km in the visible spectral range [30].

4.1.2 Interaction and phase matching

Phase-matching condition As stressed in the first chapter, modal phase-matching is considered here as fibers exhibit no birefringence in principle. Even when they do, their birefringences range between 10^{-4} and 10^{-6} , so that it is difficult to use them to compensate the refractive index dispersion to achieve a phase matching [30].

The fibers we used are designed to enable modal phase-matching involving LP_{01} and LP_{03} transverse modes for THG or degenerated TPG, *i.e.*:

$$3\omega_{\text{LP}_{03}} \leftrightarrow \omega_{\text{LP}_{01}} + \omega_{\text{LP}_{01}} + \omega_{\text{LP}_{01}}. \quad (4.3)$$

At first, the phase-matching wavelengths are inferred from the following phase-matching condition in the case where the “nonlinear” contribution presented in Section 1.3.3 is neglected, which is true for small enough input intensities:

$$n_{\text{eff}}^{01}(\omega) = n_{\text{eff}}^{03}(3\omega). \quad (4.4)$$

Figure 4.2 shows these effective indices, $n_{\text{eff}}^{01}(\omega)$ and $n_{\text{eff}}^{03}(3\omega)$, as a function of the third-harmonic wavelength in the case of a fiber core size of $a = 2.20 \mu\text{m}$. Their intersection gives the phase-matching wavelength, in compliance with Equation (4.4).

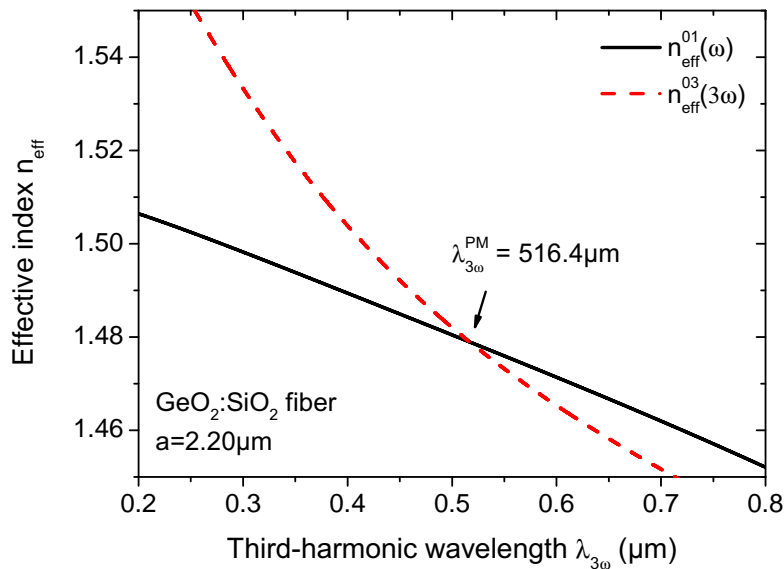


Figure 4.2 – Phase-matching condition with a $\text{SiO}_2 : \text{GeO}_2$ fiber of core radius $a = 2.20 \mu\text{m}$.

The same study performed for the four other core radii gives the phase-matching wavelengths presented as black dots in Figure 4.3. An extrapolation of these data allows to infer the phase-matching wavelengths for this modal configuration at any value of a , in particular $a = 2.19 \mu\text{m}$ for our fiber. The interpolated line also shown in Figure 4.3 follows the law:

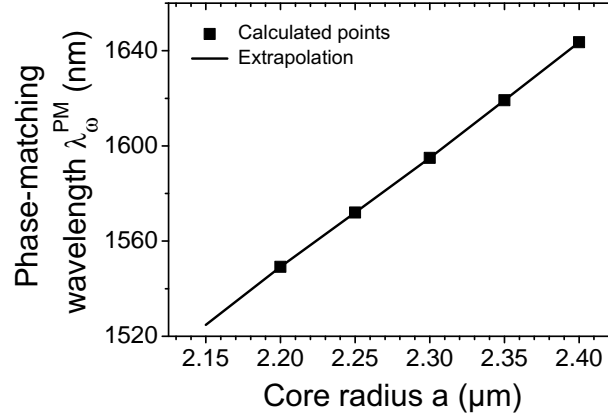


Figure 4.3 – Calculated fundamental phase-matching wavelength λ_ω (squares) as a function of the fiber core radius from experimental measurements of the effective indices in squares. The interpolation is in solid line.

core radius/ fundamental wavelength	$\tau = 15$ ps	$\tau = 10$ ns
$a = 2.2 \mu\text{m}$ $\lambda_\omega = 1548.5 \mu\text{m}$	9.6 cm	64.1 m
$a = 2.3 \mu\text{m}$ $\lambda_\omega = 1595.7 \mu\text{m}$	10.4 cm	69.2 m

Table 4.3 – Critical fiber lengths related to the temporal walk-off for the two available fibers and sources.

$$\lambda_\omega^{\text{PM}} [\text{nm}] = 510.232 + 471.972a [\mu\text{m}]. \quad (4.5)$$

Therefore, $\lambda_\omega^{\text{PM}}(a = 2.19 \mu\text{m}) = 1544 \text{ nm}$ and $\lambda_\omega^{\text{PM}}(a = 2.30 \mu\text{m}) = 1596 \text{ nm}$ are the fundamental phase-matching wavelengths for our two types of fiber.

The core radius uncertainty is estimated by the fiber supplier as $\Delta a = 6.4 \text{ nm}$, which leads to an uncertainty of $\Delta \lambda_\omega^{\text{PM}} = 3 \text{ nm}$ on the predicted phase-matching wavelength according to Figure 4.3.

Temporal walk-off The temporal walk-off between the fundamental and third-harmonic beams dictates the choice for the pulse duration of the source. As in the previous chapter, the corresponding critical length L_c gives the distance at which the temporal pulses are separated from each other by their temporal FWHM. It is given by:

$$L_c = \frac{\tau}{v_g^{-1}(3\omega) - v_g^{-1}(\omega)}, \quad (4.6)$$

where τ is the FWHM pulse duration and v_g the group velocities given in Equation (3.45). Different values of L_c are presented in Table 4.3 for the two fibers at their respective fundamental wavelengths and for the two pulse durations of the lasers available in the laboratory ($\tau = 15 \text{ ps}$ and $\tau = 10 \text{ ns}$).

It is clear from this table that the 15 ps source is ruled out since we want to use more than 10 cm of fiber to increase the conversion efficiency. On the contrary, the walk-off critical length is of the order of 65 m for the nanosecond laser, which allows us to use metric fibers without any limitation from the temporal overlap.

“Nonlinear” contribution to phase-matching We assumed so far that the “nonlinear” contributions to the phase-matching were small enough to be neglected. In the general case, self-phase modulations and cross-phase modulations have to be considered jointly to TPG, as they make the effective indices differ from the ones that have been considered up to now. Hence, we are coming back to this hypothesis and justify it for the range of pump energies that we used, up to about 1 μJ for a 10 ns pump duration and a 10 Hz repetition rate.

The effective nonlinear phase mismatch $\Delta k_{\text{eff}}^{(3)} = \Delta k_{\text{M+W}}^{(3)} + \Delta k_{\text{NL}}^{(3)}$ of Equation (1.105) is computed in the case of TPG¹. In that case, only the peak power of the pump is taken into account in $\Delta k_{\text{NL}}^{(3)}$, the powers of the triplet fields being insignificant. In other words, the phase modulation effects of the down-converted beams on themselves and of these beams on the pump can be neglected compared with the phase modulation of the pump on itself. The phase-matching wavelengths λ_i^{PM} from the previous section may be shifted by λ_i^{shift} when the “nonlinear” term is taken under consideration, such that:

$$\Delta k_{\text{eff}}^{(3)} \left(\lambda_{3\omega}^{\text{tot}} = \lambda_{3\omega}^{\text{PM}} \pm \lambda_{3\omega}^{\text{shift}}, \lambda_{\omega_1}^{\text{tot}} = \lambda_{\omega_1}^{\text{PM}} \pm \lambda_{\omega_1}^{\text{shift}}, \lambda_{\omega_2}^{\text{tot}} = \lambda_{\omega_2}^{\text{PM}} \pm \lambda_{\omega_2}^{\text{shift}} \right) = 0. \quad (4.7)$$

Note that the wavelengths λ_1 , λ_2 and λ_3 may be different from one another because of the spectral acceptance of the fiber.

Figures 4.4 give a two-dimensional representation of $\text{sinc}^2 \left(\frac{\Delta k_{\text{eff}}^{(3)} |^{\text{PM}} L}{2} \right)$ as a function of $\lambda_{\omega_1}^{\text{PM}}$ and $\lambda_{\omega_2}^{\text{PM}}$ for $L = 20$ cm (a) and $L = 1$ m (c), and $\mathcal{E}_{3\omega} = 1$ μJ . A value of 1 means perfect phase-matching. We see that although phase-matching is almost exactly fulfilled at the center of the spectral range in the case (a), *i.e.* for $\lambda_{\omega_1}^{\text{PM}} = \lambda_{\omega_2}^{\text{PM}} = \lambda_{\omega_3}^{\text{PM}} = \lambda_{3\omega}^{\text{PM}}/3$, it is obviously not the case in (c). A calculation of $\lambda_{\omega_{1,2,3}}^{\text{shift}} = 3\lambda_{3\omega}^{\text{shift}}$ is therefore performed to achieve a perfect phase-matching in both cases. It equals $\lambda_{\omega_{1,2,3}}^{\text{shift}} = 2.04$ pm for (a) and $\lambda_{\omega_{1,2,3}}^{\text{shift}} = 11.2$ pm for (c). The graphs (b) and (d) show $\text{sinc}^2 \left(\frac{\Delta k_{\text{eff}}^{(3)} |^{\text{tot}} L}{2} \right)$ as a function of $\lambda_{\omega_1}^{\text{tot}}$ and $\lambda_{\omega_2}^{\text{tot}}$ in the graphs (b) and (d) for the same experimental conditions as above.

It is clear that the frequency shifts relative to the triplet beams due to nonlinear phase effects occurring in the fiber will not be an issue as they are in the spectral bandwidth of our sources for metric fibers and our maximum pump energies (of the order of 1 μJ). Figure 4.5 gives the shifted wavelength $\lambda_{\omega}^{\text{shift}}$ as a function of the input pump energy for a 50 cm-long fiber.

¹In the case of a THG process, the expression of the nonlinear phase mismatch $\Delta k_{\text{NL}}^{(3)}$ has to be adapted by virtue of Equation (D.17), derived in Appendix D. It does not change the main conclusion here.

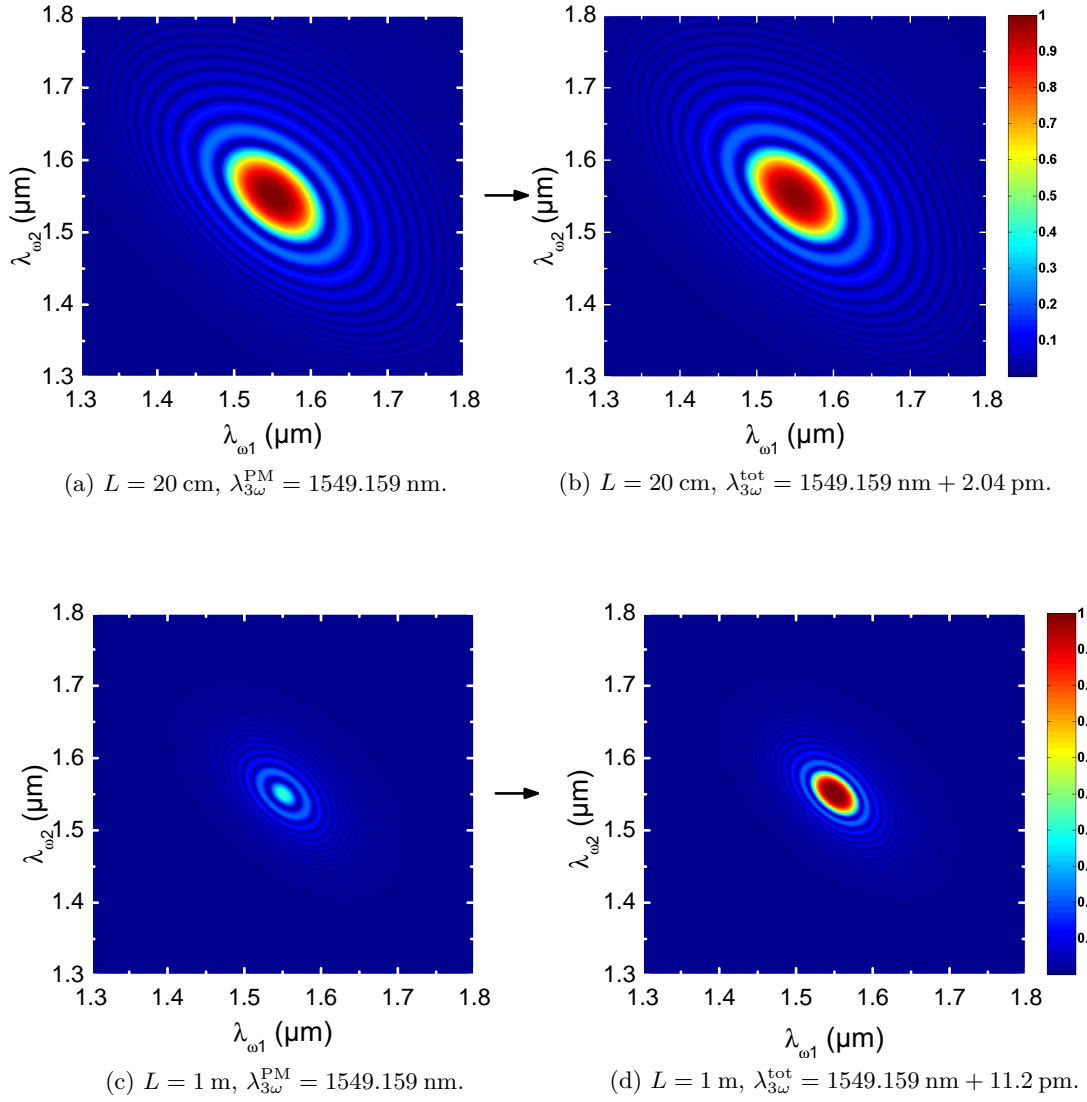


Figure 4.4 – $\text{sinc}^2 \left(\Delta k_{\text{eff}}^{(3)} (\lambda_{3\omega}, \lambda_{\omega_1}, \lambda_{\omega_2}) L/2 \right)$ as a function of two photon triplet wavelengths λ_{ω_1} and λ_{ω_2} for a core radius $a = 2.20 \mu\text{m}$. The pump beam is set at the phase-matching wavelength $\lambda_0 = 516.4 \mu\text{m}$ and its energy equals $1 \mu\text{J}$.

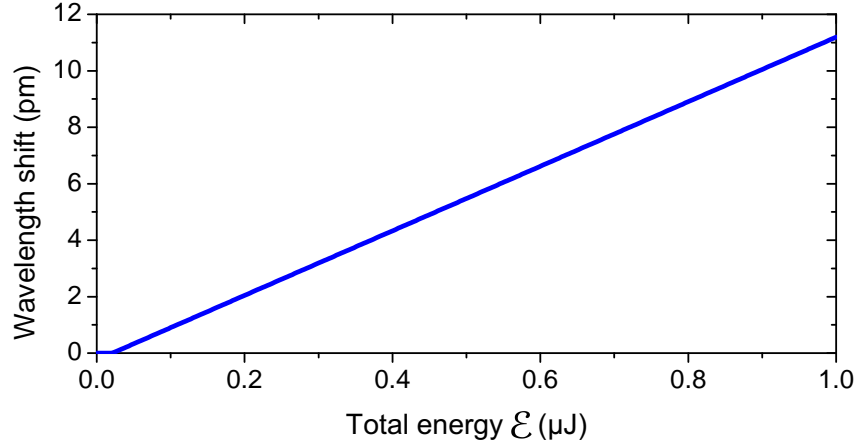


Figure 4.5 – Wavelength shift on the triplet fields to recover a perfect degenerate phase-matching, versus incident total energy ($L = 50$ cm).

4.1.3 Fiber characterization through a THG experiment

In this section, a THG involving the LP_{01} and LP_{03} modes is demonstrated experimentally. In addition, it is shown that other transverse mode configurations are also possible. Finally, interactions other than THG occurring in the fiber are also reported.

4.1.3.1 Experimental setup

The experimental setup is pictured in Figure 4.6. In the laboratory frame, the propagation axis is taken as the Z -axis, while the X - and Y -axis are arbitrarily chosen as the horizontal and vertical axes respectively.

A Nd:YAG laser source delivering 10ns pulses at a 10Hz repetition rate is tripled in frequency thanks to the combination of second-harmonic generation and sum-frequency generation in two KDP crystals. The resulting wave at 355nm is used to pump a quadratic BBO ($\beta\text{-BaB}_2\text{O}_4$) type I optical parametric oscillator that generates wavelengths from 0.41 and 2.4 μm . The spectral linewidth of the beam at 1.6 μm has been measured with a Chromex Optilas monochromator: it equals 4.9 nm (FWHM). Its divergence at 1 μm equals $\Theta_X = 20.9$ mrad and $\Theta_Y = 32.0$ mrad along the two transverse directions X and Y respectively. A telescope consisting of two spherical lenses of focal lengths 35 mm and 50 mm is then inserted right after the source to reduce these divergences.

The tunable beam is focused on the $\text{GeO}_2 : \text{SiO}_2$ fiber using an Olympus microscope objective of magnification $\times 40$ and numerical aperture 0.65. The fiber is cleaved with a diamond tip Corning cleaver, perpendicularly to the incident direction as shown in Figure 4.7. This cleaver has been kindly lent us by the “Nano-Optique et Forces” team at Institut Néel. It is placed on a Thorlabs Nanomax three-axes stage of step 1 μm . Note that the position of the focusing point behind the microscope objective according to the entrance of the fiber is very critical.

Because of the astigmatism of the OPO beam, two cylindrical lenses of focal lengths 200 mm (along X) and 130 mm (along Y) were used before the objective to improve the transverse geometry of the beam. It has indeed to match the circular transverse geometry of the fiber in

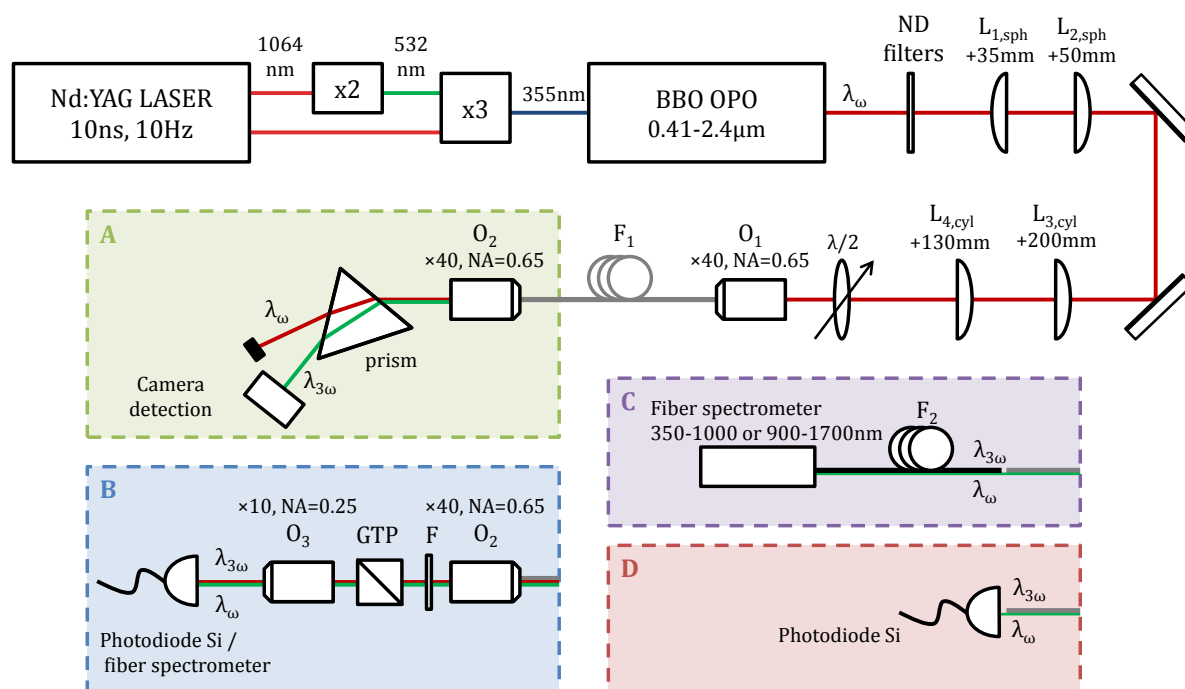


Figure 4.6 – Schematics of the experimental setup. ND stands for neutral density, L for lens, $\lambda/2$ for half-wave plate, O for microscope objective, F_i for fiber, F for dichroic filter and GTP for Glan-Taylor prism. The different units are used for specific measurements: A for mode imaging, B for polarization measurement, C for spectral properties, and D for conversion efficiency.

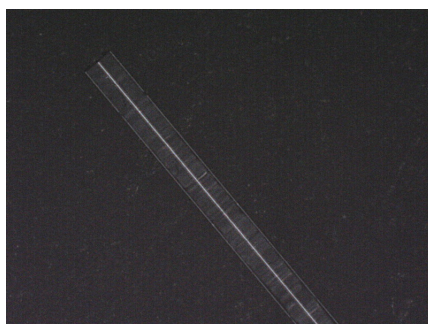


Figure 4.7 – Cleaved fiber under an optical microscope.

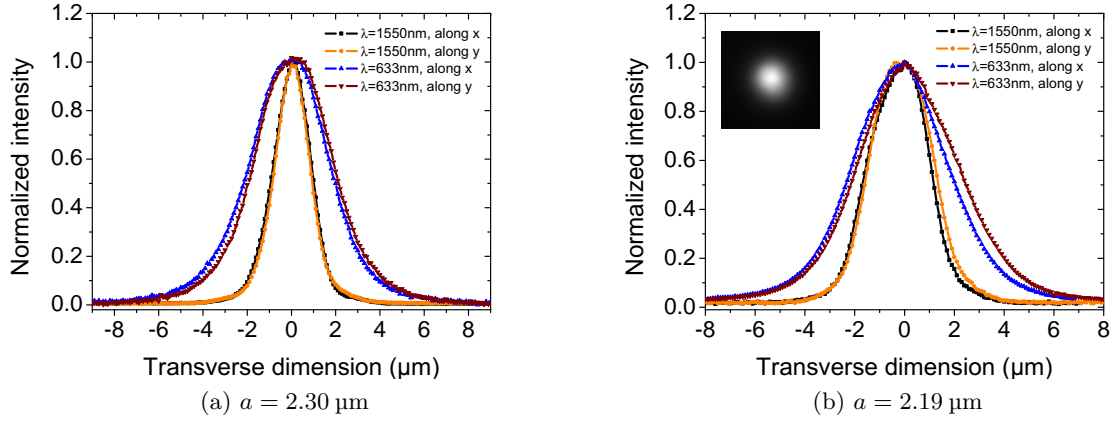


Figure 4.8 – Transverse spatial profile of the fundamental mode at the output of the fibers.

order to achieve a good coupling. Typical optimal coupling efficiencies are of the order of 10^{-3} , which extreme weak values may be explained by the poor transverse quality of the OPO. A half-wave plate in the 1100 – 2000 nm spectral range can also be inserted before the objective. Although it might seem useless since a fiber is an isotropic medium, we will show later that it is not.

The down-converted and residual input beams are collected at the output of the fiber in a second microscope objective similar to the input one. If needed, dichroic filters can be used to stop the pump beam. Alternatively, if no filter is needed, the end of the fiber can also be put very close to the detection system, the detection chip or detection fiber being bigger than the propagating mode.

The input powers are measured with Ophir PE10 and PE50 powermeters. At the output of the fiber, the fundamental and third-harmonic powers are measured using Thorlabs photodiodes calibrated with neutral density filters and the previous powermeters. These are DET410 InGaAs-based for $\lambda \in [700, 1800]$ nm and DET110 Si-based for $\lambda \in [350, 1100]$ nm. The spectral properties are measured with Ocean Optics spectrometers connected to a multimode fiber: RedTide USB650 for $\lambda \in [350 - 1000]$ nm with a resolution of 2 nm, or HR4000 for a resolution of 0.1 nm but less intensity sensitivity for $\lambda \in [200 - 1100]$ nm; and NirQuest512 for $\lambda \in [900, 1700]$ nm with a 3 nm resolution. These spectrometers can be calibrated in intensity with the photodiodes at any wavelength of interest. Finally, the imaging of the transverse modes is done using a basic color webcam, or a more sensitive monochrome Edmund Optics EO-0413M camera kindly lent us by Eric Mossang from Institut Néel. Figure 4.8 gives the transverse spatial profile of the beam going out of the two fibers considered, at two different wavelengths.

4.1.3.2 THG involving LP_{01} and LP_{03} modes

We report in this section the THG interaction between the LP_{01} and LP_{03} transverses modes. Modal, energetic, spectral and polarization properties are investigated.

1. Modal distribution The modal distribution of the third-harmonic field for the 2.19 μm core size fiber and the fundamental beam at $\lambda_\omega = 1544$ nm is observed using the configuration

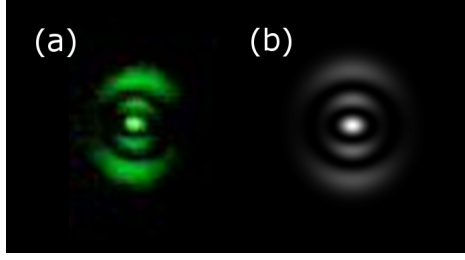


Figure 4.9 – Measured (a) and calculated (b) transverse intensity profile of the third-harmonic beam.

A pictured on the experimental setup of Figure 4.6. A prism separates the pump and generated beams, and a Microsoft LifeCam CCD camera images the transverse intensity profile as shown in Figure 4.9 (a). Compared to the LP₀₃ mode depicted in Figure 1.12c of the first chapter, this profile seems to be somewhat distorted, stretched out in the vertical direction.

In order to explain this behaviour, we intend to have a deeper look at the propagation equation given in (1.82) with the assumption that the fiber has an elliptic section. Under its scalar form:

$$\nabla^2 E(\vec{r}, t) - \frac{1}{c^2} \frac{\partial^2 E(\vec{r}, t)}{\partial t^2} = 0, \quad (4.8)$$

with ∇^2 the laplacian operator. For a plane wave $E(\vec{r}, t) = \underline{E}(\vec{r}) e^{i(kZ - \omega t)}$, it comes:

$$\left[\nabla_T^2 + \frac{\partial^2}{\partial Z^2} + 2ik \frac{\partial}{\partial Z} \right] \underline{E}(\vec{r}) = 0, \quad (4.9)$$

∇_T^2 being the transverse laplacian operator.

In the paraxial approximation that states that the field varies only gradually along the Z -axis, *i.e.* $\left| \frac{\partial^2 \underline{E}(\vec{r})}{\partial Z^2} \right| \ll \left| 2k \frac{\partial \underline{E}(\vec{r})}{\partial Z} \right|$, the equation becomes:

$$\left(\nabla_T^2 + 2ik \frac{\partial}{\partial Z} \right) \underline{E}(\vec{r}) = 0. \quad (4.10)$$

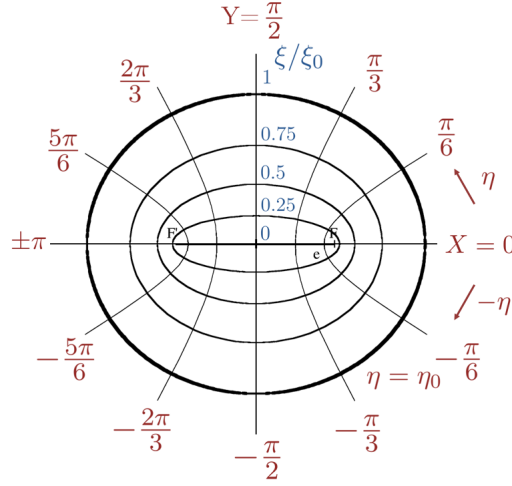
We now have to consider the transverse components in the elliptical coordinates (ξ, η) shown in Figure 4.10, with $(\xi, \eta) \in \mathbb{R}^+ \times [0, 2\pi]$. They are related to the cartesian coordinates (X, Y) through the relationships:

$$\begin{cases} X = f(Z) \cosh(\xi) \cos(\eta) \\ Y = f(Z) \sinh(\xi) \sin(\eta), \end{cases} \quad (4.11)$$

where $f(Z) = f(0) \frac{w(Z)}{w(0)}$ is the distance from the origin to a focal point of the ellipse; w the beam size given by Equation (1.32); and $Z = 0$ the entrance of the fiber. The ellipticity is defined as $\epsilon = \frac{2f^2(0)}{w^2(0)}$.

The paraxial wave equation is solved with the following variables separation:

$$\underline{E}(\xi, \eta, Z) = \Xi(\xi) N(\eta) e^{i\zeta(Z)} \psi_G(\xi, \eta, Z), \quad (4.12)$$


 Figure 4.10 – Elliptic cylindrical coordinates in the (ξ, η) plane.

where $\psi_G(\xi, \eta, Z) = \frac{w(0)}{w(Z)} \exp \left[\frac{-r^2}{w^2(Z)} + ikZ + \frac{ikr^2}{2R(Z)} - i \arctan \left(\frac{Z}{Z_R} \right) \right]$ is the lowest order solution, the Gaussian fundamental mode being given in Equations (1.30) and (1.31). The curvature radius is given by Equation (1.33), the Rayleigh length by (1.35), and $r = \sqrt{X^2 + Y^2} = f(Z) \sqrt{(\cosh(\xi) \cos(\eta))^2 + (\sinh(\xi) \sin(\eta))^2}$.

With two separation constants a and p , Equation (4.10) becomes [179, 180]:

$$\begin{cases} \frac{d^2 \Xi}{d\xi^2} - \epsilon \sinh(2\xi) \frac{d\Xi}{d\xi} - [a - p\epsilon \cosh(2\xi)] \Xi = 0 \\ \frac{d^2 N}{d\eta^2} - \epsilon \sin(2\eta) \frac{dN}{d\eta} + [a - p\epsilon \cos(2\eta)] N = 0 \\ - \left(\frac{Z^2 + z_R^2}{z_R} \right) \frac{d\zeta}{dZ} = p. \end{cases} \quad (4.13)$$

At this point, a simplification can be made as the Rayleigh distance equals $Z_R = \frac{\pi w(0)^2}{\lambda_{3\omega}} \simeq 24 \text{ m}$ at the output of our fiber, the beam radius being equal to 4 mm at 515 nm. It is therefore natural to consider $Z = 0$ everywhere in the fiber, which gives:

$$\underline{E}(\xi, \eta, Z) = \underline{E}(\xi, \eta, 0) = \Xi(\xi) N(\eta) e^{\frac{-r^2}{w^2(0)}}. \quad (4.14)$$

The solutions to the set of Equations (4.13) are written as C_{pm} and S_{pm} from Ince polynomials of order p and degree m . They are Ince-Gauss (IG) modes defined [179, 181] as:

$$\begin{cases} \text{IG}_{pm}^e(\xi, \eta, \epsilon) = \mathcal{C} C_{pm}(i\xi, \epsilon) C_{pm}(\eta, \epsilon) e^{-r^2/w^2(0)} & \text{even modes} \\ \text{IG}_{pm}^o(\xi, \eta, \epsilon) = \mathcal{S} S_{pm}(i\xi, \epsilon) S_{pm}(\eta, \epsilon) e^{-r^2/w^2(0)} & \text{odd modes} \end{cases} \quad (4.15)$$

The choice for p and m is restricted to $0 \leq m \leq p$ and $(-1)^{m+p} = 1$, *i.e.* m and p are both even (e case) or both odd (o case). The number of hyperbolic nodal lines is given by m , while the number of elliptical nodal lines by $(p - m)/2 + \delta_{k,o}$, where $k \in \{e, o\}$ and δ is the Kronecker symbol. \mathcal{C} and \mathcal{S} are normalization constants.

We are now able to give a representation in terms of Ince-Gauss modes of the third-harmonic

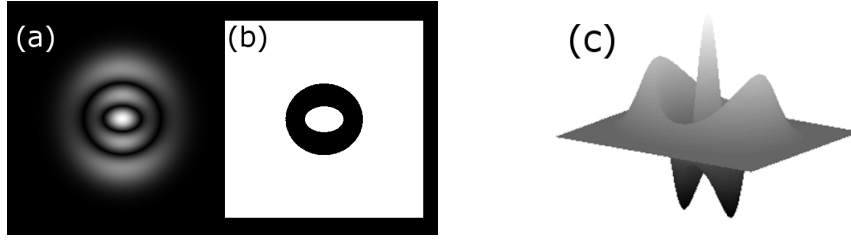


Figure 4.11 – Corresponding modulus (a) and phase (b) transverse profiles. The complex amplitude is shown in (c).

distribution that we observed: the calculated mode, IG_{40}^e , is depicted in Figure 4.9 (b), with an ellipticity of $\epsilon = 0.5$. This numerical calculation is in very nice agreement with the experimental mode, pointing out core ellipticity in our fibers. The effective interaction area will then be affected by this ellipticity.

Figure 4.11 shows calculations for the modulus (a), phase (b) and signed complex amplitude (c) of the IG_{40}^e mode.

We end up this section with several remarks.

- First of all, we point out that we get back to Laguerre-Gauss (LG) modes by setting the ellipticity to zero. We would end up with Hermite-Gauss (HG) modes by setting it to infinity, which is equivalent to considering a cartesian geometry.

$$\begin{cases} \epsilon \rightarrow 0 \text{ (towards a polar cylindrical geometry)} : & IG \rightarrow LG \text{ (Laguerre – Gauss modes)} \\ \epsilon \rightarrow +\infty \text{ (towards a cartesian geometry)} : & IG \rightarrow HG \text{ (Hermite – Gauss modes)} \end{cases}$$

In the case of our fibers with small core-cladding index difference, LG modes are equivalent to LP modes that we considered previously.

- Mathieu modes and elegant Ince-Gauss modes are also solutions to Equations (4.13) [182, 183]. However, they have not been taken into consideration here for the following reasons.

Considering Mathieu modes is mathematically equivalent to take $p \rightarrow \infty$ and $\epsilon \rightarrow 0$, such that $p \times \epsilon$ is a finite real number. This leads to an infinite extension of rings for amplitude and phase, which is not the behaviour observed here.

In addition to ellipticity, order and degree, all the modes mentionned here can be described by two gaussian complex parameters q_0 and \tilde{q}_0 at $Z = 0$. The elegant Ince-Gauss modes are mathematically described by $\tilde{q}_0 \rightarrow \infty$: in amplitude, only one elliptical nodal line is visible for all modes such that $(p - m)/2 + \delta_{k,o} > 1$. This is again not the behaviour of the third-harmonic mode shown in this section or of any other modes we observed and that are going to be exposed in Section 4.1.3.3. The spatial evolution of such modes greatly differs from the evolution of simple Ince-Gauss modes.

- One can define so-called helical Ince-Gauss modes (HIG) that we will use later. They are vortex modes carrying an azimuthal angular momentum [180], and take the form:

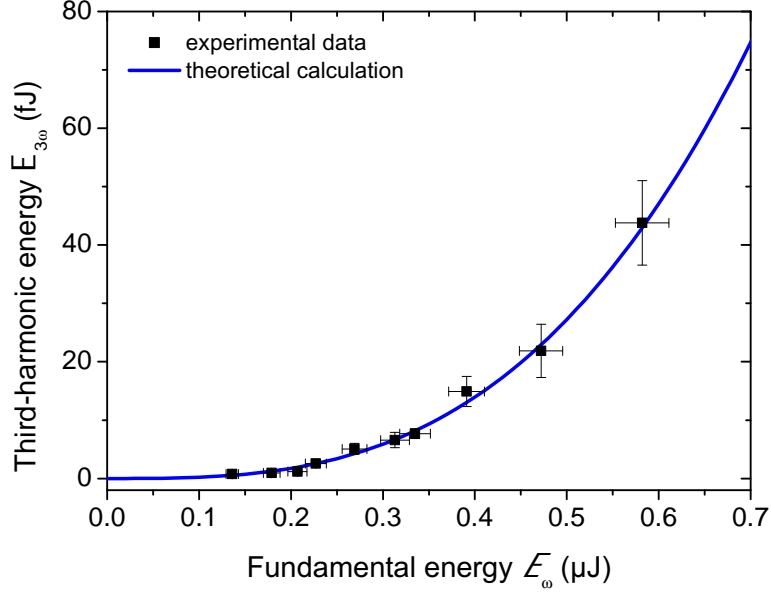


Figure 4.12 – Third-harmonic energy $\mathcal{E}_{3\omega}$ as a function of the incident energy \mathcal{E}_{ω} in a $L = 642$ mm and $a = 2.19$ μm fiber.

$$\text{HIG}_{pm}^{\pm}(\xi, \eta, \epsilon) = \text{IG}_{pm}^e(\xi, \eta, \epsilon) \pm i\text{IG}_{pm}^o(\xi, \eta, \epsilon), \quad m > 0.$$

2. Energetic properties We now turn next to the energetic properties of THG. Experimental data of the up-converted energy $\mathcal{E}_{3\omega}$ are shown in black squares in Figure 4.12 as a function of the incident fundamental energy \mathcal{E}_{ω} , for a propagation in a fiber with $L = 642$ mm and $a = 2.19$ μm . The configuration D of the experimental sketch 4.6 is adopted here.

In the approximations of Gaussian beams, undepleted and monochromatic pump, and equality of the fundamental and third-harmonic group velocities, it can be shown from the system of coupled equations (1.52) that $\mathcal{E}_{3\omega}$ as a function of \mathcal{E}_{ω} takes the form:

$$\mathcal{E}_{3\omega}(L) = \frac{128\mu_0}{3\pi\epsilon_0} \left(\frac{\chi_{\text{eff}}^{(3)}(3\omega, \omega, \omega)L}{\lambda_{\omega}} \right)^2 \frac{T_{01}^3(\omega)T_{03}(3\omega)}{(n_{\text{eff}}^{01}(\omega))^3 n_{\text{eff}}^{03}(3\omega)} \frac{1}{S_{\text{eff}}^2} \frac{\tau_{3\omega}}{\tau_{\omega}^3} \text{sinc}^2 \left(\frac{\Delta k_{\text{eff}}^{(3)}(3\omega, \omega, \omega)L}{2} \right) [\mathcal{E}_{\omega}(0)]^3, \quad (4.16)$$

where ϵ_0 and μ_0 are the vacuum permittivity and permeability respectively, L is the fiber length, λ_{ω} the incoming phase-matched wavelength, $\chi_{\text{eff}}^{(3)}$ the effective third-order nonlinear susceptibility, T the Fresnel transmission coefficient in energy, τ the pulse duration, n_{eff} the effective dispersion, S_{eff} the effective mode area, and Δk_{eff} the effective phase-mismatch defined in Section 4.1.2.

In our experiment, such assumptions are not correct as we are dealing with non-Gaussian up-converted beams on the one hand, and the pump cannot be considered as monochromatic on the other hand. However, the hypothesis of the undepleted pump still holds, and it is fair to ignore the group velocity dispersion for 10 ns temporal pulses as shown in Section 4.1.2.

We then consider a Gaussian polychromatic pump, centered around ω^c , of standard deviation $\Delta\omega$ (*i.e.* diameter at $1/e$, $\Delta\omega_{1/e} = 2\sqrt{2}\Delta\omega$). Its field can be expressed as:

$$\mathcal{A}_\omega(\omega^c, \Delta\omega) = \int_{\omega^c - \Delta\omega/2}^{\omega^c + \Delta\omega/2} d\bar{\omega} \underline{A}_\omega(\bar{\omega}) = \int_{\omega^c - \Delta\omega/2}^{\omega^c + \Delta\omega/2} d\bar{\omega} \underline{A}_\omega(\omega^c) \exp\left(-\frac{1}{2} \left(\frac{\omega - \omega^c}{\Delta\omega}\right)^2\right). \quad (4.17)$$

In our case, the theoretical central wavelength for phase matching is $\lambda_{\text{th}}^c = 1544$ nm, and the experimental one is $\lambda^c = 1550$ nm. The full width at half maximum of the energy spectrum equals $\Delta\lambda_\omega^{\text{FWHM}} = 4.9$ nm from measurement using a sub-0.1nm sensitive monochromator, *i.e.* $\Delta\lambda_\omega^{\text{FWHM}} = 6.9$ nm in field amplitude. It is related to $\Delta\omega$ via the relationship $\Delta\omega = \frac{\pi c}{\sqrt{2 \ln 2}} \frac{\Delta\lambda_\omega^{\text{FWHM}}}{(\lambda^c)^2}$.

In the undepleted pump approximation, the polychromatic nonlinear coupled equations take the form of the following equation for a propagation along the Z -axis:

$$\begin{cases} \frac{\partial \underline{A}_\omega(\omega_{1,2,3}, Z)}{\partial Z} = 0 \\ \frac{\partial \underline{A}_{3\omega}(3\omega, Z)}{\partial Z} = i \iint \frac{d\omega_1}{2\pi} \frac{d\omega_2}{2\pi} \kappa_{\text{eff}}(3\omega, \omega_1, \omega_2) \underline{A}_\omega(\omega_1, Z) \underline{A}_\omega(\omega_2, Z) \underline{A}_\omega(3\omega - \omega_1 - \omega_2, Z) \\ \quad \times f_{01-03}(3\omega, \omega_1, \omega_2) \mathcal{F}_\omega(\omega_1) \mathcal{F}_\omega(\omega_2) \mathcal{F}_\omega(3\omega - \omega_1 - \omega_2) [\mathcal{F}_{3\omega}(3\omega)]^{-1} e^{-i\Delta k_{\text{eff}}^{(3)}(\vec{r}, 3\omega, \omega_1, \omega_2)Z}, \end{cases} \quad (4.18)$$

with κ_{eff} , \mathcal{F} and $f_{01-03} = S_{\text{eff}}^{-1}$ defined as in Equations (1.107), (1.108) and (1.100) respectively. The integrals describe the spectrum of the pump beam. Note that the transverse integration has already been performed in these equations.

After integration, we get the expressions of the spectral fields at the end of the fiber $Z = L$, for every point (X, Y) of the transverse plane and at every time t :

$$\begin{cases} \underline{A}_\omega(\omega_{1,2,3}, L) = \underline{A}_\omega(\omega_{1,2,3}, 0) \\ \underline{A}_{3\omega}(3\omega, L) = iL \iint \frac{d\omega_1}{2\pi} \frac{d\omega_2}{2\pi} \kappa_{\text{eff}}(3\omega, \omega_1, \omega_2) \underline{A}_\omega(\omega_1, 0) \underline{A}_\omega(\omega_2, 0) \underline{A}_\omega(3\omega - \omega_1 - \omega_2, 0) \\ \quad \times S_{\text{eff}}^{-1}(3\omega, \omega_1, \omega_2) \mathcal{F}_\omega(\omega_1) \mathcal{F}_\omega(\omega_2) \mathcal{F}_\omega(3\omega - \omega_1 - \omega_2) [\mathcal{F}_{3\omega}(3\omega)]^{-1} \\ \quad \times \text{sinc}\left(\frac{\Delta k_{\text{eff}}^{(3)}(3\omega, \omega_1, \omega_2)L}{2}\right) e^{-i\Delta k_{\text{eff}}^{(3)}(3\omega, \omega_1, \omega_2)L/2}. \end{cases} \quad (4.19)$$

Considering a Gaussian temporal evolution and the LP₀₃ transverse profile of the third-harmonic mode, the power defined with the Equations (1.19) and (1.20) is written as:

$$\mathcal{P}_{3\omega}(L, t) = \frac{\varepsilon_0 c}{2T} \int \frac{d(3\omega)}{2\pi} n_{\text{eff}}^{03}(3\omega) |\underline{A}_{3\omega}(3\omega, L)|^2 e^{-2\left(\frac{t}{\tau_{3\omega}/2}\right)^2}, \quad (4.20)$$

with $\tau_{3\omega} = 1/\sqrt{3}\tau_\omega$ the total pulse duration of the third-harmonic beam, and T the temporal periodicity of the field.

Finally, the total up-converted energy can be calculated by integrating over time, as in Equation (1.21). We make the approximation that the linear and nonlinear parameters n_{eff} , κ_{eff} , $\chi_{\text{eff}}^{(3)}$, and the transverse parameters f_{01-03} and \mathcal{F}_ω remain constant over the spectral range, which is quite reasonable over such a small range, three frequencies being fixed by the initial

a	2.19 μm
λ_{ω}^c	1550 nm
$\Delta\lambda_{\omega}^{\text{FWHM}}$	6.9 nm
L	64.2 cm
S_{eff}	931 μm^2
τ_{ω}	10 ns
$\chi_{\text{eff}}^{(3)}$	$1.9 \times 10^{-22} \text{ m}^2\text{V}^{-2}$

Table 4.4 – Numerical values of the parameters corresponding to the THG experiment.

conditions and the last one by the energy conservation. Then, the third-harmonic energy as a function of the pump field is the following:

$$\begin{aligned}
 \mathcal{E}_{3\omega}(L) &= \frac{27\pi^{5/2}}{4\sqrt{2}} \frac{\varepsilon_0 c \tau_{3\omega} T_{01}^3(\omega^c) T_{03}(3\omega^c)}{T n_{\text{eff}}^{03}(3\omega^c)} \left(\frac{\chi_{\text{eff}}^{(3)}(3\omega^c, \omega^c, \omega^c) L [\mathcal{F}_{\omega}(\omega^c)]^3}{\lambda_{\omega}^2 S_{\text{eff}} \mathcal{F}_{3\omega}(3\omega^c)} \right)^2 \\
 &\times \alpha \int \frac{d\omega}{2\pi} \left| \iint \frac{d\omega_1}{2\pi} \frac{d\omega_2}{2\pi} \underline{A}_{\omega}(\omega_1, 0) \underline{A}_{\omega}(\omega_2, 0) \underline{A}_{\omega}(3\omega - \omega_1 - \omega_2, 0) \operatorname{sinc} \left(\frac{\Delta k_{\text{eff}}^{(3)}(3\omega, \omega_1, \omega_2) L}{2} \right) e^{-i\Delta k_{\text{eff}}^{(3)}(3\omega, \omega_1, \omega_2) L/2} \right|^2,
 \end{aligned} \tag{4.21}$$

where α is a fitting parameter that accounts for the deviation from the experimental incident energy values. It also reflects the lack of knowledge of $\chi_{\text{eff}}^{(3)}$, S_{eff} and the dispersion relationships. Note that the pump being transversally Gaussian: $\mathcal{F}_{\omega}(\omega^c) = \pi W_{\omega}^2(\omega^c)$ where W_p is the pump beam size. The Fresnel transmission coefficients, omitted so far, have been taken into account in this expression (4.21): $T_{0m}(\omega) = \frac{4n_{\text{eff}}^{0m}(\omega)}{(1 + n_{\text{eff}}^{0m}(\omega))^2}$, $m \in \{1, 3\}$.

In elliptical coordinates, the effective interaction area is defined as:

$$S_{\text{eff}} = \frac{\sqrt{\left[\iint_{\mathbb{R}^2} |F_{01}(\xi, \eta)|^2 dS \right]^3 \iint_{\mathbb{R}^2} |F_{03}(\xi, \eta)|^2 dS}}{\iint_{\mathbb{R}^2} [F_{01}^*(\xi, \eta)]^3 F_{03}(\xi, \eta) dS}, \tag{4.22}$$

with $dS = f_0^2 (\sinh^2(\xi) + \sin^2(\eta)) d\xi d\eta$ the infinitesimal surface element. For the interaction between the modes LP_{01} and LP_{03} , it is equal to $S_{\text{eff}} = 931 \mu\text{m}^2$. Two comparisons can be made. Firstly, an interaction between four LP_{01} waves in a fiber of core radius 17 μm would lead to such an overlap. Secondly, an interaction involving only LP_{01} modes in our fiber of core radius 2.19 μm would have led us to $S_{\text{eff}} = 10.9 \mu\text{m}^2$. Thus, we have: $\frac{S_{\text{eff}}|_{01-03}}{S_{\text{eff}}|_{01-01}} = 1.17\%$, which is consistent with the literature [184].

Table 4.4 gathers together the numerical values for the physical parameters. Figure 4.12 shows the calculated third-harmonic energy as a function of the fundamental energy, and its agreement with the experimental data for a fitting parameter set as $\alpha = 0.12$. The following

	\mathcal{E}	$P_{pk} = \frac{\mathcal{E}}{\tau}$	$\bar{P} = \mathcal{E} \times f$	$I = \frac{P_{pk}}{S_{\text{eff}}}$
	Pulse energy	Peak power	Average power	Intensity
ω	0.58 μJ	58.2 W	5.82 μW	6.25 MWcm^{-2}
3ω	43.8 fJ	7.59 μW	438 fW	0.81 Wcm^{-2}

Table 4.5 – Energies, powers and intensities of our THG experiment. The pulse time is 10 ns and the repetition rate $f = 10$ Hz.

table sums up the fundamental and third-harmonic energies, powers and intensities corresponding to the point of maximum input energy of Figure 4.12:

This process has an energetic conversion efficiency $\eta = \frac{\mathcal{E}_{3\omega}}{\mathcal{E}_{\omega}} = 7.6 \times 10^{-8}$.

3. Third-harmonic spectrum A third-harmonic spectrum has been measured at the output of a fiber of $L = 183$ mm and $a = 2.19$ μm using the configuration C of the experimental setup depicted in Figure 4.6. The energy of the normalized third-harmonic signal $\mathcal{E}_{3\omega}$ is measured as the input fundamental wavelength λ_{ω} is tuned spectrally. Experimental data are presented as black squares on Figure 4.13a where the third-harmonic energy is plotted as a function of the fundamental wavelength λ_{ω} .

A calculation has been done considering the polychromatic Gaussian pump with a full width at half-maximum of $\Delta\lambda_{\omega} = 6.9$ nm in field amplitude, based on the development of the previous section. It is still assumed that n_{eff} , κ_{eff} , $\chi_{\text{eff}}^{(3)}$, f_{01-03} and \mathcal{F}_p remain constant over the spectral range. Specifically, the third-harmonic field is:

$$\begin{aligned} \underline{A}_{3\omega}(3\omega, L) \propto & \iint \frac{d\omega_1}{2\pi} \frac{d\omega_2}{2\pi} \underline{A}_{\omega}(\omega_1, 0) \underline{A}_{\omega}(\omega_2, 0) \underline{A}_{\omega}(3\omega - \omega_1 - \omega_2, 0) \\ & \times \text{sinc} \left(\frac{\Delta k_{\text{eff}}^{(3)}(3\omega, \omega_1, \omega_2) L}{2} \right) e^{-i\Delta k_{\text{eff}}^{(3)}(3\omega, \omega_1, \omega_2) L/2}. \end{aligned} \quad (4.23)$$

The corresponding curve shown in green in Figures 4.13a and 4.13b (zoom) is very sharp. We see that the wideness of the peak cannot be explained by considering only the pump spectral linewidth. Note that the fiber being quite long, the acceptance parameter $L \cdot \Delta\lambda_{\omega}$ with this large pump is very close to what it would be with a monochromatic pump (1.5 nm.cm). $\Delta\lambda_{\omega}$ is here defined as the FWHM of the spectral third-harmonic peak.

In addition, the fiber core size fluctuations may be considered as not negligible. Taking into account this effect as an incoherent process, the sum over intensities can be written as:

$$I_{3\omega}(\omega, L) \propto \frac{1}{\Delta a} \int_{a_{\min}}^{a_{\max}} da \left| \underline{A}_{3\omega}(\omega, \omega^{\text{PM}}(a), L) \right|^2, \quad (4.24)$$

with $\Delta a = (a_{\max} - a_{\min})$, which is equivalent to:

$$I_{3\omega}(\omega, L) \propto \frac{1}{\Delta\omega} \int_{\omega_{\min}^{\text{PM}}}^{\omega_{\max}^{\text{PM}}} d\omega_{\text{PM}} \left| \underline{A}_{3\omega}(\omega, \omega^{\text{PM}}, L) \right|^2. \quad (4.25)$$

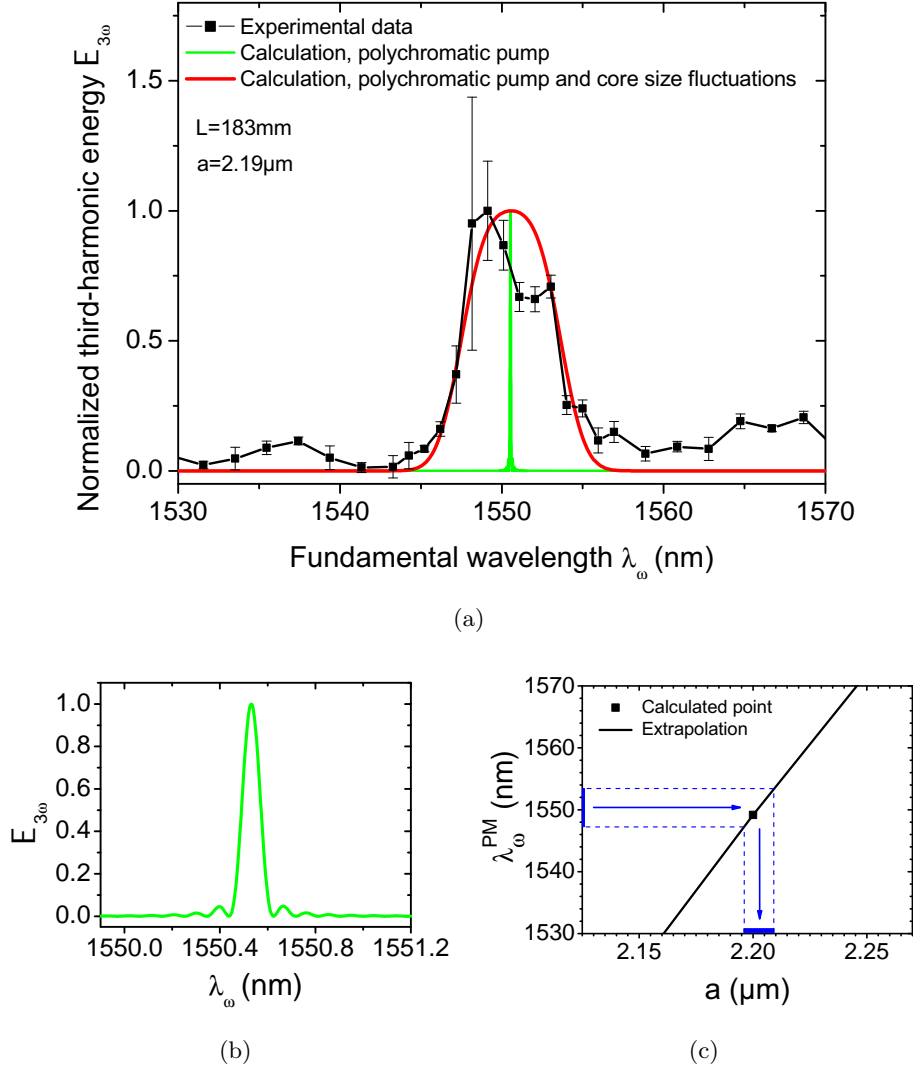


Figure 4.13 – (a) Normalized third-harmonic energy $\mathcal{E}_{3\omega}$ as a function of λ_{ω} around 1550 nm, in a $L = 183$ mm and $a = 2.19$ μm fiber. Experimental data are in squares. Calculations taking into account the spectral width of the pump (green line), and that width as well as the core size fluctuations (red solid line).

(b) Zoom on the calculation with a core size fixed at 2.19 μm .

(c) Reproduction of Figure 4.3: the blue region gives the spreading of the fundamental wavelength corresponding core radius fluctuations.

Because the optical indices n_{eff} at the fundamental and third-harmonic wavelengths that govern the phase mismatch $\Delta k_{\text{eff}}^{(3)}$ are not known for each core radius in the interval $[a_{\text{max}}, a_{\text{min}}]$, the wavelengths are reseted for the calculation of the phase mismatch so that phase matching can be achieved for each radius a in compliance with the extrapolation shown in Figure 4.3.

Considering the core size fluctuations together with the width of the pump, the calculation matches the experimental data for $\Delta a = 12$ nm as shown in red on Figure 4.13a. It represents 0.55% of the core radius. This range of core radii is shown as the blue interval on the horizontal of Figure 4.13c, which is an expanded reproduction of Figure 4.3. The corresponding phase-matching wavelengths lie in an interval of wideness $\Delta\lambda_{\omega} = 5.7$ nm, *i.e.* within the blue interval of the vertical of Figure 4.13c.

The actual acceptance $L.\Delta\lambda_{\omega}$ can be directly measured on Figure 4.13a. It equals 104nm.cm. This turns out to be an advantage as it enables to use long fibers.

We finish this section by underlining that the third-harmonic peak is here centered around 1550 nm and not 1544 nm as it is supposed to be. This may signify that the mean value of the core size is 13.1 nm above the supplier value. With the fluctuations of the core geometry, the total uncertainty of the phase-matching wavelength is 19 nm, much larger than the 3 nm expected.

4. Evidence of birefringence and polarization effects inside the fibers We show in this section that our fibers exhibit an unexpected birefringence, so that THG depends on the polarization of the incident fundamental beam. Experiments are done in the experimental configuration B of Figure 4.6. A half-wave plate (HWP) controls the polarization of the incoming beam. The fundamental and third-harmonic beams are collected in a microscope objective; they can be considered separately using appropriate filters. Glan-Taylor prisms (GTP) allow us to analyze their polarization state. The beams are focused with a microscope objective onto photodetectors.

- Neutral lines The fiber is put between parallel polarizer (HWP) and analyzer (GTP) that are rotating together. The identification of neutral lines is made where the signal is maximum. Note that it is more usual to make this experiment between cross polarizers, a neutral line then corresponding to an extinction. The measurement is not spectrally dependent, and has been carried out at different wavelengths in a 642 mm-long fiber of core radius $a = 2.19$ μm . It is presented here on Figure 4.14 at $\lambda = 1500$ nm.

We see a clear evidence of an anisotropic behaviour of the fiber, with the identification of two orthogonal neutral lines, one at 0° and the other one at 90°. At this point, it is necessary to consider that the fiber we use is a medium belonging to the uniaxial or biaxial optical classes, as it is the case for a crystal. We assume first that it is uniaxial, and we will see later on that this assumption is fully correct.

As explained in Chapter 1, the propagation in an uniaxial medium is described in the dielectric frame, written (x, y, z) , where the axis z is the optical axis of the index surface, meaning that there is isotropy according to the polarization when light propagates in this direction, while it is anisotropic along the axes x and y . The propagation axis of the fiber being identified as

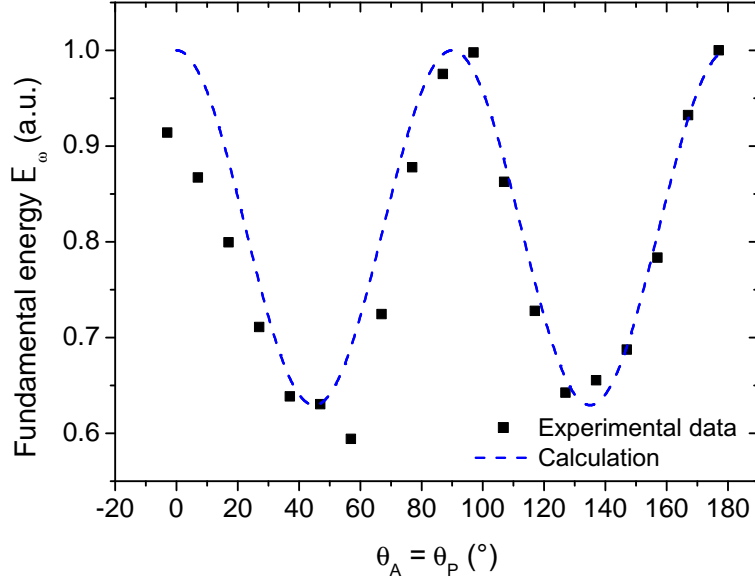


Figure 4.14 – Identification of the neutral axes of the fiber at 1500 nm put in between parallel polarizers. Experimental data are in squares; the blue dashed line is a fit based on subsequent calculations. Fiber geometry: $a = 2.19 \mu\text{m}$ and $L = 642 \text{ mm}$.

exhibiting an anisotropy, it is necessarily an axis perpendicular to the z -axis. We arbitrarily call this axis x . Then the cleaving plane of the fiber is the $(y0z)$ plane. In Figure 4.14, the axis at 0° is taken as the z -axis, while the axis at 90° is the y -axis.

We analyzed the polarization states of both the fundamental and third-harmonic waves at the exit of the same fiber ($a = 2.19 \mu\text{m}$ and $L = 642 \text{ mm}$) for different orientations of the linear polarization of the fundamental wave. θ_P and θ_A are the angles between the polarizer (HWP) or analyzer (GTP) and the z -axis of the fiber respectively. $(\vec{e}_x, \vec{e}_y, \vec{e}_z)$ are the cartesian unit vectors of the polarization in the dielectric frame. The input fundamental orientation of the polarization is at $\theta_\omega^{\text{in}} = 2\theta_P$ from the z -axis.

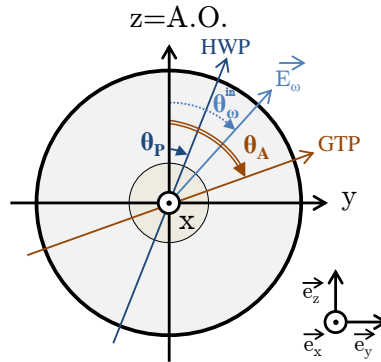


Figure 4.15 – Angle conventions in the dielectric frame (x, y, z) . The incident fundamental electric field $\vec{E}_\omega^{\text{in}}$ makes an angle $\theta_\omega^{\text{in}}$ with the z -axis. θ_P and θ_A are the angles of the polarizer (HWP) or analyzer (GTP) with the z -axis respectively.

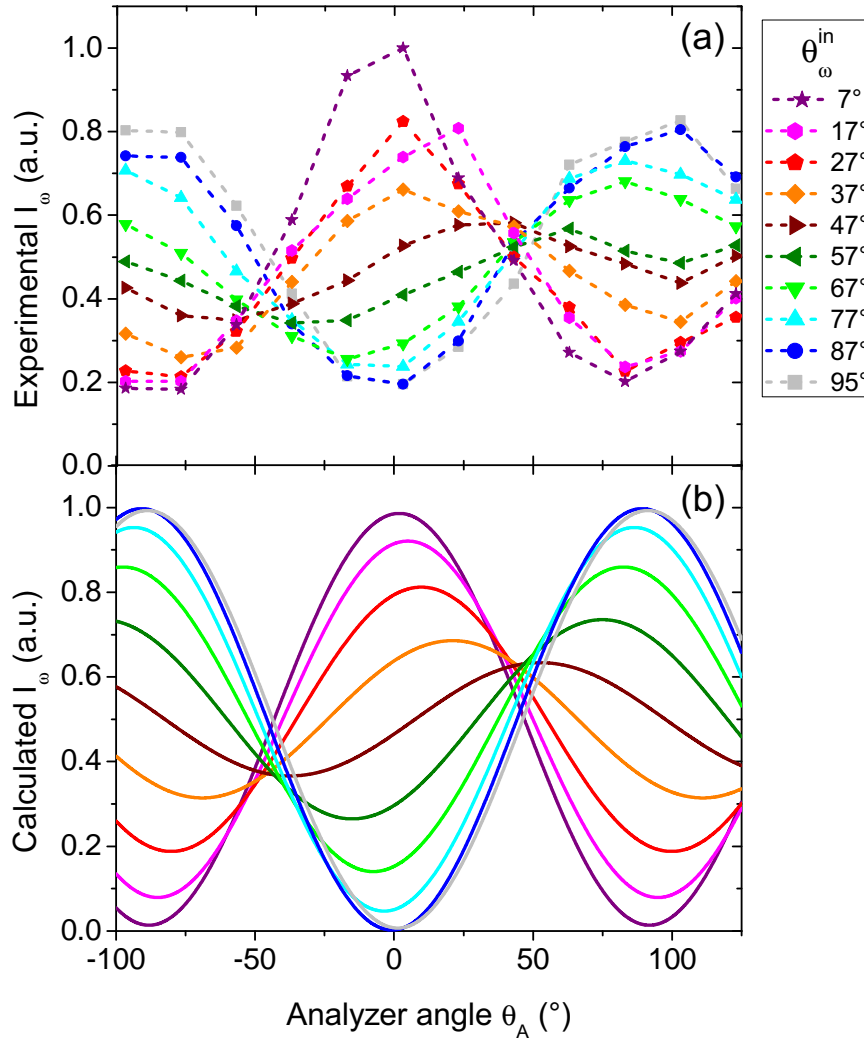


Figure 4.16 – Measured (a) and calculated (b) intensities analyzed as a function of the angle θ_A of the fundamental beam at λ_ω , at the output of the fiber for different input polarization angles $\theta_\omega^{\text{in}}$. Fiber geometry: $a = 2.19 \mu\text{m}$ and $L = 642 \text{ mm}$.

- Fundamental beam polarization state Firstly, the intensity of the fundamental phase-matched beam at $\lambda_\omega \simeq 1550 \text{ nm}$ is analyzed at the output of the fiber for different orientations of the input polarization. The experimental results are shown in Figure 4.16(a). All angles are expressed in the dielectric frame. Note that it has been carefully checked that the fiber was not twisted around its revolution axis. Corresponding analytical calculations are shown in (b), and explained just below.

Just behind the half-wave plate (HWP), the electric field vector of the fundamental wave is written:

$$\vec{E}_1 = \begin{cases} E_0 \sin(\theta_\omega^{\text{in}}) e^{i(\omega t_0 - kx_0)} \vec{u}_y \\ E_0 \cos(\theta_\omega^{\text{in}}) e^{i(\omega t_0 - kx_0)} \vec{u}_z, \end{cases} \quad (4.26)$$

where x_0 and t_0 can be taken as zero.

It is then refracted in the fiber and propagates over a length L , which gives at the exit of the fiber:

$$\vec{E}_2 = \begin{cases} E_0 \sin(\theta_\omega^{\text{in}}) e^{i(\omega t - 2\pi \frac{L}{\lambda} n_y)} \vec{u}_y & = E_0 \sin(\theta_\omega^{\text{in}}) e^{i(\omega t + \Delta\varphi)} \vec{u}_y \\ E_0 \cos(\theta_\omega^{\text{in}}) e^{i(\omega t - 2\pi \frac{L}{\lambda} n_z)} \vec{u}_z & = E_0 \cos(\theta_\omega^{\text{in}}) e^{i\omega t} \vec{u}_z, \end{cases} \quad (4.27)$$

where $\Delta\varphi = 2\pi \frac{L}{\lambda} (n_z - n_y) = \pm 2\pi \frac{L}{\lambda} \Delta n$ is the dephasing angle between the two components of the electric field, and Δn the birefringence.

Finally, behing the Glan-Taylor polarizor (GTP), the analyzed electric field is:

$$\begin{aligned} \|\vec{E}_3\| &= E_0 \left[\cos(\theta_\omega^{\text{in}}) \cos(\theta_A) \cos(\omega t) + \sin(\theta_\omega^{\text{in}}) \sin(\theta_A) \cos(\omega t + \Delta\varphi) \right] \\ &= E_0 \left[\cos(\theta_\omega^{\text{in}}) \cos(\theta_A) + \sin(\theta_\omega^{\text{in}}) \sin(\theta_A) \cos(\Delta\varphi) \right] \cos(\omega t) \\ &\quad - E_0 \left[\sin(\theta_\omega^{\text{in}}) \sin(\theta_A) \sin(\Delta\varphi) \right] \sin(\omega t). \end{aligned} \quad (4.28)$$

We consider the corresponding intensity, $I_3 \propto \langle \|\vec{E}_3 \cdot \vec{E}_3^*\| \rangle_T$. As $\langle \cos^2(\omega t) \rangle_T = \langle \sin^2(\omega t) \rangle_T = \frac{1}{2}$ and $\langle \sin(\omega t) \cos(\omega t) \rangle_T = 0$, it comes:

$$I_3 = I_0 \left[\cos^2(\theta_\omega^{\text{in}} + \theta_A) + \sin(2\theta_\omega^{\text{in}}) \sin(2\theta_A) \cos^2(\Delta\varphi/2) \right], \quad (4.29)$$

with I_0 the input intensity.

The expression (4.29) allows us to compute the behaviour in polarization of the beam at λ_ω , which is in very good agreement with the measurements as shown in Figure 4.16. Nevertheless, we can notice that the calculated curves go down to zero, contrary to our experiment. This discrepancy can be explained by a certain degree of inhomogeneity of the fiber leading to paths where the anisotropy does not apply.

Let us focus on the particular case where the input polarization and analyzer are parallel, *i.e.* $\theta_\omega^{\text{in}} = \theta_A$. It comes from Equation (4.29):

$$I_3 = I_0 \left[1 - \sin^2(2\theta_\omega^{\text{in}}) \sin^2(\Delta\varphi/2) \right]. \quad (4.30)$$

The dephasing $\Delta\varphi$ is used as a fitting parameter that enables us to fit the data of Figure 4.14 as shown in the blue dashed curve. It is set to $\Delta\varphi \simeq 75^\circ$ or $285^\circ \pm 5^\circ [360^\circ]$.

Note that the birefringence Δn is linked to this dephasing through the relationship:

$$\Delta\varphi = 2\pi \left(\frac{L}{\lambda_\omega} \Delta n + q \right), \quad q \in \mathbb{Z}. \quad (4.31)$$

It is yet impossible to infer it as q cannot be known.

- Third-harmonic beam polarization state We now turn next to the measurement of the third-harmonic beam intensity at $\lambda_{3\omega} = \lambda_\omega^{\text{PM}}/3$ as a function of the angle of the analyzer θ_A , for different orientations of the input polarization of the fundamental beam at λ_ω . Experimental and calculation results are shown in Figure 4.17.

The understanding of this complex behaviour requires to know the relative magnitudes of the coefficients of the third-order electric susceptibility tensor, which is presented below. It is then

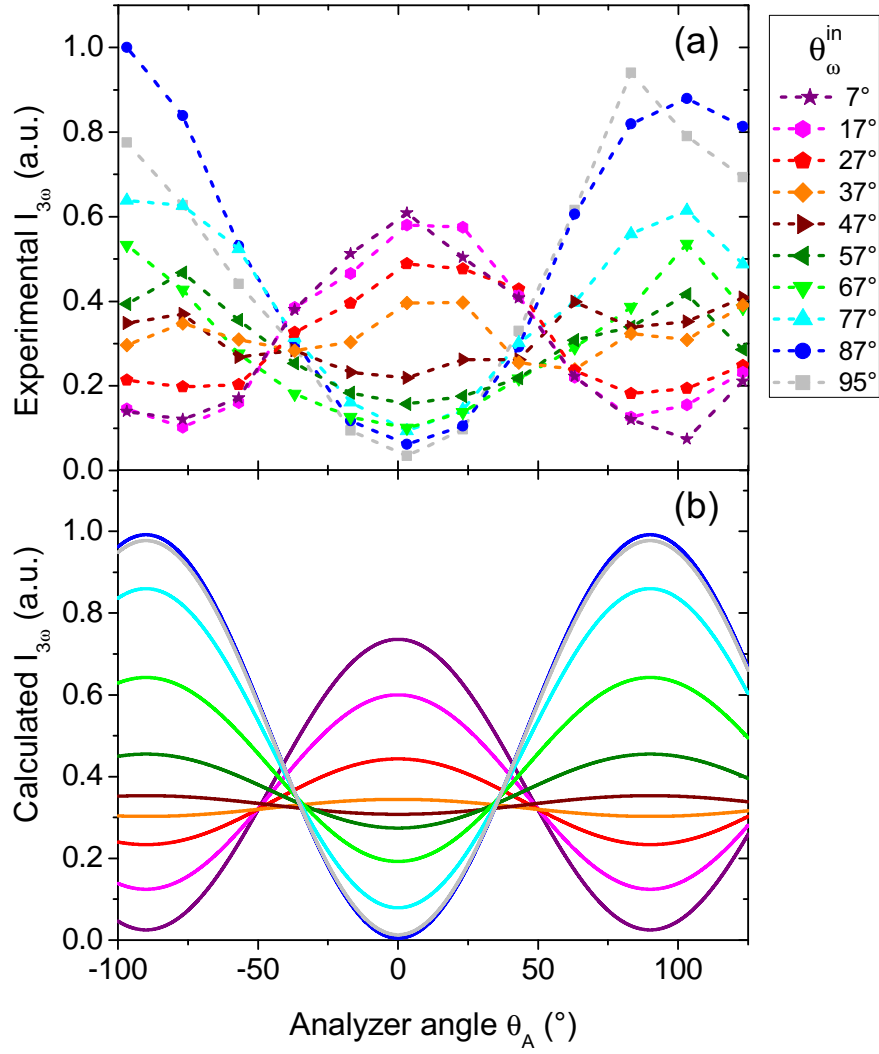


Figure 4.17 – Measured (a) and calculated (b) intensities of the third-harmonic beam analyzed at the angle θ_A for different polarization angles $\theta_\omega^{\text{in}}$ of the incoming fundamental beam. Fiber geometry: $a = 2.19 \mu\text{m}$ and $L = 642 \text{ mm}$.

necessary to know the orientation symmetry class of our uniaxial fiber. We make the assumption that it belongs to the infinite group $\{A_\infty/m, \infty m\}$, the infinite axis A_∞ being along the z axis of the dielectric frame. This symmetry group corresponds to the case of an isotropic medium under an uniaxial strain [105]. Using the Neumann principle [25] and assuming the Kleinman approximation, the non-zero nonlinear elements of the third-order susceptibility tensor are:

$$\begin{cases} \chi_{xxxx} = \chi_{yyyy} \\ \chi_{zzzz} \\ \chi_{xxzz} = \chi_{xzzx} = \chi_{zxzx} = \chi_{zzxx} = \chi_{zzxz} = \chi_{yyyz} = \chi_{yyzy} = \chi_{zyyz} = \chi_{zyzy} = \chi_{zzyy} = \chi_{yzzz} \\ \chi_{xxyy} = \chi_{xyxy} = \chi_{yxyx} = \chi_{xyyx} = \chi_{yyxx} = \chi_{xyxx} = \chi_{xxxx}/3. \end{cases} \quad (4.32)$$

The first index refers to the wave at 3ω , while the three last indices stand for the waves at ω .

The possible optical nonlinear interactions governed by such a tensor can be sorted into three categories depending on the polarizations that are solicited for each of the interacting waves. The corresponding effective third-order nonlinear coefficients defined in Equation (1.53) are expressed as a function of $e_{y,z}^\omega$ and $e_{y,z}^{3\omega}$, which are the Cartesian coordinates of the fundamental and third-harmonic unit electric field projected onto the two neutral lines, *i.e.* the y and z axes. It gives for all the possible types, written as $a - bcd$, the first label standing for the wave at 3ω and the three others for the fundamental wave, where each label can be o or e (o for ordinary, e for extraordinary) :

– type A: $o - ooo$ and $e - eee$

$$\begin{cases} \chi_{\text{eff}}^{\text{A1}} = \chi_{yyyy} e_y^{3\omega} (e_y^\omega)^3 = \chi_{yyyy} e_y^{3\omega} \sin^3(\theta_\omega^{\text{in}}) \\ \chi_{\text{eff}}^{\text{A2}} = \chi_{zzzz} e_z^{3\omega} (e_z^\omega)^3 = \chi_{zzzz} e_z^{3\omega} \cos^3(\theta_\omega^{\text{in}}); \end{cases} \quad (4.33)$$

– type B: $o - eee$ and $e - ooo$

$$\chi_{\text{eff}}^{\text{B}} = 0; \quad (4.34)$$

– type C: $o - oee$, $o - eoe$, $o - eeo$ and $e - eoo$, $e - oeo$, $e - ooe$.

$$\begin{cases} \chi_{\text{eff}}^{\text{C1}} = 3\chi_{yyzz} e_y^{3\omega} e_y^\omega (e_z^\omega)^2 = 3\chi_{yyzz} e_y^{3\omega} \cos(\theta_\omega^{\text{in}}) \sin^2(\theta_\omega^{\text{in}}) \\ \chi_{\text{eff}}^{\text{C2}} = 3\chi_{zzyy} e_z^{3\omega} e_z^\omega (e_y^\omega)^2 = 3\chi_{yyzz} e_z^{3\omega} \sin(\theta_\omega^{\text{in}}) \cos^2(\theta_\omega^{\text{in}}). \end{cases} \quad (4.35)$$

The intensities measured in the experiment presented in Figure 4.17 are projected on the angle of the analyzer θ_A . Therefore, by integrating the corresponding coupled equations under the undepleted pump approximation, we get the total third-harmonic intensity behind the analyzer, *i.e.* :

$$I^{\text{tot}}(\theta_\omega^{\text{in}}, \theta_A) \propto \left[(\chi_{\text{eff}}^{\text{A1}})^2 + (\chi_{\text{eff}}^{\text{C1}})^2 \right] \sin^2(\theta_A) + \left[(\chi_{\text{eff}}^{\text{A2}})^2 + (\chi_{\text{eff}}^{\text{C2}})^2 \right] \cos^2(\theta_A). \quad (4.36)$$

Note that the sum of the different processes A1, A2, C1 and C2 in Equation (4.36) is relative to intensities and not to electric fields. Only this incoherent view (as opposed to coherent) can account for the constancy of the position of the extrema of the output third-harmonic angles θ_A^* for all fundamental input angle $\theta_\omega^{\text{in}}$ as observed experimentally in Figure 4.17 (a). Indeed:

$$\begin{aligned}
 & - \text{ for an incoherent scheme: } \left. \frac{\partial I^{\text{tot}}}{\partial \theta_A} \right|_{\theta_A^*} = 0 \Rightarrow \theta_A^* \equiv 0 \text{ or } \frac{\pi}{2} [\pi]; \\
 & - \text{ for a coherent scheme: } \left. \frac{\partial I^{\text{tot}}}{\partial \theta_A} \right|_{\theta_A^*} = 0 \\
 & \Rightarrow \theta_A^* \equiv \arctan \left(\frac{\sin^3(\theta_\omega^{\text{in}}) + 3\beta \cos^2(\theta_\omega^{\text{in}}) \sin(\theta_\omega^{\text{in}})}{\alpha \cos^3(\theta_\omega^{\text{in}}) + 3\beta \sin^2(\theta_\omega^{\text{in}}) \cos(\theta_\omega^{\text{in}})} \right) - a [\pi], \quad a \in \left\{ 0, \frac{\pi}{2} \right\}.
 \end{aligned}$$

Because we cannot access any other direction of propagation than that corresponding to the fiber axis, *i.e.* the x -axis of the dielectric frame, it is not possible to determine the absolute magnitude of the different elements of the third-order electric susceptibility tensor of the fiber, as it can be done in a bulk crystal [149]. However, from the measured polarization pattern of Figure 4.17 and Equation (4.36), it is possible to access to the relations of order between the tensor elements from the following ratii: $\alpha = \frac{\chi_{yyyy}}{\chi_{zzzz}}$ and $\beta = \frac{\chi_{yyzz}}{\chi_{zzzz}}$.

In order to reduce the uncertainty of the calculation, we work with integrated intensities $I_{\text{int}}^{\text{tot}}$ over the output angles θ_A , for a particular fundamental orientation of the input polarization $\theta_\omega^{\text{in}}$. They are:

$$I_{\text{int}}^{\text{tot}}(\theta_\omega^{\text{in}}) \propto \frac{1}{2\pi} \int_0^{2\pi} d\theta_A I^{\text{tot}}(\theta_\omega^{\text{in}}, \theta_A) \quad (4.37)$$

$$\Leftrightarrow I_{\text{int}}^{\text{tot}}(\theta_\omega^{\text{in}}) \propto \frac{1}{2} \left[\chi_{yyyy}^2 \sin^6(\theta_\omega^{\text{in}}) + \chi_{zzzz}^2 \cos^6(\theta_\omega^{\text{in}}) + \frac{9}{4} \chi_{yyzz}^2 \sin^2(2\theta_\omega^{\text{in}}) \right]. \quad (4.38)$$

To get rid of the proportionnality constant, we consider the ratio between two integrated intensities corresponding to two different fundamental input polarizations denoted as $\theta_\omega^{\text{in}}$ and $\tilde{\theta}_\omega^{\text{in}}$, which gives:

$$\frac{I_{\text{int}}^{\text{tot}}(\theta_\omega^{\text{in}})}{I_{\text{int}}^{\text{tot}}(\tilde{\theta}_\omega^{\text{in}})} = \frac{\alpha^2 \sin^6(\theta_\omega^{\text{in}}) + \cos^6(\theta_\omega^{\text{in}}) + \frac{9}{4} \beta^2 \sin^2(2\theta_\omega^{\text{in}})}{\alpha^2 \sin^6(\tilde{\theta}_\omega^{\text{in}}) + \cos^6(\tilde{\theta}_\omega^{\text{in}}) + \frac{9}{4} \beta^2 \sin^2(2\tilde{\theta}_\omega^{\text{in}})} \quad (4.39)$$

$$\begin{aligned}
 \Leftrightarrow \alpha^2 \left[\sin^6(\theta_\omega^{\text{in}}) - \left(\frac{I_{\text{int}}^{\text{tot}}(\theta_\omega^{\text{in}})}{I_{\text{int}}^{\text{tot}}(\tilde{\theta}_\omega^{\text{in}})} \right) \sin^6(\tilde{\theta}_\omega^{\text{in}}) \right] &+ \left[\cos^6(\theta_\omega^{\text{in}}) - \left(\frac{I_{\text{int}}^{\text{tot}}(\theta_\omega^{\text{in}})}{I_{\text{int}}^{\text{tot}}(\tilde{\theta}_\omega^{\text{in}})} \right) \cos^6(\tilde{\theta}_\omega^{\text{in}}) \right] \\
 &+ \frac{9}{4} \beta^2 \left[\sin^2(2\theta_\omega^{\text{in}}) - \left(\frac{I_{\text{int}}^{\text{tot}}(\theta_\omega^{\text{in}})}{I_{\text{int}}^{\text{tot}}(\tilde{\theta}_\omega^{\text{in}})} \right) \sin^2(2\tilde{\theta}_\omega^{\text{in}}) \right] = 0. \quad (4.40)
 \end{aligned}$$

From this last equation, two experimental relative integrated intensities jointly with their fundamental angles are needed to infer the two unknown coefficients α and β . In other words, three absolute integrated intensities are needed. Precisely, for $\theta_\omega^{\text{in}} = 47^\circ$ and 95° , and for $\tilde{\theta}_\omega^{\text{in}} = 17^\circ$, we get $\frac{I_{\text{int}}^{\text{tot}}(\theta_\omega^{\text{in}})}{I_{\text{int}}^{\text{tot}}(\tilde{\theta}_\omega^{\text{in}})} = 0.91$ and 1.37 respectively. In the end, we get :

$$\begin{cases} \alpha = 1.14 \\ \beta = 0.50, \end{cases} \quad (4.41)$$

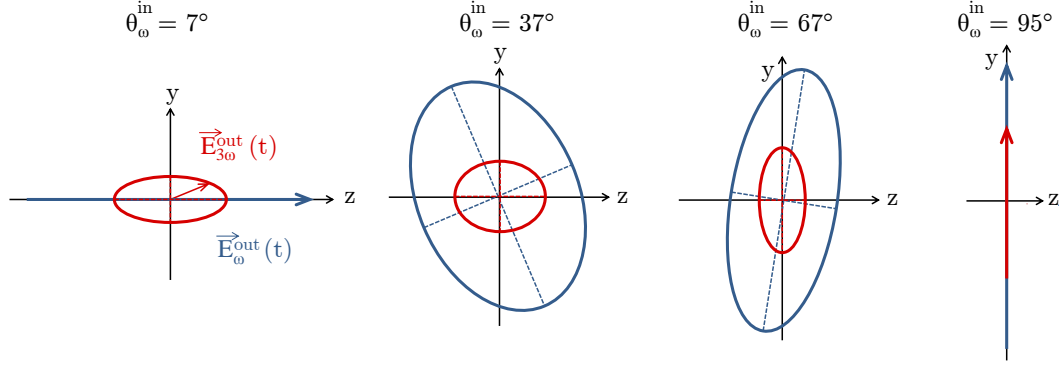


Figure 4.18 – Representation of the orientation of the output polarization of the λ_ω (in blue) and $\lambda_{3\omega}$ (in red) waves, for four different input linear polarizations of the fundamental beam: 7° , 37° , 67° and 95° .

with uncertainties $\Delta\alpha \simeq \Delta\beta \simeq 0.02$. Equation (4.41) implies the following relations of order:

$$\chi_{yyzz} < \chi_{zzzz} < \chi_{yyyy}. \quad (4.42)$$

The numerical values (4.41) and analytical expression (4.36) are used to calculate the intensity curves of the frame (b) of Figure 4.17. They enable a perfect description of the polarization behavior observed experimentally in the frame (a), which validates our hypothesis of an uniaxial fiber belonging the infinite group $\{A\infty, \infty m\}$.

Note finally that if the fundamental analyzed curves from Figure 4.16 do not go down to zero intensity because of some inhomogeneity in the anisotropy, it should be also the case for the third-harmonic analyzed curve. However, it is not the case in our experimental data as Figure 4.17 shows.

The results on the fundamental and third-harmonic polarization states at the output of the fiber can be summarized schematically as in Figure 4.18. The corresponding electric fields $E_{3\omega}^{\text{in}}$ and $E_{3\omega}^{\text{out}}$, given for four different fundamental input linear polarizations, describe the blue and red prints respectively in the plane tranverse to the x -axis. The relative magnitudes of the fields $E_{3\omega}^{\text{in}}$ (resp. $E_{3\omega}^{\text{out}}$) are respected.

To finish on the polarization analysis, we can extract some more information on the graphs 4.16 and 4.17. In Figure 4.19 are shown the output angles for maximum output transmission at λ_ω and conversion efficiency at $\lambda_{3\omega}$ with respect to the input polarization angles of the beam at λ_ω together with calculations.

In Figure 4.20, the integrated intensity of the third-harmonic beam $I_{3\omega}$ is plotted as a function of the input angle $\theta_\omega^{\text{in}}$ of the fundamental beam, and compared to the analytical calculation. It is clear that this result is in agreement with the order relation given by Equation (4.42) since we have: $\mathcal{E}_{3\omega}(\theta_\omega^{\text{in}} = 45^\circ) < \mathcal{E}_{3\omega}(\theta_\omega^{\text{in}} = 0^\circ) < \mathcal{E}_{3\omega}(\theta_\omega^{\text{in}} = 90^\circ)$.

- Evidence of birefringence Figure 4.21 constitutes a direct proof of a small birefringence in the fibers. It shows third-harmonic spectra for three different incident polarization configurations of the fundamental beam, measured at the output of a 258mm-long fiber of core size $a = 2.19\mu\text{m}$

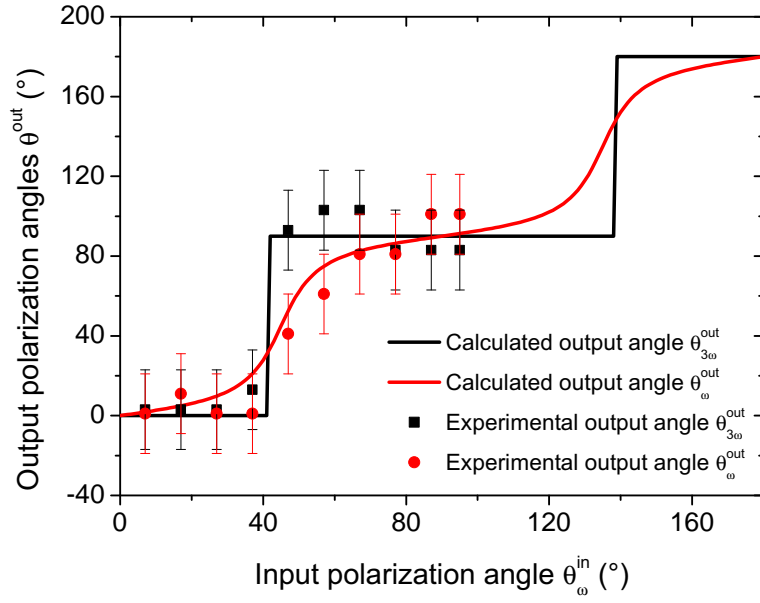


Figure 4.19 – Output angles for maximum transmission of the wave at λ_{ω} (in red) and a maximum conversion efficiency of the wave at $\lambda_{3\omega}$ (in black) with respect to the input polarization angle of the fundamental wave at λ_{ω} . Experimental data in symbols, calculations in solid lines. Fiber geometry: $a = 2.19 \mu\text{m}$ and $L = 642 \text{ mm}$.

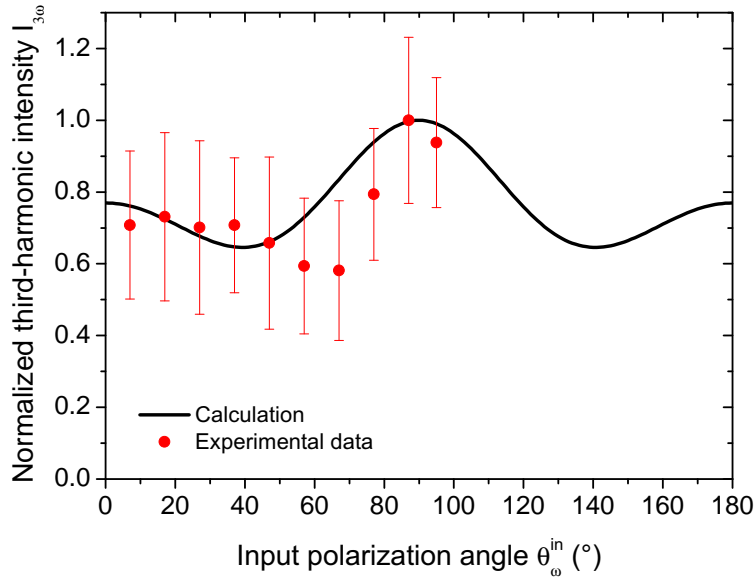


Figure 4.20 – Normalized integrated third-harmonic intensity over the output angles as a function of the input polarization angle of the fundamental beam. Dots correspond to experimental data and the solid line to calculation. Fiber geometry: $a = 2.19 \mu\text{m}$ and $L = 642 \text{ mm}$.

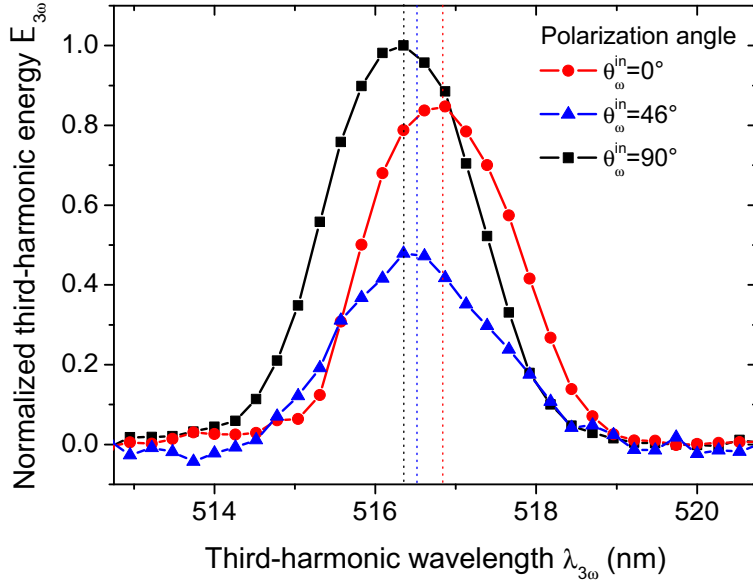


Figure 4.21 – Normalized spectra of the generated third-harmonic wave for various orientations of the fundamental wave polarizations. Fiber geometry: $a = 2.19 \mu\text{m}$ and $L = 258 \text{ mm}$.

with a 0.1 nm-sensitive spectrometer. It is clear that the phase-matching wavelength shifts a bit with respect to this incoming polarization, highlighting a birefringence: at $\theta_\omega = 0^\circ$, $\lambda_{3\omega} = 516.9 \text{ nm}$, while at $\theta_\omega = 90^\circ$, $\lambda_{3\omega} = 516.4 \text{ nm}$.

4.1.3.3 THG involving other modes than LP_{01} and LP_{03}

The THG between the modes IG_{00}^e and IG_{40}^e that was previously considered is interesting since it is phase-matched. But we experimentally identified many other mode configurations enabling phase-matching. They are described in this section.

1. Third-harmonic spectrum The measurements of the third-harmonic spectrum are performed using the experimental setup depicted in the frame C of Figure 4.6. Figures 4.22 and 4.23 show two spectra corresponding to the two core sizes $a = 2.19 \mu\text{m}$ and $a = 2.30 \mu\text{m}$ respectively. The third-harmonic energy is averaged on time and on several acquisitions so as to reduce the error due to the temporal fluctuations of the laser, the experiments being quite long. We will show in the next subsection that the various peaks we can see involve different transverse distributions for the third-harmonic beam.

The peak expected theoretically for the $\text{LP}_{01}/\text{LP}_{03}$ THG is found at a slightly higher wavelength than the theoretical one, which may be explained by a core size a bit larger than expected as it was already emphasized before:

- From Figure 4.22 ($a = 2.19 \mu\text{m}$): $\lambda_{\text{exp}} = 1550 \text{ nm}$; $\lambda_{\text{th}} = 1544 \text{ nm}$.
- From Figure 4.23 ($a = 2.30 \mu\text{m}$): $\lambda_{\text{exp}} = 1602 \text{ nm}$; $\lambda_{\text{th}} = 1596 \text{ nm}$.

2. Transverse mode analysis We pictured the transverse distributions associated with the third-harmonic peaks seen in Figure 4.22. The experiment is performed in the 64.2 cm-long fiber

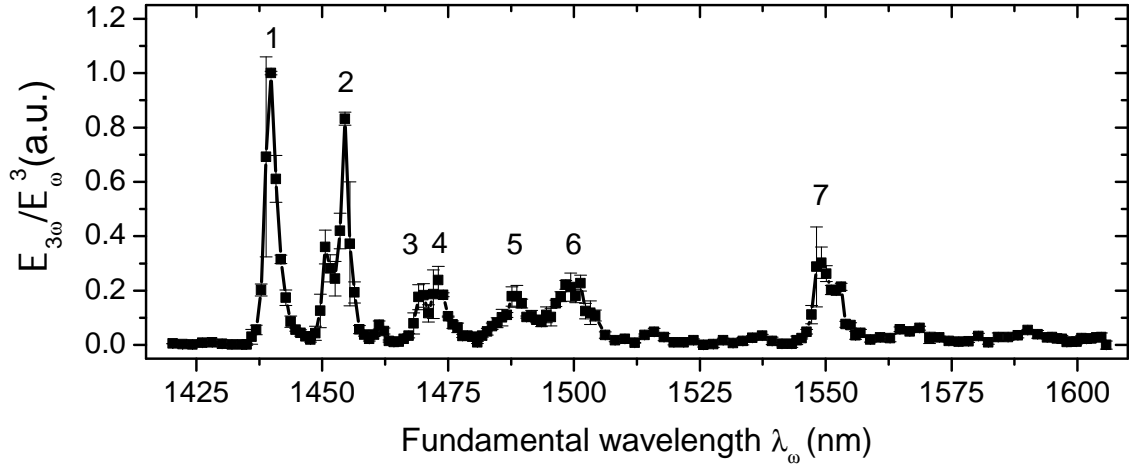


Figure 4.22 – Normalized third-harmonic spectrum in the fiber with a core size $a = 2.19 \mu\text{m}$ and a length $L = 64.2 \text{ cm}$. \mathcal{E}_ω and $\mathcal{E}_{3\omega}$ are the fundamental and third-harmonic energies respectively.

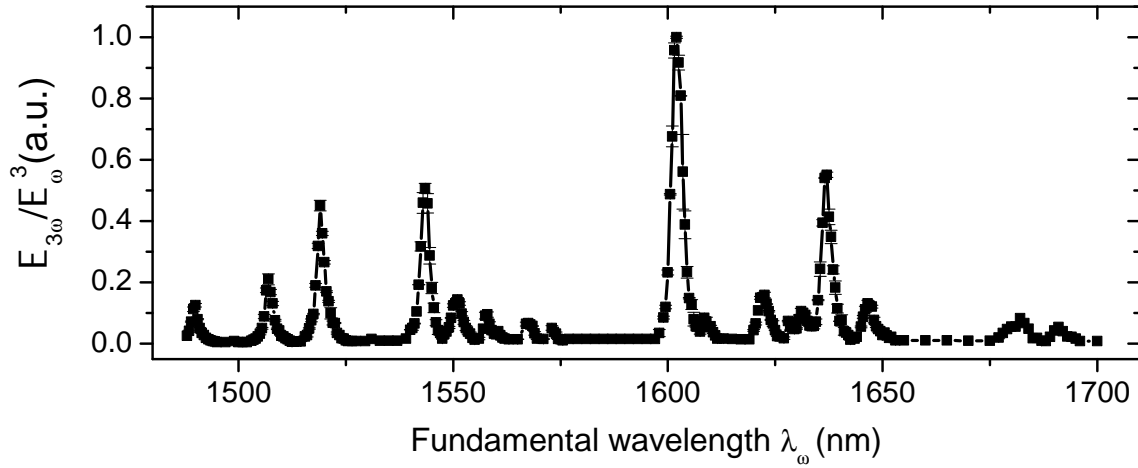


Figure 4.23 – Normalized third-harmonic spectrum in the fiber with a core size $a = 2.30 \mu\text{m}$ and a length $L = 9.2 \text{ cm}$. \mathcal{E}_ω and $\mathcal{E}_{3\omega}$ are the fundamental and third-harmonic energies respectively.

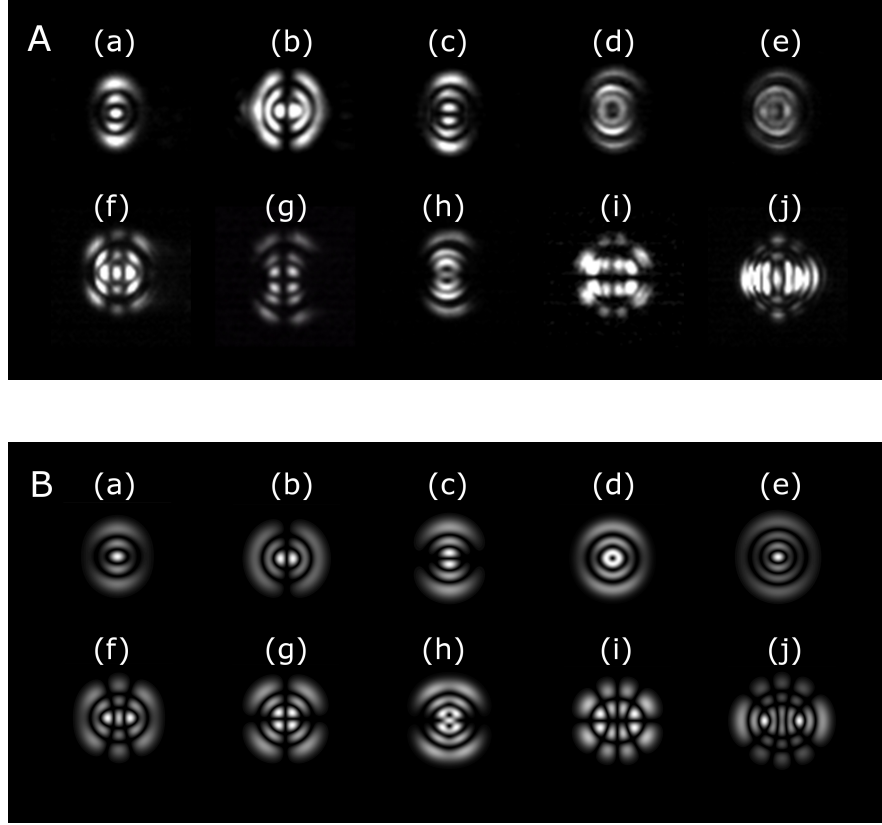


Figure 4.24 – Observed (A) and calculated (B) third-harmonic transverse intensity distributions.

with a core radius of $2.19\mu\text{m}$ using the setup described in frame A of Figure 4.6. Figure 4.24 (A) exhibits experimental modes, while (B) corresponds to calculations. Those distributions can be interpreted as Ince-Gauss modes as in Section 4.1.3.2, implying once more ellipticity in the fiber core.

Table 4.6 gives the names of the modes presented in Figure 4.24: they are labeled as $\text{IG}_{p,m,\epsilon}^k$ where p and m are the order and degree respectively, ϵ the ellipticity, and $k \in \{o, e\}$ stands for odd and even; or $\text{HIG}_{p,m,\epsilon}^k$ with $k \in \{+, -\}$ in the case of helical beams.

The transverse field and phase distributions corresponding to the intensities shown in Figure

Mode label	a	b	c	d	e
Mode name	$\text{IG}_{4,0,0.5}^e$	$\text{IG}_{5,1,0.5}^e$	$\text{IG}_{5,1,0.5}^o$	$\text{HIG}_{5,1,0.75}^\pm$	$\text{IG}_{6,0,0.25}^e$
	f	g	h	i	j
	$\text{IG}_{6,2,2}^e$	$\text{IG}_{6,2,0.5}^o$	$\text{IG}_{6,0,1}^e + i\text{IG}_{6,2,1}^e$	$\text{IG}_{6,4,2}^o$	$\text{IG}_{8,4,2}^e$

Table 4.6 – Designation of the transverse modes, as $\text{IG}_{p,m,\epsilon}^k$: p is the order, m the degree, ϵ the ellipticity, and $k \in \{o, e, +, -\}$ in the case of odd, even or helical beams.

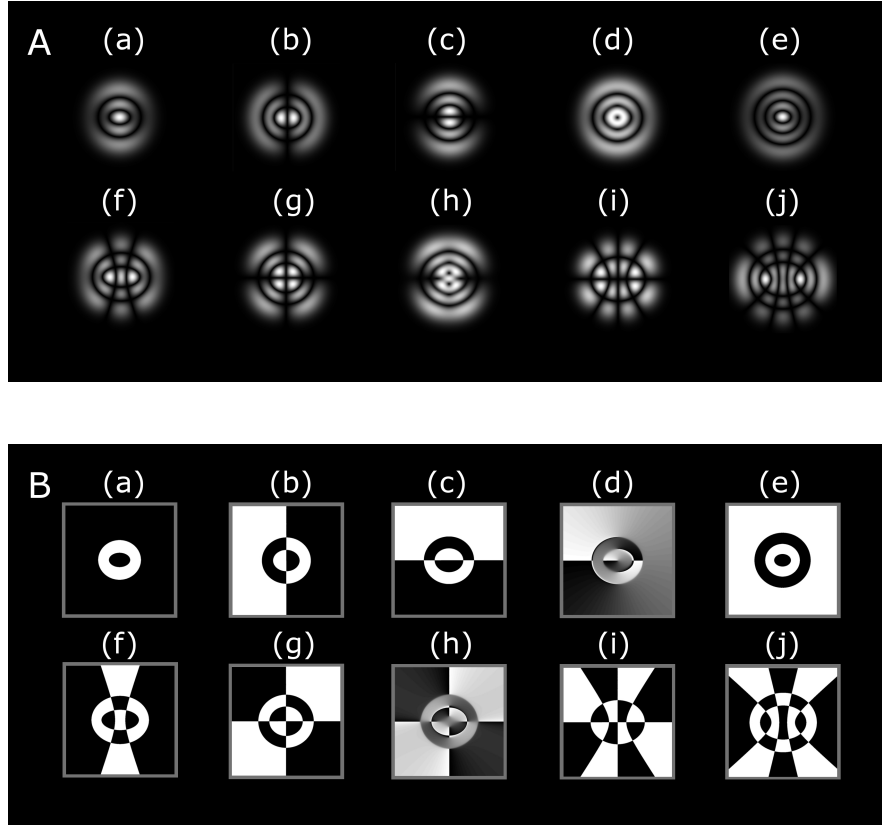


Figure 4.25 – Calculated third-harmonic transverse field (A) and phase (B) distributions.

Peak number	1	2	3	4	5	6	7
$\lambda_\omega(\text{nm})$	1440	1454.5	1470	1473	1490	1501	1549
$\lambda_{3\omega} = \lambda_\omega/3$ (nm)	480	484.8	490	491	496.7	500.3	516.3
Transverse distribution	c, g, h	d, e, f, g	c, f, i, j	c, i, j	b, i	not captured	a

Table 4.7 – Link between the various phase-matching wavelengths and the observed transverse modes.

4.24 have also been computed. They are shown in Figure 4.25 (frame A for the modulus, frame B for the phase). On Figure 4.26 are given the three-dimensional representations of these modes for a better clarity of the signs.

Table 4.7 brings together Figures 4.22 and 4.24: it links the peaks of the third-harmonic spectrum (labeled with numbers 1 to 7) to the modal distributions that are observed (labeled with lower case letters a to j).

Lastly, we end this section by having a look at the effective interaction areas for the different interaction configurations corresponding to Figure 4.22. They are defined in Equation (4.22).

Considering the fundamental Gaussian mode as the fundamental beam, the overlap integral can be zero due to geometrical considerations [54, 55]. This is the case if the field $F_{3\omega}$ changes

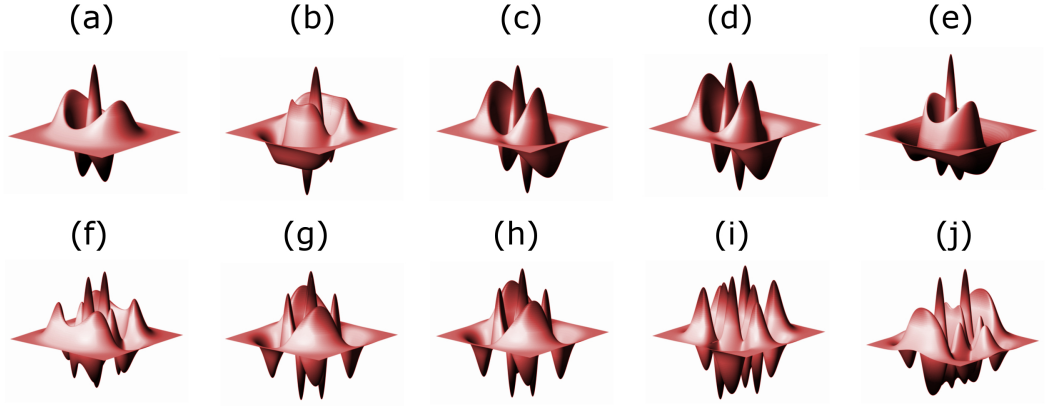


Figure 4.26 – 3-dimensional representation of the calculated third-harmonic transverse field distributions.

Modes IG	Modes LP	λ_c (μm)	Modes IG	Modes LP	λ_c (μm)	Modes IG	Modes LP	λ_c (μm)
$\text{IG}_{0,0}^e$	LP_{01}	none	$\text{IG}_{1,1}^{e/o}$	LP_{11}	2.39	$\text{IG}_{3,3}^{e/o}$	LP_{31}	1.12
$\text{IG}_{2,0}^e$	LP_{02}	1.50	$\text{IG}_{3,1}^{e/o}$	LP_{12}	1.04	$\text{IG}_{5,3}^{e/o}$	LP_{32}	0.68
$\text{IG}_{2,2}^{e/o}$	LP_{21}		$\text{IG}_{5,1}^{e/o}$	LP_{13}	0.66	$\text{IG}_{7,3}^{e/o}$	LP_{33}	0.50
$\text{IG}_{4,0}^e$	LP_{03}	0.82	$\text{IG}_{7,1}^{e/o}$	LP_{14}	0.49			
$\text{IG}_{4,2}^{e/o}$	LP_{22}							
$\text{IG}_{6,0}^e$	LP_{04}	0.57						
$\text{IG}_{6,2}^{e/o}$	LP_{23}							

Table 4.8 – Link between IG and LP modal distributions and corresponding cut-off frequencies for $a = 2.19 \mu\text{m}$.

sign, and if the sum of its positive values equals the sum of its negative ones over the transverse plane. For instance, the mode IG_{51}^e (mode b in Figure 4.24) cannot be generated from a fundamental Gaussian mode, their overlap integral reducing to zero. We stress that we indeed do not deal with intensities here. Therefore, the understanding of each third-harmonic mode requires to consider every transverse mode possible for the fundamental beam. Their existence relies on the values of the cut-off frequencies that can be calculated for LP modes from Equation (1.94) and the values of the normalized frequencies shown in Figure 1.12. The corresponding cut-off wavelengths are listed in Table 4.8, and related to IG modes.

- For $\lambda_\omega \geq 1.5 \mu\text{m}$ (peak 7, *i.e.* mode a), only IG_{00}^e and $\text{IG}_{11}^{e/o}$ exist.
- For $1.425 \mu\text{m} \leq \lambda_\omega \leq 1.5 \mu\text{m}$ (all other cases, 1 to 5, *i.e.* modes b to j), modes IG_{20}^e and $\text{IG}_{22}^{e/o}$ exist in addition to the previous ones.

The values of the effective interaction areas are summarized in Table 4.9. The symbol ∞ means that the effective interaction area is infinite, hence the overlap integral zero.

		Modes at λ_ω					
Modes at $\lambda_{3\omega}$		$\text{IG}_{0,0}^e$	$\text{IG}_{1,1}^e$	$\text{IG}_{1,1}^o$	$\text{IG}_{2,0}^e$	$\text{IG}_{2,2}^e$	$\text{IG}_{2,2}^o$
(a)	$\text{IG}_{4,0,0.5}^e$	931	∞	∞	/	/	/
(b)	$\text{IG}_{5,1,0.5}^e$	∞	103	∞	∞	∞	∞
(c)	$\text{IG}_{5,1,0.5}^o$	∞	∞	87.5	∞	∞	∞
(d)	$\text{HIG}_{5,1,0.75}^\pm$	∞	160	123	∞	∞	∞
(e)	$\text{IG}_{6,0,0.25}^e$	1.21×10^4	436	∞	79.5	∞	5.23×10^3
(f)	$\text{IG}_{6,2,2}^e$	1.24×10^4	295	∞	191	∞	68.5
(g)	$\text{IG}_{6,2,0.5}^o$	∞	∞	353	∞	71.7	∞
(h)	$\text{IG}_{6,0,1}^e$ $+i\text{IG}_{6,2,1}^e$	1.90×10^4	∞	∞	51.0	106	1.7×10^3
(i)	$\text{IG}_{6,4,2}^o$	∞	∞	304	∞	95.4	∞
(j)	$\text{IG}_{8,4,2}^e$	1.78×10^5	834	∞	5.23×10^3	∞	871

Table 4.9 – Table of the effective interaction areas (in μm^2) of each third-harmonic mode observed experimentally with respect to the possible fundamental modes. For the fiber of core size $a = 2.19 \mu\text{m}$.

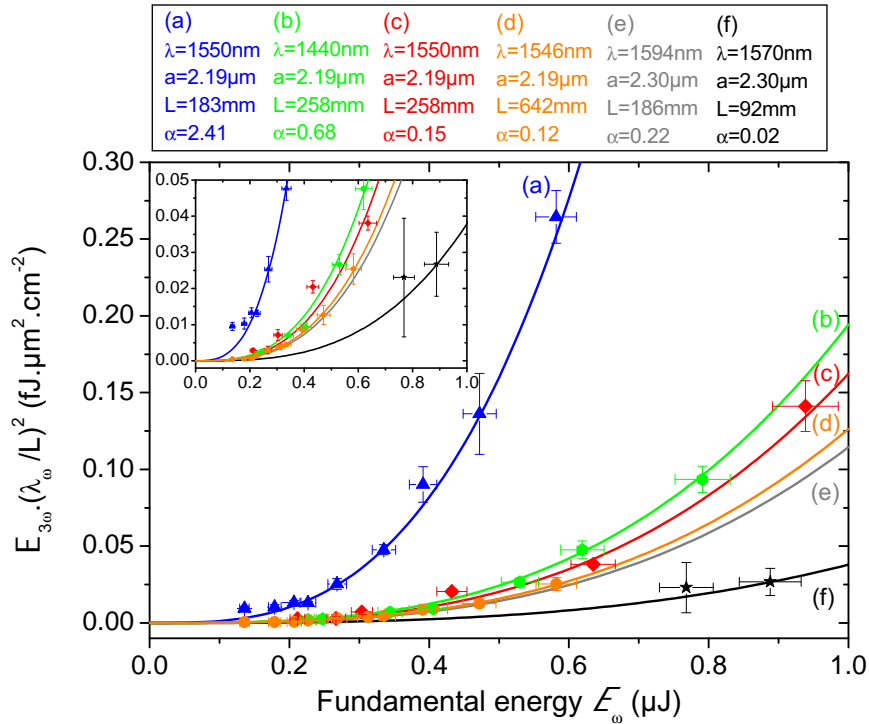


Figure 4.27 – Measured (symbols) and calculated (continuous lines) third-harmonic energies $\mathcal{E}_{3\omega}$ as a function of the fundamental energies \mathcal{E}_{ω} , rescaled by the factor $(\lambda_{\omega}/L)^2$, for the two types of fiber (core sizes $a = 2.19 \mu\text{m}$ and $a = 2.30 \mu\text{m}$) and different lengths and input wavelengths. α is a fitting parameter accounting for misknowledge of some parameters. Calculations take into account the polychromaticity of the pump beam.

We see that each third-harmonic modal distribution we observed can be explained by a fundamental wave that is allowed to propagate in the fiber. However, the fundamental beam we used is supposed to be Gaussian and then it supports only the $IG_{0,0}^e$ mode, even though its transverse “quality” is quite poor as coming out from an OPO. It is also known that a large number of modes can be excited if the beam size is not properly chosen, or if it is laterally or angularly misaligned with respect to the fiber [185].

3. Energetic properties An energy graph for different modal configurations in various fibers is presented on Figure 4.27. The third-harmonic energy $\mathcal{E}_{3\omega}$ plotted as a function of the fundamental energy \mathcal{E}_ω is normalized by the factor $(\lambda_\omega^c/L)^2$, so that all the curves can be directly compared. The solid lines are analytical calculations with a polychromatic fundamental beam based on Equation (4.21). The effective interaction area S_{eff} is taken from the previous calculations (Table 4.9). Reasonable fitting parameters α allow a good agreement with the experimental data, and still account for a misknowledge of several parameters as the effective indices, the nonlinear $\chi_{\text{eff}}^{(3)}$ coefficient, or the input energy really consumed in the THG processes.

4. Polarization properties This last section gives qualitative behaviours of the polarization of the waves. Some examples of modal distributions for two incident orientations of the polarization of the fundamental beam ($\theta_\omega^{\text{in}}$) and two orientations of the analyzer (θ_A) are presented in Table 4.10. It appears that the third-harmonic modes are elliptically polarized, sometimes linearly polarized. In addition, they are not phase-matched for every input polarization. Indeed:

- at $\lambda_\omega = 1440\text{nm}$, the two fundamental input polarizations considered allow different modal distributions (g or h) to propagate;
- at $\lambda_\omega = 1470\text{ nm}$, the four modes (c, f, i, j) do not exist for every input polarization, some of them coexisting but being not identically polarized;
- at $\lambda_\omega = 1549\text{ nm}$, the corresponding third-harmonic mode is IG_{40}^e (a) whatever its input polarization.

4.1.3.4 Interactions other than THG

THG is not the only nonlinear interaction occurring in our fibers. We give here a brief description of the other phenomena that we observed.

Infrared spectra The spectrum of Figure 4.28 consists of different peaks. The highest one corresponds to the incident wave. The others can be the result of a four-wave mixing process (FWM) or Raman scattering (RS). These two interactions have been introduced in Section 1.1.3 of Chapter 1: the first one is radiative only, while the second one has a dissipative phononic part.

The FWM interaction can be schemed as $\omega_p + \omega_p \rightarrow \omega_1 + \omega_2$, ω_p being the pump beam frequency and ω_1 and ω_2 the down-converted frequencies, as depicted in Figure 4.29 (d). In

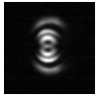




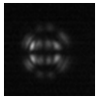

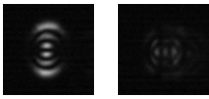
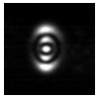

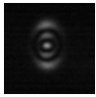
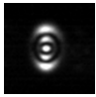
λ_ω (nm)	$\theta_\omega^{\text{in}}$	$\theta_A = -10^\circ$	$\theta_A = 80^\circ$
1440 (#1)	-10°		
	80°		
1470 (#3)	-10°		
	80°		
1549 (#7)	-10°		
	80°		

Table 4.10 – Examples of transverse distributions for two incident orientations of the polarization of the fundamental beam, and two analyzing angles.

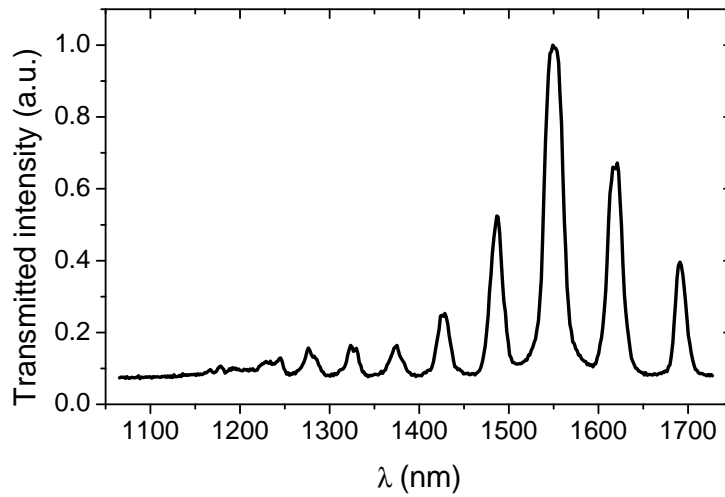


Figure 4.28 – Example of an infrared spectrum for an input wavelength $\lambda = 1549$ nm in a fiber with a core radius $a = 2.30$ μm (NIRQuest spectrometer).

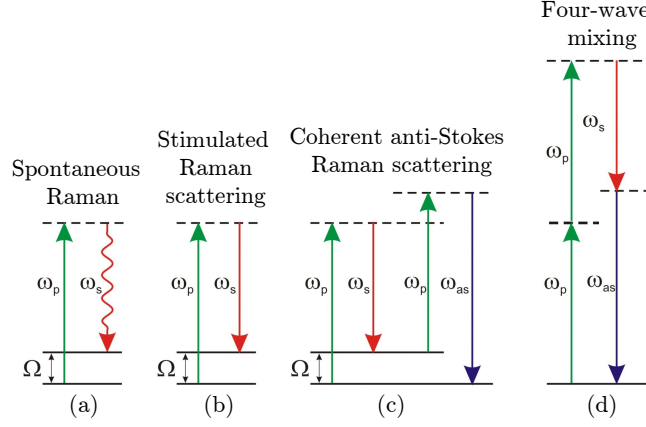


Figure 4.29 – Energetic diagrams of Raman scattering (a to c) and four-wave mixing (d) processes. Adapted from [186].

Figure 4.28, $\lambda_p = 1549$ nm, and λ_1 and λ_2 take many values. For instance, $\lambda_1 = 1486.5$ nm and $\lambda_2 = 1616$ nm; or $\lambda_1 = 1425$ nm and $\lambda_2 = 1691$ nm; and so on.

The energy conservation relationship is here fulfilled, *i.e.*:

$$\Delta E = 2\hbar\omega_p - \hbar\omega_1 - \hbar\omega_2 \simeq 10^{-28} \text{ J}, \quad (4.43)$$

while the phase-matching relationship in the collinear case is not:

$$\Delta k = \frac{1}{c} [2n_{\text{eff}}(\omega_p)\omega_p - n_{\text{eff}}(\omega_1)\omega_1 - n_{\text{eff}}(\omega_2)\omega_2] \simeq 10^3 \text{ to } 10^5 \text{ rad.m}^{-1}. \quad (4.44)$$

Those latter calculations have been done for every transverse mode existing at those wavelengths, with the available dispersion equations. As a consequence, FWM is not very likely to occur here.

Note that the “nonlinear” part of the effective indices, so far neglected, cannot compensate the “linear” phase mismatch. To do so, a calculation of the total phase mismatch indicates that a pump mean power higher than 1000 W would be needed.

We turn now to Raman scattering. Spontaneous Raman scattering is a bare non elastic diffusion phenomena: the optical frequency is reduced via energetic transfert on the vibrational modes of the medium, the phonons, of frequency Ω . They are optical phonons in the case of Raman scattering, while they are acoustic phonons in the case of Brillouin scattering, their energies being shorter as sketched in Figure 4.30. The outgoing photon is called “Stokes”, of frequency ω_S . The energetic relationship of this process goes by $\omega_p \rightarrow \omega_S + \Omega$.

The same process can happen with an “anti-Stokes” photon, of frequency $\omega_{AS} > \omega_S$, via the relation $\omega_p + \Omega \rightarrow \omega_{AS}$. Nonetheless, its probability is less important than the Stokes one since that interaction needs the presence of a phonon to occur. Therefore the energies of the Stokes \mathcal{E}_S and anti-Stokes \mathcal{E}_{AS} contributions obey $\mathcal{E}_{AS} \ll \mathcal{E}_S$.

Afterwards, the nonlinear phenomena of stimulated Raman scattering (SRS) can occur, which can be seen as an amplification of the Stokes photon by coherent stimulation. This is a $\chi^{(3)}$ process, ruled by $\omega_p + \omega_S \rightarrow \omega_S + \omega_S + \Omega$. It is then possible to generate anti-Stokes photons: this is the coherent anti-Stokes Raman scattering (CARS) process. As a result, $\omega_p + \omega_p \rightarrow \omega_S + \omega_{AS}$ is still occurring, hence satisfying the energy conservation equation as above.

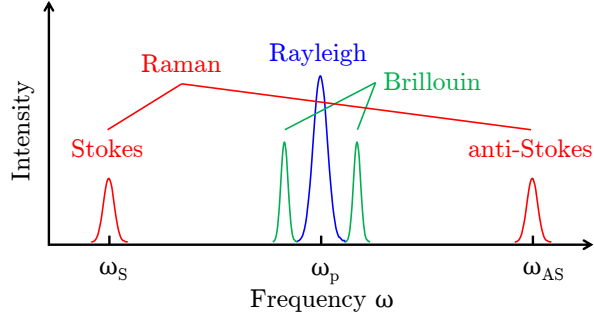
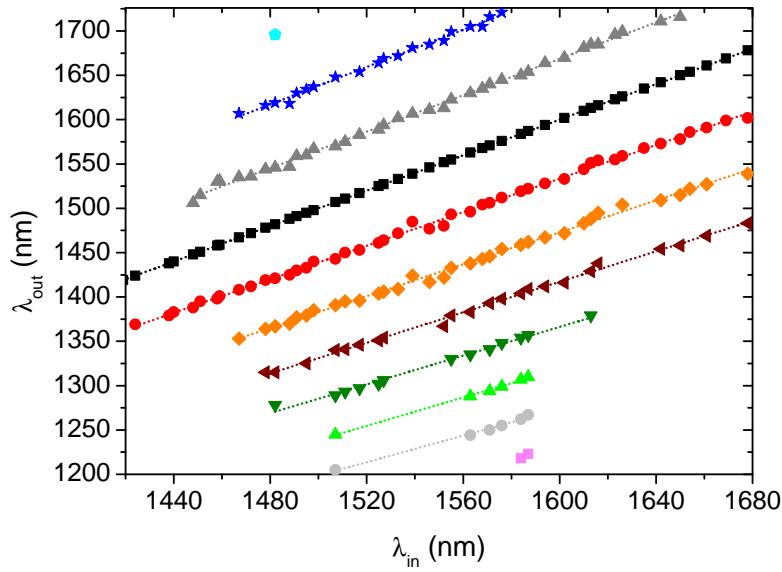


Figure 4.30 – Sketches of Raman and Brillouin scattering spectra.

Figure 4.31 – Generated wavelengths in the IR range as a function of the input wavelengths, measured in a $a = 2.19 \mu\text{m}$ fiber with a NirQuest spectrometer.

From our experimental data, the momentum conservation relationship is truly fulfilled if the Raman momentum shift ranges between 250 cm^{-1} and 315 cm^{-1} . This Raman shift is defined as $\Delta k = \frac{\Delta \lambda}{\lambda^2}$, without the 2π factor as traditionally in spectroscopy. According to the literature [111, 187, 188], the Raman shift is reported to equal 330 cm^{-1} to 440 cm^{-1} in fused silica fibers. It is then actually highly possible that the many intense peaks experimentally observed originate from RS processes. In addition, the experimental Stokes peaks are more intense than the anti-Stokes ones, a particularity of this interaction since CARS only relies on SRS as stated previously.

Figure 4.31 shows the various experimental generated wavelengths λ_{out} in the IR range as the incoming wavelength λ_{in} is tuned. It is easy to check from the linear extrapolation of these data that the energy conservation law is verified, and that the Raman shift lies around 300 cm^{-1} .

Visible spectra We give in Figure 4.32 two examples of spectra in the visible range. The third-harmonic peak can be clearly seen at $\lambda_{3\omega} = 515 \text{ nm}$. Besides, an other peak appears as well,

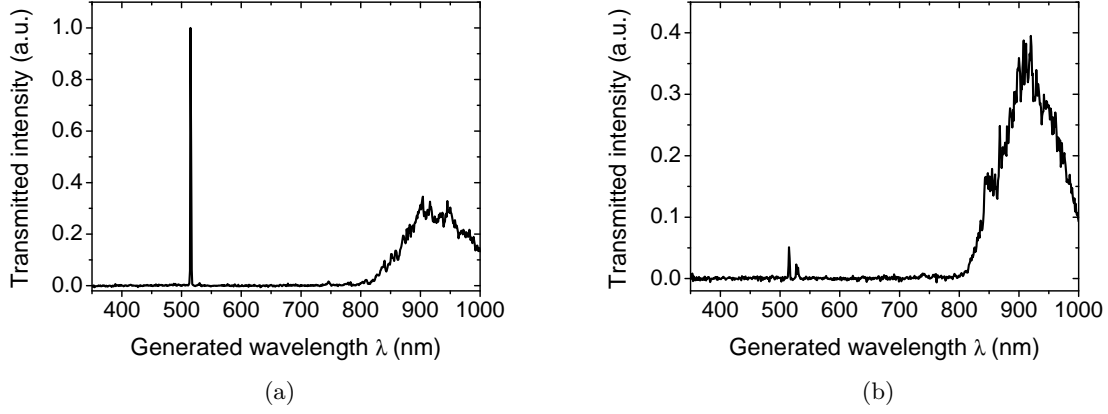


Figure 4.32 – Two examples of visible spectra, for an input wavelength $\lambda = 1545$ nm, in a $a = 2.19$ μm fiber, taken with a RedTide spectrometer.

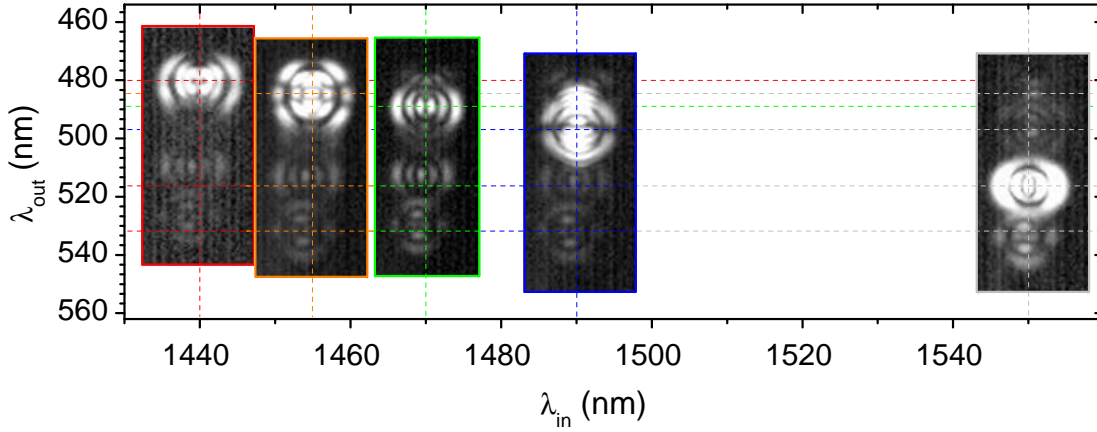


Figure 4.33 – Generated wavelengths in the visible range as a function of the input wavelengths (RedTide spectrometer), together with transverse clichés captured with a Edmund Optics camera, in a $a = 2.19$ μm fiber.

more obviously on the second graph. This is also a THG signature, but arising from another fundamental beam coming from down-conversion through Raman scattering, as just discussed previously: $\lambda'_{3\omega} = 530 \text{ nm} = \frac{1590}{3} \text{ nm}$.

Finally, a bump around 900nm which origin has not been determined, comes out of the fiber very wide and intense. Its temporal dynamics follows the one of the THG.

Figure 4.33 shows the experimental generated wavelengths λ_{out} and the corresponding transverse distributions in the visible range as a function of the fundamental wavelengths λ_{in} . Several modes are visible. It comes from the fact that the incoming wavelength generates other frequencies in the IR through Raman processes. These frequencies are very likely to give birth to a third-harmonic signal when positionned at a phase-matching frequency.

4.1.4 Spontaneous TPG

The previous part devoted to THG allows us to define at best an intermodal spontaneous degenerated TPG experiment. TPG being the reverse process of THG, the pump beam, at $\lambda_{3\omega} = 516.5$ nm, will have a LP₀₃ modal distribution, while the triplet beam, at $\lambda_{\omega} = 1549.5$ nm, will exhibit a LP₀₁ distribution. This section gives theoretical estimates on the numbers of generated triple photons in these conditions. They differ quite a lot from numbers reported elsewhere [16, 119], but are in good agreement with other calculations [12, 109]. The present calculation results in an extremely low generation rate, for the present experimental configuration. We give insights to overcome the smallness of this conversion efficiency. The preparation of the experiment is also the subject of this section.

4.1.4.1 Conversion efficiencies calculation

The quantum model derived previously in the group and presented in Section 2.2.1.4 allows us to calculate the number of photons that can be generated in our fibers in the spontaneous TPG regime. The expression of the spectral density is the term T_4 of Equation (2.10), derived in the case of an undepleted, classical and monochromatic pump. The δ function had not been taken into account for the reasons mentioned in Section 2.2.1.4. As not spectrally restrictive, the physical meaning of this characteristic time had been difficult to comprehend. Its absence leaves the expression incorrectly dimensioned. However, its understanding becomes clear by performing a full polychromatic calculation, which main ideas are done in the present section.

Analytical integral expression In the weak gain hypothesis, the resolution of the evolution equation (1.132) of one of the triplet mode gives [16, 120]:

$$\hat{a}_1(\omega_1, L) = \hat{a}_1(\omega_1, 0) - i \iint \frac{d\omega_0}{2\pi} \frac{d\omega_2}{2\pi} \Phi(\omega_0, \omega_1, \omega_2, L) \hat{a}_0(\omega_0, L) \hat{a}_2^\dagger(\omega_2, L) \hat{a}_3^\dagger(\omega_0 - \omega_1 - \omega_2, L), \quad (4.45)$$

where Φ and Γ are defined in Equations (2.11) and (1.128) respectively, and reminded below:

$$\begin{cases} \Phi(\omega_0, \omega_1, \omega_2, L) = \Gamma(\omega_0, \omega_1, \omega_2) L \text{sinc}\left(\frac{\Delta k^{(3)}(\omega_0, \omega_1, \omega_2)L}{2}\right) e^{-i \frac{\Delta k_{\text{eff}}^{(3)}(\omega_0, \omega_1, \omega_2)L}{2}} \\ \Gamma(\omega_0, \omega_1, \omega_2) = \frac{\hbar}{4\epsilon_0 c^2 S_{\text{eff}}} \sqrt{\frac{\omega_0 \omega_1 \omega_2 (\omega_0 - \omega_1 - \omega_2)}{n(\omega_0) n(\omega_1) n(\omega_2) n(\omega_0 - \omega_1 - \omega_2)}} \chi_{\text{eff}}^{(3)}(\omega_0, \omega_1, \omega_2). \end{cases} \quad (4.46)$$

We consider the pump as classical, $\hat{a}_0 \rightarrow a_0$, and polychromatic. In the parametric fluorescence regime, the spectral density of field 1 is written as:

$$\begin{aligned} n_1(\omega_1, L) &= \langle 0_1, 0_2, 0_3 | \hat{a}_1^\dagger(\omega_1, L) \hat{a}_1(\omega_1, L) | 0_1, 0_2, 0_3 \rangle \\ &= \iiint \frac{d\omega_0}{2\pi} \frac{d\omega_2}{2\pi} \frac{d\omega'_0}{2\pi} \frac{d\omega'_2}{2\pi} \Phi^*(\omega'_0, \omega_1, \omega'_2, L) \Phi(\omega_0, \omega_1, \omega_2, L) |a_0(\omega_0, L)|^2 \\ &\quad \times \langle 0_1, 0_2, 0_3 | \hat{a}_3(\omega'_0 - \omega_1 - \omega'_2, L) \hat{a}_2(\omega'_2, L) \hat{a}_2^\dagger(\omega_2, L) \hat{a}_3^\dagger(\omega_0 - \omega_1 - \omega_2, L) | 0_1, 0_2, 0_3 \rangle \\ \Leftrightarrow n_1(\omega_1, L) &= \iint \frac{d\omega_0}{2\pi} \frac{d\omega_2}{2\pi} |\Phi(\omega_0, \omega_1, \omega_2, L)|^2 n_0(\omega_0, L). \end{aligned} \quad (4.47)$$

The correspondance with the monochromatic pump can be performed by doing $\mathcal{A}_0(\omega_0^c, L) = \int d\omega a_0(\omega, L)$, *i.e.* $\mathcal{A}_0(\omega_0^c, L) = \frac{\Delta\omega}{2\pi} a_0(\omega_0^c, L)$. $\Delta\omega$ is the discretisation interval in frequency: it is linked to the length of an unidimensional discretisation box, written L' , large in front of all characteristic lengths of the physical problem, through $\Delta\omega = \frac{2\pi c}{L'}$ [59]. Its numerical value is not obvious to assign. Then Equation (4.47) becomes:

$$n_1(\omega_1, L) = \int \frac{d\omega_2}{2\pi} |\Phi(\omega_0, \omega_1, \omega_2, L) \mathcal{A}_0(\omega_0, L)|^2 \frac{2\pi}{\Delta\omega}, \quad (4.48)$$

with $\frac{2\pi}{\Delta\omega}$ playing the role of the Dirac delta function, that cannot be put aside. Albeit Equations (4.47) and (4.48) are equivalent, the first one is straightforward and does not involve any physical complication.

Note that other processes can occur simultaneously to TPG in the fiber, as it was the case for THG. Self- and cross-phase modulations will have major contributions since they are always phase-matched. Their effects are taken into account in the nonlinear part to the effective phase-mismatch.

Numerical values We consider a $\text{GeO}_2 : \text{SiO}_2$ fiber with a core radius $a = 2.19 \mu\text{m}$ and a length $L = 1 \text{ m}$. Because the spectral acceptance of the fiber is 104 nm.cm due to core size fluctuations (see Section 4.1.3.2), the whole spectrum of the pump will be involved in the process if its linewidth is smaller than 1 nm FWHM .

Based on Equation (4.22), the interaction between the modes LP_{01} and LP_{03} in this fiber involves the large effective interaction area $S_{\text{eff}} = 931 \mu\text{m}^2$ (see Section 4.1.3.2). The laser pump source delivers 10 ns pulses at 10 Hz . We consider that an energy $\mathcal{E}_0(516.4 \text{ nm}) = 1 \mu\text{J}$ enters the fiber, which is of the order of magnitude of what was injected in the IR range for the THG experiment described in Section 4.1.3. Finally, the third-order electric susceptibility is set at $2 \times 10^{-22} \text{ m}^2\text{V}^{-2}$ [30].

The application of Equation (4.47) gives the spectra shown in Figure 4.34, in the case of a monochromatic pump (a) and a polychromatic pump of spectral wideness 1 nm FWHM (b). In the second case which is more realistic, the spectral broadening is substantial. Naturally, both cases lead to the same number of generated triplets: 4.70×10^{-8} photons per second. In the insets are shown the pump spectra.

Note that in the LP description of weak guidance, the effective mode area equals $S_{\text{eff}} = 251 \mu\text{m}^2$. This big discrepancy makes the previous number of generated triplets increase by a factor 13.8.

Comparison to works previously published To evaluate the validity of our calculation, a comparison can be made with the one performed in the group of Alfred U'Ren [12, 109]. This group suggests to perform a modal phase matching between a HE_{12} (LP_{02} for weak guidance) mode at 532 nm and HE_{11} (LP_{01}) modes at 1596 nm in a fused silica fiber with a core radius of $0.395 \mu\text{m}$. The corresponding nonlinear parameter equals $\gamma = \frac{\chi_{\text{eff}}^{(3)} \omega_0}{4\varepsilon_0 c^2 n(\omega_0) S_{\text{eff}}} = 19 (\text{kmW})^{-1}$,

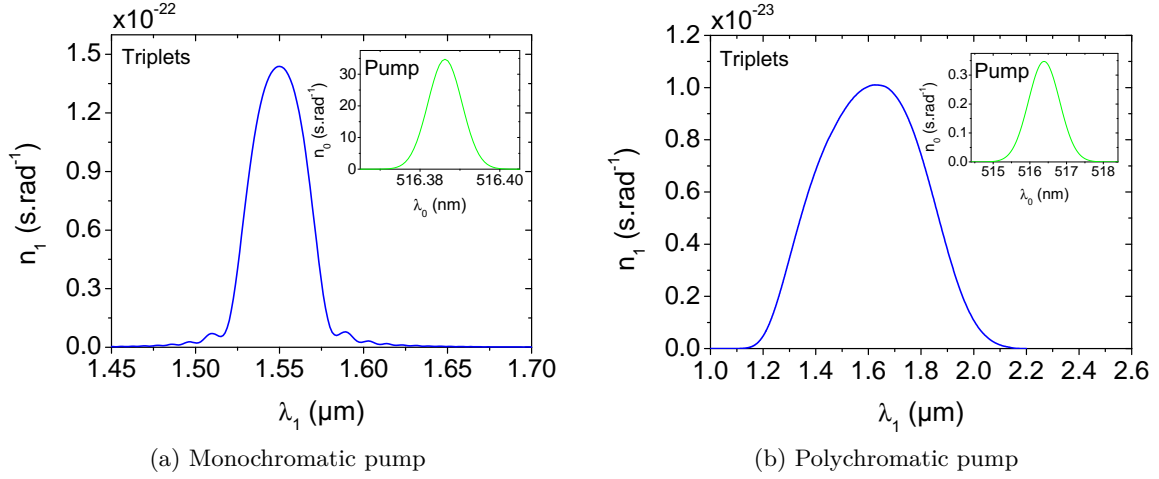


Figure 4.34 – Field 1 spectral density spectrum for $L = 1$ m and $\mathcal{E}_0 = 1$ μ J. Pump spectral density spectra are in the insets. Both calculations are performed with polychromatic pumps: (a) $\Delta\lambda^{\text{FWHM}} = 0.01$ nm that reduces to monochromaticity; and (b) $\Delta\lambda^{\text{FWHM}} = 1$ nm.

which corresponds to $\Gamma = 4.7 \times 10^{-22} \text{ s m}^{-1}$, from Equation (4.46). For a nonlinear susceptibility of $2 \times 10^{-22} \text{ m}^2 \text{ V}^{-2}$, the effective interaction area equals $S_{\text{eff}} = 8.3 \mu\text{m}^2$, which is much smaller than in our case. Their calculation is performed in a 10 cm-long fiber, with a laser of repetition rate of 100 MHz delivering 2 nJ per pulse of 100 ps. It leads to the generation of 3.8 triplets per second.

Applying our equation (4.47) to these particular values gives 0.29 triplets per second, *i.e.* a discrepancy of one order of magnitude with the calculation of the U'Ren, which may be explained by the fact that their effective indices are not known and have consequently been replaced by ours.

The semi-classical resolution from S. Richard *et al.* states that a generation of 0.2 triplets per second can be achieved in a 1 m-long fiber, with 1 W average power [119]. The modal configuration is the LP₀₁/LP₀₃ largely discussed so far, in the $a = 2.30 \mu\text{m}$ fiber. Our quantum resolution leads to 2.61×10^{-3} triplets per second (1 per 6 minutes). Note however that an average power of 1 W is much too high for our laser source as it would correspond to 0.1 J per pulse.

Effective interaction area We come back here to the definition of the effective interaction area S_{eff} . In the case of cross-phase modulations (XPM) between LP₀₁ and LP₀₃ transverse modes, we remind that $S_{\text{eff}}^{\text{XPM}}$ writes as:

$$S_{\text{eff}}^{\text{XPM}} = \frac{\iint_{\mathbb{R}^2} |F_{01}(\vec{r}_t)|^2 dS \iint_{\mathbb{R}^2} |F_{03}(\vec{r}_t)|^2 dS}{\iint_{\mathbb{R}^2} |F_{01}(\vec{r}_t)|^2 |F_{03}(\vec{r}_t)|^2 dS}, \quad (4.49)$$

with \vec{r}_t the transverse coordinate vector. This expression is different from the one involved for TPG, *i.e.* from Equation (4.22). We remind that it indeed comes naturally from the coupled equations in field amplitudes (see Section 1.3.3). Yet, it may seem physically acceptable that

the overlap between the two modal configurations remains unchanged in the cases of TPG or XPM as they precisely involve the same modes. This actually corresponds to a vision where the intensities, and not the fields, are involved in Equation (4.22). In that case, $S_{\text{eff}}^{\text{XPM}} = 16.6 \mu\text{m}^2$. The numerical application of Equation (4.47) with our experimental setup gives 1.47×10^{-4} triplet photons per second, *i.e.* 1 triplet every other hour. This number is four orders of magnitude higher than the one arising from the calculation with S_{eff} from Equation (4.22). It is still low, but the detection of triplets should be achievable with the avalanche photodiode (APD) presented afterwards in a subsequent section. Performing the experiment would then be the only way to solve this question.

Outlook

- The easiest (but more expensive!) idea to generate enough triplets to be detected is to use a high repetition rate laser. Energies coupled in the fiber will be of the order of the nJ. With a 100 MHz repetition rate, the pulse duration of the source has to be of less than the nanosecond. For instance, a number of 4.67×10^{-3} triphotons per second can be generated, *i.e.* 1 every 3.6 minutes, for 1 nJ of pump with 10 ps pulses at a repetition rate of 100 MHz injected in a 10 cm-long fiber².
It is also possible to use a continuous laser source. An equivalent number of triplets can be generated with a 0.1 W average power in a 10 cm-long fiber. In that case, longer fibers can be used.
- An alternative is to confine even more the electromagnetic field so that the overlap integral increases, as in the theoretical proposal of Corona *et al.* Taking their effective interaction area of $8.3 \mu\text{m}^2$, with our 10Hz source and a fundamental energy of 1 μJ leads to 5.89×10^{-4} triplets generated per second, *i.e.* 1 every 28 minutes.
- Increasing the interaction length over several meters would lead to a decrease of the acceptance as it can be seen in Figures 4.4b and 4.4d. In other words, all the pump photons would not participate in the process.
- The incoming energy could as well be increased: the coupling efficiency may be improved with an incoming beam geometry more suitable to the fiber.
- Lastly, materials with higher third-order nonlinear susceptibilities can be considered. This is the case of the chalcogenide family. The last section 4.2 is dedicated to them.

4.1.4.2 Towards the experiment

This section introduces the phase masks necessary for the preparation of the modal distribution of interest, and the detection stage.

²It is indeed important to adapt the length of the fiber to about 10 cm in the picosecond regime because of the temporal walk-off between the interacting waves (see Section 4.1.2).

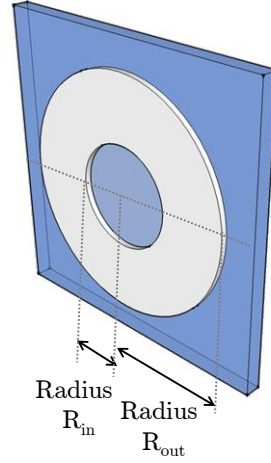


Figure 4.35 – Design of a phase mask for a conversion between LP₀₁ and LP₀₃ modes.

Phase masks In order to achieve the nonlinear interaction between the LP₀₁ and LP₀₃ modal distributions, it is important to prepare the Gaussian pump beam generated by the OPO described in Section 4.1.3.1 into a LP₀₃ mode. To do so, a phase mask has been fabricated at the Laboratoire de Photonique et Nanostructure of Marcoussis. It consists of a metallic layer deposited as a ring on a glass plate as pictured in Figure 4.35.

Its transmission is either 1 (in the blue region) or -1 (in the gray region). The thickness e of the metallic ring film is calculated so that the dephasing of the wave equals π for λ according to:

$$e(\lambda) = \frac{\lambda}{2(n(\lambda) - 1)}, \quad (4.50)$$

where n is the refractive index of the deposited material. The mask geometry has been calculated by Chen [185] by integrating the amplitude of the LP mode of interest over the transverse plane and taking into account the transmission of the phase mask. The ratio between the inner and outer radii R_{in} and R_{out} is given by:

$$\frac{R_{\text{in}}}{R_{\text{out}}} = 0.414. \quad (4.51)$$

Lastly, the modal interaction is optimized for a given waist of the optical beam W_{opt} before the entrance of the fiber (*i.e.* after the focusing microscope objective), and for given radii R_{in} and R_{out} if the mask is put at the waist position. The optimal values of these quantities are [185]:

$$\begin{cases} W_{\text{opt}} = 2.20W_c \\ R_{\text{in}} = 0.541W_c \\ R_{\text{out}} = 1.31W_c, \end{cases} \quad (4.52)$$

where W_c is the characteristic beam radius for our fiber, defined as $W_c = \sqrt{\frac{2}{v}}a$, v being the normalized frequency defined in Equation (1.85) and a the fiber core radius. Therefore, for a fiber with a core radius of 2.19 μm and at $\lambda_{3\omega} = 516.5$ nm, the previous equations lead to

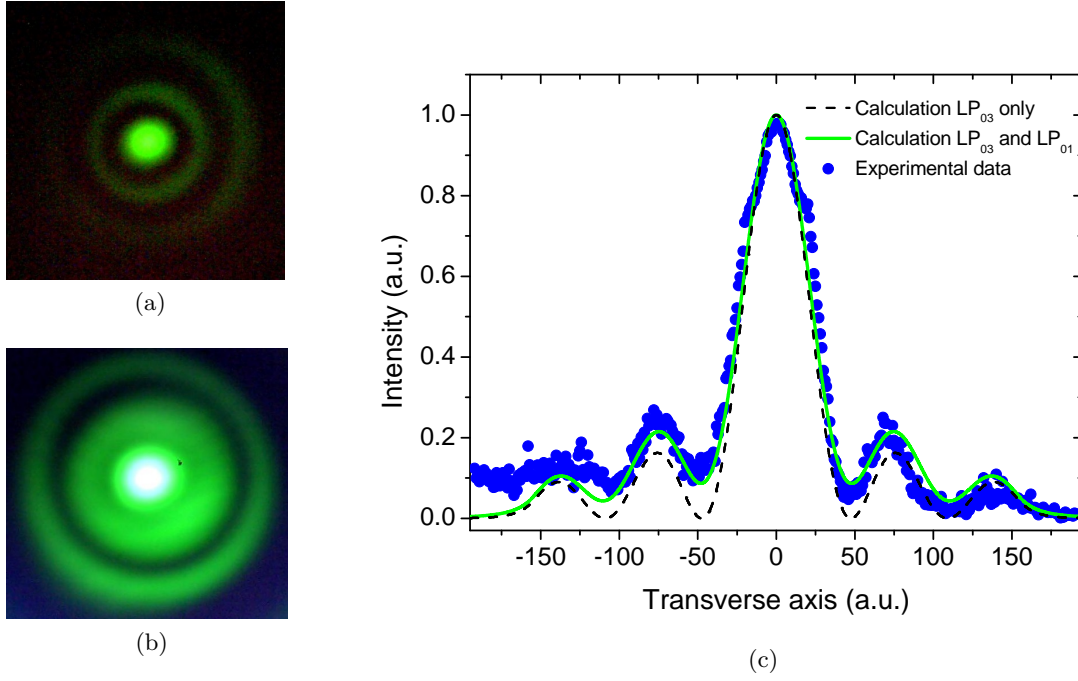


Figure 4.36 – Transverse distributions of the LP_{03} mode generated through the phase mask: without (a) and with (b) saturation. Calculated and experimental profiles in (c), corresponding to (a).

$W_c = 1.26 \mu\text{m}$, $W_{\text{opt}} = 2.77 \mu\text{m}$, $R_{\text{in}} = 0.68 \mu\text{m}$ and $R_{\text{out}} = 1.65 \mu\text{m}$. The optimal values before the microscope objective can then be calculated knowing its magnification. Note also that LP_{03} is the strongest mode excited for $W > 0.62W_c = 0.78 \mu\text{m}$ [185].

From an experimental point of view, it may be convenient to use a lens on a translation stage in front of the mask so as to adapt the beam and mask sizes, and therefore find easily the optimal coupling.

According to the theoretical work of [185], the mode conversion efficiency reaches 76.9% if there is no transverse misalignment. The remainder is converted into other modes.

We have available phase masks with inner radii ranging from 50 to 500 μm , by step of 50 μm . A transverse profile of the beam after propagation through a phase mask is shown on Figure 4.36a. Because the contrast of this picture makes the rings hard to see, Figure 4.36b presents the same profile with more input power. A unidimensional section of the non-saturating picture 4.36a is presented as blue dots on Figure 4.36c. The calculation for the LP_{03} mode using Equations (1.88) and (1.97) is shown in black dashed line. It does not explain that the minima are not zeroes. Another calculation that takes into account two contributions, 90% of LP_{03} and 10% of LP_{01} , is then performed because the conversion efficiency of the mask does not equal 1. The corresponding curve is shown as the green solid line and is in better agreement with the experimental data. We do not need to consider any other mode. The modal conversion efficiency of our phase mask is then around 90%, much more than the 77% predicted by the theory. Note that there is a drift on the left-hand side of the figure that is likely due to external light coming from the environnement during the capture, and might as well be taken in consideration in the calculations.

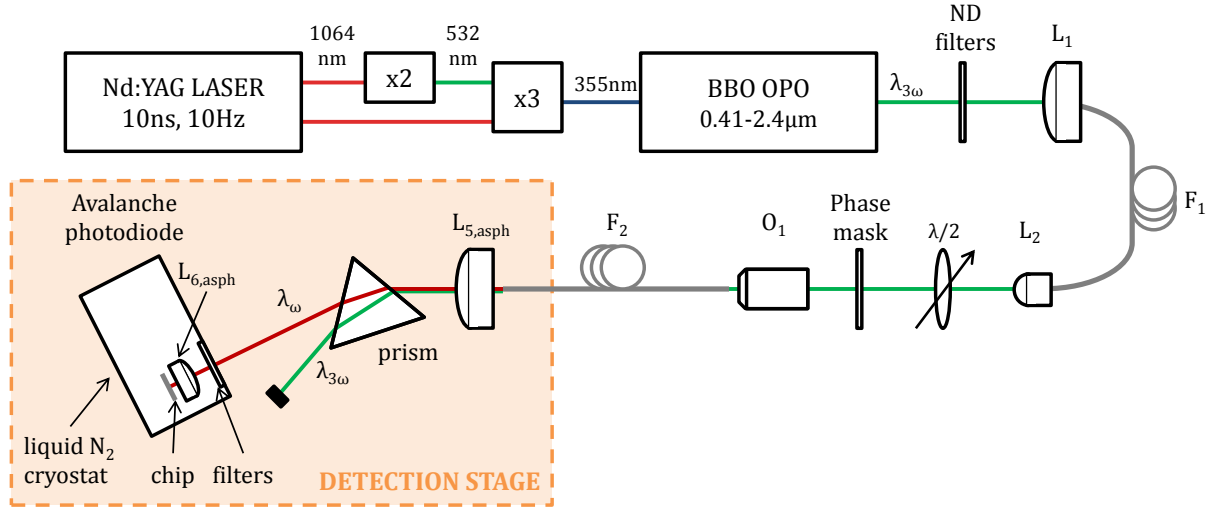


Figure 4.37 – Experimental setup used for TPG.

Experimental setup The experimental setup is very similar to the one described in Section 4.1.3.1 for THG. The input beam is also generated from the quadratic OPO pumped by the nanosecond Nd:YAG laser at 10 Hz, but here at $\lambda_{3\omega} = 516$ nm. The phase mask is inserted before the focalizing microscope objective O_1 . At the output of the fiber, the beam is collected in an aspherical lens $L_{5,\text{asph}}$ of focal length 1.45 mm. The fundamental and triplet waves are spatially separated in a prism. Two filters connected to an avalanche photodiode (APD) are put on the triplet beamline. The first one is a 6 mm thick RG850 filter, AR coated at 1550 nm, that absorbs any photon at $\lambda < 850$ nm that would come from the environment. The second filter aims to remove frequencies that may perturbate the electronics of the detection. The beam is then focused on the $2.5 \times 3 \text{ mm}^2$ chip of an APD with an aspherical lens of focal length 6 mm put within the detector, so that its size on the chip is $16 \times 16 \mu\text{m}^2$. The smaller the focalisation, the smaller the response time. The APD is put in a cryostat, cooled down with liquid nitrogen, and put on two translation and a rotation stages. Its presentation is the subject of the next subsection.

We have seen in Figures 4.32 from Section 4.1.3.4 that non-expected nonlinear processes were generated, in addition to THG. This would be a serious issue here that parasitic generations occur if their wavelengths are close enough to λ_ω to be well separated by the prism. We therefore checked with our usual infrared spectrometer that this is not the case, even though it is not as sensitive as the APD.

Another filtering stage have been investigated as an alternative to the previous one. It consists of splicing our fiber to another fiber which is monomode and then does not allow the fundamental LP_{03} beam to propagate. This second fiber could be directly connected to the APD chip. The fiber splicer has been lent us nicely by Olivier Arcizet from Institut Néel. This scheme is depicted in Figure 4.38. It suffers from two major drawbacks. First, the mode conversion efficiency through the phase mask does not reach 100%, so that the fundamental beam may have a LP_{01} component that can propagate in the second fiber. In addition, some diffusion of the visible light at the fibers splice has been evidenced by our experimental tests, which may be

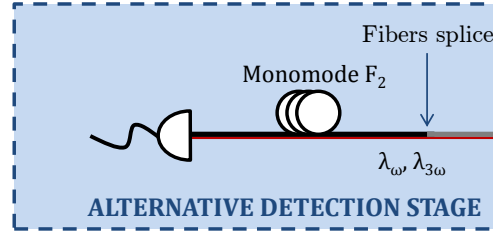
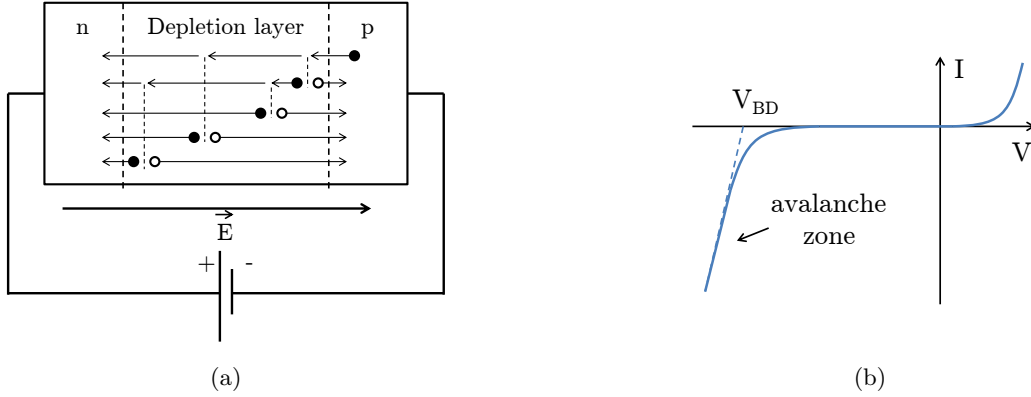


Figure 4.38 – Alternative setup for the filtering stage.


 Figure 4.39 – Schematic of an avalanche process in an APD (a). Current-voltage characteristics (b). V_{BD} stands for break-down voltage.

detrimental to our objective of keeping the correlations of the triplet state.

Avalanche photodiode The detector that we intend to use for this experiment is a HgCdTe APD that has been specially developed by Johan Rothman and collaborators at CEA-LETI, Grenoble, and mounted inside a cryostat with its electronic stages at Institut Néel by the pôle Electronique and the pôle Cryogénie within a collaboration that started in 2013. Briefly, an APD is a p-i-n junction on which is applied a high reverse bias voltage. This depletes of charge carriers a region close to the junction interface. Then, the absorption of a photon by the material creates an electron-hole pair. Due to the reverse external applied electric field, the electron (respectively hole) drifts towards the n-doped (resp. p-doped) side of the junction. And because of the high magnitude of the applied field, the electron (hole) can collide with an atom of the lattice and ionize it, which results in a new generation of an electron-hole pair. The process grows in a chain reaction, and the intensity becomes high enough to be detected [189]. Figure 4.39 gives schematic representations of the avalanche process, and of the current-voltage characteristics.

In the Grenoble APD, the transit time of the carriers in the depletion layer is in the order of 10 to 50 ps. The avalanche is stopped through a RC filter evacuation of these carriers. The photon counting time resolution is then much smaller than the triplet production rate. This events rate being lower than the repetition rate of our laser, the applied voltage on the p-i-n junction could also be synchronized with the laser pulse emission so that the avalanche is reset at each pulse.

This HgCdTe APD has several advantages compared with standard silicon or III-V semiconductor APD that we list here. Firstly, the gain increases exponentially without avalanche

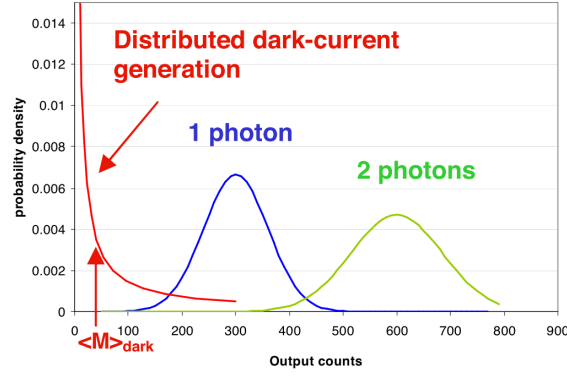


Figure 4.40 – Multiplication gain distributions for 1 and 2 photons events, and for a uniformly distributed dark current generation in the multiplication layer from [190].

break-down, which corresponds to exclusive electron multiplication [190]. Then, the excess noise factor, defined as the ratio of the input / output signal to noise ratios, is close to unity and enables a proportional photon counting. The number of photons arriving simultaneously at the depletion layer is then distinguishable, as shown in Figure 4.40. This is the strength of this APD for our goal of achieving triplet photons detection generated from parametric fluorescence according to the extreme weakness of their number. In addition, an integration detection mode is possible.

In addition, a low excess noise factor makes possible to discriminate our photonic events from the non-amplified dark current. This dark current has no photonic origin but comes from the generation of electron-hole pairs from the breaking of valence bonds thermally induced by phononic vibrations. Some standard properties of HgCdTe are interesting as well, as its very high internal quantum efficiency (collected electronic charges over incident detected photons) close to unity.

A useless millimetric piece of APD substrate has been used to estimate its transmission coefficient and optical damage threshold at 532 nm, *i.e.* around the pump phase-matching wavelength. The transmission coefficient lies around 10^{-2} at that wavelength. The sample has been put in the laser beam of growing energy, up to $33 \pm 7 \mu\text{J}$. No damage has been identified after half an hour.

4.1.5 Conclusion

In this section, THG and TPG in germanium-doped silica fibers were investigated. Although their third-order nonlinear effective susceptibilities are slightly lower than that of the oxides previously considered, fibers enable a strong confinement of the electromagnetic field over long interaction lengths, and without any pollution by quadratic processes.

The fibers that we used are designed to enable a frequency-degenerated modal phase-matching between the LP_{01} and LP_{03} transverse modes for the λ_ω and $\lambda_{3\omega}$ respectively. Because THG and TPG exhibit the same phase-matching condition, and because TPG efficiency is much weaker than THG, a full characterization of the fibers through THG is of prime importance for designing at best TPG. The nonlinear contribution to the phase-matching is negligible for the incident

energy range of the experiment.

Modal, spectral, energetic and polarization properties have been studied in fibers of core radii $a = 2.19 \mu\text{m}$ and $2.30 \mu\text{m}$, in the nanosecond regime. The corresponding phase-matching wavelengths that were measured are $\lambda_\omega = 3\lambda_{3\omega} = 1550 \text{ nm}$ and 1602 nm respectively. Due to core size fluctuations, their spectral acceptance is as high as $L\delta\lambda_\omega = 104 \text{ nm.cm}$. The transverse distribution of the 3ω wave can be interpreted as a IG_{40}^e mode rather than LP_{03} , pointing out core ellipticity. The effective interaction area therefore equals $931 \mu\text{m}^2$. The experimental conversion efficiency of the THG is quite low, of the order of 8×10^{-8} . Anisotropy has been highlighted through identification of neutral lines in the fiber and through a spectral shift of the third-harmonic signal with respect to the incident fundamental polarization. The analysis of the polarization states of the λ_ω and $\lambda_{3\omega}$ waves at the output of the fiber has enabled to conclude that the fibers belong to the uniaxial optical class, and to determine the relative magnitude between the three non-zero elements of the third-order susceptibility tensor.

Many other modal configurations for phase-matched THG have also been identified. The corresponding phase-matching wavelengths and interacting modes have been methodically studied. The experimental energetic properties are in a good agreement with theoretical calculations.

In addition to THG, Raman scattering was also highlighted, leading to the generation of many intense peaks in the infrared range.

Theoretical calculations for spontaneous TPG have been performed considering quantum polychromatic fields in the undepleted pump approximation. They imply that 4.7×10^{-8} triplets per second can be generated in 1 m-long fiber, in the case of the $\text{LP}_{01}/\text{LP}_{03}$ interaction and for $1 \mu\text{J}/\text{pulse}$ of input fundamental energy (10 ns pulses, 10 Hz repetition rate). To increase this generation rate, several options are possible: the use of either a high repetition rate or continuous laser source, of smaller core size fibers or of nonlinear materials with higher nonlinearities.

As these options are not currently available at the lab, methods for producing non-Gaussian beams and for filtering in preparation for single photon counting have been investigated. Phase masks, necessary to perform the modal conversion between the modes LP_{01} and LP_{03} have been tested, and their conversion efficiencies reach about 90%.

Nonetheless, several interpretations of the effective interaction area S_{eff} lead to conversion efficiencies with different from four orders of magnitude. It has not been possible to perform the experiment in the framework of this thesis.

4.2 Phase-matching properties of chalcogenide fibers

The last section of this manuscript deals with a theoretical study of THG and TPG in chalcogenide photonic-crystal fibers (PCF) chosen because of their giant non-linearity. We perform calculations so as to find couples of phase-matched wavelengths for a possible high efficiency TPG experiment in the future. To do so, the knowledge of the effective indices for the propagating modes is required. This task is not as straightforward with PCF as it was with step-index fibers. But we benefit here from the work done at ONERA-Palaiseau during the PhD of Claire Alhenc-Gelas and Master's degree of Laura Di Bianca in the team of Pierre Bourdon and Anne Durécu. This work is based on fibers fabricated at the Laboratoire des Verres et Céramiques de Rennes and at Laboratoire Interdisciplinaire Carnot de Bourgogne.

4.2.1 Chalcogenides photonic-crystal fibers

4.2.1.1 Properties of chalcogenides

The very high third-order nonlinear susceptibilities of chalcogenides (elements belonging to group 16 of the periodic table) is typically three orders of magnitude higher than that of oxides, as already highlighted in Section 2.2.1.3 of Chapter 2. It means that the TPG efficiency can be increased by six orders of magnitude compared to oxides. Table 4.11 gathers together third-order nonlinear coefficients $\chi_{\text{eff}}^{(3)}$ from nonlinear index n_2 measurements reported in the literature. Note that n_2 here is n_{Kerr} from Section 3.1.3.2. Its conversion into $\chi_{\text{eff}}^{(3)}$ is performed using Equation (3.10) and the linear optical coefficients are from [44, 105].

However, an important limitation comes from their weak threshold of optical damage. Table 4.12 summarizes some measurements of surface damage thresholds reported in the literature, with their experimental conditions. In the case of small laser repetition rates, the intensity damage threshold of a material is inversely proportional to the square root of the pulse duration, *i.e.* $I^{\text{th}} \propto 1/\sqrt{\tau}$. This empirical law is valid from nanosecond to picosecond pulse durations. According to that, we find that the damage threshold of the chalcogenide fibers ranges between 300 and 1300 MWcm⁻² in our experimental conditions (10 ns, 10 Hz).

The chalcogenide materials are also widely transparent, from the near infrared to about 20 μm , depending of their compositions. Figure 4.41 shows transmission spectra of millimetric chalcogenide glasses (sulfide, selenide and telluride) compared to those of silica and fluorides [199]. The typical attenuation is around 1 dBm⁻¹ at 1.56 μm [191].

4.2.1.2 Photonic-crystal fibers

Geometry Motivated by achieving low-loss fibers for telecommunications, photonic-crystal fibers, also called holey or microstructured fibers, have been introduced for the first time by P. Kaiser and coworkers in 1973 [200]. Such fibers have really aroused interest in the community since the work done by Jonathan Knight and collaborators in the mid-90s [201]. A PCF consists of a core pure of a given material surrounded by air holes structured with a given symmetry. The first chalcogenide PCF was reported in 2000 [202].

Chalcogenide	As-S	As-Se	As-S-Se	Ge-Se	Ge-As-Se	Ge-Se-Te	Ge-Se-Sb
Nonlinear coefficient $\chi_{\text{eff}}^{(3)}$ ($\times 10^{-19} \text{ m}^2 \text{ V}^{-2}$)	0.48 [191]	2.0 [191]	0.84 – 1.2 [191]	1.6 – 2.2 [103]	2.1 – 3.9 [103]	0.48 [192]	0.79 [192]
	0.72 – 0.75 [104]	4.8 [193]		0.88 – 1.8 [104]	1.5 – 2.8 [104]		
		1.1 [192]		0.26 [192]			

Table 4.11 – Effective third-order nonlinear coefficients, from n_2 measurements, [191]: spectrally resolved two-beam coupling technique, 1.55 μm ; [103]: Z-scan, 1.064 μm ; [104]: Z-scan and Mach-Zender interferometry, 1.064 μm ; [193]: Kerr spectra measurement, 1.55 μm ; [192]: Z-scan, 1.5 μm .

References	[105]	[194]	[195]	[196]	[197]	[198]
Chalcogenide	$\text{Ge}_{33}\text{As}_{12}\text{Se}_{55}$	As_2S_3	$\text{As}_{38}\text{Se}_{62}$	As_2S_3	As_2S_3	As_2S_3
Medium form	bulk glass	bulk glass	fiber	fiber	fiber	fiber
Wavelength λ (μm)	11	1.064	1.995	1.553	-	1.9
Repetition rate f (Hz)	10	10	$< 500 \times 10^6$	5	-	10
Pulse duration τ (ns)	22×10^{-3}	25×10^{-3}	10	2	-	2
Optical damage threshold (MW cm^{-2})	≥ 150	8400	300	1000	1000	2900
						2800

Table 4.12 – Optical damage thresholds of chalcogenide materials, and experimental conditions of their measurements.

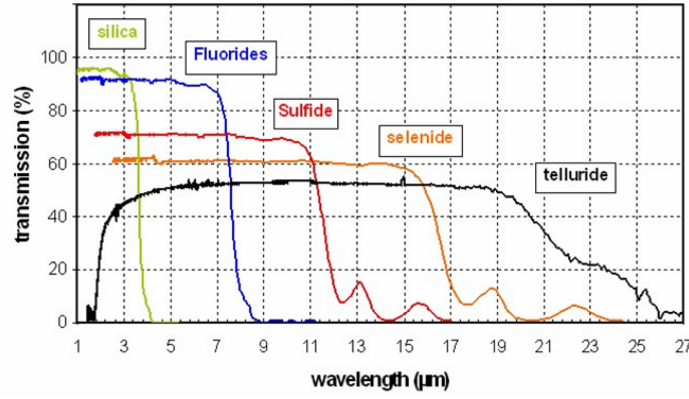


Figure 4.41 – Transmission spectra in the IR range of various glasses of few mm thickness, from [199].

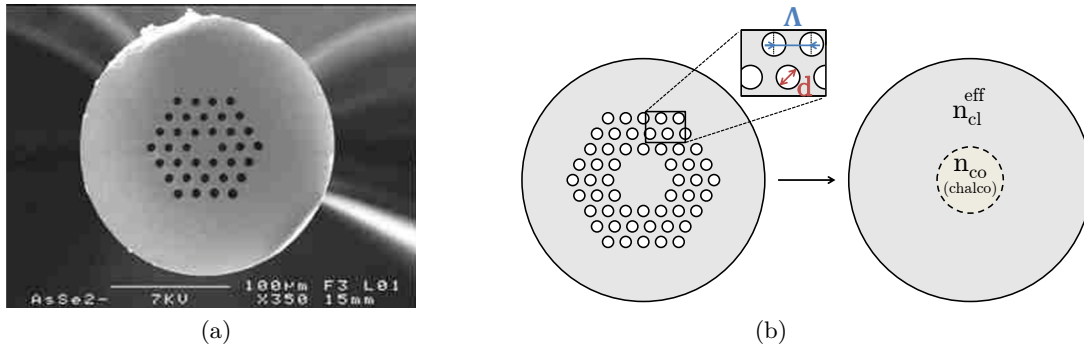


Figure 4.42 – MEB picture of an hexagonal array As_2Se_3 photonic fiber of geometric parameters $d = 3.3 \mu\text{m}$ and $\Lambda = 10 \mu\text{m}$, from [44] (a). Schematic representation and its equivalent step-index fiber (b).

Figure 4.42a shows a hexagonal array of air holes embedded in As_2Se_3 [44]. Two relevant geometrical parameters are pictured in Figure 4.42b: the diameter of the hole d , and the distance between two successive holes, or pitch of the hexagonal array, Λ .

Propagation We are considering a solid glass surrounded by air holes. In that case, the guidance occurs through modified total internal reflection similarly to conventional fibers as the effective index at the center of the fiber is higher than that of the surrounding air-material area [203]. Note also that another kind of guidance is possible in PCF, for example in hollow core PCF. In such fibers, the guidance is based on the photonic band gap effect: the light is confined in the core since the periodic structure of the cladding index gives rise to a photonic band-gap that forbid propagation in the cladding [204, 205].

Advantages Such fibers offer the possibility of having small core size, which intensify the nonlinear phenomenon. Furthermore, the choice for the geometrical parameters d and Λ enables to engineer the index of the cladding, hence the guiding properties, but also the desired phase-matching conditions.

	A	B	C
As_2S_3	5.41	0.20	0.14
As_2Se_3	7.56	1.03	0.12

 Table 4.13 – Cauchy coefficients for the As_2S_3 and As_2Se_3 glasses [211].

Fabrication process The main steps of fabrication of a PCF are the same as any conventional step-index fiber. What differs is the realization of the preform. Different fabrication processes of the preform have been proposed. A regular pattern of holes can be drilled in a chalcogenide glass rod mechanically [206] or through ultrasonic impact grinding [207]. The pattern can also be created by extrusion through a microstructured die under high temperature and high pressure [207]. Lastly, the “Stack and Draw” fabrication technique can be used but leads to high absorption losses: hollow capillaries are stacked together into a jacket tube, and drawn to obtain a fiber [201, 202, 208].

4.2.1.3 Modelling of the photonic crystal fiber

As already mentionned before, the effective indices of the propagating modes n_{eff} are needed to perform phase-matching calculations. Most accurate methods to get them are numerical, as the finite element method (FEM). But because they are very time consuming, the results through FEM only serve as a reference to improve an approximate method, referred to as effective index method (EIM). It models the PCF as an equivalent step-index fiber, as pictured in Figure 4.42b. In this approximation, the core is constituted by the chalcogenide material and the inhomogeneous cladding is replaced by an effective cladding [44, 209, 210]. The core refractive index n_{co} is therefore the one of the chalcogenide, and the effective cladding index $n_{\text{cl}}^{\text{eff}}$ becomes an homogeneous index which magnitude is lower than that of the core because of the presence of the air holes. This modelling enables to obtain analytically this effective cladding index, as well as the effective core radius a^{eff} . We will not enter into all the details that constituted the work done at ONERA, but give the necessary elements for the understanding of the model.

Core index The refractive index of the chalcogenide materials considered take the form of the following Cauchy equation:

$$n(\lambda) = \sqrt{A + \frac{B}{\lambda^2} + \frac{C}{\lambda^4}}, \quad (4.53)$$

with λ expressed in microns and the Cauchy coefficients given in Table 4.13.

Effective cladding index The guiding of a mode in the core of the fiber by total internal reflection requires that Equation (1.80) is verified, *i.e.* $k_{\text{cl}}(\omega) < \beta(\omega) < k_{\text{co}}(\omega)$. Consequently, k_{cl} has to be the highest possible, otherwise β could take values that would authorise propagation in the cladding. The mode corresponding to this cladding wavevector is referred to as the fundamental space filling mode (FSFM), since it distributes its energy more in the glass than in the air holes.

The cladding is then replaced by a single material which refractive index is equal to the effective index of the FSFM [210]. The FSFM having the same periodicity as the PCF, assumed of infinite extension, the study of the cladding can then be restricted to an hexagonal cell centered on an air hole, approximated by a circular cell of diameter $\Lambda/2$ [44]. The application of the boundary conditions on the vectorial propagation equation for the electromagnetic field on each cell limit (the derivative of the electric field vanishes) and on the air-glass interface (continuity of the tangential components of the fields) leads to the following eigenvalue equation [210]:

$$\left(\frac{P'_1(U)}{UP_1(U)} + \frac{I'_1(W)}{WI_1(W)} \right) \left(n_c^2 \frac{P'_1(U)}{UP_1(U)} + n_a^2 \frac{I'_1(W)}{WI_1(W)} \right) = \left(\frac{1}{U^2} + \frac{1}{W^2} \right) (n_{cl}^{\text{FSFM}})^2, \quad (4.54)$$

with

$$P_1(U) = J_1(U) Y_1(u) - J_1(u) Y_1(U). \quad (4.55)$$

J and Y are first and second kind Bessel functions respectively; I is the modified Bessel function of first kind; the prime symbol indicates a differentiation with respect to the argument; n_c , n_a and n_{cl}^{FSFM} are the chalcogenide, air and FSFM cladding optical indices respectively; and u , U and W fulfill:

$$\begin{cases} U &= k_0 \frac{d}{2} \sqrt{n_c^2 - (n_{cl}^{\text{FSFM}})^2} \\ W &= k_0 \frac{d}{2} \sqrt{(n_{cl}^{\text{FSFM}})^2 - n_a^2} \\ u &= k_0 \frac{\Lambda}{2} \sqrt{n_c^2 - (n_{cl}^{\text{FSFM}})^2}, \end{cases} \quad (4.56)$$

where k_0 is the vacuum propagation constant.

The effective cladding index n_{cl}^{FSFM} is deduced from the resolution of the eigenvalue equation (4.54).

Effective core radius Various empirical formulae for the effective core radius a^{eff} have been proposed and validated for silica PCF up to 2.5 μm . They are listed below:

$$\begin{aligned} a^{\text{eff}} &= 0.64\Lambda && \text{Birks } et \text{ al.} \quad [203] \\ a^{\text{eff}} &= \frac{\Lambda c_1}{1 + \exp\left(\frac{\frac{d}{\Lambda} - c_3}{c_2}\right)} && \text{Park and Lee} \quad [212] \\ a^{\text{eff}} &= \Lambda \sum_{i=0}^5 \sum_{\substack{j=0 \\ j \neq i}}^5 m_{ij} \left(\frac{\lambda}{\Lambda}\right)^i \left(\frac{d}{\Lambda}\right)^j && \text{Li } et \text{ al.} \quad [213] \end{aligned}$$

The coefficients c_i and m_{ij} are optimized from the values reported for silica PCF. The expression from Birks *et al.* is a first good approximation, but too simple to be accurate for a

	α_1	β_1	α_2	β_2	α_3	β_3	γ_3
As ₂ S ₃	-0.05113	0.7707	-0.2260	0.6505	-0.04471	0.04223	1.52
As ₂ Se ₃	-0.03325	0.7603	-0.1383	0.6282	-0.003843	0.03853	1.51

 Table 4.14 – Coefficients involved in the effective radius equation, for $\Lambda = 5 \mu\text{m}$.

wide variation of the wavelength. The proposition from Park and Lee increases the precision of the method by taking into account the ratio d/Λ , but still do not describe the spectral dependence. Lastly, the formula from Li *et al.* makes the error decrease by two orders of magnitude and takes into account the spectral variations. However, 36 empirical coefficients are required. Their optimisation is not very robust as they depend strongly on the material considered, and m_{00} does not reduce to 0.64 of the Birks' model as it is the case for silica PCF. In addition, the optimized coefficients are not unique for each Λ value [214].

A refinement has been done at ONERA by taking into account a frequency dependence in the model of Park and Lee, by comparison to the finite element method performed on the software Comsol Multiphysics [214, 215]. The effective core radius becomes:

$$a^{\text{eff}} = \frac{\Lambda c_1(\lambda)}{1 + \exp\left(\frac{\frac{d}{\Lambda} - c_3(\lambda)}{c_2(\lambda)}\right)}, \quad (4.57)$$

with

$$\begin{cases} c_1 &= \alpha_1 \frac{d}{\Lambda} + \beta_1 \\ c_2 &= \alpha_2 \frac{d}{\Lambda} + \beta_2 \\ c_3 &= \alpha_3 \left(\frac{d}{\Lambda}\right)^2 + \beta_3 \frac{d}{\Lambda} + \gamma_3. \end{cases} \quad (4.58)$$

The optimized coefficients are given in Table 4.14.

Modal effective indices The microstructured fiber being now replaced by a step-index fiber of core index n_{co} , cladding index $n_{\text{cl}}^{\text{FSFM}}$ and core size a^{eff} , the development given in Section 1.3.2 of the first chapter applies and enables the knowledge of the effective indices n_{eff} according to Equation (1.98).

This development rests on the continuity equation (1.91), obtained through a scalar resolution for weak guiding. This equation leads to the parameters u expressed as in Equations (1.96) for the fundamental mode and (1.97) for the higher order modes. A vectorial resolution is also possible, see *e.g.* [43, 212].

Validity of the model The whole model with the effective core radius from Equation (4.57) has been compared by the group at ONERA to the Li and unmodified Park and Lee models by comparison to the Comsol FEM [214]. The relative error on the fundamental mode effective

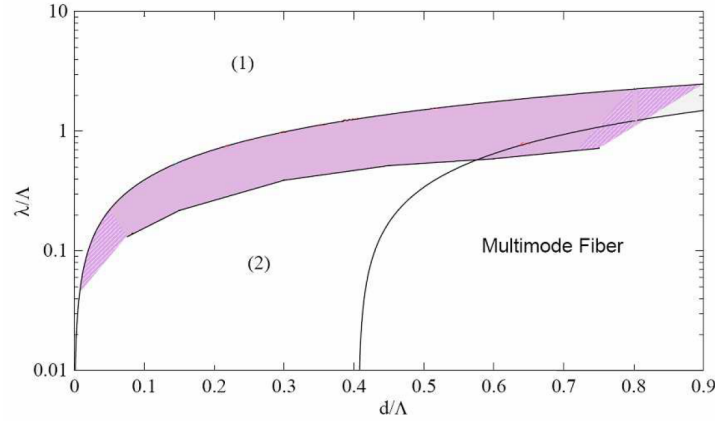


Figure 4.43 – Guidance regimes in a PCF, from [216]. (1) Mode spread in the cladding; (2) confinement of the mode in the core; transition zone in pink.

index is of about 2×10^{-5} in As_2S_3 for $\Lambda = 5 \mu\text{m}$ and $d/\Lambda = 0.8$, much below the error of the non-modified Park and Lee model (3×10^{-4}) but higher than the Li model (6×10^{-6}). It is however rather satisfactory as the coefficients are more robust than previously from one material to another, and with the pitch parameter Λ .

It is suitable in this model to consider that the extension of the microstructure is infinite. FEM calculations have shown that three hole rings are sufficient for the effective index to be precise to 10^{-5} [214].

Lastly, Figure 4.43 shows that the wavelength has to be smaller than the pitch of the microstructure for the mode to be confined in the core and the present step-index fiber model to be appropriate (see the zone 2) [216]. In addition, it is important for the coming calculations to notice that $d/\Lambda = 0.4$ is the minimum value for achieving a multimode propagation [217].

4.2.2 Phase-matching condition and fiber design

With the previous model, we are now able to perform the phase-matching calculations for TPG (or THG because it is the same from that point of view). The phase mismatch of the four interacting waves, centered at the wavelengths $\lambda_{0,1,2,3}^{\text{PM}}$, is:

$$\begin{aligned} \Delta k_{\text{eff}}^{(3)}(\lambda_0^{\text{PM}}, \lambda_1^{\text{PM}}, \lambda_2^{\text{PM}}) &= 0 \\ &= 2\pi \left[\frac{n_{\text{eff}}^{n_0 m_0}(\lambda_0^{\text{PM}})}{\lambda_0^{\text{PM}}} - \frac{n_{\text{eff}}^{n_1 m_1}(\lambda_1^{\text{PM}})}{\lambda_1^{\text{PM}}} - \frac{n_{\text{eff}}^{n_2 m_2}(\lambda_2^{\text{PM}})}{\lambda_2^{\text{PM}}} - \frac{n_{\text{eff}}^{n_3 m_3} \left(1/\lambda_0^{\text{PM}} - 1/\lambda_1^{\text{PM}} - 1/\lambda_2^{\text{PM}} \right)}{1/\lambda_0^{\text{PM}} - 1/\lambda_1^{\text{PM}} - 1/\lambda_2^{\text{PM}}} \right]. \end{aligned} \quad (4.59)$$

We neglect here at first the nonlinear term of the phase mismatch: the subsequent development is then true for small enough incident powers, but we will come back to this approximation later. The transverse distributions of the four interacting beams $n_i m_i$, $i \in \{0, 1, 2, 3\}$, are only restricted by their cut-off wavelengths. According to the transparency ranges of these materials, it is reasonable to consider that the minimum value for the pump wavelength λ_0^{PM} is $1.5 \mu\text{m}$.

For the calculation, we use the indices data for As_2S_3 and As_2Se_3 , and we can also play with the two degrees of freedom Λ and d , with two constraints: $\lambda < \Lambda$ on the one hand, and

LP modes	λ_c (μm)
LP ₀₁	none
LP ₁₁	6.82 μm
LP ₀₂ , LP ₂₁	3.04 μm
LP ₀₃ , LP ₂₂	0.902 μm

 Table 4.15 – Cut-off wavelengths λ_c with a As₂S₃ fiber with $\Lambda = 5 \mu\text{m}$ and $d = 0.85\Lambda$.

$d/\Lambda < 0.4$ for a monomode interaction or $d/\Lambda > 0.4$ for a multimode interaction on the other hand.

Fundamental monomode interaction No solution arises from the consideration of an interaction involving four LP₀₁ beams, even with the flexibility that authorizes the setting of the geometrical parameters.

Intermodal phase-matching Table 4.15 gives as an example the cut-off wavelengths in the particular case where the indices are computed from a As₂S₃ fiber with $\Lambda = 5 \mu\text{m}$ and $d = 0.85\Lambda$.

Two sets of intermodal phase-matching solutions have been identified.

- The first one involves a LP₂₁ pump around 1.96 μm and LP₁₁ triplet beams around 6 μm and non-degenerated in frequency. The interaction occurs in a As₂S₃ fiber with $\Lambda = 5 \mu\text{m}$ and $d = 0.6\Lambda$. However, the effective interaction area defined in Equation (1.100) is zero for these modal distributions. This phase-matched configuration becomes therefore useless.
- The second set involves a LP₀₂ pump and LP₀₁ triplet beams in a As₂S₃ fiber with $\Lambda = 5 \mu\text{m}$ and $d = 0.85\Lambda$. The corresponding phase-matching wavelengths are not degenerated either. Several values are possible, *e.g.*:

$$\lambda_0^{\text{PM}} = 1550.5 \text{ nm}$$

$$\begin{cases} \lambda_1^{\text{PM}} = 4439 \text{ nm} \\ \lambda_2^{\text{PM}} = 4471 \text{ nm} \\ \lambda_3^{\text{PM}} = 5102 \text{ nm} \end{cases} (A); \quad \begin{cases} \lambda_1^{\text{PM}} = 4540 \text{ nm} \\ \lambda_2^{\text{PM}} = 4530 \text{ nm} \\ \lambda_3^{\text{PM}} = 4903 \text{ nm} \end{cases} (B); \quad \begin{cases} \lambda_1^{\text{PM}} = 4766 \text{ nm} \\ \lambda_2^{\text{PM}} = 4766 \text{ nm} \\ \lambda_3^{\text{PM}} = 4438 \text{ nm} \end{cases} (C). \quad (4.60)$$

We make sure that the step-index fiber model is appropriate, as $\lambda < \Lambda$, and that a multimode interaction is possible since $d/\Lambda > 0.4$. This situation is interesting because the effective interaction area is non-zero, and it involves frequencies in the mid-IR.

The phase-matching map is shown in Figure 4.44a: it represents the phase mismatch $\Delta k_{\text{eff}}^{(3)}$ as a function of the the wavelengths λ_1 and λ_2 . The pump wavelength is fixed to $\lambda_0^{\text{PM}} = 1.55 \mu\text{m}$, and λ_3 can be found by applying the energy conservation relationship. $\Delta k_{\text{eff}}^{(3)} = 0$ means perfect phase matching. Note that the frequency-degenerated configuration is not phased-matched for this set of geometrical parameters, for any pump wavelength.

Figure 4.44b is a close-up of the previous figure around one spectral range of interest. *A*, *B*, and *C* spot the three previous particular phase-matching sets of wavelengths. *A*₁ and *A*₂ are equivalent; likewise for dots *B*, and dots *C*.

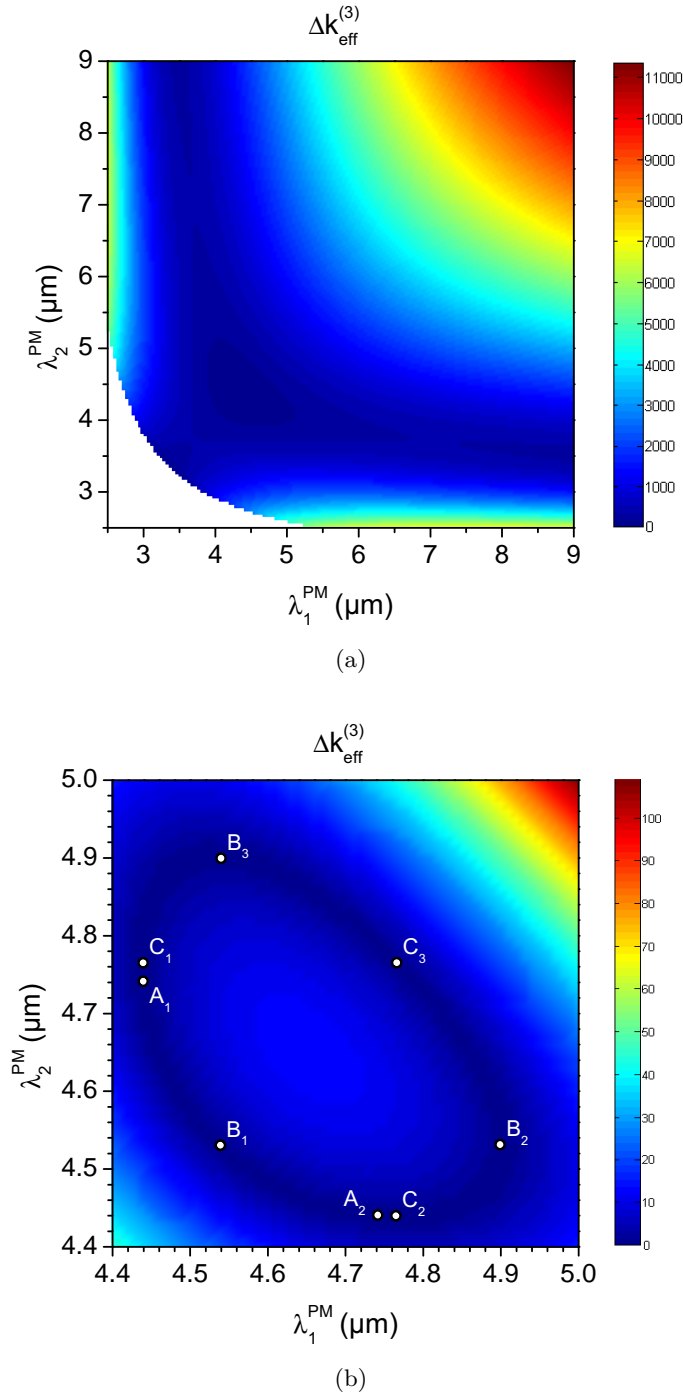


Figure 4.44 – (a) Phase-matching map: $\Delta k_{\text{eff}}^{(3)}$ as a function of λ_1^{PM} and λ_2^{PM} ; $\lambda_0^{\text{PM}} = 1551 \text{ nm}$, $\Lambda = 5 \mu\text{m}$ and $d = 0.85\Lambda = 4.25 \mu\text{m}$. (b) Restricted spectral range. A_1 and A_2 (resp. B_1 , B_2 and B_3 ; C_1 , C_2 and C_3) are equivalent phase-matching sets of wavelengths.

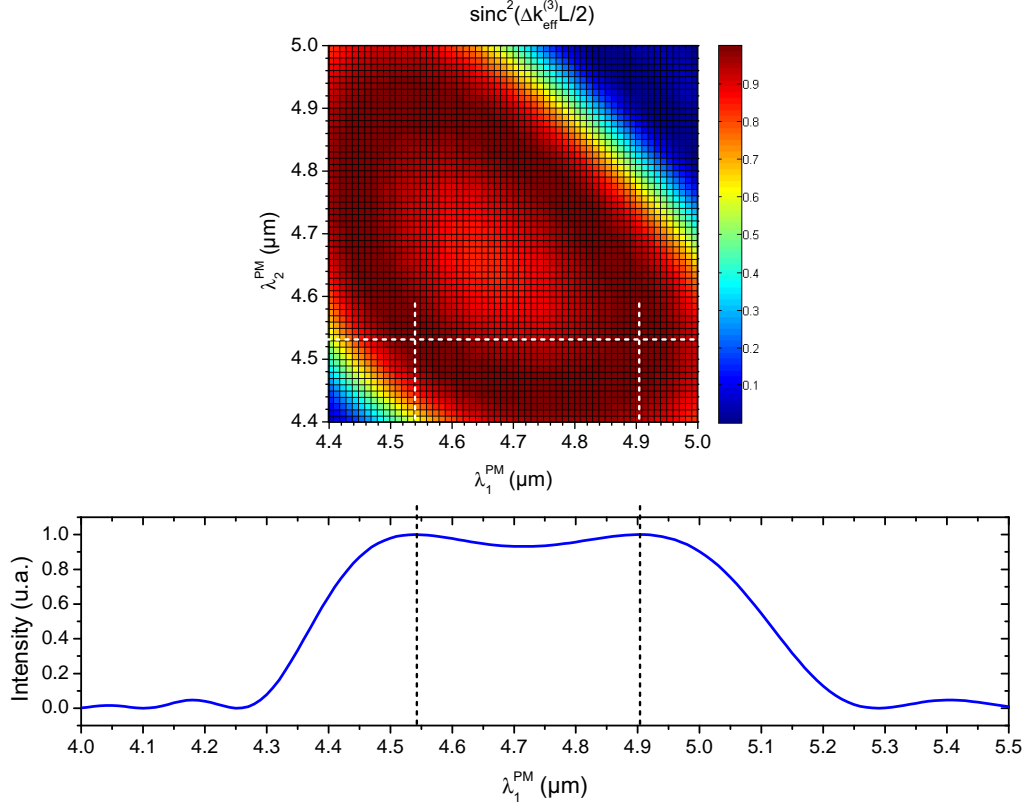
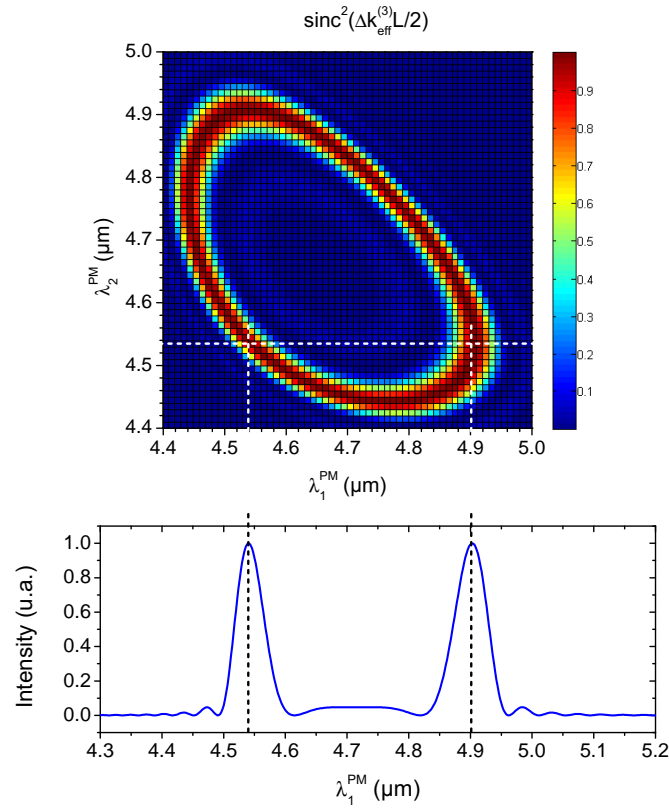

 (a) $L = 10$ cm

 (b) $L = 1$ m

Figure 4.45 – Upper graphs: $\text{sinc}^2(\Delta kL/2)$ for the pump wavelength fixed at $\lambda_0 = 1550.5$ nm. Lower graphs: cross-section at $\lambda_2^{\text{PM}}(B) = 4.53$ μm .

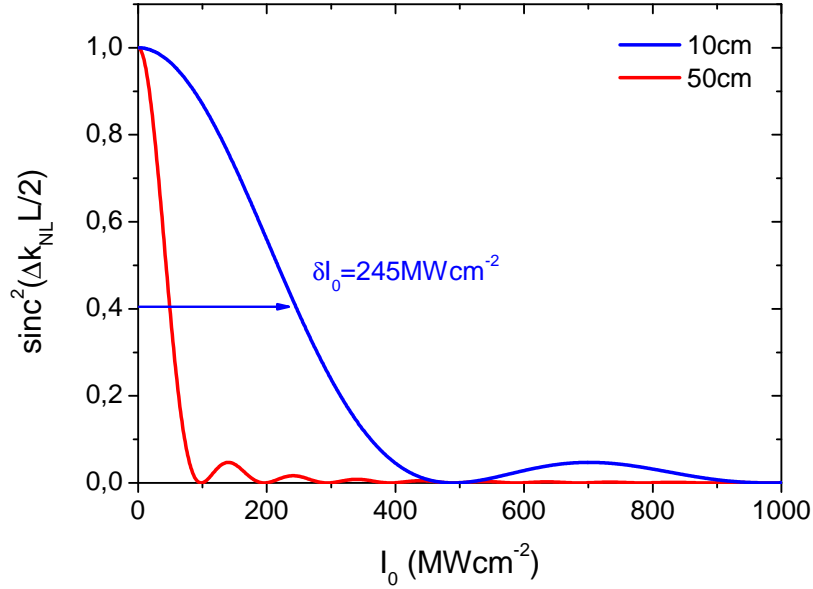


Figure 4.46 – Intensity acceptance for $L = 10$ cm (blue) and 50 cm (red).

The two surfaces of Figure 4.45 show the $\text{sinc}^2(\Delta k_{\text{eff}}^{(3)} L/2)$ function for two fiber lengths: 10 cm (a) and 1 m (b). They represent the wideness of the spectral range of the emitted triple photons. Below these graphs are plotted cross-sections for $\lambda_2^{\text{PM}} = 4.53 \mu\text{m}$, part of the set of phase-matching wavelengths B of Equation (4.60).

In As_2Se_3 fibers, the phase mismatch is decreasing when Λ decreases and/or d increases. This is not really satisfactory as the pitch becomes of the order of the wavelength. We then interrupt the investigation in this material since the model may not be relevant anymore.

Nonlinear contribution in the phase mismatch We have shown in Section 4.1.2 that the nonlinear contribution to the phase matching Δk_{NL} in silica fibers was insignificant according to the incident powers of our experiments. Here, albeit the optical damage threshold demands to work with smaller powers in chalcogenide fibers, the nonlinear susceptibility is three orders of magnitude above that of silica. It is therefore important to look at Δk_{NL} carefully.

The effect of the pump intensity on the total phase mismatch $\Delta k_{\text{L}} + \Delta k_{\text{NL}}$ can be calculated. Depending on the materials, Section 4.2.1.1 tells us that the maximum intensity that can be used ranges between 100 MWcm^{-2} and 1 GWcm^{-2} . We consider here the interaction B of Equation (4.46) with the linear phase-matching Δk_{L} truly fulfilled, *i.e.* $\Delta k_{\text{L}} = 0$. Figure 4.46 shows the function $\text{sinc}^2(\Delta k_{\text{NL}} L/2)$ for $L = 10$ cm and 50 cm as a function of the pump intensity I_0 up to 1 GWcm^{-2} . In order to quantify the effect of the nonlinear term, we define an “acceptance in intensity”, written $L\delta I_0$ where δI_0 is the full width of the sinc^2 peak at 0.405 of the maximum. It is actually the same definition as for any other acceptance, in terms of wavelength, angle or temperature. We find $L\delta I_0 = 2.45 (\text{GWcm}^{-2}) \times \text{cm}$. For instance, the triplet energy is reduced by half due to the phase mismatch when working with a 50 cm-long fiber and an intensity of 44 MWcm^{-2} .

With a 10ns laser source and the present chalcogenide fibers, the maximum intensities corre-

spond to maximum energies ranging from $\mathcal{E}_{\text{tot}} = 0.2 \mu\text{J}$ to $2 \mu\text{J}$. By performing the calculation of the total phase mismatch as in Section 4.1.2, one can recover perfect phase matching by shifting the previous wavelengths by $\Delta\lambda_{1,2,3}(0.2 \mu\text{J}) \simeq 0.48 \text{ nm}$ to $\Delta\lambda_{1,2,3}(2 \mu\text{J}) \simeq 4.64 \text{ nm}$ and $\Delta\lambda_0 = \Delta\lambda_{1,2,3}/3$. The nonlinear effective susceptibility has been taken equal to $\chi_{\text{eff}}^{(3)} = 10^{-19} \text{ m}^2\text{V}^{-2}$. A tunable incident beam enables to do this.

4.2.3 Conclusion

A family of material with giant nonlinearities, the chalcogenides, have been investigated in the purpose of performing TPG. This prospective work leans on research done at ONERA-Palaiseau. The fibers are As_2S_3 and As_2Se_3 photonic-crystal fibers, characterized geometrically by d , the diameter of the holes, and Λ , the distance between two successive holes. The propagation occurs through modified total internal reflection. An intermodal phase-matching between LP_{01} and LP_{02} transverse modes has been found in As_2S_3 , for $d = 4.25 \mu\text{m}$ and $\Lambda = 5 \mu\text{m}$. Several non-frequency degenerated phase-matching wavelengths are possible: they range in between 4.5 and $5 \mu\text{m}$ for the triplet fields and equal $1.5505 \mu\text{m}$ for the pump. The consideration of the nonlinear contribution to the phase-mismatch shifts them by a few nanometers.

Conclusion

“It is not good to want a thing too much. It sometimes drives luck away.
You must want it just enough.”

– John Steinbeck, *The pearl*

Triple photons are three-particle states of light, strongly correlated, that belong to the GHZ or W entanglement class. The correlations among these states differ from those of twins and are truly non-classical, as highlighted for instance by their Wigner function that exhibits an interference pattern and negativities. This makes them interesting objects of study for exploring N -particle quantum states, more particularly in quantum optics. As twin photons have opened up the doors of quantum information, triple photons might also have their own influence on this field.

Over the recent years, several strategies have been used to generate triplets. The most attractive is the direct splitting of a single photon of higher energy, through a third-order optical interaction with a nonlinear media. More indirectly, they can also be created from two successive second-order nonlinear interactions; or from the “quantum eraser” experiment of coherent superposition of two twin photons for example.

This thesis deals with the direct generation of photonic triplets from a third-order nonlinear optical interaction. It follows on from the work that began ten years ago by the experimental demonstration of triple photon generation (TPG), seeded by two additional beams, in the team of Benoît Boulanger in Grenoble. Such stimulation beams were actually needed to overcome the extreme weakness of the conversion efficiency that makes direct TPG a challenge in the field of nonlinear optics. However, these stimulation beams also concealed the correlations between triple photons. Our objective was then obvious: enabling to perform an efficient generation with as little stimulation as possible, ideally none. To do so, two experimental strategies were adopted in the course of this work. Their goals are summed up as follows:

- 1. TPG in bulk crystals, in an OPO configuration. This would artificially increase the length of the interaction, and consequently increase the conversion efficiency so as to be able to get rid of some stimulation photons;

- 2. TPG in optical fibers. Optical fibers present the advantage of confining the electromagnetic field in addition to making possible the use of long interaction length; furthermore, no quadratic process, which conversion efficiencies are much higher than third-order processes, can remain. Once again, it would therefore allow to get rid of the injection.

The contribution of this work of the two previous points 1. and 2. are summarized below.

1. Two anisotropic bulk crystals, KTP and rutile TiO_2 , have been investigated in free wave or cavity configurations. These crystals enable TPG through a birefringent phase matching.

In KTP, spectral and energetic studies have been performed in the picosecond regime, still with two injection beams. Our model with polychromatic fields successfully explained the experimental results by taking into account a parasitic Kerr effect that modifies the phase-mismatch and the beam geometries. It consequently comes to attenuate the TPG conversion efficiency when the intensities are large enough.

For TiO_2 , a characterization of the phase-matching properties is done by the way of a third-harmonic generation (THG) experiment for fundamental wavelengths ranging between 1836 nm and 4449 nm. It allows us to refine the dispersion equation of its refractive indices. The absolute magnitude of the χ_{18} nonlinear coefficient has been determined; and its sign is opposite to that of χ_{16} . TPG phase-matching conditions have been calculated, but none of our experimental attempts enabled us to demonstrate TPG in rutile TiO_2 , even with two stimulation fields. Some of the refractive indices involved in the TPG process were actually not sollicitated during THG experiment. This implies a prejudicial unaccuracy of them. Further work in this crystal should either get a better estimate of these refractive indices, or perform TPG at higher wavelengths with a suitable detection stage.

Finally, two proposals of a synchronously pumped OPO were considered theoretically, both concerning KTP and TiO_2 . The OPO has to be pumped with a high repetition rate laser in the picosecond regime. The first proposal is a mono-injected doubly resonant OPO. The second one is a triply resonant OPO, without any injection: in that case, the cavity is without any loss before the extraction at a desired time. The coherence properties of photons belonging to the same triplet have not been studied here. It is an important point to care about, as correlations are intended to be maintained.

2. Step-index germanium-doped silica optical fibers and chalcogenide PCF have been studied. An intermodal phase matching has been performed since these materials are isotropic.

The $\text{GeO}_2 : \text{SiO}_2$ fibers that we used, of core radii $a = 2.19 \mu\text{m}$ or $2.30 \mu\text{m}$, are designed to enable a frequency-degenerated modal phase-matching between the LP_{01} and LP_{03} transverse modes for the λ_ω and $\lambda_{3\omega}$ respectively. A full characterization of the fibers through THG has been performed first for the two following reasons: their two corresponding phase-matching conditions are strictly the same, and the conversion efficiency of THG is higher than that of TPG. Their modal, spectral, energetic and polarization properties have been studied in the nanosecond regime. The experimental phase-matching wavelengths are very close the calculated ones. We pointed out fluctuations of the core size, ellipticity of the transverse section of the core and anisotropy. This led respectively to a large spectral acceptance, which constitutes an

advantage as longer fibers can be used; elliptical Ince-Gauss modal distributions, LP_{03} becoming IG_{40}^e , which results in a lower overlap of the incident LP modes; and a conversion efficiency that can be maximized for a particular input fundamental polarization. The effective interaction area is 60 times higher than the core surface.

This LP_{01}/LP_{03} THG configuration is not the only interaction allowed in the fiber: other modal configurations for phase-matched THG have also been identified and studied; lastly, Raman scattering has been highlighted.

Quantum theoretical calculations for spontaneous TPG, *i.e.* the third-order parametric fluorescence, in the case of the previous LP_{01}/LP_{03} interaction have been performed and lead to extremely low conversion efficiencies. For instance, 4.7×10^{-8} triplets/sec can be generated in 1 m-long fiber, for 1 μ J/pulse of input fundamental energy (10 ns pulses, 10 Hz repetition rate). This generation rate could be increased by using a high repetition rate or continuous laser source, smaller core size fibers or of nonlinear materials with higher nonlinearities.

Phase masks enable to generate efficiently the non-Gaussian transverse profile LP_{03} of the fundamental beam for TPG. Filtering has also been investigated. If one of the requirements for increasing the TPG conversion efficiency mentioned above is met, the experimental realization of TPG should be achievable with an APD that enables proportionnal photon counting with integration over time. Such a detector will be soon available thanks to a collaboration with Johan Rothman from CEA-LETI Grenoble.

Finally, the phase-matching properties for TPG in chalcogenides PCF, materials with a giant nonlinearity, have been investigated. An intermodal phase-matching between LP_{01} and LP_{02} transverse modes is possible in As_2S_3 , for a particular set of geometrical parameters of the PCF ($d = 4.25 \mu\text{m}$, $\Lambda = 5 \mu\text{m}$). It leads to phase-matching wavelengths that equals 1550.5 nm for the pump field, and that range in between 4.5 and $5 \mu\text{m}$ for the triplet fields. This work is performed in collaboration with the group of Pierre Bourdon at ONERA Palaiseau. The previous APD, which transparency range covers the mid-IR, could be used for that configuration too.

Table 4.16 gives a summary of the present work and outlook by comparing the various configurations of generation of triple photons from parametric fluorescence that have been investigated experimentally and/or theoretically.

			Strategy 1.		Strategy 2.	
			Bulk crystals		Optical fibers	
			KTP	Rutile TiO ₂	GeO ₂ : SiO ₂	Chalcogenides
						Triggered OPO
						KTP
Nonlinear medium and interaction properties	L	1 cm			1 m 10 cm	3 cm
	$\chi_{\text{eff}}^{(3)}$ [m ² V ⁻²]	1.5×10^{-21}	5×10^{-21}		10^{-22}	10^{-19}
	S, S_{eff} [μm ²]	8000		900	120	1.5×10^{-21}
Pump source properties	I	40 GWcm ⁻²		100 MWcm ⁻² 100 kWcm ⁻²	10 MWcm ⁻² 10 kWcm ⁻²	40 MWcm ⁻²
	τ	15 ps		10 ns 15 ps		15 ps
	f	10 Hz		10 Hz 100 MHz ^a	10 Hz 100 MHz ^b	80 MHz
Triplet properties	λ [μm]	~ 1.5		~ 1.5	~ 4.5	~ 1.5
	N_{tr} [tr/s]	7.7×10^{-9}	3.4×10^{-8}	4.7×10^{-7} 3.1×10^{-2}	2.8 1.9×10^5	up to 2.0×10^{13}

Table 4.16 – Comparison of the triple photons conversion efficiencies generated from spontaneous down-conversion in the configurations considered experimentally and theoretically in this thesis.

For the two kinds of optical fibers, two configurations are presented, with a black number (above) and a blue one (below) in the table cells. L and $\chi_{\text{eff}}^{(3)}$ are the length and effective nonlinear cubic susceptibility of the nonlinear medium respectively, S and S_{eff} the (effective) interaction area. The pump laser is characterized by its intensity I , its pulse duration τ and its repetition rate f . λ and N_{tr} are the wavelengths and number of triplets generated.

^aor CW laser of mean power 1W.

^bor CW laser of mean power 0.1W.

Conclusion

“Some” steps are still needed to achieve spontaneous TPG from direct cubic optical nonlinear interaction. “Some” more steps will then be necessary to make it compatible with quantum measurements. This is not an easy task, but it will then be possible to probe the coherence of the triplet state and demonstrate its non-classical properties, for instance through coincidence measurements or quantum tomography. Our colleagues Kamel Bencheikh and Ariel Levenson at Laboratoire de Photonique et Nanostructures in Marcoussis, and Nicolas Gisin and Hugo Zbinden at Université de Genève would be happy to help.

One day then, many steps ahead maybe, these states might be part of quantum information protocols.



Figure 4.47 – From Time magazine.

Notation table

APD	Avalanche photodiode
CARS	Coherent anti-Stokes Raman scattering
CCD	Charge-coupled device
CW	Continuous-wave
DFG	Difference-frequency generation
DROPO	Doubly resonant optical parametric oscillator
EIM	Effective index method
FEM	Finite element method
FSFM	Fundamental space filling mode
FWHM	Full width at half maximum
EH	Electric magnetic (hybrid)
FWM	Four-wave mixing
GHZ	Greenberger-Horne-Zeilinger
GTP	Glan-Taylor prism
HE	Magnetic electric (hybrid)
HIG	Helical Ince-Gauss
HWP	Half-wave plate
IG	Ince-Gauss
IR	Infrared
LG	Laguerre-Gauss
LP	Linearly polarized
NA	Numerical aperture
OPA	Optical parametric amplifier
OPG	Optical parametric generator
OPO	Optical parametric oscillator
PCF	Photonic-crystal fiber
PM	Phase matching
RS	Raman scattering

SFG	Sum-frequency generation
SHG	Second-harmonic generation
SOSFG	Second-order sum-frequency generation
SPM	Self-phase modulation
SRS	Stimulated Raman scattering
TE	Transverse electric
THG	Third-harmonic generation
TM	Transverse magnetic
TOSFG	Third-order sum-frequency generation
TPG	Triple photon generation
TROPO	Triply resonant optical parametric oscillator
XPM	Cross-phase modulation

TPG phase-matching in rutile TiO₂

In this appendix are shown the various birefringent phase-matching conditions for TPG in rutile TiO₂. The seven polarization configurations of the system (1.75) are computed. Two of the three triplets wavelengths are spectrally degenerated so as to perform a bi-stimulation at first:

$$\lambda_0^{(o)} \rightarrow \lambda_1^{(e/o)} + \lambda_2^{(e/o)} + \lambda_2^{(e/o)}; \quad (\text{B.1})$$

(*o*) and (*e*) stand for ordinary and extraordinary polarized waves respectively. The pump wavelength is taken as $\lambda_0 = 532$ or 1064 nm, as a Nd:YAG laser that can be frequency-doubled is intended to be used. These computations require the Sellmeier equations given in Equations (3.33) and (3.34).

Existing solutions are represented in Figures (B.1) to (B.7), in the transparency range of the crystal. Note however that the transmittance decreases drastically above 4.5 μm , as shown in Figure (3.7).

The frames (a), (b) and (c) depict the phase-matching angle θ_{PM} with respect to the wavelengths λ_1 , λ_2 and the absolute value of the effective cubic nonlinear coefficient $|\chi_{\text{eff}}^{(3)}|$ respectively.

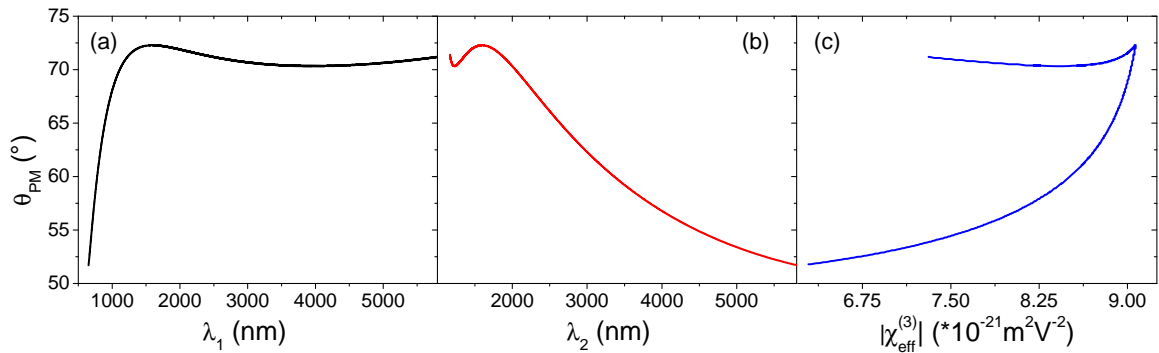
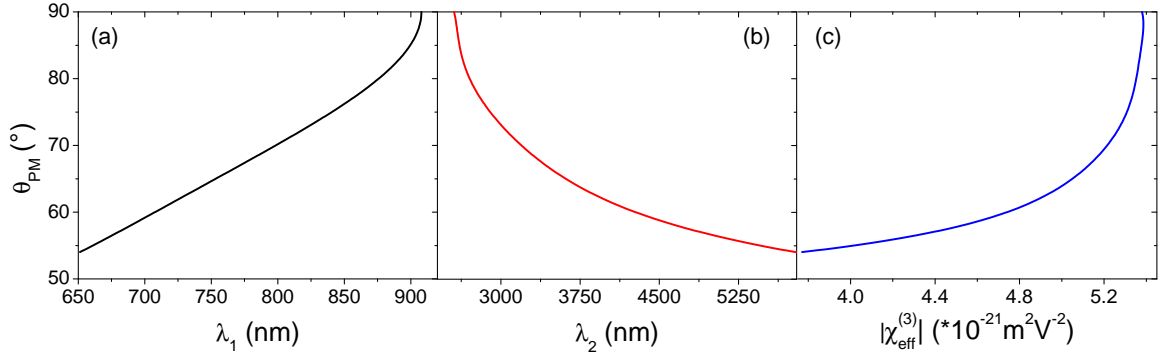
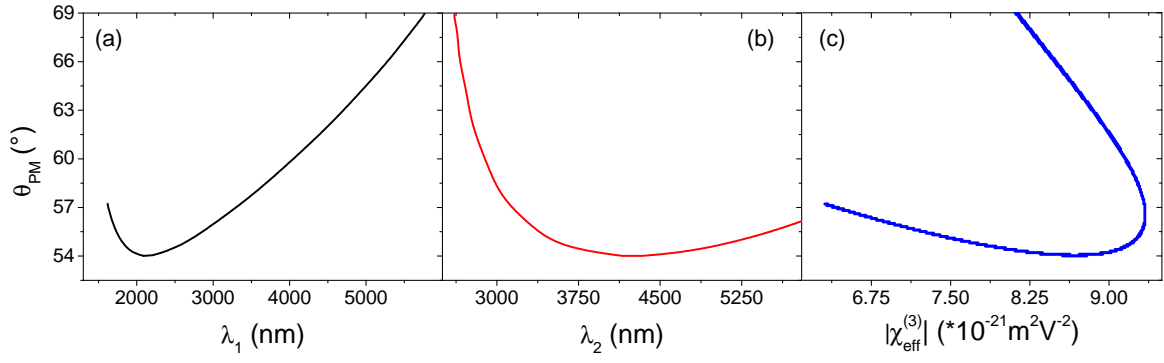
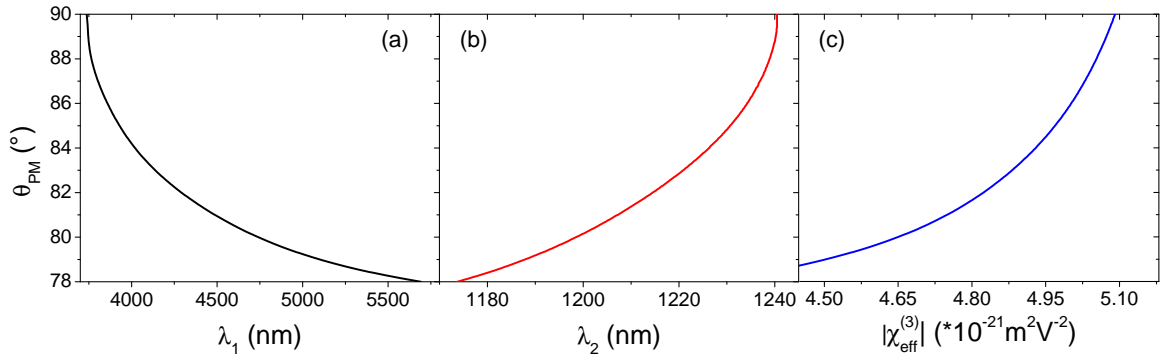
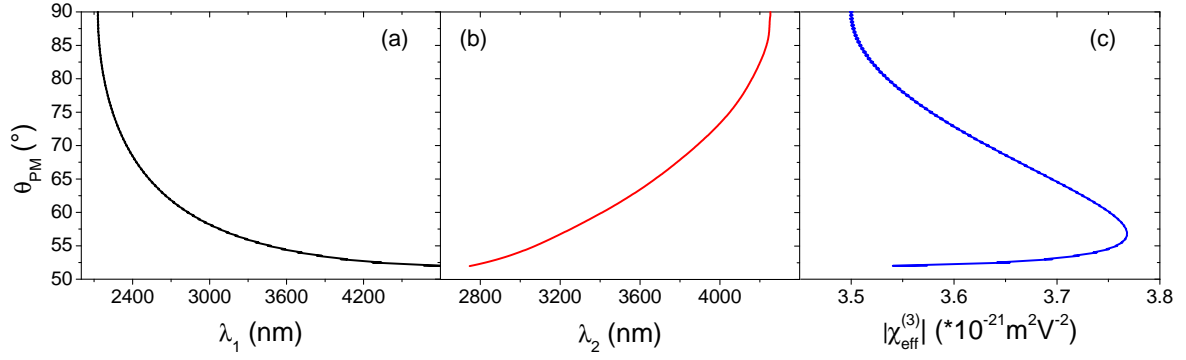
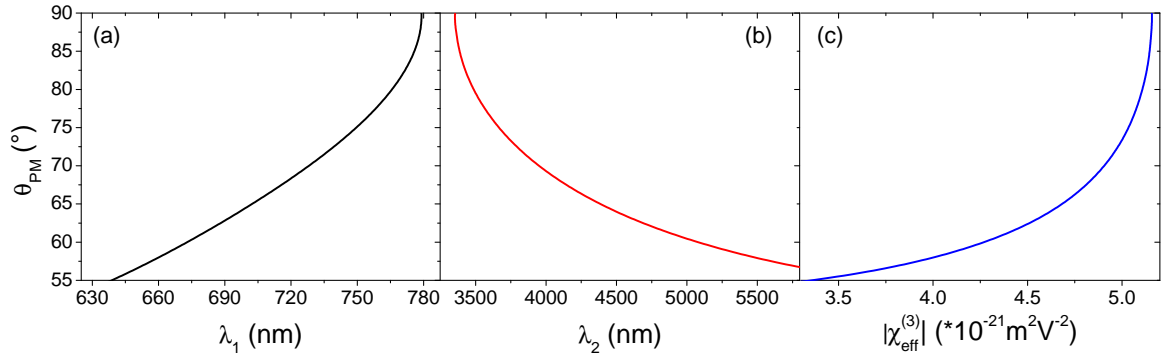
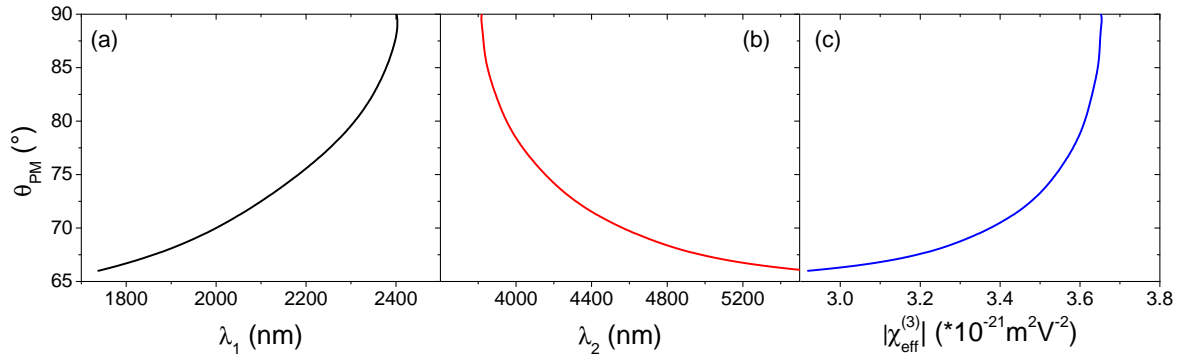


Figure B.1 – Type I; $532 \text{ nm}^{(o)} \rightarrow \lambda_1^{(e)} + \lambda_2^{(e)} + \lambda_2^{(e)}$.


 Figure B.2 – Type IIa=IIb; $532 \text{ nm}^{(o)} \rightarrow \lambda_1^{(e)} + \lambda_2^{(e)} + \lambda_2^{(o)}$

 Figure B.3 – Type IIa=IIb; $1064 \text{ nm}^{(o)} \rightarrow \lambda_1^{(e)} + \lambda_2^{(e)} + \lambda_2^{(o)}$

 Figure B.4 – Type IIc; $532 \text{ nm}^{(o)} \rightarrow \lambda_1^{(o)} + \lambda_2^{(e)} + \lambda_2^{(e)}$


 Figure B.5 – Type IIc; $1064 \text{ nm}^{(o)} \rightarrow \lambda_1^{(o)} + \lambda_2^{(e)} + \lambda_2^{(e)}$

 Figure B.6 – Type IIIa; $532 \text{ nm}^{(o)} \rightarrow \lambda_1^{(e)} + \lambda_2^{(o)} + \lambda_2^{(o)}$

 Figure B.7 – Type IIIa; $1064 \text{ nm}^{(o)} \rightarrow \lambda_1^{(e)} + \lambda_2^{(o)} + \lambda_2^{(o)}$

Threshold intensities of the OPO configuration

This present appendix gives the details of the calculations of the OPO threshold intensities given in the section 3.3. The resolution is made with monochromatic fields.

C.1 Doubly resonant OPO

We consider the non-degenerate interaction, $\omega_0 \rightarrow \omega_1 + \omega_2 + \omega_3$, mono-injected by the wave at λ_1 . The coupled equations (3.47) are:

$$\begin{cases} \frac{\partial \underline{E}_0(\omega_0, t)}{\partial t} = \frac{\partial \underline{E}_1(\omega_1, t)}{\partial t} = 0 \\ \tau_{\text{cav}} \frac{\partial \underline{E}_2(\omega_2, t)}{\partial t} = -\mathcal{T}(\omega_2) \underline{E}_2(\omega_2, t) + j\kappa(\omega_2) \chi_{\text{eff}}^{(3)}(\omega_0, \omega_1, \omega_2) L_{\text{cav}} \underline{E}_0(\omega_0, t) \underline{E}_1^*(\omega_1, t) \underline{E}_3^*(\omega_3, t) \\ \tau_{\text{cav}} \frac{\partial \underline{E}_3(\omega_3, t)}{\partial t} = -\mathcal{T}(\omega_3) \underline{E}_3(\omega_3, t) + j\kappa(\omega_3) \chi_{\text{eff}}^{(3)}(\omega_0, \omega_1, \omega_2) L_{\text{cav}} \underline{E}_0(\omega_0, t) \underline{E}_1^*(\omega_1, t) \underline{E}_2^*(\omega_2, t), \end{cases} \quad (\text{C.1})$$

where all the notations are given in Section 3.3.2.1. In the undepleted pump approximation, this system can be simplified into the following:

$$\begin{cases} \underline{E}_0(\omega_0, t) = \underline{E}_1(\omega_1, t) = 0, \forall t \\ \tau_{\text{cav}} \frac{\partial \underline{E}_2(\omega_2, t)}{\partial t} = -\mathcal{T}(\omega_2) \underline{E}_2(\omega_2, t) + j\kappa(\omega_2) \chi_{\text{eff}}^{(3)}(\omega_0, \omega_1, \omega_2) L_{\text{cav}} \underline{E}_0(\omega_0, 0) \underline{E}_1^*(\omega_1, 0) \underline{E}_3^*(\omega_3, t) \\ \tau_{\text{cav}} \frac{\partial \underline{E}_3(\omega_3, t)}{\partial t} = -\mathcal{T}(\omega_3) \underline{E}_3(\omega_3, t) + j\kappa(\omega_3) \chi_{\text{eff}}^{(3)}(\omega_0, \omega_1, \omega_2) L_{\text{cav}} \underline{E}_0(\omega_0, 0) \underline{E}_1^*(\omega_1, 0) \underline{E}_2^*(\omega_2, t). \end{cases} \quad (\text{C.2})$$

Performing a derivation with respect to time and injecting the previous equations:

$$\frac{\partial^2 |\underline{E}_{2,3}(\omega_2, t)|}{\partial t^2} + (\alpha_2 + \alpha_3) \frac{\partial |\underline{E}_{2,3}(\omega_2, t)|}{\partial t} + (\alpha_2 \alpha_3 - \beta_2 \beta_3) |\underline{E}_{2,3}(\omega_2, t)| = 0, \quad (\text{C.3})$$

with the following notations to simplify the expressions:

$$\begin{cases} \alpha_2 &= \kappa(\omega_2) \chi_{\text{eff}}^{(3)}(\omega_0, \omega_1, \omega_2) L_{\text{cav}} |\underline{E}_0(\omega_0, 0)| |\underline{E}_1(\omega_1, 0)| / \tau_{\text{cav}} \\ \alpha_3 &= \kappa(\omega_3) \chi_{\text{eff}}^{(3)}(\omega_0, \omega_1, \omega_2) L_{\text{cav}} |\underline{E}_0(\omega_0, 0)| |\underline{E}_1(\omega_1, 0)| / \tau_{\text{cav}} \\ \beta_2 &= \beta_3 = \mathcal{T}(\omega_{2,3}) / \tau_{\text{cav}}. \end{cases} \quad (\text{C.4})$$

The resolution of (C.3) is straightforward:

$$|\underline{E}_{2,3}(\omega_{2,3}, t)| = \frac{1}{r^+ - r^-} \left[\frac{\partial |\underline{E}_{2,3}(\omega_{2,3}, t)|}{\partial t} \Big|_{t=0} (r^+ e^{r^- t} - r^- e^{r^+ t}) + |\underline{E}_{2,3}(\omega_{2,3}, 0)| (e^{r^+ t} - e^{r^- t}) \right], \quad (\text{C.5})$$

with

$$r^\pm = -\frac{1}{2}(\alpha_2 + \alpha_3) \pm \frac{1}{2}\sqrt{\Delta},$$

and

$$\Delta = (\alpha_2 + \alpha_3)^2 - 4(\alpha_2 \alpha_3 - \beta_2 \beta_3).$$

The threshold condition (equality between gain and losses):

$$|\underline{E}_{2,3}(\omega_{2,3}, 0)|_{th} = p(\omega_{2,3}) |\underline{E}_{2,3}(\omega_{2,3}, \tau_L)|_{th}, \quad (\text{C.6})$$

with p defined in Equation (3.49) and τ_L the travelling time in the crystal. Therefore:

$$|\underline{E}_{2,3}(\omega_{2,3}, 0)|_{th} = \frac{p}{r^+ - r^-} \left[\frac{\partial |\underline{E}_{2,3}(\omega_{2,3}, t)|_{th}}{\partial t} \Big|_{t=0} (r^+ e^{r^- \tau_L} - r^- e^{r^+ \tau_L}) + |\underline{E}_{2,3}(\omega_{2,3}, 0)|_{th} (e^{r^+ \tau_L} - e^{r^- \tau_L}) \right]. \quad (\text{C.7})$$

Combining Equations (C.7) and (C.2), we come up with the following matricial system:

$$\begin{pmatrix} 1 - \frac{p}{r^+ - r^-} \left[(r^+ + \alpha_2) e^{r^- \tau_L} - (r^- + \alpha_2) e^{r^+ \tau_L} \right] & \frac{p\beta_2}{r^+ - r^-} (e^{r^+ \tau_L} - e^{r^- \tau_L}) \\ \frac{p\beta_3}{r^+ - r^-} (e^{r^+ \tau_L} - e^{r^- \tau_L}) & 1 - \frac{p}{r^+ - r^-} \left[(r^+ + \alpha_3) e^{r^- \tau_L} - (r^- + \alpha_3) e^{r^+ \tau_L} \right] \end{pmatrix} \cdot \begin{pmatrix} |\underline{E}_2(\omega_2, 0)|_{th} \\ |\underline{E}_3(\omega_3, 0)|_{th} \end{pmatrix} = 0 \quad (\text{C.8})$$

where

$$\begin{aligned} & \left[(r^+ + \alpha_{2,3}) e^{r^- \tau_L} - (r^- + \alpha_{2,3}) e^{r^+ \tau_L} \right] \\ &= e^{-(\alpha_{2,3} + \alpha_{3,2})\tau_L/2} \left[\sqrt{\Delta} \cosh(\sqrt{\Delta}\tau_L/2) + (\alpha_{3,2} - \alpha_{2,3}) \sinh(\sqrt{\Delta}\tau_L/2) \right]. \end{aligned} \quad (\text{C.9})$$

The determinant of the matrix in Equation (C.8) has to be nil for the solutions to be non-zero. Then, after long calculations and the use of hyperbolic trigonometry, it comes:

$$1 - 2pe^{-(\alpha_2 + \alpha_3)\tau_L/2} \cosh(\sqrt{\Delta}\tau_L/2) + p^2 e^{-(\alpha_2 + \alpha_3)\tau_L} = 0. \quad (\text{C.10})$$

This second-order polynomial equations solve easily as:

$$p = \exp \left(-(\alpha_2 + \alpha_3) \tau_L / 2 \pm \sqrt{(\alpha_2 + \alpha_3)^2 - 4(\alpha_2 \alpha_3 - \beta_2 \beta_3) \tau_L / 2} \right). \quad (\text{C.11})$$

Replacing α_2 , α_3 , β_2 and β_3 of Equations (C.4) into (C.11), and electric fields into intensities through $I(\omega, Z) = \frac{1}{2} \varepsilon_0 c n(\omega) |\underline{E}(\omega, Z)|^2$, we find Equation (3.48):

$$I_0^{\text{th}}(\omega_0, 0) I_1^{\text{th}}(\omega_1, 0) = \frac{\varepsilon_0^2 c^2 n(\omega_0) n(\omega_1)}{4 [\chi_{\text{eff}}^{(3)}]^2} \times \left| \frac{\tau_{\text{cav}} \ln p(\omega_{2,3}) (\kappa(\omega_2^+) + \kappa(\omega_3^-))}{2\tau_L L_{\text{cav}} \kappa(\omega_2^+) \kappa(\omega_3^-)} \right. \\ \left. - \sqrt{\left(\frac{\tau_{\text{cav}} \ln p(\omega_{2,3}) (\kappa(\omega_2^+) - \kappa(\omega_3^-))}{2\tau_L L_{\text{cav}} \kappa(\omega_2^+) \kappa(\omega_3^-)} \right)^2 + \frac{1}{\kappa(\omega_2^+) \kappa(\omega_3^-)} \left(\frac{\mathcal{T}(\omega_{2,3})}{L_{\text{cav}}} \right)^2} \right|^2. \quad (\text{C.12})$$

C.2 Triply resonant OPO

We consider here the frequency-degenerated cubic nonlinear interaction $\omega_0 \rightarrow \omega_s + \omega_s + \omega_s$ ($\omega_0 = 3\omega_s$) between a pump (0) and a signal (s) waves in the undepleted pump approximation and at perfect phase-matching. The coupled equations in the spatial coordinates are:

$$\begin{cases} \frac{\partial \underline{E}_0(\omega_0, Z)}{\partial Z} = 0 \\ \frac{\partial \underline{E}_s(\omega_s, Z)}{\partial Z} = i\kappa(\omega_s) \chi_{\text{eff}}^{(3)}(\omega_0, \omega_s, \omega_s) \underline{E}_0(\omega_0, Z) \underline{E}_s^*(\omega_s, Z) \underline{E}_s(\omega_s, Z). \end{cases} \quad (\text{C.13})$$

Then:

$$\begin{cases} \underline{E}_0(\omega_0, Z) = \underline{E}_0(\omega_0, 0), \quad \forall Z \\ \frac{\partial \underline{E}_s(\omega_s, Z)}{[\underline{E}_s^*(\omega_s, Z)]^2} = i\kappa(\omega_s) \chi_{\text{eff}}^{(3)}(\omega_0, \omega_s, \omega_s) \underline{E}_0(\omega_0, 0) \partial Z. \end{cases} \quad (\text{C.14})$$

For a round trip in the crystal of length L :

$$\int_{\underline{E}_s(\omega_s, 0)}^{\underline{E}_s(\omega_s, L)} \frac{d\underline{E}_s(\omega_s, Z)}{[\underline{E}_s^*(\omega_s, Z)]^2} = i\kappa(\omega_s) \chi_{\text{eff}}^{(3)}(\omega_0, \omega_s, \omega_s) L \underline{E}_0(\omega_0, 0), \quad (\text{C.15})$$

which leads to

$$\underline{E}_s^*(\omega_s, L) = \frac{1}{\frac{1}{\underline{E}_s^*(\omega_s, 0)} - i\kappa(\omega_s) \chi_{\text{eff}}^{(3)}(\omega_0, \omega_s, \omega_s) L \underline{E}_0(\omega_0, 0)}. \quad (\text{C.16})$$

The threshold condition for the signal wave can be written as:

$$\underline{E}_s^{\text{th}}(\omega_s, 0) = \underline{E}_s^{\text{th}}(\omega_s, RT), \quad (\text{C.17})$$

where RT stands for return trip. The losses are brought about by the Fresnel reflexion and the transmission coefficients of the input and output mirrors:

$$\underline{E}_s^{\text{th}}(\omega_s, RT) = p(\omega_s) \underline{E}_s^{\text{th}}(\omega_s, L), \quad (\text{C.18})$$

with $p(\omega_s) = \sqrt{(T_F(\omega_s))^4 R_A(\omega_s) R_B(\omega_s)}$ with the notations of Section 3.3.2.2. The expression (C.16) together with the threshold condition (C.17) leads to:

$$\underline{E}_s^{\text{th}*}(\omega_s, 0) = \frac{(T_F(\omega_s))^2 \sqrt{R_A(\omega_s) R_B(\omega_s)}}{\frac{1}{\underline{E}_s^{\text{th}*}(\omega_s, 0)} - i\kappa(\omega_s) \chi_{\text{eff}}^{(3)}(\omega_0, \omega_s, \omega_s) L \underline{E}_0^{\text{th}}(\omega_0, 0)}, \quad (\text{C.19})$$

$$\left| \underline{E}_s^{\text{th}}(\omega_s, 0) \underline{E}_0^{\text{th}}(\omega_0, 0) \right| = \frac{1 - (T_F(\omega_s))^2 \sqrt{R_A(\omega_s) R_B(\omega_s)}}{\kappa(\omega_s) \chi_{\text{eff}}^{(3)}(\omega_0, \omega_s, \omega_s) L}. \quad (\text{C.20})$$

Then, in intensities:

$$\begin{aligned} I_p^{\text{th}}(\omega_0, 0) I_s^{\text{th}}(\omega_s, 0) &= \frac{1}{4\pi^2 \varepsilon_0^2 c^2 n(\omega_0) n^3(\omega_s)} \left(\frac{\lambda_s}{\chi_{\text{eff}}^{(3)}(\omega_0, \omega_s, \omega_s) L} \right)^2 \\ &\times \left(1 - (T_F(\omega_s))^2 \sqrt{(1 - T_A(\omega_s))(1 - T_B(\omega_s))} \right)^2. \end{aligned} \quad (\text{C.21})$$

Appendix D

Form of the nonlinear component of the effective phase mismatch

In order to simplify the equations, we assume here that all electric fields are monochromatic with no loss of generality as for the purpose of this appendix: determining the form of the nonlinear component of the effective phase mismatch. We also compact the notations by writing the fields: $\underline{E}_j = \underline{E}_j(X, Y, Z, \omega_j) = \underline{A}_j(Z, \omega_j) \underline{F}_j(X, Y, \omega_j)$, $j \in \{0, 1, 2, 3\}$.

The coupled equations that rule the evolution of the fields for a cubic interaction of type A, together with self- and cross-phase modulations are the following:

$$\begin{cases} \frac{\partial \underline{E}_0}{\partial Z} = i \frac{\Gamma_0}{2} |\underline{E}_0|^2 \underline{E}_0 + i \Gamma_0 \left[|\underline{E}_1|^2 + |\underline{E}_2|^2 + |\underline{E}_3|^2 \right] \underline{E}_0 + i \Gamma_0 \underline{E}_1 \underline{E}_2 \underline{E}_3 e^{-i \Delta k_L^{(3)} Z} \\ \frac{\partial \underline{E}_1}{\partial Z} = i \frac{\Gamma_1}{2} |\underline{E}_1|^2 \underline{E}_1 + i \Gamma_1 \left[|\underline{E}_0|^2 + |\underline{E}_2|^2 + |\underline{E}_3|^2 \right] \underline{E}_1 + i \Gamma_1 \underline{E}_0 \underline{E}_2^* \underline{E}_3^* e^{+i \Delta k_L^{(3)} Z} \\ \frac{\partial \underline{E}_2}{\partial Z} = i \frac{\Gamma_2}{2} |\underline{E}_2|^2 \underline{E}_2 + i \Gamma_2 \left[|\underline{E}_0|^2 + |\underline{E}_1|^2 + |\underline{E}_3|^2 \right] \underline{E}_2 + i \Gamma_2 \underline{E}_0 \underline{E}_1^* \underline{E}_3^* e^{+i \Delta k_L^{(3)} Z} \\ \frac{\partial \underline{E}_3}{\partial Z} = i \frac{\Gamma_3}{2} |\underline{E}_3|^2 \underline{E}_3 + i \Gamma_3 \left[|\underline{E}_0|^2 + |\underline{E}_1|^2 + |\underline{E}_2|^2 \right] \underline{E}_3 + i \Gamma_3 \underline{E}_0 \underline{E}_1^* \underline{E}_2^* e^{+i \Delta k_L^{(3)} Z} \end{cases}, \quad (\text{D.1})$$

where $\Delta k_L^{(3)}$ is here the “linear” contribution to the phase-mismatch (see Section 1.3), and

$$\Gamma_j = \frac{\omega_j}{2n(\omega_j)c} \chi_{\text{eff}}^{(3)}(\{\omega_{j,k,l,m}\}), \quad (\text{D.2})$$

with $\{j, k, l, m\} \in \{0, 1, 2, 3\}$; n the optical index and $\chi_{\text{eff}}^{(3)}$ the effective cubic susceptibility. The Kerr contribution (or SPM) is in blue, the XPM contribution in green and the TPG one in red.

We decompose the electric fields into their longitudinal and transverse components, and integrate over the transverse plane. It comes:

$$\begin{cases} \frac{\partial \underline{A}_0}{\partial Z} = i \left[\frac{\tilde{\Gamma}_0}{2} |\underline{A}_0|^2 + \tilde{\Gamma}_{01} |\underline{A}_1|^2 + \tilde{\Gamma}_{02} |\underline{A}_2|^2 + \tilde{\Gamma}_{03} |\underline{A}_3|^2 \right] \underline{A}_0 + i\tilde{\Gamma}_{0123} \underline{A}_1 \underline{A}_2 \underline{A}_3 e^{-i\Delta k_L^{(3)} Z} \\ \frac{\partial \underline{A}_1}{\partial Z} = i \left[\frac{\tilde{\Gamma}_1}{2} |\underline{A}_1|^2 + \tilde{\Gamma}_{01} |\underline{A}_0|^2 + \tilde{\Gamma}_{12} |\underline{A}_2|^2 + \tilde{\Gamma}_{13} |\underline{A}_3|^2 \right] \underline{A}_1 + i\tilde{\Gamma}_{1023} \underline{A}_0 \underline{A}_2^* \underline{A}_3^* e^{+i\Delta k_L^{(3)} Z} \\ \frac{\partial \underline{A}_2}{\partial Z} = i \left[\frac{\tilde{\Gamma}_2}{2} |\underline{A}_2|^2 + \tilde{\Gamma}_{02} |\underline{A}_0|^2 + \tilde{\Gamma}_{12} |\underline{A}_1|^2 + \tilde{\Gamma}_{23} |\underline{A}_3|^2 \right] \underline{A}_2 + i\tilde{\Gamma}_{2013} \underline{A}_0 \underline{A}_1^* \underline{A}_3^* e^{+i\Delta k_L^{(3)} Z} \\ \frac{\partial \underline{A}_3}{\partial Z} = i \left[\frac{\tilde{\Gamma}_3}{2} |\underline{A}_3|^2 + \tilde{\Gamma}_{03} |\underline{A}_0|^2 + \tilde{\Gamma}_{13} |\underline{A}_1|^2 + \tilde{\Gamma}_{23} |\underline{A}_2|^2 \right] \underline{A}_3 + i\tilde{\Gamma}_{3012} \underline{A}_0 \underline{A}_1^* \underline{A}_2^* e^{+i\Delta k_L^{(3)} Z} \end{cases}, \quad (\text{D.3})$$

with

$$\begin{aligned} \tilde{\Gamma}_j &= \Gamma_j \frac{\mathcal{F}_j^2}{A_{\text{eff } j}}, \\ \tilde{\Gamma}_{jk} &= \Gamma_j \frac{\mathcal{F}_k^2}{S_{\text{eff } j,k}^{\text{XPM}}}, \\ \tilde{\Gamma}_{jklm} &= \Gamma_j f_{jklm} \mathcal{F}_j^{-1} \mathcal{F}_k \mathcal{F}_l \mathcal{F}_m, \end{aligned} \quad (\text{D.4})$$

and $A_{\text{eff } j}$, $S_{\text{eff } j,k}^{\text{XPM}}$, f_{jklm} and \mathcal{F} defined in Equations (1.99), (1.104), (1.100) and (1.108) respectively.

D.1 Triplet photon generation

In the case of triplet photon generation, we work under the following hypotheses:

- the pump field is strong so that the undepleted pump approximation holds;
- consequently, the pump field is stronger than the triplet fields.

Therefore:

- for the evolution of the pump field 0: only the SPM contribution is considered;
- for the evolutions of fields 1, 2 and 3: SPM for triplet fields on themselves are neglected, as well as XPM between one triplet field and another triplet field.

It comes:

$$\begin{cases} \frac{\partial \underline{A}_0}{\partial Z} = i \frac{\tilde{\Gamma}_0}{2} |\underline{A}_0|^2 \underline{A}_0 \\ \frac{\partial \underline{A}_1}{\partial Z} = i\tilde{\Gamma}_{01} |\underline{A}_0|^2 \underline{A}_1 + i\tilde{\Gamma}_{0123} \underline{A}_0 \underline{A}_2^* \underline{A}_3^* e^{+i\Delta k_L^{(3)} Z} \\ \frac{\partial \underline{A}_2}{\partial Z} = i\tilde{\Gamma}_{02} |\underline{A}_0|^2 \underline{A}_2 + i\tilde{\Gamma}_{0123} \underline{A}_0 \underline{A}_1^* \underline{A}_3^* e^{+i\Delta k_L^{(3)} Z} \\ \frac{\partial \underline{A}_3}{\partial Z} = i\tilde{\Gamma}_{03} |\underline{A}_0|^2 \underline{A}_3 + i\tilde{\Gamma}_{0123} \underline{A}_0 \underline{A}_1^* \underline{A}_2^* e^{+i\Delta k_L^{(3)} Z} \end{cases}. \quad (\text{D.5})$$

It is of prime importance to note that the Kerr effect (SPM) and XPM may change the phase-matching properties as it has been seen in Section 3.1.3, but do not change the intensity of each field as the corpuscular schematics make it clear. It is then possible to evaluate their effect on the phase mismatch by solving the equations without the triplet terms (in red) at first, and then considering their contribution as a modulation of the triplet part.

Then, the consideration of the phase modulation term alone in the equations gives:

$$\frac{\partial \underline{A}_j}{\partial Z} = i\tilde{\Gamma} |\underline{A}_0|^2 \underline{A}_j, \quad (\text{D.6})$$

for $j \in \{0, 1, 2, 3\}$, with $\tilde{\Gamma} \in \left\{ \frac{\tilde{\Gamma}_0}{2}, \tilde{\Gamma}_{0j} \right\}$, which is easily solved as:

$$\underline{A}_j(Z) = \underline{A}_j(0) e^{i\tilde{\Gamma} |\underline{A}_0|^2 Z}. \quad (\text{D.7})$$

The modulation of the phase of the electric fields induced by the SPM and XPM processes (hence their names) is included in the full system of Equations (D.5), *i.e.* the substitution $\underline{A}_j(Z) \rightarrow \underline{A}_j(Z) e^{i\tilde{\Gamma} |\underline{A}_0|^2 Z}$ is performed. It gives:

$$\begin{cases} \frac{\partial \underline{A}_1}{\partial Z} = i\tilde{\Gamma}_{0123} \underline{A}_0 \underline{A}_2^* \underline{A}_3^* e^{+i\Delta k_{\text{tot}}^{(3)} Z} \\ \frac{\partial \underline{A}_2}{\partial Z} = i\tilde{\Gamma}_{0123} \underline{A}_0 \underline{A}_1^* \underline{A}_3^* e^{+i\Delta k_{\text{tot}}^{(3)} Z}, \\ \frac{\partial \underline{A}_3}{\partial Z} = i\tilde{\Gamma}_{0123} \underline{A}_0 \underline{A}_1^* \underline{A}_2^* e^{+i\Delta k_{\text{tot}}^{(3)} Z} \end{cases} \quad (\text{D.8})$$

with

$$\Delta k_{\text{tot}}^{(3)} = \Delta k_{\text{L}}^{(3)} + \left[\frac{\tilde{\Gamma}_0}{2} - (\tilde{\Gamma}_{01} + \tilde{\Gamma}_{02} + \tilde{\Gamma}_{03}) \right] |\underline{A}_0|^2. \quad (\text{D.9})$$

The pump power is expressed as:

$$P_0 = \frac{1}{2} n \varepsilon_0 c |\underline{A}_0|^2, \quad (\text{D.10})$$

as the integral over the transverse plane has already been performed previously. In the end, the total phase mismatch takes the form already presented in Equation (1.105):

$$\begin{aligned} \Delta \mathbf{k}_{\text{tot}}^{(3)} &= \Delta k_{\text{L}}^{(3)} + \Delta k_{\text{NL}}^{(3)} \\ &= \Delta \mathbf{k}_{\text{L}}^{(3)} + [\gamma_0 - 2(\gamma_{01} + \gamma_{02} + \gamma_{03})] P_0, \end{aligned} \quad (\text{D.11})$$

where

$$\begin{aligned} \gamma_j &= \frac{\omega_j \chi_{\text{eff}}^{(3)}}{2\varepsilon_0 c^2 n^2(\omega_j) A_{\text{eff}j}}, \\ \gamma_{jk} &= \frac{\omega_j \chi_{\text{eff}}^{(3)}}{2\varepsilon_0 c^2 n(\omega_j) n(\omega_k) S_{\text{eff}j,k}}. \end{aligned} \quad (\text{D.12})$$

D.2 Third-harmonic generation

In the case of third-harmonic generation, the signal (p) and pump (s) fields interact through the energy law: $\omega_p + \omega_p + \omega_p \rightarrow \omega_s$. The coupled equations are therefore:

$$\begin{cases} \frac{\partial \underline{A}_s}{\partial Z} = i \left[\frac{\tilde{\Gamma}_s}{2} |\underline{A}_s|^2 + \tilde{\Gamma}_{sp} |\underline{A}_p|^2 \right] \underline{A}_s + i \tilde{\Gamma}_{sppp} [\underline{A}_p]^3 e^{-i\Delta k_L^{(3)} Z} \\ \frac{\partial \underline{A}_p}{\partial Z} = i \left[\frac{\tilde{\Gamma}_p}{2} |\underline{A}_p|^2 + \tilde{\Gamma}_{ps} |\underline{A}_s|^2 \right] \underline{A}_p + i \tilde{\Gamma}_{pspp} \underline{A}_s [\underline{A}_p^*]^2 e^{+i\Delta k_L^{(3)} Z} \end{cases}, \quad (\text{D.13})$$

By comparing the orders of magnitude of the different terms, we see that the Kerr effect of the signal vanishes on the signal equation, and that only the Kerr component remains in the pump equation:

$$\begin{cases} \frac{\partial \underline{A}_s}{\partial Z} = i \tilde{\Gamma}_{sp} |\underline{A}_p|^2 \underline{A}_s + i \tilde{\Gamma}_{sppp} [\underline{A}_p]^3 e^{-i\Delta k_L^{(3)} Z} \\ \frac{\partial \underline{A}_p}{\partial Z} = i \frac{\tilde{\Gamma}_p}{2} |\underline{A}_p|^2 \underline{A}_p \end{cases}. \quad (\text{D.14})$$

Then, integrating the pump equation and substituting its solution into the signal one, we have:

$$\frac{\partial \underline{A}_s}{\partial Z} = i \tilde{\Gamma}_{sppp} [\underline{A}_p(0)]^3 e^{-i\Delta k_{\text{tot}}^{(3)} Z}, \quad (\text{D.15})$$

with

$$\Delta k_{\text{tot}}^{(3)} = \Delta k_L^{(3)} + \left[3 \frac{\tilde{\Gamma}_p}{2} - \tilde{\Gamma}_{sp} \right] |\underline{A}_p|^2, \quad (\text{D.16})$$

or equivalently

$$\begin{aligned} \Delta \mathbf{k}_{\text{tot}}^{(3)} &= \Delta k_L^{(3)} + \Delta k_{NL}^{(3)} \\ &= \Delta \mathbf{k}_L^{(3)} + [3\gamma_p - 2\gamma_{sp}] \mathbf{P}_p. \end{aligned} \quad (\text{D.17})$$

Besides, the integration of Equation (D.15) is straightforward, and gives:

$$\underline{A}_s(Z) = i \tilde{\Gamma}_{sppp} [\underline{A}_p(0)]^3 Z \text{sinc} \left(\Delta k_{\text{tot}}^{(3)} Z / 2 \right) e^{-i\Delta k_{\text{tot}}^{(3)} Z / 2} \quad (\text{D.18})$$

Résumé en français

Cette thèse porte sur la génération de triplets de photons par interaction paramétrique optique non linéaire du troisième ordre avec la matière solide.

Un triplet de photon, ou plus simplement triplet, est un état à trois particules fortement corrélées. La manière la plus directe de générer un tel état est offerte par l’optique non linéaire du troisième ordre, *i.e.* par le couplage entre quatre ondes électromagnétiques. La vision corpusculaire de la lumière en donne une interprétation simple : un photon se sépare en trois photons d’énergies moindres, un triplet, pendant son interaction avec le milieu non linéaire. L’énergie est alors conservée. Le couplage entre la lumière et la matière se fait à travers la susceptibilité électrique du troisième ordre. Le milieu d’interaction est traditionnellement un cristal, puisqu’il permet de réaliser la conservation du moment linéaire, ou condition d’accord de phase du point de vue de l’optique ondulatoire. La forte cohérence de l’état ainsi généré s’explique par le fait que les trois photons sont créés simultanément du même photon “parent”.

Ce phénomène est analogue à celui qui conduit à la génération de photons jumeaux par interaction non linéaire du second ordre. L’apparition des photons jumeaux dans les années 1970 a été au cœur de nombreux développements dans le domaine de l’optique quantique, comme par exemple pour la démonstration de la violation des inégalités de Bell [1]. Aujourd’hui, ils sont des briques de base fondamentales à l’information quantique. Les triplets de photons pourraient éventuellement également être impliqués dans cette histoire. Ils pourraient par exemple être utilisés dans des protocoles de paires annoncées [2], dans lequel un des trois photons annonce les deux autres, formant alors une paire. Mais les motivations pour générer des états avec cette intrigante propriété d’intrication sont avant tout purement fondamentales : leur caractère non classique est différent de celui des états jumeaux, et leur génération est un réel challenge expérimental [3–14].

La première démonstration expérimentale de génération de triplets de photons (TPG, de l’anglais “triple photon generation”) a été réalisée dans notre groupe à Grenoble en 2004, dans une configuration légèrement différente de celle qui a été décrite plus haut [13]. Deux autres faisceaux étaient en effet utilisés pour stimuler le processus, et ainsi augmenter la probabilité de générer des triplets, comme représenté sur la Figure E.1. La génération spontanée, c’est-à-dire sans stimulation, est appelée fluorescence paramétrique du troisième ordre et n’a aujourd’hui

encore jamais été démontrée expérimentalement. Son efficacité de conversion est en effet extrêmement faible dans les cristaux massifs puisque les ondes ne sont pas étroitement confinées, et cela malgré des intensités incidentes importantes, de l'ordre de 100 GWcm^{-2} [15]. Néanmoins, il a été démontré que le nombre important de photons de stimulation cache les corrélations entre triplets [16] (voir Figure E.2).

Etat de l'art de la génération de triplets de photons (1)

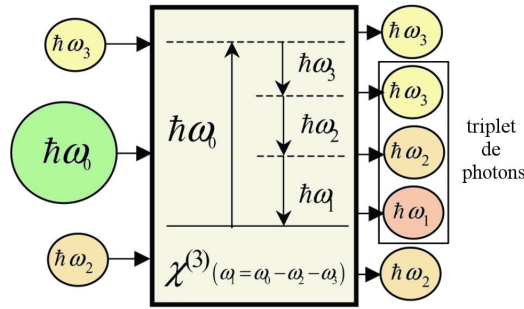


Figure E.1 – Génération bi-injectée de triplets de photons.

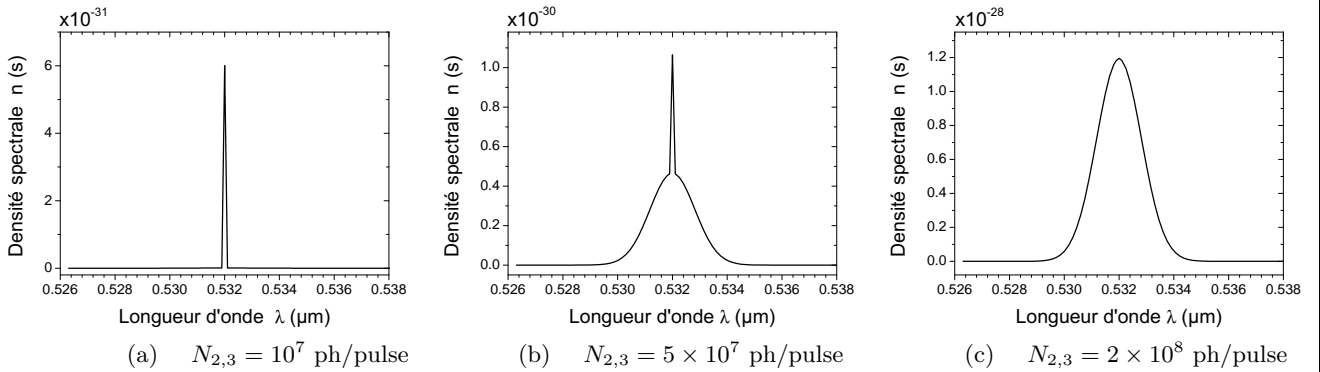


Figure E.2 – Spectres de recombinaison pour différents niveaux d'injection par les champs 2 et 3, dans le régime de bi-stimulation. Deux cristaux de KTP usinés selon l'axe x sont utilisés pour la génération ainsi que la recombinaison, avec des longueurs respectives de 10 et 0.1 mm. La densité de puissance de la pompe monochromatique à 532 nm est égale à 25 GWcm^{-2} (4×10^{13} photons/pulse). Le pic de Dirac, signature quantique des corrélations, est masqué lorsque le niveau d'injection est trop élevé. Adapté de [120].

Il est donc important de trouver une configuration qui permette de générer des triplets de photons efficacement, avec peu de photons d'injection, voire aucun, pour conserver la cohérence de cet état. Le but de ce travail est précisément de répondre à ce besoin en étudiant deux stratégies des points de vue expérimentaux et théoriques. La première stratégie traite de la TPG dans des cristaux massifs. Ces cristaux pourraient alors être placés en cavité pour augmenter artificiellement la longueur d'interaction. La seconde se concentre sur la TPG dans des fibres optiques, de sorte que non seulement la longueur d'interaction est importante, mais qu'également

le champ électromagnétique est bien plus confiné, entraînant des intensités générées plus grandes. Un dernier avantage des fibres isotropes réside dans le fait qu’aucun processus du second ordre ne peut venir polluer la TPG.

Nous résumons ici par chapitre les travaux exposés dans ce manuscrit.

Le [chapitre 1](#) donne les éléments de théorie nécessaires à la compréhension de ce travail. Le sujet est introduit par des notions générales d’optique paramétrique classique, en champs électromagnétiques polychromatiques. Il est montré que toute interaction non linéaire satisfait les conditions de conservation de l’énergie et du moment linéaire (ou accord de phase). Une attention particulière est portée à la maximisation du coefficient effectif non linéaire et des recouvrements spatial et temporel.

Ces considérations générales sont ensuite adaptées aux cas spécifiques de l’optique cristalline d’une part, et de l’optique des fibres d’autre part. Dans ces deux cas, deux types d’accord de phase différents peuvent être réalisés : un accord de phase par biréfringence dans le premier cas, et un accord de phase intermodal dans le second.

Enfin, les états étudiés ne pouvant être compris complètement avec une vision classique, des bases d’optique quantique sur les interactions non linéaires sont données.

Le [chapitre 2](#) donne les motivations quant à l’étude des états triplets de photons. Il fait également un état de l’art sur la génération et les études de corrélations de tels états, avant de rappeler une nouvelle fois nos stratégies.

Les triplets de photons sont des états de la lumière à trois particules, étroitement corrélés, qui appartiennent aux classes d’intrication GHZ [\[78\]](#) ou W [\[10\]](#). Ces corrélations sont différentes de celles des photons jumeaux et non classiques, comme en témoignent par exemple les négativités et les motifs d’interférences de leur fonction de Wigner représentée [Figure E.3](#). Les triplets sont donc des objets intéressants pour l’exploration de la mécanique quantiques des états à N -particules, $N > 2$, et plus particulièrement pour l’optique quantique. Ils pourraient également être le support de nouveaux protocoles d’information quantique.

Ces dernières années, différentes stratégies ont été utilisées pour générer des triplets de photons. La plus attirante, mais la plus difficile expérimentalement, est la génération directe : la scission spontanée d’un photon en trois photons d’énergies moindres, par interaction paramétrique optique d’ordre trois avec un milieu non linéaire. Différents matériaux non linéaires ont été étudiés. Plus indirectement, ces triplets peuvent aussi être créés par deux interactions successives du deuxième ordre ([Figure E.4b](#)) [\[14\]](#) ; ou via l’expérience de “gomme quantique” basée sur la superposition cohérente de deux paires de photons par exemple ([Figure E.4a](#)) [\[6\]](#).

L’état des recherches actuelles sur l’étude des corrélations des états triplets, par recombinaison dans un second milieu non linéaire, par tomographie quantique ou par mesures de coïncidences, est enfin donné.

Etat de l'art de la génération de triplets de photons (2)

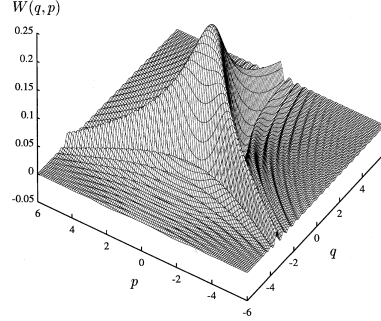


Figure E.3 – Distribution de Wigner de l'état triplet dégénéré en fréquence et en polarisation, dans l'espace des quadratures du champ électrique. D'après [3].

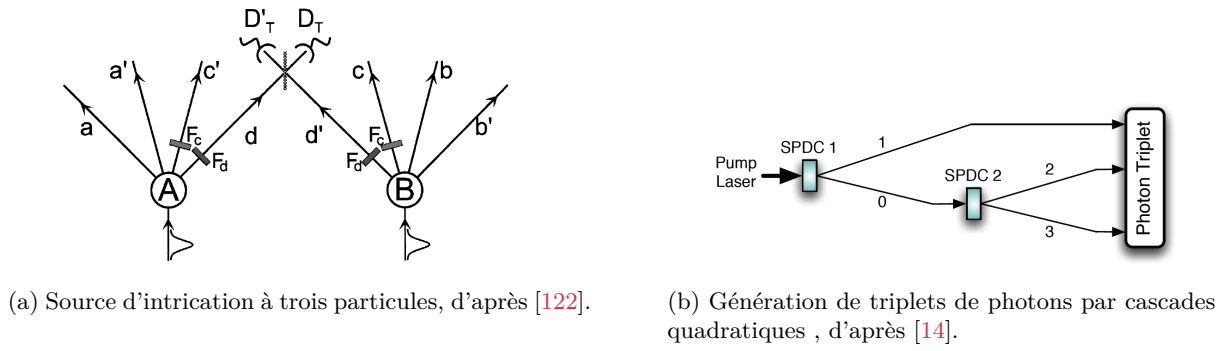


Figure E.4 – Protocoles indirects de générations de triplets de photons.

Nous rappelons dans ce chapitre que cette thèse porte sur la génération directe de triplets de photons par interaction non linéaire optique d'ordre trois. Elle se situe dans la continuité de travaux qui ont commencé il y a dix ans par la première démonstration expérimentale de TPG, stimulée par deux faisceaux additionnels, dans l'équipe de Benoît Boulanger à Grenoble. De tels faisceaux de stimulation étaient en effet nécessaires pour surmonter l'extrême faiblesse du rendement de conversion qui fait de la TPG directe un défi en optique non linéaire. Cependant, ces faisceaux de stimulation eurent également pour conséquence de masquer les corrélations entre photons d'un triplet. Notre objectif est donc évident : permettre une génération efficace avec aussi peu de photons de stimulation que possible, idéalement aucun. Ainsi, deux stratégies expérimentales sont adoptées au cours de ces travaux. Leurs objectifs sont résumés ici :

- 1. TPG dans des cristaux massifs, en configuration OPO. La mise en cavité augmente artificiellement la longueur d'interaction, et donc le rendement de conversion de sorte qu'il devient possible de diminuer le niveau d'injection.
- 2. TPG dans des fibres optiques. Les fibres optiques présentent l'avantage de confiner le champ électromagnétique, en plus de rendre possible l'utilisation de grandes longueurs

d'interaction. De plus, aucune interaction du second ordre, dont les rendements de conversion sont bien plus importants que ceux des interactions du troisième ordre, ne peut exister. Cette fois encore, il devient possible de se débarrasser des faisceaux de stimulation.

Le [chapitre 3](#) est dédié à l'étude de deux oxydes cristallins massifs anisotropes : KTP et TiO_2 sous sa forme rutil. Ces cristaux permettent de réaliser la TPG par accord de phase par biréfringence. Les configurations d'ondes libres et d'ondes en cavité sont étudiées.

Une étude expérimentale des propriétés spectrales et énergétiques de la TPG bi-stimulée dans KTP est réalisée en régime picoseconde, sur l'expérience à l'état de l'art avec deux faisceaux d'injection : $532^{(-)} \rightarrow 1478^{(+)} + 1662^{(-)} + 1662^{(+)} \text{ nm}$. Notre modèle impliquant la polychromaticité des champs en interaction et un effet Kerr explique avec succès les résultats expérimentaux ([Figure E.5](#)). L'effet Kerr modifie le désaccord de phase et la géométrie des faisceaux. Par conséquent, cet effet parasite atténue l'efficacité de conversion de la TPG quand les intensités sont suffisamment importantes. Le rendement de conversion maximum obtenu avec ce générateur de triplets est de 3.5 %. Des intensités allant jusqu'à 300 GWcm^{-2} ont été focalisées dans le cristal de KTP sans endommagement.

Ensuite, les propriétés linéaires et non linéaires du dioxyde de titane sous sa forme rutil sont examinées expérimentalement à travers une génération de troisième harmonique (THG) pour des longueurs d'onde fondamentales situées entre 1836 nm et 4449 nm ([Figure E.6a](#)). Son rendement de conversion atteint environ 1%. La THG est le processus inverse de la TPG totalement dégénérée en énergie : trois photons fusionnent en un unique photon d'énergie plus importante. Cette expérience a permis de raffiner les équations de dispersion de ses indices de réfraction ([Figure E.6b](#)). La valeur absolue de l'amplitude du coefficient non linéaire χ_{18} a été déterminée ; ainsi que son signe, opposé à χ_{16} .

Les calculs de conditions d'accord de phase pour la TPG ont indiqué l'existence de configurations à l'accord de phase. Cependant, aucune de nos tentatives expérimentales ont conduit à une démonstration de la TPG dans le TiO_2 rutil, même avec deux champs de stimulation. L'onde à 532 nm impliquée dans le processus de TPG n'avait en fait pas pu être sollicité au cours de l'expérience de THG. Ceci implique une inexactitude préjudiciable de son indice principal ordinaire, et selon toute vraisemblance un accord de phase inexistant. Les travaux à venir sur ce cristal devront viser ou bien à l'obtention d'une meilleure estimation de ces indices de réfraction, ou bien à la réalisation d'une TPG à de plus hautes longueurs d'onde si l'étage de détection le permet.

Enfin, l'usage des deux cristaux KTP and TiO_2 dans un oscillateur paramétrique optique (OPO) à pompage synchrone est étudié sur le plan théorique, et donne lieu à deux propositions. L'OPO doit être pompé par un laser à haute fréquence de répétition dans le régime picoseconde. La première proposition, représentée sur la [Figure E.7a](#), est un OPO mono-injecté et doublement résonant. Une énergie $\mathcal{E}_{2,3} = 40 \text{ nJ}$ peut être générée pour $\mathcal{E}_0 = 300 \text{ nJ}$ d'énergie de pompe, $\mathcal{E}_1 = 30 \text{ nJ}$ d'injection, et une transmission du miroir M_A de $T_A = 1 \%$ ([Figure E.7b](#)). La seconde proposition, schématisée sur la [Figure E.8a](#), est un OPO triplement résonant, sans aucun faisceau d'injection : dans ce cas, la cavité est sans perte jusqu'à extraction du signal

généralisé au temps voulu grâce à une cellule acousto-optique. Environ 10^6 aller-retours dans la cavité sont nécessaires pour générer des impulsions triplets de l'ordre du μJ (Figure E.8b). Il est également possible, en particulier pour des expériences de coïncidences ou de tomographie quantique, d'extraire le signal lorsque seulement quelques triplets de photons sont générés. Les propriétés de cohérence des photons appartenant aux mêmes triplets n'ont pas été étudiées ici. C'est cependant un point important qu'il faut garder à l'esprit, puisque les corrélations doivent être conservées.

Génération de triplets de photons dans des cristaux massifs anisotropes

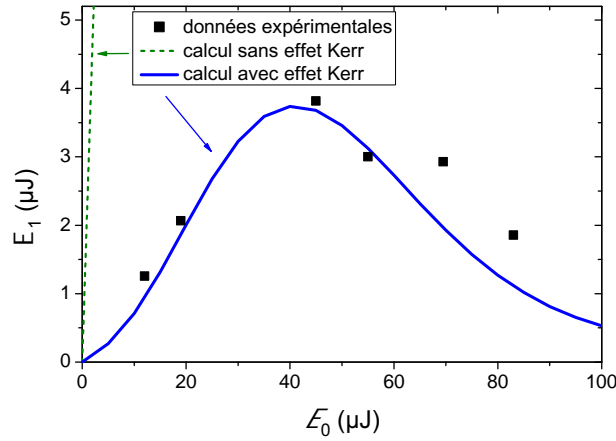
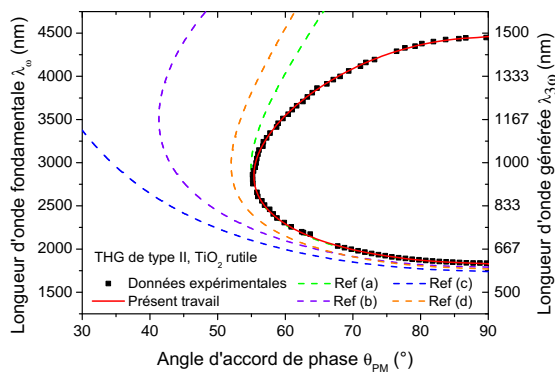
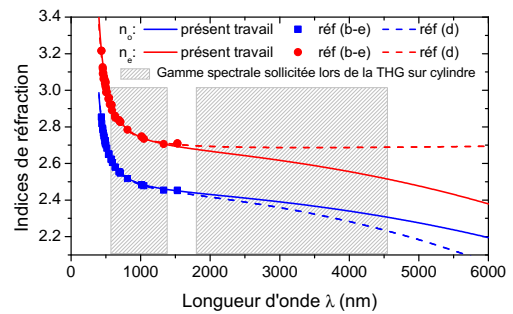


Figure E.5 – Energie générée sur le champ 1 en fonction de l'énergie du champ pompe 0. L'énergie des champs de stimulation est fixée à $\mathcal{E}_2 + \mathcal{E}_3 = 63 \mu\text{J}$. Deux paramètres de fits $v = 0.388$ et $\mu = 0.6$ sont utilisés dans le modèle.



(a) Courbe d'accord de phase de THG de type II du TiO_2 rutile. Les données expérimentales de l'expérience du cylindre sont représentées en carré noirs, et leur interpolation numérique est la courbe rouge. Les courbes d'accord de phase en pointillés sont calculées à partir de données bibliographiques.



(b) Indices principaux ordinaires n_o et extraordinaires n_e de TiO_2 en fonction de la longueur d'onde déterminés par ce travail en lignes continues ; et par s'autres travaux en symboles (expériences) et lignes pointillées (calculs).

Figure E.6 – Etude d'accord de phase du TiO_2 rutile. Références : [107] (a), [154] (b), [155] (c), [156] (d) et [157] (e).

Génération de triplets de photons en cavité à pompage synchrone

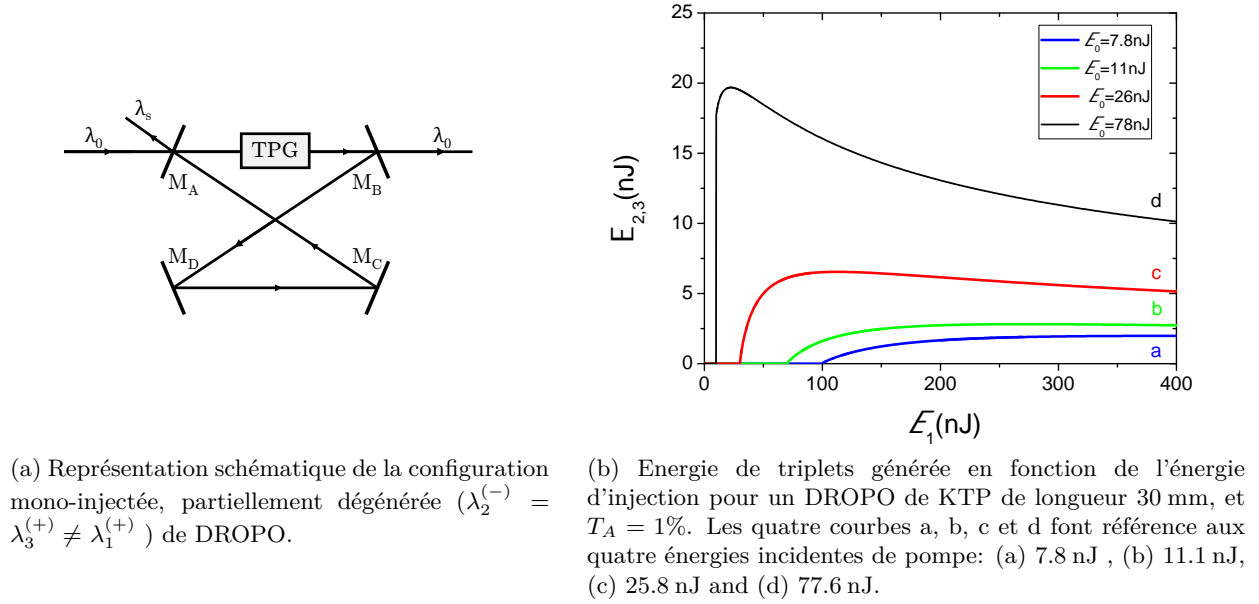


Figure E.7 – OPO doublement résonant (DROPO) du troisième ordre.

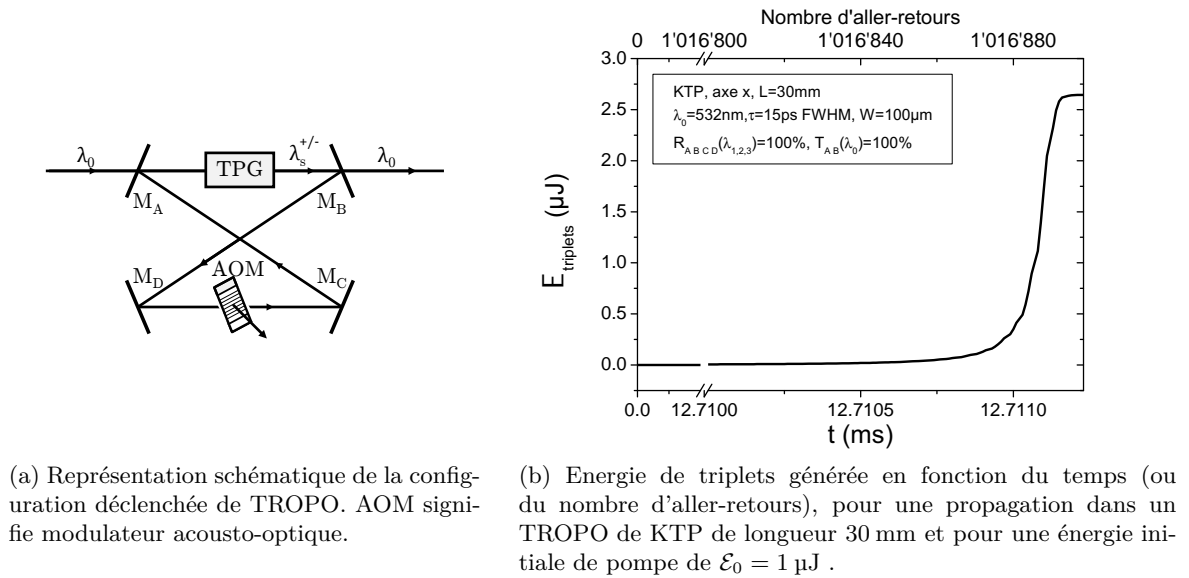


Figure E.8 – OPO triplement résonant (TROPO) du troisième ordre.

Le [chapitre 4](#) traite de la TPG dans des fibres optiques. Des fibres à saut d'indice en silice dopées germanium et des fibres à cristaux photoniques (PCF) en chalcogénures sont considérées. Un accord de phase modal est réalisé, ces matériaux étant isotropes.

Génération de triplets de photons dans des fibres optiques de silice

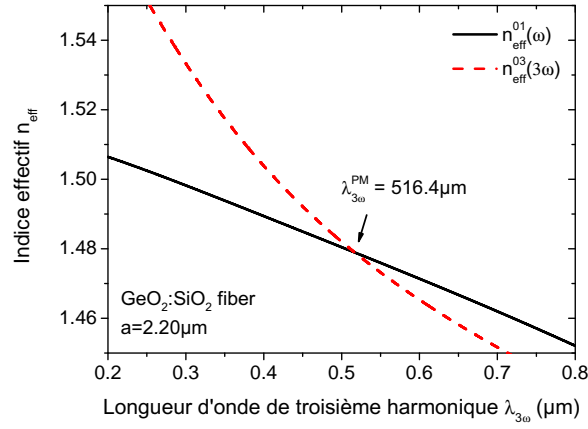


Figure E.9 – Condition d'accord de phase dans une fibre de silice dopée germanium, de rayon de cœur $a = 2.20\mu\text{m}$.

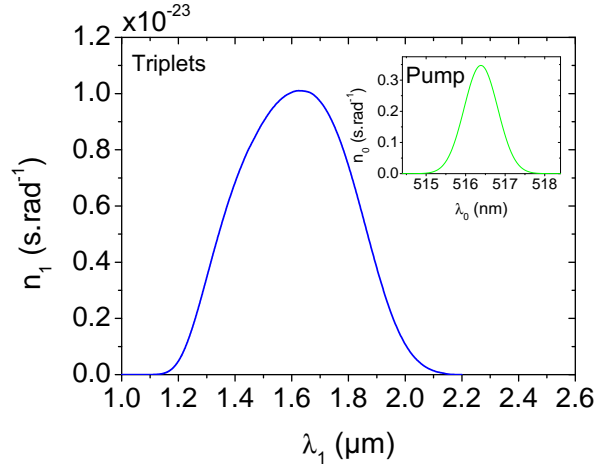


Figure E.10 – Densité spectrale de photons dans le champ 1 pour $L = 1\text{ m}$ et $\mathcal{E}_0 = 1\mu\text{J}$. L'encart représente la densité spectrale de photons pompe ($\Delta\lambda_0^{\text{FWHM}} = 1\text{ nm}$).

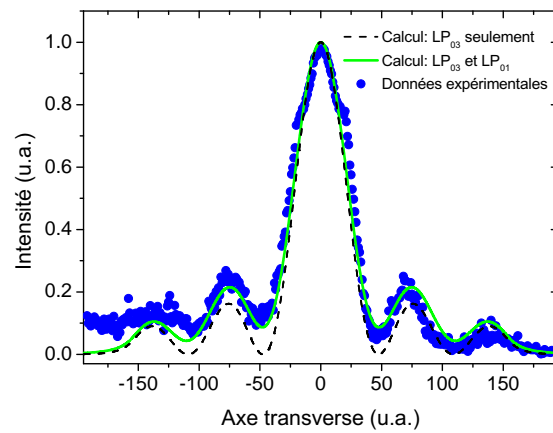


Figure E.11 – Profils transverses calculés et expérimental du mode LP_{03} généré après propagation dans le masque de phase.

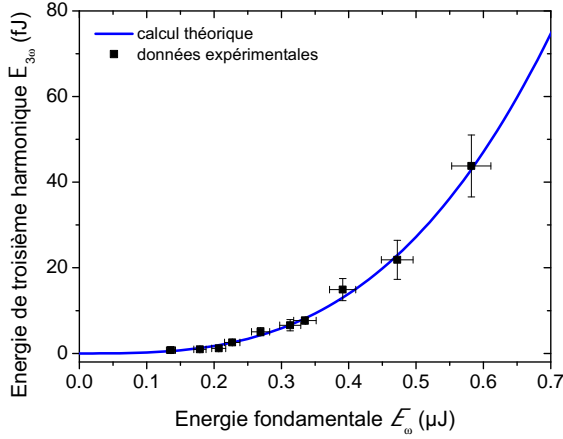
Des fibres de SiO₂ dopées par GeO₂, de rayons de cœur $a = 2.19 \mu\text{m}$ et $2.30 \mu\text{m}$ sont utilisées. Elles ont été conçues pour permettre la réalisation d'un accord de phase modal dégénéré en fréquence entre les modes transverses LP₀₁ et LP₀₃ pour les longueurs d'onde λ_ω et $\lambda_{3\omega}$ respectivement (Figure E.9). Le rendement de conversion de la THG étant plus important que celui de la TPG, et ces deux processus satisfaisant la même condition d'accord de phase, la THG est considérée en premier lieu pour concevoir au mieux l'expérience de TPG. Une caractérisation expérimentale complète est réalisée dans ces fibres en régime nanoseconde. Sont étudiées les propriétés spectrales, énergétiques, modales et de polarisation. Les longueurs d'onde expérimentales d'accord de phase sont très proches des longueurs d'onde calculées : $\lambda_\omega = 3\lambda_{3\omega} = 1550 \text{ nm}$ et 1602 nm pour les fibres de rayons de cœur $2.19 \mu\text{m}$ et $2.30 \mu\text{m}$ respectivement. Nous avons mis en évidence des fluctuations de la taille du cœur, une ellipticité de la section transverse du cœur et de l'anisotropie. Ceci conduit respectivement à une grande acceptation spectrale, $L\delta\lambda_\omega = 104 \text{ nm.cm}$, ce qui constitue un avantage puisque des fibres de tailles plus importantes peuvent être utilisées ; des modes transverses elliptiques sous la forme mathématique de modes de Ince-Gauss, LP₀₃ devenant IG₄₀^e, ce qui implique un recouvrement moins important des modes LP incidents ; et un rendement de conversion qui peut être maximisé pour une orientation particulière de la polarisation fondamentale incidente. Précisément, l'analyse des états de polarisation des ondes à λ_ω et $\lambda_{3\omega}$ en sortie de fibres nous ont permis de conclure que ces fibres appartiennent à la classe optique uniaxe, et d'en déduire des valeurs relatives pour les éléments non nuls du tenseur de susceptibilité du troisième ordre (Figure E.12b). Enfin, l'aire d'interaction effective est 60 fois plus grande que la surface du cœur de la fibre : $S_{\text{eff}} = 931 \mu\text{m}^2$. Pour cette raison et du fait d'intensités incidentes faibles, le rendement de conversion est extrêmement faible, de l'ordre de 8×10^{-8} (Figure E.12a).

Cette configuration de THG entre modes LP₀₁ et LP₀₃ n'est pas l'unique interaction non linéaire existant dans ces fibres : d'autres configurations modales pour la THG à l'accord de phase ont été identifiées et étudiées (Figures E.12c et E.12d) ; enfin, de l'effet Raman a été mis en évidence conduisant à la génération de nombreux pics intenses dans l'infrarouge.

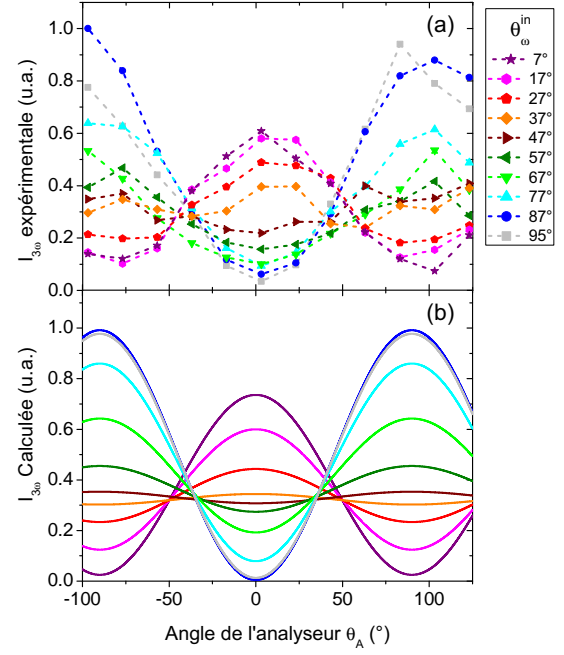
Des calculs quantiques théoriques pour la TPG spontanée, *i.e.* la fluorescence paramétrique du troisième ordre, dans le cas de l'interaction précédente entre modes LP₀₁ et LP₀₃ dans ces mêmes fibres ont été réalisés et conduisent à des rendements de conversion extrêmement faibles dans la situation expérimentale actuelle. Par exemple, la Figure E.10 montre que 4.7×10^{-8} triplets/sec peuvent être générés dans une fibre de 1m, pour une énergie fondamentale incidente de $1 \mu\text{J}/\text{pulse}$ (10ns de temps de pulses, 10Hz de fréquence de répétition). Ce taux de génération pourrait être amélioré en utilisant une source laser à fort taux de répétition, des fibres à plus petits cœurs ou encore des matériaux avec des non-linéarités nettement plus importantes.

La préparation modale du faisceau fondamental de TPG a été réalisée : des masques de phase permettent de générer avec une efficacité de 90% le profil LP₀₃, non Gaussien (Figure E.11). L'étage de filtrage a également été étudié. Si l'une des conditions nécessaires à l'augmentation du taux de production de triplets mentionnée plus haut est satisfaite, la réalisation expérimentale de la TPG devrait être possible avec une photodiode à avalanche (APD) qui permet le comptage proportionnel de photons, et l'intégration temporelle. Un tel détecteur sera prochainement disponible, grâce à une collaboration avec Johan Rothman du CEA-LETI de Grenoble.

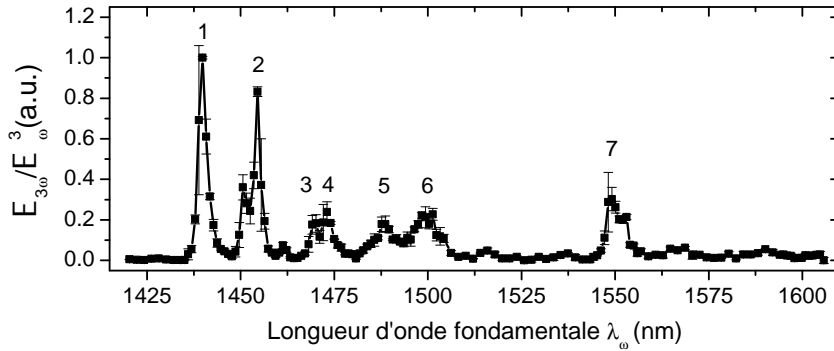
Génération de troisième harmonique dans des fibres optiques de silice



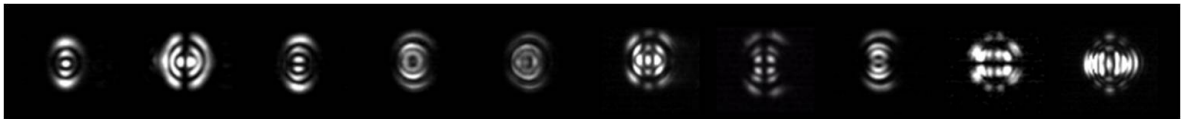
(a) Energie de troisième harmonique $\mathcal{E}_{3\omega}$ en fonction de l'énergie incidente \mathcal{E}_{ω} .



(b) Intensités de expérimentales (a) et calculées (b) du signal de troisième harmonique analysé à l'angle θ_A pour différentes configurations de polarisation du faisceau incident fondamental.



(c) Spectre de troisième harmonique normalisé. \mathcal{E}_{ω} et $\mathcal{E}_{3\omega}$ sont les énergies fondamentales et de troisième harmonique respectivement.



(d) Clichés expérimentaux des distributions transverses d'intensité des ondes de troisième harmonique.

Figure E.12 – Expériences de génération de troisième harmonique (THG) dans une fibre de silice dopée germanium de rayon de cœur $a = 2.19 \mu\text{m}$ et de longueur $L = 642 \text{ mm}$.

Enfin, les propriétés d'accord de phase pour la TPG dans des PCF de chalcogénures sont étudiées dans le cadre d'une collaboration avec le groupe de Pierre Bourdon à l'ONERA de

Palaiseau. Ces matériaux ont des non-linéarités géantes, trois ordres de grandeur au-dessus de celles des oxydes. Un accord de phase intermodal entre modes transverses LP_{01} et LP_{02} est possible dans As_2S_3 , pour un jeu particulier de paramètres géométriques de la PCF : $d = 4.25\mu m$ le diamètre d'un trou, $\Lambda = 5\mu m$ la distance entre deux trous (Figure E.13). Il conduit à des longueurs d'onde d'accord de phase de 1550.5 nm pour la pompe, et situées entre 4.5 et $5\mu m$ pour les triplets (Figure E.14). La prise en compte de la contribution non linéaire au désaccord de phase déplace ces longueurs d'onde de quelques nanomètres. L'APD dont il était question précédemment, dont la gamme de transparence couvre le moyen infra-rouge, pourrait être utilisée dans ce cadre également.

Génération de triplets de photons dans des fibres optiques de chalcogénures

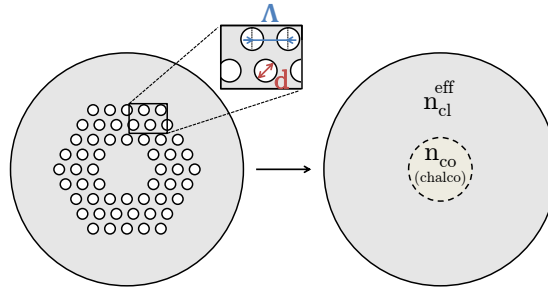


Figure E.13 – Représentations schématiques d'une fibre à cristal photonique, et sa fibre à saut d'indice équivalente.

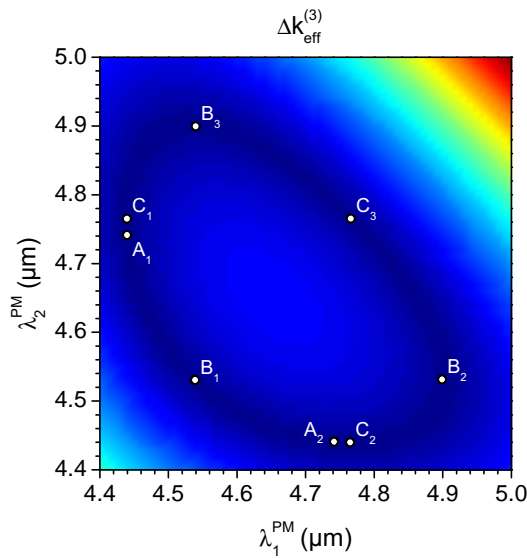


Figure E.14 – Carte d'accord de phase : $\Delta k_{\text{eff}}^{(3)}$ en fonction de λ_1^{PM} et λ_2^{PM} ; $\lambda_0^{\text{PM}} = 1551\text{ nm}$, $\Lambda = 5\mu m$ and $d = 0.85\Lambda = 4.25\mu m$. A_1 et A_2 (resp. B_1 , B_2 et B_3 ; C_1, C_2 et C_3) sont des jeux de longueurs d'onde en accord de phase équivalents.

Quelques pas seront encore nécessaires à la réalisation d'une génération directe et spontanée de triplets de photons par interaction non linéaire optique du troisième ordre.

Quelques pas supplémentaires veilleront ensuite à rendre cette génération compatible avec des mesures quantiques. Certainement malaisés, ils permettront alors l'étude des propriétés de cohérence de ces états triplets et la démonstration de leurs propriétés non classiques, par exemple à travers des mesures de coïncidence ou de tomographie quantique.

Un jour alors, de nombreux pas plus loin, ces états pourront éventuellement faire partie des protocoles d'information quantique...

Scientific production related to this PhD work

F.1 Publications

- **A Borne**, T Katsura, C Félix, B Doppagne, P Segonds, K Bencheikh, JA Levenson, B Boulanger, Multiple intermodal phase-matched third-harmonic generations in a silica optical fiber, Opt. Lett. (to be submitted).
- **A Borne**, T Katsura, C Félix, B Doppagne, P Segonds, K Bencheikh, JA Levenson, B Boulanger, Anisotropy analysis of third-harmonic generation in a germanium-doped silica optical fiber, Opt. Lett., **40**, 6, 982-985 (2015).
- **A Borne**, P Segonds, B Boulanger, C Félix, and J Debray, Refractive indices, phase-matching directions and third-order nonlinear coefficients of rutile TiO₂ from third-harmonic generation, Opt. Mat. Expr., **2**, 12, 1797-1802 (2012).
- A Dot, **A Borne**, B Boulanger, P Segonds, C Félix, K Bencheikh, and JA Levenson, Energetic and spectral properties of triple photon down-conversion in a phase-matched KTiOPO₄ crystal, Opt. Lett., **37**, 12, 2334-2336 (2012).
- A Dot, **A Borne**, B Boulanger, K Bencheikh, and JA Levenson, Quantum theory analysis triple photons generated by a $\chi^{(3)}$ process, Phys. Rev. A, **85**, 023809 (2012).

F.2 Oral communications

F.2.1 International invited conferences

- Boulanger, **A Borne**, K Bencheikh, JA Levenson, P Segonds and C Felix, New state of light from third-order parametric down-conversion processes, IEEE Photonics Conference, San Diego, 12-16 October 2014.
- B Boulanger, A Dot, **A Borne**, P Segonds, K Bencheikh, JA Levenson, and S Richard, $\chi^{(3)}$ third-harmonic generation and triple photon generation, Photonics West, San Francisco,

21 - 26 January 2012.

F.2.2 Oral communications in international conferences

- **A Borne**, A Dot, B Boulanger, P Segonds, C Félix, K Bencheikh, and JA Levenson, Triple photons: a new chapter of nonlinear and quantum optics, 50 Years of Non Linear optics International Symposium, Barcelona, Spain, October 8-10, 2012.
- **A Borne**, A Dot, B Boulanger, P Segonds, C Félix, K Bencheikh, and JA Levenson, Energetic and spectral properties of triple photon down-conversion in a phase-matched KTiOPO₄ crystal, Nonlinear Photonics - EOS Annual Meeting, Aberdeen, Scotland UK, September 25-28, 2012.

F.2.3 Posters in international conferences

- **A Borne**, T Katsura, B Doppagne, B Boulanger, C Félix, P Segonds, K Bencheikh, and JA Levenson, Intermodal third-harmonic generation in anisotropic germanium-doped silica optical fiber, Advanced Solid-State Lasers, Shanghai, 16-21 November 2014.
- **A Borne**, T Katsura, B Doppagne, B Boulanger, C Félix, P Segonds, K Bencheikh, and JA Levenson, Intermodal third-harmonic generation in germanium-doped silica optical fiber, 6th Europhoton, Neuchâtel, Switzerland, 24-29 August 2014.
- **A Borne**, T Katsura, B Doppagne, B Boulanger, C Félix, P Segonds, K Bencheikh, and JA Levenson, Anisotropy of phase-matched third-harmonic generation in germanium-doped silica optical fiber, Advanced Photonics, Barcelona, Spain, 28-31 July 2014.
- **A Borne**, A Dot, B Boulanger, P Segonds, C Félix, K Bencheikh, and JA Levenson, Experiments and modeling of energetic and spectral properties of triple photons third-order down-conversion in KTiOPO₄, 5th Europhoton, Stockholm, Sweden, August 26-31, 2012.
- **A Borne**, A Dot, B Boulanger, K Bencheikh, JA Levenson, P Segonds and C Félix, Theoretical and experimental analysis of the quantum triplet state of light, Quantum Malta 2012: fundamental problems in quantum physics, La Valette, Malta, April 24-27, 2012.
- A Dot, **A Borne**, B Boulanger, K Bencheikh, JA Levenson, P Segonds and C Félix, Theoretical analysis of the photon triplet state of light, Frontiers of Condensed Matter Summer School, Les Houches, France, September 5-16, 2011.

F.2.4 Oral communications in national conferences

- **A Borne**, A Dot, B Boulanger, P Segonds, C Félix, Generation and quantum correlations of the triplet photon state of light, Annual meeting of the GDR "Information Quantique, Fondements et Applications", Grenoble, November 28-30, 2012.

Bibliography

- [1] A. Aspect, P. Grangier, and G. Roger, “Experimental tests of realistic local theories via Bell’s theorem,” *Physical Review Letters*, vol. 47, no. 7, p. 460, 1981. [1](#), [46](#), [187](#)
- [2] A. Cabello and F. Sciarrino, “Loophole-free Bell test based on local precertification of photon’s presence,” *Physical Review X*, vol. 2, no. 2, p. 021010, 2012. [1](#), [187](#)
- [3] K. Banaszek and P. L. Knight, “Quantum interference in three-photon down-conversion,” *Physical Review A*, vol. 55, no. 3, p. 2368, 1997. [1](#), [61](#), [187](#), [190](#)
- [4] T. Felbinger, S. Schiller, and J. Mlynek, “Oscillation and generation of nonclassical states in three-photon down-conversion,” *Physical Review Letters*, vol. 80, no. 3, p. 492, 1998. [61](#), [95](#)
- [5] K. J. Resch, P. Walther, and A. Zeilinger, “Full characterization of a three-photon Greenberger-Horne-Zeilinger state using quantum state tomography,” *Physical Review Letters*, vol. 94, no. 7, p. 070402, 2005. [62](#)
- [6] D. Bouwmeester, J.-W. Pan, M. Daniell, H. Weinfurter, and A. Zeilinger, “Observation of three-photon Greenberger-Horne-Zeilinger entanglement,” *Physical Review Letters*, vol. 82, no. 7, p. 1345, 1999. [55](#), [56](#), [62](#), [189](#)
- [7] J.-W. Pan, D. Bouwmeester, M. Daniell, H. Weinfurter, and A. Zeilinger, “Experimental test of quantum nonlocality in three-photon Greenberger–Horne–Zeilinger entanglement,” *Nature*, vol. 403, no. 6769, pp. 515–519, 2000. [55](#), [62](#)
- [8] D. Greenberger, M. Horne, and A. Zeilinger, *Bell’s theorem, quantum theory, and conceptions of the universe*. Edited by M. Kafatos (Kluwer Academic, Dordrecht), 1989, ch. “Going beyond Bell’s theorem”, pp. 73–76. [47](#)
- [9] A. Zeilinger, M. Horne, and D. Greenberger, “Nasa conf. publ. no. 3135.” National Aeronautics and Space Administration, Code NTT, Washington, DC, 1997. [47](#)
- [10] N. Kiesel, M. Bourennane, C. Kurtsiefer, H. Weinfurter, D. Kaszlikowski, W. Laskowski, and M. Zukowski, “Three-photon W-state,” *Journal of Modern Optics*, vol. 50, no. 6-7, pp. 1131–1138, 2003. [47](#), [62](#), [189](#)

-
- [11] P. van Loock and A. Furusawa, “Detecting genuine multipartite continuous-variable entanglement,” *Physical Review A*, vol. 67, p. 052315, 2003. [47](#)
 - [12] M. Corona, K. Garay-Palmett, and A. B. U’Ren, “Third-order spontaneous parametric down-conversion in thin optical fibers as a photon-triplet source,” *Physical Review A*, vol. 84, no. 3, p. 033823, 2011. [33](#), [52](#), [145](#), [146](#)
 - [13] J. Douady and B. Boulanger, “Experimental demonstration of a pure third-order optical parametric downconversion process,” *Optics Letters*, vol. 29, no. 23, pp. 2794–2796, 2004. [1](#), [49](#), [187](#)
 - [14] H. Hübel, D. R. Hamel, A. Fedrizzi, S. Ramelow, K. J. Resch, and T. Jennewein, “Direct generation of photon triplets using cascaded photon-pair sources,” *Nature*, vol. 466, no. 7306, pp. 601–603, 2010. [1](#), [56](#), [57](#), [62](#), [187](#), [189](#), [190](#)
 - [15] K. Bencheikh, F. Gravier, J. Douady, A. Levenson, and B. Boulanger, “Triple photons: a challenge in nonlinear and quantum optics,” *Comptes Rendus Physique*, vol. 8, no. 2, pp. 206–220, 2007. [2](#), [52](#), [61](#), [62](#), [188](#)
 - [16] A. Dot, A. Borne, B. Boulanger, K. Bencheikh, and J. Levenson, “Quantum theory analysis of triple photons generated by a $\chi^{(3)}$ process,” *Physical Review A*, vol. 85, p. 023809, 2012. [2](#), [43](#), [53](#), [54](#), [58](#), [145](#), [188](#)
 - [17] A. Yariv and P. Yeh, *Optical waves in crystal*. New York: Wiley, 2003. [4](#), [7](#), [8](#), [22](#)
 - [18] J. Pérez, R. Carlos, and R. Fleckinger, *Électromagnétisme, Fondements et applications*, 2nd ed. Masson, 1996. [5](#)
 - [19] B. Boulanger and J. Zyss, *Nonlinear optical properties*. International Union of Crystallography, 2006, ch. 1.7, pp. 178–219. [5](#), [16](#), [21](#), [22](#), [23](#), [77](#)
 - [20] P. Franken, A. Hill, C. Peters, and G. Weinreich, “Generation of optical harmonics,” *Physical Review Letters*, vol. 7, pp. 118–119, Aug 1961. [5](#)
 - [21] J. Armstrong, N. Bloembergen, J. Ducuing, and P. Pershan, “Interactions between Light Waves in a Nonlinear Dielectric,” *Physical Review*, vol. 127, no. 6, pp. 1918–1939, 1962. [5](#), [12](#), [18](#), [49](#)
 - [22] N. Bloembergen, *Nonlinear optics*. New York: Benjamin, 1965. [5](#), [16](#), [18](#), [71](#)
 - [23] M. Born and E. Wolf, *Principles of Optics*, 6th ed. Pergamon Press, 1980. [6](#), [8](#), [20](#), [22](#), [82](#)
 - [24] J. Jackson, *Classical electrodynamics*, 3rd ed. New York: Wiley, 1998. [7](#)
 - [25] J. Nye, *Physical properties of crystals*. Clarendon Press, 1957. [9](#), [12](#), [20](#), [130](#)
 - [26] O. Svelto and D. Hanna, *Principles of lasers*, 5th ed. Springer, 1976. [10](#)
 - [27] A. Siegman, *Lasers*. Mill Valley, CA: University Science Books, 1986. [10](#), [105](#)
-

- [28] A. Hadni, *Essentials of modern physics applied to the study of the infrared*. Oxford: Pergamon Press, 1967. 11, 84
- [29] I. Jacobs, *Optical fiber communication technology and system overview*, in *Handbook of Optics*. McGraw Hill, 2010, vol. V Atmospheric optics, modulators, fiber optics, X-ray and neutron optics, ch. 9. 11
- [30] G. Agrawal, *Nonlinear fiber optics*, 5th ed. Academic Press, 2013. 11, 34, 109, 110, 146
- [31] D. Kleinman, “Nonlinear dielectric polarization in optical media,” *Physical Review*, vol. 126, pp. 1977–1979, Jun 1962. 12
- [32] G. Grynberg and P. Berman, “Quantized-field approach to parametric mixing and pressure-induced resonances: Schrödinger picture,” *Physical Review A*, vol. 43, no. 7, p. 3994, 1991. 13
- [33] J. Fève, B. Boulanger, and J. Douady, “Specific properties of cubic optical parametric interactions compared to quadratic interactions,” *Physical Review A*, vol. 66, p. 063817, Dec 2002. 13, 17, 49, 99
- [34] A. Yariv, *Introduction to optical electronics*. Holt, Rinehart and Winston, Inc., New York, NY, 1976. 15, 104
- [35] G. New, *Introduction to Nonlinear Optics*. Cambridge University Press, 2011. 17
- [36] J. Yao and T. S. Fahlen, “Calculations of optimum phase match parameters for the biaxial crystal KTiOPO₄,” *Journal of Applied Physics*, vol. 55, no. 1, pp. 65–68, 1984. 20
- [37] L. Shuvalov, *Modern Crystallography IV: Physical properties of crystals*. Springer-Verlag, 1987. 21
- [38] B. Boulanger and G. Marnier, “Field factor calculation for the study of the relationships between all the three-wave nonlinear optical interactions in uniaxial and biaxial crystals,” *Journal of Physics: Condensed Matter*, vol. 3, no. 43, p. 8327, 1991. 24
- [39] M. Hobden, “Phase-matched second-harmonic generation in biaxial crystals,” *Journal of Applied Physics*, vol. 38, no. 11, pp. 4365–4372, 2004. 24
- [40] B. Boulanger, J. Fève, and G. Marnier, “Field-factor formalism for the study of the tensorial symmetry of four-wave nonlinear optical parametric interactions in uniaxial and biaxial crystals,” *Physical Review E*, vol. 48, pp. 4730–4751, Dec 1993. 24, 78
- [41] M. Adams, *An introduction to optical waveguides*. Wiley, 1981. 26
- [42] F. Mitschke, *Fiber optics: physics and technology*. Springer, 2009. 26, 27, 30, 32
- [43] C. Alhenc-Gelas, P. Bourdon, G. Canat, F. Druon, and A. Durecu, “Theoretical and experimental study of microstructured chalcogenide As₂S₃ fibers for frequency conversion,” in *Advances in Optical Materials*. Optical Society of America, 2011, p. AITHD5. 26, 160

-
- [44] C. Alhenc-Gelas, “Etude de la conversion de fréquence par amplification paramétrique dans les fibres optiques transparentes dans l’infrarouge,” Ph.D. dissertation, Université Paris-Sud XI, 2012. [26](#), [27](#), [155](#), [157](#), [158](#), [159](#)
 - [45] C. Lin, W. Reed, H.-T. Shang, and A. Pearson, “Phase matching in the minimum-chromatic-dispersion region of single-mode fibers for stimulated four-photon mixing,” *Optics Letters*, vol. 6, no. 10, pp. 493–495, 1981. [27](#), [33](#)
 - [46] D. Gloge, “Weakly guiding fibers,” *Applied Optics*, vol. 10, no. 10, pp. 2252–2258, 1971. [27](#), [29](#), [31](#)
 - [47] J. Buck, *Fundamentals of optical fibers, chap. 3*, 2nd ed. Wiley, 2004. [28](#), [31](#)
 - [48] J. M. Jonathan, “Guided and coupled waves: an overview of optical fiber-sand derived components for optical communications,” Institut d’Optique, <http://paristech.institutoptique.fr/site.php?id=368&fileid=6868>, 2013. [28](#)
 - [49] D. Gloge, “Dispersion in weakly guiding fibers,” *Applied Optics*, vol. 10, no. 11, pp. 2442–2445, 1971. [28](#)
 - [50] A. Snyder and W. Young, “Modes of optical waveguides,” *Journal of the Optical Society of America*, vol. 68, no. 3, pp. 297–309, 1978. [28](#), [29](#), [30](#)
 - [51] J. Buck, *Nonlinear fiber optics*, 3rd ed. Wiley Series in Pure and Applied Optics, 1995. [28](#)
 - [52] P. Lecoy, *Fiber-optic communications*. John Wiley & Sons, 2010, vol. 51. [30](#)
 - [53] P.-A. Belanger, *Optical fiber theory: A supplement to applied electromagnetism*. World Scientific, 1993, vol. 5. [30](#)
 - [54] R. Stolen and J. Bjorkholm, “Parametric amplification and frequency conversion in optical fibers,” *Quantum Electronics, IEEE Journal of*, vol. 18, no. 7, pp. 1062–1072, 1982. [33](#), [137](#)
 - [55] G. I. Stegeman and R. H. Stolen, “Waveguides and fibers for nonlinear optics,” *Journal of the Optical Society of America B: Optical Physics*, vol. 6, no. 4, pp. 652–62, 1989. [33](#), [137](#)
 - [56] B. Huttner, S. Serulnik, and Y. Ben-Aryeh, “Quantum analysis of light propagation in a parametric amplifier,” *Physical Review A*, vol. 42, pp. 5594–5600, 1990. [35](#), [37](#)
 - [57] I. Abram, “Quantum theory of light propagation: Linear medium,” *Physical Review A*, vol. 35, no. 11, p. 4661, 1987. [35](#)
 - [58] L. Mandel and E. Wolf, *Optical coherence and quantum optics*. Cambridge university press, 1995. [35](#), [42](#), [43](#)
 - [59] K. Blow, R. Loudon, S. Phoenix, and T. Shepherd, “Continuum fields in quantum optics,” *Physical Review A*, vol. 42, no. 7, p. 4102, 1990. [35](#), [36](#), [146](#)
-

- [60] B. Dayan, “Theory of two-photon interactions with broadband down-converted light and entangled photons,” *Physical Review A*, vol. 76, no. 4, p. 043813, 2007. [35](#), [43](#), [53](#), [54](#), [58](#)
- [61] M. Scully and M. Zubairy, *Quantum optics*, 6th ed. Cambridge University Press, 2008. [41](#)
- [62] R. Glauber, “Coherent and incoherent states of the radiation field,” *Physical Review*, vol. 131, no. 6, p. 2766, 1963. [41](#)
- [63] E. Schrödinger, “Die gegenwärtige Situation in der Quantenmechanik,” *Naturwissenschaften*, vol. 23, p. 844, 1935. [42](#), [46](#)
- [64] M. Rubin, D. Klyshko, Y. Shih, and A. Sergienko, “Theory of two-photon entanglement in type-II optical parametric down-conversion,” *Physical Review A*, vol. 50, no. 6, pp. 5122–5133, 1994. [42](#)
- [65] R. H. Brown and R. Twiss, “Correlation between photons in two coherent beams of light,” *Nature*, vol. 177, no. 4497, pp. 27–29, 1956. [42](#)
- [66] B. Schumaker, “Noise in homodyne detection,” *Optics Letters*, vol. 9, no. 5, pp. 189–191, 1984. [42](#)
- [67] E. Wigner, “On the quantum correction for thermodynamic equilibrium,” *Physical Review*, vol. 40, no. 5, p. 749, 1932. [43](#)
- [68] U. Leonhardt, *Quantum optics, from quantum measurements to black holes*. Cambridge University Press, 2010. [43](#)
- [69] H. Bachor and T. Ralph, *A Guide to Experiments in Quantum Optics*, 2nd ed. Wiley-VCH, 2004. [43](#)
- [70] I. Abram, R. Raj, J. Oudar, and G. Dolique, “Direct observation of the second-order coherence of parametrically generated light,” *Physical Review Letters*, vol. 57, no. 20, p. 2516, 1986. [43](#), [58](#)
- [71] A. Einstein, B. Podolsky, and N. Rosen, “Can quantum-mechanical description of physical reality be considered complete?” *Physical Review*, vol. 47, no. 10, pp. 777–780, 1935. [46](#)
- [72] J. S. Bell, “On the Einstein-Podolsky-Rosen paradox.” *Physics*, vol. 1, no. 3, pp. 195–200, 1964. [46](#)
- [73] A. Aspect, J. Dalibard, and G. Roger, “Experimental test of Bell’s inequalities using time-varying analyzers,” *Physical Review Letters*, vol. 49, no. 25, p. 1804, 1982. [46](#)
- [74] A. Aspect, P. Grangier, G. Roger *et al.*, “Experimental realization of Einstein-Podolsky-Rosen-Bohm Gedankenexperiment: a new violation of Bell’s inequalities,” *Physical Review Letters*, vol. 49, no. 2, pp. 91–94, 1982. [46](#)
- [75] W. Tittel, J. Brendel, H. Zbinden, and N. Gisin, “Violation of Bell inequalities by photons more than 10 km apart,” *Physical Review Letters*, vol. 81, no. 17, p. 3563, 1998. [47](#)

-
- [76] W. Dür, G. Vidal, and J. I. Cirac, “Three qubits can be entangled in two inequivalent ways,” *Physical Review A*, vol. 62, no. 6, p. 062314, 2000. 47
- [77] A. Acin, D. Bruß, M. Lewenstein, and A. Sanpera, “Classification of mixed three-qubit states,” *Physical Review Letters*, vol. 87, no. 4, p. 040401, 2001. 47
- [78] D. M. Greenberger, M. A. Horne, A. Shimony, and A. Zeilinger, “Bell’s theorem without inequalities,” *American Journal of Physics*, vol. 58, no. 12, pp. 1131–1143, 1990. 47, 189
- [79] J. Franson, “Bell inequality for position and time,” *Physical Review Letters*, vol. 62, no. 19, pp. 2205–2208, 1989. 47
- [80] C. Law, I. Walmsley, and J. Eberly, “Continuous frequency entanglement: effective finite Hilbert space and entropy control,” *Physical Review Letters*, vol. 84, no. 23, p. 5304, 2000.
- [81] J. C. Howell, R. S. Bennink, S. J. Bentley, and R. Boyd, “Realization of the Einstein-Podolsky-Rosen paradox using momentum-and position-entangled photons from spontaneous parametric down conversion,” *Physical Review Letters*, vol. 92, pp. 210 403–210 403, 2004. 47
- [82] P. G. Kwiat, “Hyper-entangled states,” *Journal of Modern Optics*, vol. 44, no. 11-12, pp. 2173–2184, 1997. 47
- [83] J. Wen and M. H. Rubin, “Distinction of tripartite Greenberger-Horne-Zeilinger and W states entangled in time (or energy) and space,” *Physical Review A*, vol. 79, no. 2, p. 025802, 2009. 47
- [84] C. Śliwa and K. Banaszek, “Conditional preparation of maximal polarization entanglement,” *Physical Review A*, vol. 67, no. 3, p. 030101, 2003. 48
- [85] S. Barz, G. Cronenberg, A. Zeilinger, and P. Walther, “Heralded generation of entangled photon pairs,” *Nature Photonics*, vol. 4, no. 8, pp. 553–556, 2010. 48
- [86] C. Wagenknecht, C.-M. Li, A. Reingruber, X.-H. Bao, A. Goebel, Y.-A. Chen, Q. Zhang, K. Chen, and J.-W. Pan, “Experimental demonstration of a heralded entanglement source,” *Nature Photonics*, vol. 4, no. 8, pp. 549–552, 2010. 48
- [87] A. K. Ekert, “Quantum cryptography based on Bell’s theorem,” *Physical Review Letters*, vol. 67, no. 6, pp. 661–663, 1991. 48
- [88] D. Naik, C. Peterson, A. White, A. Berglund, and P. Kwiat, “Entangled state quantum cryptography: Eavesdropping on the Ekert protocol,” *Physical Review Letters*, vol. 84, no. 20, p. 4733, 2000. 48
- [89] W. Tittel, J. Brendel, H. Zbinden, and N. Gisin, “Quantum cryptography using entangled photons in energy-time Bell states,” *Physical Review Letters*, vol. 84, no. 20, p. 4737, 2000. 48
-

- [90] T. Jennewein, C. Simon, G. Weihs, H. Weinfurter, and A. Zeilinger, “Quantum cryptography with entangled photons,” *Physical Review Letters*, vol. 84, no. 20, p. 4729, 2000. 48
- [91] R. Ursin, F. Tiefenbacher, T. Schmitt-Manderbach, H. Weier, T. Scheidl, M. Lindenthal, B. Blauensteiner, T. Jennewein, J. Perdigues, P. Trojek, B. Omer, M. Furst, M. Meyenburg, J. Rarity, Z. Sodnik, C. Barbieri, H. Weinfurter, and A. Zeilinger, “Entanglement-based quantum communication over 144 km,” *Nature Physics*, vol. 3, no. 7, pp. 481–486, 2007. 48
- [92] A. Karlsson and M. Bourennane, “Quantum teleportation using three-particle entanglement,” *Physical Review A*, vol. 58, pp. 4394–4400, 1998. 48
- [93] W. K. Wootters and W. H. Zurek, “A single quantum cannot be cloned,” *Nature*, vol. 299, no. 5886, pp. 802–803, 1982. 48
- [94] D. Bruß, D. P. DiVincenzo, A. Ekert, C. A. Fuchs, C. Macchiavello, and J. A. Smolin, “Optimal universal and state-dependent quantum cloning,” *Physical Review A*, vol. 57, no. 4, p. 2368, 1998. 48
- [95] V. Bužek and M. Hillery, “Quantum copying: Beyond the no-cloning theorem,” *Physical Review A*, vol. 54, no. 3, p. 1844, 1996. 48
- [96] J. Douady, “Génération de tierce harmonique et production de triplets de photons pour l’optique quantique,” Ph.D. dissertation, Université Joseph Fourier, 2004. 49, 51
- [97] J. Douady and B. Boulanger, “Calculation of quadratic cascading contributions associated with a phase-matched cubic frequency difference generation in a KTiOPO_4 crystal,” *Journal of Optics A: Pure and Applied Optics*, vol. 7, no. 9, p. 467, 2005. 50, 51
- [98] B. Stuart, M. Feit, A. Rubenchik, B. Shore, and M. Perry, “Laser-induced damage in dielectrics with nanosecond to subpicosecond pulses,” *Physical Review Letters*, vol. 74, no. 12, p. 2248, 1995. 50
- [99] B. Boulanger, I. Rousseau, and G. Marnier, “Cubic optical nonlinearity of KTiOPO_4 ,” *Journal of Physics B: Atomic, Molecular and Optical Physics*, vol. 32, no. 2, p. 475, 1999. 50, 70
- [100] F. Gravier and B. Boulanger, “Triple-photon generation: comparison between theory and experiment,” *Journal of the Optical Society of America B*, vol. 25, no. 1, pp. 98–102, 2008. 51, 86
- [101] F. Gravier, “Conception et étude d’un générateur et d’un corrélateur de triplets de photons basés sur KTiOPO_4 et TiO_2 ,” Ph.D. dissertation, Université Joseph Fourier, 2007. 51
- [102] A. Dot, A. Borne, B. Boulanger, P. Segonds, C. Félix, K. Bencheikh, and J. A. Levenson, “Energetic and spectral properties of triple photon downconversion in a phase-matched KTiOPO_4 crystal,” *Optics Letters*, vol. 37, no. 12, pp. 2334–2336, 2012. 51

-
- [103] F. Smektala, C. Quemard, V. Couderc, and A. Barthélémy, “Non-linear optical properties of chalcogenide glasses measured by Z-scan,” *Journal of Non-Crystalline Solids*, vol. 274, no. 1, pp. 232–237, 2000. 51, 156
- [104] G. Boudebs, F. Sanchez, J. Troles, and F. Smektala, “Nonlinear optical properties of chalcogenide glasses: comparison between Mach–Zehnder interferometry and Z-scan techniques,” *Optics Communications*, vol. 199, no. 5, pp. 425–433, 2001. 156
- [105] J. Douady, B. Boulanger, E. Fuchs, F. Smektala, and J. Troles, “Symmetry and phase-matching properties of third-harmonic generation under the photoelastic effect in Ge-As-Se chalcogenide glasses,” *Journal of the Optical Society of America B*, vol. 22, no. 7, pp. 1486–1492, 2005. 51, 130, 155, 156
- [106] J. Feve and B. Boulanger, “Suppression of quadratic cascading in four-photon interactions using periodically poled media,” *Physical Review A*, vol. 65, no. 6, p. 063814, 2002. 51
- [107] F. Gravier and B. Boulanger, “Cubic parametric frequency generation in rutile single crystal,” *Optics Express*, vol. 14, no. 24, pp. 11 715–11 720, 2006. 51, 76, 77, 80, 82, 83, 84, 87, 192
- [108] F. Gravier and B. Boulanger, “Third-order frequency generation in TiO_2 rutile and KTiOPO_4 ,” *Optical Materials*, vol. 30, no. 1, pp. 33–36, 2007. 51, 76, 86
- [109] M. Corona, K. Garay-Palmett, and A. B. U’Ren, “Experimental proposal for the generation of entangled photon triplets by third-order spontaneous parametric downconversion in optical fibers,” *Optics Letters*, vol. 36, no. 2, pp. 190–192, 2011. 52, 145, 146
- [110] K. Bencheikh, S. Richard, G. Mélin, G. Krabshuis, F. Gooijer, and J. Levenson, “Phase-matched third-harmonic generation in highly germanium-doped fiber,” *Optics Letters*, vol. 37, no. 3, pp. 289–291, 2012. 52, 108
- [111] J. Gabriagues, “Third-harmonic and three-wave sum-frequency light generation in an elliptical-core optical fiber,” *Optics Letters*, vol. 8, no. 3, pp. 183–185, 1983. 52, 143
- [112] A. Efimov, A. Taylor, F. Omenetto, J. Knight, W. Wadsworth, and P. Russell, “Phase-matched third harmonic generation in microstructured fibers,” *Optics Express*, vol. 11, no. 20, pp. 2567–2576, 2003. 52
- [113] V. Grubsky and J. Feinberg, “Phase-matched third-harmonic UV generation using low-order modes in a glass micro-fiber,” *Optics Communications*, vol. 274, no. 2, pp. 447–450, 2007. 52
- [114] B. Kibler, R. Fischer, G. Genty, D. N. Neshev, and J. M. Dudley, “Simultaneous fs pulse spectral broadening and third harmonic generation in highly nonlinear fibre: experiments and simulations,” *Applied Physics B*, vol. 91, no. 2, pp. 349–352, 2008. 52
- [115] R. Stolen and W. Leibolt, “Optical fiber modes using stimulated four photon mixing,” *Applied Optics*, vol. 15, no. 1, pp. 239–243, 1976. 52
-

- [116] L. Misoguti, S. Backus, C. Durfee, R. Bartels, M. Murnane, and H. Kapteyn, “Generation of broadband VUV light using third-order cascaded processes,” *Physical Review Letters*, vol. 87, no. 1, p. 013601, 2001. [52](#)
- [117] V. Grubsky and A. Savchenko, “Glass micro-fibers for efficient third harmonic generation,” *Optics Express*, vol. 13, no. 18, pp. 6798–6806, 2005. [52](#)
- [118] K. Tarnowski, B. Kibler, C. Finot, and W. Urbanczyk, “Quasi-phase-matched third harmonic generation in optical fibers using refractive-index gratings,” *IEEE Journal of Quantum Electronics*, vol. 47, no. 5, pp. 622–629, 2011. [52](#)
- [119] S. Richard, K. Bencheikh, B. Boulanger, and J. Levenson, “Semiclassical model of triple photons generation in optical fibers,” *Optics Letters*, vol. 36, no. 15, pp. 3000–3002, 2011. [52](#), [145](#), [147](#)
- [120] A. Dot, “Etude théorique et expérimentale de la génération et des corrélations quantiques de photons triplets générés par interaction non linéaire d’ordre trois,” Ph.D. dissertation, Université de Grenoble, 2011. [53](#), [54](#), [58](#), [59](#), [61](#), [145](#), [188](#)
- [121] S. N. Gupta, “Multiple photon production in electron-positron annihilation,” *Physical Review*, vol. 96, no. 5, p. 1453, 1954. [55](#)
- [122] A. Zeilinger, M. A. Horne, H. Weinfurter, and M. Zukowski, “Three-particle entanglements from two entangled pairs,” *Physical Review Letters*, vol. 78, no. 16, pp. 3031–3034, 1997. [55](#), [190](#)
- [123] M. Eibl, N. Kiesel, M. Bourennane, C. Kurtsiefer, and H. Weinfurter, “Experimental realization of a three-qubit entangled W state,” *Physical Review Letters*, vol. 92, no. 7, p. 63, 2004. [55](#), [62](#)
- [124] J. Rarity and P. Tapster, “Three-particle entanglement from entangled photon pairs and a weak coherent state,” *Physical Review A*, vol. 59, p. 35, 1999. [55](#)
- [125] J. Persson, T. Aichele, V. Zwiller, L. Samuelson, and O. Benson, “Three-photon cascade from single self-assembled InP quantum dots,” *Physical Review B*, vol. 69, no. 23, p. 233314, 2004. [56](#)
- [126] H. Mikami, Y. Li, K. Fukuoka, and T. Kobayashi, “New high-efficiency source of a three-photon W state and its full characterization using quantum state tomography,” *Physical Review Letters*, vol. 95, no. 15, p. 150404, 2005. [56](#), [62](#)
- [127] L. K. Shalm, D. R. Hamel, Z. Yan, C. Simon, K. J. Resch, and T. Jennewein, “Three-photon energy-time entanglement,” *Nature Physics*, vol. 9, no. 1, pp. 19–22, 2013. [56](#), [62](#)
- [128] T. E. Keller, M. H. Rubin, Y. Shih, and L.-A. Wu, “Theory of the three-photon entangled state,” *Physical Review A*, vol. 57, no. 3, p. 2076, 1998. [56](#), [57](#)

-
- [129] D. A. Antonosyan, T. V. Gevorgyan, and G. Y. Kryuchkyan, “Three-photon states in nonlinear crystal superlattices,” *Physical Review A*, vol. 83, no. 4, p. 043807, 2011. 56, 61, 95
- [130] J.-J. Zondy, A. Douillet, A. Tallet, E. Ressayre, and M. Le Berre, “Theory of self-phase-locked optical parametric oscillators,” *Physical Review A*, vol. 63, no. 2, p. 023814, 2001. 56
- [131] G. Y. Kryuchkyan and N. Muradyan, “Toward the multiphoton parametric oscillators,” *Physics Letters A*, vol. 286, no. 2, pp. 113–120, 2001. 56
- [132] P. V. Gorelik, F. N. Wong, D. Kolker, and J.-J. Zondy, “Cascaded optical parametric oscillation with a dual-grating periodically poled lithium niobate crystal,” *Optics Letters*, vol. 31, no. 13, pp. 2039–2041, 2006. 56
- [133] H. Guo, Y. Qin, and S. Tang, “Parametric downconversion via cascaded optical nonlinearities in an aperiodically poled MgO:LiNbO₃ superlattice,” *Applied Physics Letters*, vol. 87, no. 16, p. 161101, 2005. 56
- [134] J. Wen, P. Xu, M. H. Rubin, and Y. Shih, “Transverse correlations in triphoton entanglement: Geometrical and physical optics,” *Physical Review A*, vol. 76, no. 2, p. 023828, 2007. 56
- [135] R. Andrews, H. Rabin, and C. Tang, “Coupled parametric downconversion and upconversion with simultaneous phase matching,” *Physical Review Letters*, vol. 25, no. 13, p. 902, 1970. 56
- [136] A. Ferraro, M. G. Paris, M. Bondani, A. Allevi, E. Puddu, and A. Andreoni, “Three-mode entanglement by interlinked nonlinear interactions in optical χ^2 media,” *Journal of the Optical Society of America B*, vol. 21, no. 6, pp. 1241–1249, 2004. 56
- [137] J. Wen, E. Oh, and S. Du, “Tripartite entanglement generation via four-wave mixings: narrowband triphoton W state,” *Journal of the Optical Society of America B*, vol. 27, no. 6, pp. A11–A20, 2010. 57
- [138] K. Wódkiewicz, L. Wang, and J. Eberly, “Perfect correlations of three-particle entangled states in cavity QED,” *Physical Review A*, vol. 47, no. 4, p. 3280, 1993. 57
- [139] A. Rauschenbeutel, G. Nogues, S. Osnaghi, P. Bertet, M. Brune, J.-M. Raimond, and S. Haroche, “Step-by-step engineered multiparticle entanglement,” *Science*, vol. 288, no. 5473, pp. 2024–2028, 2000. 57
- [140] B. Dayan, A. Pe’er, A. A. Friesem, and Y. Silberberg, “Two photon absorption and coherent control with broadband down-converted light,” *Physical Review Letters*, vol. 93, no. 2, p. 023005, 2004. 58
- [141] A. Pe’Er, B. Dayan, A. A. Friesem, and Y. Silberberg, “Temporal shaping of entangled photons,” *Physical Review Letters*, vol. 94, no. 7, p. 073601, 2005. 58
-

- [142] B. Dayan, Y. Bromberg, I. Afek, and Y. Silberberg, “Spectral polarization and spectral phase control of time-energy entangled photons,” *Physical Review A*, vol. 75, no. 4, p. 043804, 2007. 58
- [143] D. C. Burnham and D. L. Weinberg, “Observation of simultaneity in parametric production of optical photon pairs,” *Physical Review Letters*, vol. 25, no. 2, p. 84, 1970. 58
- [144] V. D’Auria, S. Fornaro, A. Porzio, S. Solimeno, S. Olivares, and M. Paris, “Full characterization of gaussian bipartite entangled states by a single homodyne detector,” *Physical Review Letters*, vol. 102, no. 2, p. 020502, 2009. 61
- [145] T. Gevorgyan and G. Y. Kryuchkian, “Pulsed three-photon light,” *arXiv preprint arXiv:1205.3879*, 2012. 61
- [146] A. Coelho, F. Barbosa, K. Cassemiro, A. Villar, M. Martinelli, and P. Nussenzveig, “Three-color entanglement,” *Science*, vol. 326, no. 5954, pp. 823–826, 2009. 62, 95
- [147] “<http://www.unitedcrystals.com/ktpprop.html>.” 68
- [148] “<http://www.cristal-laser.com/>.” 70
- [149] B. Boulanger, M. Fejer, R. Blachman, and P. Bordui, “Study of KTiOPO₄ gray-tracking at 1064, 532, and 355 nm,” *Applied Physics Letters*, vol. 65, no. 19, pp. 2401–2403, 1994. 71, 131
- [150] A. Gerrard and J. M. Burch, “Introduction to matrix methods in optics,” 1994. 72, 82
- [151] Y. W. Lee, J. H. Yi, Y. H. Cha, Y. J. Rhee, B. C. Lee, and B. D. Yoo, “Numerical analysis of soft-aperture Kerr-lens mode locking in Ti:Sapphire laser cavities by using nonlinear ABCD Matrices,” *Journal of the Korean Physical Society*, vol. 46, no. 5, pp. 1131–1136, 2005. 73
- [152] V. Magni, G. Cerullo, and S. De Silvestri, “ABCD matrix analysis of propagation of Gaussian beams through Kerr media,” *Optics Communications*, vol. 96, no. 4, pp. 348–355, 1993. 73
- [153] M. Straumanis, T. Ejima, and W. James, “The TiO₂ phase explored by the lattice constant and density method,” *Acta Crystallographica*, vol. 14, no. 5, pp. 493–497, 1961. 76
- [154] “Data from Almaz Optics Inc. www.almazoptics.com/TiO2.htm.” 76, 83, 84, 85, 192
- [155] J. R. DeVore, “Refractive indices of rutile and sphalerite,” *Journal of the Optical Society of America*, vol. 41, no. 6, pp. 416–417, 1951. 84, 85, 192
- [156] J. Rams, A. Tejada, and J. Cabrera, “Refractive indices of rutile as a function of temperature and wavelength,” *Journal of Applied Physics*, vol. 82, no. 3, pp. 994–997, 1997. 83, 84, 85, 192
- [157] D. C. Cronmeyer, “Electrical and optical properties of rutile single crystals,” *Physical Review*, vol. 87, no. 5, p. 876, 1952. 76, 84, 85, 192

-
- [158] N. Khadzhiiski and N. Koroteev, “Coherent raman ellipsometry of crystals: determination of the components and the dispersion of the third-order nonlinear susceptibility tensor of rutile,” *Optics Communications*, vol. 42, no. 6, pp. 423–427, 1982. 77, 87
- [159] R. Adair, L. Chase, and S. A. Payne, “Nonlinear refractive index of optical crystals,” *Physical Review B*, vol. 39, no. 5, p. 3337, 1989. 77
- [160] T. Hashimoto, T. Yoko, and S. Sakka, “Sol-gel preparation and third-order nonlinear optical properties of TiO_2 thin films,” *Bulletin of the Chemical Society of Japan*, vol. 67, no. 3, pp. 653–660, 1994. 77
- [161] H. Long, A. Chen, G. Yang, Y. Li, and P. Lu, “Third-order optical nonlinearities in anatase and rutile TiO_2 thin films,” *Thin Solid Films*, vol. 517, no. 19, pp. 5601–5604, 2009. 77
- [162] M. Lines, “Influence of d orbitals on the nonlinear optical response of transparent transition-metal oxides,” *Physical Review B*, vol. 43, no. 14, p. 11978, 1991. 77
- [163] J. Feve, B. Boulanger, and Y. Guillien, “Efficient energy conversion for cubic third-harmonic generation that is phase matched in KTiOPO_4 ,” *Optics Letters*, vol. 25, no. 18, pp. 1373–1375, 2000. 78
- [164] G. Marnier and B. Boulanger, “The sphere method: A new technique in linear and nonlinear crystalline optical studies,” *Optics Communications*, vol. 72, no. 3, pp. 139–143, 1989. 79
- [165] B. Boulanger, P. Segonds, J. Fève, O. Pacaud, B. Ménaert, and J. Zaccaro, “Spheres and cylinders in parametric nonlinear optics,” *Optical Materials*, vol. 26, no. 4, pp. 459–464, 2004. 79
- [166] O. Pacaud, “Oscillateurs paramétriques optiques basés sur des cristaux de géométrie cylindrique,” Ph.D. dissertation, Université Joseph Fourier, 2001. 79, 80
- [167] O. Pacaud, J. Fève, B. Boulanger, and B. Ménaert, “Cylindrical KTiOPO_4 crystal for enhanced angular tunability of phase-matched optical parametric oscillators,” *Optics Letters*, vol. 25, no. 10, pp. 737–739, 2000. 80
- [168] Y. Guillien, B. Ménaert, J. Fève, P. Segonds, J. Douady, B. Boulanger, and O. Pacaud, “Crystal growth and refined Sellmeier equations over the complete transparency range of RbTiOPO_4 ,” *Optical Materials*, vol. 22, no. 2, pp. 155–162, 2003. 81
- [169] “Data from <http://refractiveindex.info/?shelf=glass&book=BK7&page=SCHOTT>.” 82
- [170] R. C. Miller, “Optical second harmonic generation in piezoelectric crystals,” *Applied Physics Letters*, vol. 5, no. 1, pp. 17–19, 1964. 86
- [171] S. Reynaud, “Generation of twin photon beams by a nondegenerate optical parametric oscillator,” *Europhysics Letters*, vol. 4, no. 4, p. 427, 1987. 94
-

- [172] M. Ebrahimzadeh, “Mid-infrared ultrafast and continuous-wave optical parametric oscillators,” in *Solid-state mid-infrared laser sources*. Springer, 2003, pp. 184–224. [94](#)
- [173] A. S. Villar, M. Martinelli, C. Fabre, and P. Nussenzveig, “Direct production of tripartite pump-signal-idler entanglement in the above-threshold optical parametric oscillator,” *Physical Review Letters*, vol. 97, no. 14, p. 140504, 2006. [95](#)
- [174] E. Rosencher and C. Fabre, “Oscillation characteristics of continuous-wave optical parametric oscillators: beyond the mean-field approximation,” *Journal of the Optical Society of America B*, vol. 19, no. 5, pp. 1107–1116, 2002. [97](#)
- [175] A. Godard and E. Rosencher, “Energy yield of pulsed optical parametric oscillators: a rate-equation analysis,” *Quantum Electronics, IEEE Journal of*, vol. 40, no. 6, pp. 784–790, 2004. [97](#)
- [176] I. Malitson, “Interspecimen comparison of the refractive index of fused silica,” *Journal of the Optical Society of America*, vol. 55, no. 10, pp. 1205–1208, 1965. [108](#), [109](#)
- [177] J. W. Fleming, “Dispersion in $\text{GeO}_2 - \text{SiO}_2$ glasses,” *Applied Optics*, vol. 23, no. 24, pp. 4486–4493, 1984. [108](#), [109](#)
- [178] A. Wada, S. Okude, T. Sakai, and R. Yamauchi, “ GeO_2 concentration dependence of nonlinear refractive index coefficients of silica-based optical fibers,” *Electronics and Communications in Japan (Part I: Communications)*, vol. 79, no. 11, pp. 12–19, 1996. [109](#)
- [179] M. A. Bandres and J. Gutiérrez-Vega, “Ince-Gaussian beams,” *Optics Letters*, vol. 29, no. 2, pp. 144–146, 2004. [118](#)
- [180] W. N. Plick, M. Krenn, R. Fickler, S. Ramelow, and A. Zeilinger, “Quantum orbital angular momentum of elliptically symmetric light,” *Physical Review A*, vol. 87, no. 3, p. 033806, 2013. [118](#), [119](#)
- [181] M. A. Bandres and J. C. Gutiérrez-Vega, “Ince-Gaussian modes of the paraxial wave equation and stable resonators,” *Journal of the Optical Society of America A*, vol. 21, no. 5, pp. 873–880, 2004. [118](#)
- [182] M. A. Bandres, “Elegant ince-gaussian beams,” *Optics Letters*, vol. 29, no. 15, pp. 1724–1726, 2004. [119](#)
- [183] M. A. Bandres, J. C. Gutiérrez-Vega *et al.*, “Elliptical beams,” *Optics Express*, vol. 16, no. 25, pp. 21 087–21 092, 2008. [119](#)
- [184] B. Morasse, S. Chatigny, C. Desrosiers, É. Gagnon, M.-A. Lapointe, and J.-P. de Sandro, “Simple design for singlemode high power CW fiber laser using multimode high NA fiber,” in *SPIE LASE: Lasers and Applications in Science and Engineering*. International Society for Optics and Photonics, 2009, pp. 719 505–719 505. [122](#)
- [185] C.-L. Chen, “Excitation of higher order modes in optical fibers with parabolic index profile,” *Applied Optics*, vol. 27, no. 11, pp. 2353–2356, 1988. [140](#), [149](#), [150](#)

-
- [186] “<http://dariopolli.wordpress.com/coherent-raman/>.” 142
- [187] D. Nicácio, E. Gouveia, N. M. Borges, and A. Gouveia-Neto, “Third-harmonic generation in GeO₂-doped silica single-mode optical fibers,” *Applied Physics Letters*, vol. 62, no. 18, pp. 2179–2181, 1993. 143
- [188] R. Stolen and E. Ippen, “Raman gain in glass optical waveguides,” *Applied Physics Letters*, vol. 22, no. 6, pp. 276–278, 1973. 143
- [189] E. Rosencher and B. Vinter, *Optoelectronics*. Cambridge University Press, 2002. 152
- [190] J. Rothman, E. de Borniol, S. Bisotto, L. Mollard, F. Guellec, F. Pistone, S. Courtas, and X. Lefoule, “HgCdTe APD-Focal Plane Array development at DEFIR for low flux and photon-counting applications,” in *Quantum of Quasars workshop*, 2009. 153
- [191] J. Sanghera, C. Florea, L. Shaw, P. Pureza, V. Nguyen, M. Bashkansky, Z. Dutton, and I. Aggarwal, “Non-linear properties of chalcogenide glasses and fibers,” *Journal of Non-Crystalline Solids*, vol. 354, no. 2, pp. 462–467, 2008. 155, 156
- [192] G. Lenz, J. Zimmermann, T. Katsufuji, M. Lines, H. Hwang, S. Spälter, R. Slusher, S.-W. Cheong, J. Sanghera, and I. Aggarwal, “Large Kerr effect in bulk Se-based chalcogenide glasses,” *Optics Letters*, vol. 25, no. 4, pp. 254–256, 2000. 156
- [193] R. E. Slusher, G. Lenz, J. Hodelin, J. Sanghera, L. B. Shaw, and I. D. Aggarwal, “Large Raman gain and nonlinear phase shifts in high-purity As₂Se₃ chalcogenide fibers,” *Journal of the Optical Society of America B*, vol. 21, no. 6, pp. 1146–1155, 2004. 156
- [194] R. Stegeman, G. Stegeman, P. Delfyett, L. Petit, N. Carlie, K. Richardson, and M. Couzi, “Raman gain measurements and photo-induced transmission effects of germanium-and arsenic-based chalcogenide glasses,” *Optics Express*, vol. 14, no. 24, pp. 11 702–11 708, 2006. 156
- [195] J. Troles, Q. Coulombier, G. Canat, M. Duhant, W. Renard, P. Toupin, L. Calvez, G. Renversez, F. Smektala, M. El Amraoui, J. Adam, T. Chartier, D. Mechin, and L. Brilland, “Low loss microstructured chalcogenide fibers for large non linear effects at 1995 nm,” *Optics Express*, vol. 18, no. 25, pp. 26 647–26 654, 2010. 156
- [196] O. P. Kulkarni, C. Xia, D. J. Lee, M. Kumar, A. Kuditcher, M. N. Islam, F. L. Terry, M. J. Freeman, B. G. Aitken, S. C. Currie, J. E. McCarthy, M. L. Powley, and D. A. Nolan, “Third order cascaded Raman wavelength shifting in chalcogenide fibers and determination of Raman gain coefficient,” *Optics Express*, vol. 14, no. 17, pp. 7924–7930, 2006. 156
- [197] J. Sanghera and I. Aggarwal, “Active and passive chalcogenide glass optical fibers for IR applications: a review,” *Journal of Non-Crystalline Solids*, vol. 256, pp. 6–16, 1999. 156
- [198] R. T. White and T. M. Monro, “Cascaded raman shifting of high-peak-power nanosecond pulses in As₂S₃ and As₂Se₃ optical fibers,” *Optics Letters*, vol. 36, no. 12, pp. 2351–2353, 2011. 156
-

- [199] M. Duhant, “Etude des sources supercontinuum à fibres transparentes dans le moyen infrarouge,” Ph.D. dissertation, Université de Bourgogne, 2012. 155, 157
- [200] P. Kaiser, E. Marcatili, and S. Miller, “A new optical fiber,” *Bell System Technical Journal*, vol. 52, no. 2, pp. 265–269, 1973. 155
- [201] J. Knight, T. Birks, P. S. J. Russell, and D. Atkin, “All-silica single-mode optical fiber with photonic crystal cladding,” *Optics Letters*, vol. 21, no. 19, pp. 1547–1549, 1996. 155, 158
- [202] T. M. Monro, Y. D. West, D. W. Hewak, N. G. Broderick, and D. J. Richardson, “Chalcogenide holey fibres,” *Electronics Letters*, vol. 36, no. 24, pp. 1998–2000, 2000. 155, 158
- [203] T. A. Birks, J. C. Knight, and P. S. J. Russell, “Endlessly single-mode photonic crystal fiber,” *Optics Letters*, vol. 22, no. 13, pp. 961–963, 1997. 157, 159
- [204] P. Russell, “Photonic crystal fibers,” *Science*, vol. 299, no. 5605, pp. 358–362, 2003. 157
- [205] J. M. Dudley, G. Genty, and S. Coen, “Supercontinuum generation in photonic crystal fiber,” *Reviews of Modern Physics*, vol. 78, no. 4, p. 1135, 2006. 157
- [206] M. El-Amraoui, G. Gadret, J. Jules, J. Fatome, C. Fortier, F. Désévéday, I. Skripatchev, Y. Messaddeq, J. Troles, L. Brilland, W. Gao, T. Suzuki, Y. Ohishi, and F. Smektala, “Microstructured chalcogenide optical fibers from As₂S₃ glass: towards new IR broadband sources,” *Optics Express*, vol. 18, no. 25, pp. 26 655–26 665, 2010. 158
- [207] X. Feng, A. K. Mairaj, D. W. Hewak, and T. M. Monro, “Nonsilica glasses for holey fibers,” *Journal of Lightwave Technology*, vol. 23, no. 6, p. 2046, 2005. 158
- [208] F. Désévéday, G. Renversez, L. Brilland, P. Houizot, J. Troles, Q. Coulombier, F. Smektala, N. Traynor, and J.-L. Adam, “Small-core chalcogenide microstructured fibers for the infrared,” *Applied Optics*, vol. 47, no. 32, pp. 6014–6021, 2008. 158
- [209] J. Knight, T. Birks, P. S. J. Russell, and J. De Sandro, “Properties of photonic crystal fiber and the effective index model,” *Journal of the Optical Society of America A*, vol. 15, no. 3, pp. 748–752, 1998. 158
- [210] R. Sinha and A. D. Varshney, “Dispersion properties of photonic crystal fiber: comparison by scalar and fully vectorial effective index methods,” *Optical and Quantum Electronics*, vol. 37, no. 8, pp. 711–722, 2005. 158, 159
- [211] G. Boudebs, S. Cherukulappurath, M. Guignard, J. Troles, F. Smektala, and F. Sanchez, “Linear optical characterization of chalcogenide glasses,” *Optics Communications*, vol. 230, no. 4, pp. 331–336, 2004. 158
- [212] K. N. Park and K. S. Lee, “Improved effective-index method for analysis of photonic crystal fibers,” *Optics Letters*, vol. 30, no. 9, pp. 958–960, 2005. 159, 160

- [213] Y. Li, Y. Yao, M. Hu, L. Chai, and C. Wang, “Improved fully vectorial effective index method for photonic crystal fibers: evaluation and enhancement,” *Applied Optics*, vol. 47, no. 3, pp. 399–406, 2008. 159
- [214] L. D. Bianca, “Modélisation de fibres microstructurées en verres de chalcogénures pour l’amplification paramétrique,” Master’s thesis, Supélec, 2012. 160, 161
- [215] P. Bourdon, A. Durécu, C. Alhenc-Gelas, L. Di Bianca, G. Canat, and F. Druon, “Effective index numerical modelling of microstructured chalcogenide-glass fiber for frequency conversion to the mid-infrared band,” in *SPIE LASE*. International Society for Optics and Photonics, 2013, pp. 86 011L–86 011L. 160
- [216] B. Kuhlmei, R. McPhedran, C. de Sterke, P. Robinson, G. Renversez, and D. Maystre, “Microstructured optical fibers: where’s the edge?” *Optics Express*, vol. 10, no. 22, pp. 1285–1290, 2002. 161
- [217] L. Bigot, P. Roy *et al.*, “Fibres à cristal photonique: 10 ans d’existence et un vaste champ d’applications,” *Images de la physique*, pp. 71–80, 2007. 161

Résumé — Ce travail porte sur la génération directe de triplets de photons par interaction optique non linéaire du troisième ordre avec la matière solide. Les trois photons constituant l'état triplet proviennent de la scission d'un unique photon, et sont donc étroitement corrélés. Des champs supplémentaires peuvent stimuler le processus, et ainsi augmenter son efficacité de conversion, mais au détriment de la conservation des corrélations de l'état triplet. Deux stratégies sont adoptées pour générer efficacement ces triplets tout en conservant leurs propriétés de cohérence. La première porte sur génération de triplets dans des oxydes massifs cristallins, rendue possible à travers la réalisation d'accords de phase par biréfringence. Ces cristaux peuvent être placés en cavité de manière à augmenter artificiellement la longueur d'interaction. Dans ce contexte, KTP et TiO_2 sous sa forme rutile sont étudiés expérimentalement ; la configuration en cavité fait l'objet d'une étude théorique. La seconde stratégie se concentre sur la génération de triplets dans des fibres optiques, à travers un accord de phase modal. Leurs longueurs, le confinement du champ électromagnétique, ainsi que la non-existence de processus quadratiques pouvant polluer la génération de triplets sont des avantages importants. Des expériences de génération de troisième harmonique dans des fibres de silice dopées germanium sont réalisées ; et les propriétés d'accord de phase dans des fibres à cristaux photoniques en chalcogénures sont calculées.

Mots-clefs : interactions cubiques, optique non linéaire, optique cristalline, optique guidée, optique quantique.

Abstract — This work concentrates on the direct generation of triple photons through third-order nonlinear optical interactions with solid-state matter. The three photons constituting the triplet state arise from the splitting of a single photon, and are therefore highly correlated. Additional fields can stimulate this process and thus increase its conversion efficiency, but at the cost of losing the correlations of the triplet states. In order to generate efficiently the triplets while preserving their coherence properties, two strategies are investigated. In the first one, the interaction occurs in oxide bulk crystals, thanks to a birefringent phase matching. These crystals can be put into a cavity so as to artificially increase the interaction length. In this context, KTP and rutile TiO_2 are studied experimentally; the cavity configuration is subjected to a theoretical work. The second strategy focuses on the generation in optical fibers, through a modal phase matching. Their length, the confinement of the electromagnetic field, and the non-existence of polluting second-order nonlinear processes are key advantages. Third-harmonic generation experiments on germanium-doped silica fibers are performed; and phase-matching properties in chalcogenide photonic-crystal fibers are calculated.

Keywords: cubic interactions, nonlinear optics, crystal optics, fiber optics, quantum optics.
